Inkjet Printing for Solid Oxide Electrochemical Reactors

Nicholas M. Farandos

Department of Chemical Engineering

Imperial College London

London SW7 2AZ

United Kingdom

A THESIS SUBMITTED FOR THE DEGREE OF DOCTOR OF PHILOSOPHY OF IMPERIAL COLLEGE LONDON AND THE DIPLOMA OF MEMBERSHIP OF IMPERIAL COLLEGE LONDON

May 2018

Declaration

I hereby declare, that this thesis is my own work and all references made to other work have been acknowledged and referenced in the text.

Copyright Notice

Imperial College of Science, Technology and Medicine, Department of Chemical Engineering.

Title: Inkjet Printing for Solid Oxide Electrochemical Reactors

'The copyright of this thesis rests with the author and is made available under a Creative Commons Attribution Non-Commercial No Derivatives license. Researchers are free to copy, distribute or transmit the thesis on the condition that they attribute it, that they do not use it for commercial purposes and that they do not alter, transform or build upon it. For any reuse or redistribution, researchers must make clear to others the license terms of this work.'

© 2018 Nicholas Farandos

n.farandos14@imperial.ac.uk

Published by:

Nicholas M. Farandos, Department of Chemical Engineering, Imperial College London, South Kensington Campus, London SW7 2AZ, United Kingdom.

www.imperial.ac.uk

Abstract

The increasing reliance of electricity grids globally on intermittent renewable energy resources necessitates large-scale energy storage to balance supply and demand. This could be achieved by converting surplus electrical energy into chemical bonds, and sequentially vice versa, using high-temperature, reversible solid oxide electrochemical reactors (SOERs). However, SOER performances are limited by irreproducible and unpredictable electrode microstructures when fabricated by conventional composite powder-mixing. Hence, this project aimed to test the hypothesis that inkjet printing, a potentially more environmentally benign fabrication technique, could achieve geometrically reproducible SOER microstructures with predictable, and ultimately enhanced, electrochemical performances.

Aqueous-based colloidally stable and printable inks were developed for the conventional SOER materials: yttria-stabilised zirconia (YSZ), gadolinium-doped ceria (CGO), lanthanum strontium manganite (LSM), and NiO. Inkjet-printed LSM deposits from the aqueous-based ink were destroyed by heat treatment, so a butanol-based LSM ink formulation was developed. Inkjet-printed YSZ electrolytes for the SOER: CO/CO_2|Ni-YSZ|YSZ (printed)|YSZ-LSM|LSM|O_2 achieved 0.78 A cm^{-2} at 809 °C in electrolysis mode, a performance comparable to that with electrolytes fabricated by powder-mixing. Inkjet printed composite YSZ-LSM electrodes resulted in enhanced electrochemical performances compared to conventionally-fabricated electrodes in fuel cell and electrolyser modes with H_2 and CO/CO_2, respectively; at 788 °C, a fuel cell peak power density of 0.69 W cm^{-2} and an electrolyser current density of 3.3 A cm^{-2} at the thermoneutral potential difference of *ca*. 1.5 V, were achieved.

To steer 3D geometries to be printed, spatial distributions of overpotentials, gas compositions, and current densities were predicted using finite element models. Inkjet-printed YSZ pillar arrays with diameter and height of *ca*. 35 and 140 μm, respectively, were subsequently inkjet printed with LSM to fabricate the oxygen-electrodes. Their electrochemical performance was *ca*. 50 % lower than that of the composite YSZ-LSM electrodes, due to LSM detaching from the electrolyte during sintering.

To replace the composite electrode support, NiO and LSM inks were used to fabricate the SOER: Ni(O) (printed)|YSZ|LSM (printed). Electrochemical performance was limited by Ni coarsening, but a YSZ pillar support could solve this problem, enabling future SOERs to be completely inkjet-printed.

Acknowledgements

I'd like to thank my project supervisors Professor Geoff Kelsall and Dr. Camille Petit for enabling this project which has been exceptionally rewarding. I am particularly indebted to Geoff for his inspiration, knowledge and guidance, without which, the last three years would not have been possible. Additional thanks go to Imperial College London for awarding me the President's Scholarship to fund this research. I would also like to acknowledge Dr. Tao Li, his supervisor Professor Kang Li, and Dr. Lisa Kleiminger for their technical assistance. Many thanks also go to Franky, Anna, Chi, and all the others at ICL without whose friendship my time here would not have been as enjoyable. I also gratefully acknowledge my parents and wife, Emma, for everything else. I hope that the results of this research justify the time and effort that everybody has given me, unconditionally.

Table of Contents

Nomenclature, Abbreviations, and Acronyms 19

1. Introduction 25
- **1.1. Grid-scale Energy Storage 26**
- **1.2. Energy Storage Technologies 27**
- **1.3. Power-to-gas 29**
  - 1.3.1. Conventional Gas Production Techniques 30
  - 1.3.2. Electrochemical Production of H_2 and CO_2 32

2. Theory and Literature Review 36
- **2.1. Electrochemical Theory 37**
  - 2.1.1. A Select History of Electrochemistry 37
  - 2.1.2. Thermodynamics 38
  - 2.1.3. Kinetics 40
- **2.2. Solid Oxide Electrochemical Reactors 44**
  - 2.2.1. A Brief History of Solid Oxide Electrochemical Reactors 44
  - 2.2.2. Theory of Operation 45
  - 2.2.3. Materials for Solid Oxide Electrochemical Reactors 47
  - 2.2.4. Thermodynamics 49
  - 2.2.5. Kinetics 50
- **2.3. Literature Review 58**
  - 2.3.1. Conventional SOER Fabrication Processes and their Limitations* 58
  - 2.3.2. Introduction to Additive Manufacturing 59
  - 2.3.3. Laser Lithography 60
  - 2.3.4. Micro-extrusion 64
  - 2.3.5. Inkjet Printing 65
  - 2.3.6. Inkjet Printing Ceramics 67
  - 2.3.7. Inkjet Printed Solid Oxide Electrochemical Reactors 76
  - 2.3.8. Electrochemical Characterisation 90
- **2.4. Conclusions 93**

3. Project Objectives 95
- **3.1. Research Objectives Introduction 96**
- **3.2. Aqueous Inks Formulation 96**
- **3.3. Improving Lateral Resolution 96**
- **3.4. Electrochemical Performance Validation 97**
- **3.5. Printing 3D Microstructures 97**
- **3.6. Conclusions 98**

4. Experimental Equipment 99
- **4.1. Ink Formulation and Characterisation 100**
- **4.2. Inkjet Printing 102**
- **4.3. Solid Oxide Electrochemical Reactor Characterisation 103**

5. Inks Formulation 104
- **5.1. Yttria-stabilised Zirconia Ink 105**
  - 5.1.1. Materials and Methods 106
  - 5.1.2. Results and Discussion 108
  - 5.1.3. Conclusions 115
- **5.2. Gadolinium-doped Ceria Ink 115**

5.2.1. Materials and Methods 116
5.2.2. Results and Discussion 118
5.2.3. Conclusions 122
5.3. Lanthanum Strontium Manganite Inks 123
5.3.1. Materials and Methods 126
5.3.2. Results and Discussion 128
5.3.3. Conclusions 135
5.4. Nickel Oxide Ink 135
5.4.1. Materials and Methods 137
5.4.2. Results and Discussion 138
5.4.3. Conclusions 144

6. Inkjet Printed YSZ Electrolyte 145
6.1. Introduction 146
6.2. Materials and Methods 146
6.2.1. Reactor Fabrication 146
6.2.2. Electrochemical Characterisation 146
6.3. Results and Discussion 147
6.3.1. Reactor Fabrication 147
6.3.2. Electrochemical Characterisation 148
6.4. Conclusions 149

7. Inkjet Printed YSZ-LSM Electrode 150
7.1. Introduction 151
7.2. Materials and Methods 151
7.2.1. Substrate Fabrication* 151
7.2.2. Electrolyte Fabrication 152
7.2.3. Oxygen-electrode Fabrication 153
7.2.4. LSM Current Collection Layer Fabrication 153
7.2.5. Electrochemical Characterisation 153
7.3. Results and Discussion 154
7.3.1. Reactor Fabrication 154
7.3.2. Electrochemical Characterisation 156
7.3.3. Hydrogen – Air Fuel Cell Operation 156
7.3.4. Electrolysis with CO/CO_2 158
7.3.5. Electrode Degradation 159
7.4. Conclusions 160

8. Inkjet Printing Microstructures 162
8.1. Introduction 163
8.2. Materials and Methods 163
8.2.1. Ink Formulation 163
8.2.2. Substrate Fabrication 163
8.2.3. Inkjet Printed Microstructures 163
8.3. Results and Discussion 164
8.3.1. Pillar Arrays 164
8.3.2. Square Lattice 165
8.4. Challenges 166
8.5. Conclusions 166

9. Microstructure Electrochemical Simulations 168
9.1. Introduction 169
9.2. Materials and Methods 170

9.2.1. Model Software, Setup, and Hardware ... 170
9.2.2. Governing Equations ... 172
9.2.3. Boundary Conditions ... 173
9.3. Results and Discussion ... 173
9.3.1. Running Simulations ... 173
9.3.2. Spatial Distributions ... 173
9.3.3. Parametric Sweep Results ... 174
9.3.4. Pillar Array Lattice ... 176
9.4. Conclusions ... 177

10. Solid Oxide Electrochemical Reactors with Tailored Microstructure ... 179
10.1. Introduction ... 180
10.1.1. Phase Percolation ... 180
10.1.2. Electrode Degradation ... 180
10.2. Materials and Methods ... 182
10.2.1. Ink Formulation ... 182
10.2.2. Substrate Fabrication ... 182
10.2.3. Reactor Fabrication ... 182
10.2.4. Sintering and Microstructural Characterisation ... 183
10.2.5. Electrochemical Characterisation ... 183
10.3. Results ... 183
10.3.1. Reactor Fabrication ... 183
10.3.2. Electrochemical Characterisation ... 187
10.3.3. Hydrogen – Air Fuel Cell Operation ... 187
10.3.4. Electrolysis with CO/CO_2 ... 188
10.4. Discussion ... 190
10.5. Conclusions ... 192

11. Inkjet Printed NiO Electrode ... 194
11.1. Introduction ... 195
11.2. Materials and Methods ... 195
11.2.1. Substrate ... 195
11.2.2. Fuel-electrode Fabrication ... 195
11.2.3. Oxygen-electrode Fabrication ... 195
11.2.4. Electrochemical Characterisation ... 196
11.3. Results and Discussion ... 196
11.3.1. Reactor Fabrication ... 196
11.3.2. Electrochemical Characterisation ... 197
11.4. Conclusions ... 202

12. Conclusions and Future Work ... 203
12.1. Conclusions ... 204
12.2. Aqueous Inks Formulation ... 204
12.3. Improving Lateral Resolution ... 204
12.4. Inkjet Printing 3D Microstructures ... 205
12.5. Electrochemical Performance Validation ... 206

13. Bibliography ... 207

14. Appendices ... 225
14.1. Appendix 1: DLVO Theory for Aqueous Dispersions ... 225
14.2. Appendix 2: Modelling Centrifugation ... 227
14.3. Appendix 3: Particle Surface Coverage ... 228
14.4. Appendix 4: Natsurf 265 Surface Tension Effects ... 230

14.5. Appendix 5: Critical Cracking Thickness Calculations....231
14.6. Appendix 6: Evaluating Infinite Shear Rate Viscosity....232
14.7. Appendix 7: Formulation of Aqueous LSCF Ink....233
14.7.1. Introduction 233
14.7.2. Materials and Methods 233
14.7.3. Results and Discussion 234
14.8. Appendix 8: Preliminary Electrochemical Characterisation of Inkjet Printed CGO Functional Layers 237
14.8.1. Materials and Methods 237
14.8.2. Results and Discussion 238
14.9. Appendix 9: Electrochemical Characterisation of YSZ-LSM SOERs....241
14.10. Appendix 10: Effect of Scan Rate on CO_2 Reduction Measurements 243
14.11. Appendix 11: Reduction of Oxygen-electrode Overpotential with pO_2 244
14.12. Appendix 12: Electrochemical Characterisations of Pillar-array Oxygen-electrodes .245
14.13. Appendix 13: Collaboration with the Department of Energy Conversion and Storage, Technical University of Denmark (DTU) 247
14.13.1. Introduction 247
14.13.2. Materials and Methods 247
14.13.3. Results and Discussion 248
15. Re-use of Content from the Literature....250

Table	Caption	Page
Table 1	Physical and chemical properties for power-to-gas energy storage materials. IDLH (immediately dangerous to life or health) concentrations are shown. Specific energy is for complete combustion at 298 K (23-27).	30
Table 2	Classification of different fuel cell / electrolyser technologies with details of operation, materials, and maturity. Reproduced and modified from (52).	35
Table 3	The most common materials for the functional layers of SOERs, showing conducted species and chemical formulae (88-93).	48
Table 4	Values of constants and the kinetic parameters for the oxygen-electrode. SOE and SOFC denote overall cell operation, *i.e.* anodic and cathodic electrode polarisation, respectively.	52
Table 5	Values of constants and kinetic parameters for the fuel-electrode operating with H_2 / H_2O mixtures.	54
Table 6	Common doping oxides for zirconia, and the required concentration for full stabilisation (125).	57
Table 7	Conductivity expressions for varying T, for conventional SOER materials (126).	57
Table 8	Dimensionless number constraints for printability and printed deposits without defects.	68
Table 9	Correlations between relative viscosity (μ_r) and intrinsic viscosity ($[\mu]_1$), for ϑ_p in the range $0 \leq \vartheta_p \leq \vartheta_{p,T}$.	70
Table 10	Summary of Inkjet-printed SOER layers.	77
Table 11	Ink formulation and characterisations, with corresponding equipment and experimental procedures.	100
Table 12	The experimental inkjet printing equipment and characterisation procedures.	102
Table 13	Equipment used for producing and electrochemically characterising SOERs in this research project.	103
Table 14	The YSZ binding affinity of common dispersant functional groups (227).	106
Table 15	Physical properties of the ink formulations, with corresponding printing parameters.	110
Table 16	List of electrostatic dispersants, with their chemical description and manufacturer, trialled for aqueous, colloidal LSM.	126
Table 17	Approximate high-frequency arc summit frequencies for each operating temperature, for the SOERs with cathodes sintered at different temperatures.	158
Table 18	Summary of the structural parameters, with values for the porous LSM phase, taken from reference (112).	171
Table 19	The approximate maximum packing densities (specific to projected area) of the regular tessellations, specified by Schläfli symbols, in descending order of density (308).	177
Table 20	Summit frequencies for the Nyquist plots given in **Figure 92** and **Figure 94**.	188

Table 21	The summit frequencies for the Nyquist plots in **Figure 97**, where distinguishable, and OCPDs after NiO reduction.	198
Table 22	The overlapped area for varying droplet diameter overlap, for both square and hexagonal droplet deposition lattices (between pairs and 3 droplets), as a fraction of a single droplet (projected) area.	228
Table 23	Summary of dispersants trialled for aqueous LSCF dispersions.	234
Table 24	Summit frequencies for the arcs in the Nyquist plots in **Figure 111b**.	240
Table 25	Granted copyright permissions for re-use of content from the literature.	250

Figure	Caption	Page
Figure 1	Electrical energy source, and its fraction of the total power generation in the UK, from 1970 - 2016. Data taken from reference (6).	26
Figure 2	(a) Power generation in England and Wales for January 2017; and (b) wind and solar generation as a fraction of their total installed capacities. Data taken from reference (3).	27
Figure 3	(a) Summary of energy storage technologies with characteristic timescales and powers, highlighted by type: electrical (red), mechanical (blue), electrochemical (green), thermal (purple) and chemical (black). Data from (11-14); and (b) maturity of energy storage technologies. Reproduced with permission from (15).	28
Figure 4	Map of hydroelectric facilities in Europe with > 1 MW power. Reproduced from (19).	29
Figure 5	Technology routes to produce common fuels (green) with well-established industrial processes (yellow), without the requirement for fossil fuels. Electrochemical conversion processes are shown in blue. Abundant and environmentally benign raw material inputs are omitted.	32
Figure 6	Electrical power of alkaline (diamond) and PEM (square) electrolysers installed in operational power-to-gas plants worldwide. Reproduced with permission from (33).	33
Figure 7	(a) Voltaic pile (1801 design, R & G Knight, London, England, 1801-1838). Reproduced with permission from (70)	37
Figure 8	Energy balance on an electrochemical reactor.	38
Figure 9	Schematic showing definitions of overpotential and electrode potential for ‘positive’ (pos) and ‘negative’ (neg) electrode potentials for electrolyser and fuel cell operation.	41
Figure 10	Typical fuel cell and electrolyser performance, showing the regimes under which different polarisation loss mechanisms dominate. Reproduced with permission from (52).	42
Figure 11	Schematic of the Gibbs energy relationship between an identical reactant (red) and product (green), and after application of a potential difference (dashed).	42
Figure 12	Schematic showing the principle of operation for an SOFC (black arrows) or SOE (red arrows) operating with H_2 / H_2O and O_2.	47
Figure 13	Potential difference variation with temperature and concentration for reaction (37) coupled with reaction: (a) (39); and (b) (38). Ni/NiO oxidation / reduction potential difference with reaction (37) is shown at equivalent temperature.	49
Figure 14	Effect of temperature on thermoneutral potential difference for CO_2 and H_2O (g) electrolysis. Thermodynamic data from (27).	50
Figure 15	3D reconstructed FIB-SEM image of composite YSZ-LSM electrode. Reproduced with permission from (112).	55
Figure 16	Schematic of the ZrO_2 lattice doped with Y_2O_3, and the creation of an oxygen vacancy.	56
Figure 17	Real Ni-YSZ electrode reconstruction by FIB-SEM showing (a) phases; and (b) percolating (blue) and non-percolating (red) TPBs. Reproduced with permission from (137).	59

Figure 18	Variation of fabrication time (per mm^3) and lateral resolution for different AM technologies, as of 2017, that have been used to fabricate ceramic components (145, 157-170).	60
Figure 19	Schematic of the operating principle of laser lithography printers.	61
Figure 20	Schematic of a 3D single-nozzle micro-extrusion printer, showing the process of solids deposition and the composition of the precursor dispersion.	65
Figure 21	(a) Schematic of a 3D, multi-nozzle, DOD printer; and (b) the appearance of a monolayer of dried deposited droplets in a hexagonal lattice with no inter-droplet overlap.	66
Figure 22	Photographs of droplet ejection and flight for (a, b) $Oh^{-1} > 10$; and (c, d) $1 < Oh^{-1} < 10$. Reproduced with permission from (203).	69
Figure 23	Graph showing the constraints of printability.	69
Figure 24	Effect of (a) P_d on u_0 (at 10 kHz); (b) V_p on droplet volume and u_0 at P_d = 30 μs, 10 kHz; and (c) the droplet volume relationship with reciprocal of frequency (t_p), for a study with paraffin solvent (236), normalised by the optimal P_d (= τ) = 30 μs. Reproduced, with annotations, with permission from (185).	75
Figure 25	SEM photomicrographs showing inkjet printed and sintered (a) YSZ on Ni-YSZ; and (b) SDC on Ni-SDC. Reproduced with permission from (170).	82
Figure 26	SEM photomicrograph of the cross section of the inkjet printed CGO|CGO-LSCF structure layer. Reproduced with permission from (251).	84
Figure 27	SEM photomicrographs showing cracking in the sintered LSCF layers at a luminosity setting of (a) 50; (b) 100; and (c) 150. Reproduced with permission from (249).	86
Figure 28	SEM photomicrograph showing significant coffee staining for an un-sintered inkjet printed LSCF deposit. Reproduced with permission from (250).	87
Figure 29	Cross sectional SEM photomicrographs of layers produced using NiO particles (a) r_p = 15 nm; and (b) r_p = 150 nm. Reproduced with permission from (247).	88
Figure 30	SEM photomicrographs of (a) the hexagonal; (b) square CGO microstructures; and (c) cross-sectional view of the CGO layer on the square LSM substrate. The red shaded region shows where the printed CGO layer exceeded the confines of the substrate. Reproduced with permission from (246).	90
Figure 31	Variation of reported fuel cell mode peak power densities with temperature and inkjet printed YSZ electrolyte thickness. Cross markers indicate testing in dry H_2 at the anode, otherwise humidified H_2 was used; all cathodes were exposed to air. Data from (168, 170, 243, 247, 248, 252).	91
Figure 32	Effect of current density on SOFC potential difference and power density for (a) hand-pasted; and (b) inkjet printed cathode. Reproduced with permission from (252).	92
Figure 33	Variation of zeta potential with pH of 4 commercially-available YSZ powders in water. Reproduced with permission from (261).	105
Figure 34	Zeta potential variation of (a) SA particles in water with varying pH; and (b) SA (blue circle) and FCM (red diamond) YSZ particles with Dispex A40 concentration at neutral conditions.	109

Figure 35	PSDs of the SA (Inks 1, 3, 5) and FCM (Inks 2, 4) particles. Reproduced with permission from (145).	109
Figure 36	SEM surface view images of sintered planar structures fabricated with (a) 12 layers of Ink 1; (b) 25 layers of Ink 2; (c) 16 layers of Ink 3; (d) 40 layers of Ink 4; and (e) 20 layers of Ink 5. Droplet overlap was 40 % for Ink 1, and 20 % for Inks 2–5. Reproduced with permission from (145).	110
Figure 37	Schematic of the inter-particle depletion potential inducing a destabilisation potential as drying progresses.	112
Figure 38	Sintering behaviour with varying temperature of the particles (solid lines) and substrate compositions (dotted lines) used in this study, with respect to (a) original length; and (b) time.	114
Figure 39	Cross sectional SEM photomicrograph of a co-sintered, inkjet printed YSZ layer on NiO-YSZ.	114
Figure 40	(a) Zeta potential – pH relationship for CGO particles dispersed in water; and (b) concentration of dissolved Ce^{IV} / Gd^{III} with varying pH. Reproduced with permission from (275).	116
Figure 41	Photographs of dispersed CGO with Duramax D3005 (3 wt%) over 3 hours, sediment level is shown with dotted red line.	116
Figure 42	Effects on zeta potential of (a) pH; and (b) Dispex A40 concentration at pH 7 for CGO particles in water with 10^{-2} kmol m^{-3} KCl.	119
Figure 43	PSD of the filtered CGO particles in water, by intensity (red) or volume (black) counts.	119
Figure 44	Viscosity – shear rate relationship for the aqueous CGO ink.	120
Figure 45	Dilatometry results for CGO (blue), NiO-CGO (green), and YSZ (red) powders used for the substrate and electrolyte, in terms of length change (solid lines) and rate (dashed lines).	121
Figure 46	SEM images of sintered (a) CGO electrolyte; and (b) co-sintered YSZ electrolyte and CGO boundary layer.	122
Figure 47	Effect of pH on LSM: (a) zeta potential; and (b) constituent elements' aqueous solubilities. Reproduced with permission from (281).	124
Figure 48	(a) Effect of PVP 40000 concentration on average LSM particle size, after initially dispersing (black cross) and after 72 h (orange circle); and (b) photographs of LSM dispersions stabilised with different mass fractions (relative to LSM) of PVP 360000 after standing for 1 h.	124
Figure 49	Variation of zeta potential of LSM particles with (a) pH; and (b) dispersed Aluminon concentration (chemical structure shown).	129
Figure 50	PSD of the LSM particles dispersed in water, after centrifugation and filtering.	129
Figure 51	Viscosity variation with shear rate, for the composite YSZ-LSM BtOH (black) and aqueous (red)-based inks.	130
Figure 52	The optimal pulses for the inks containing LSM (blue and red), and YSZ-LSM (green, black), with solvents in parentheses.	131

Figure 53	Photographs of the printed LSM-YSZ deposit from the aqueous-based ink (a) before heat treatment; (b) after combustion at 550 °C at 1 °C min^{-1}; and (c) after sintering at 1200 °C (different sample).	131
Figure 54	Thermogravimetric analysis (TGA) results of the effective dispersants.	132
Figure 55	SEM surface photomicrographs of the sintered, aqueous-based LSM ink on printed YSZ at (a) low; and (b) high magnification.	132
Figure 56	SEM photomicrographs of (a) side view of the sintered NiO-YSZ|YSZ|YSZ-LSM; and (b) surface view of the YSZ-LSM.	133
Figure 57	Schematic showing how a 'skin' formation results when advection dominates.	134
Figure 58	Variation with pH in water of (a) Ni^{2+} concentration; (b) zeta potential for Ni and NiO particles; and (c) NiO zeta potential dispersed with PMAA. (a) and (b) reproduced (adapted) with permission from (291), copyright (2005), American Chemical Society. (c) reproduced with permission from (292).	136
Figure 59	Variation of NiO zeta potential in water with (a) pH; and (b) Darvan-C concentration.	138
Figure 60	PSD of the NiO particles dispersed in water, by intensity counts.	139
Figure 61	Viscosity of the aqueous NiO ink with varying shear rate.	139
Figure 62	Time-lapse photographs of the NiO ink ejection, with intervals of 5 μs.	140
Figure 63	TGA measurements for Darvan-C.	141
Figure 64	SEM surface view photomicrographs of the printed NiO deposit sintered at (a,c) 1300 °C; and (b) 1400 °C.	141
Figure 65	Top-down view (a) photograph of the sintered NiO (1300 °C) film on YSZ; and (b) SEM-EDX result showing alumina (pink) present on the surface.	142
Figure 66	Post-sintering (a) photograph; (b) cross sectional; and (c) surface view SEM photomicrographs of the NiO films.	144
Figure 67	Planar CO_2(-CO)|Ni-YSZ|YSZ|YSZ-LSM|LSM|O_2 cell experimental assembly. Reproduced with permission from (145).	147
Figure 68	SEM photomicrograph of the cross section of the electrolyser.	148
Figure 69	Effects of temperature and applied current density on CO_2(-CO)|Ni-YSZ|YSZ|YSZ-LSM|LSM|air cell potential differences. Reproduced with permission from (145).	148
Figure 70	Electrochemical impedance spectra of CO_2(-CO)|Ni-YSZ|YSZ|YSZ-LSM|LSM|air cell at OCPD; filled markers indicate frequency decades (10^5 – 0.1 Hz). Reproduced with permission from (145).	149
Figure 71	Droplet photographs of the ejected (a) YSZ; and (b) YSZ-LSM inks from a single nozzle, with time intervals of 10 and 5 μs, respectively. Nozzle number ("3") of the printhead in (b) is shown, and could not be removed from the images.	154
Figure 72	Side view SEM photomicrographs of the SOERs, post-testing; the YSZ-LSM electrode was sintered at 1100 °C (a,c) and 1200 °C (b,d).	155

Figure 73	Effect of current density on power densities for SOERs operating with H_2 at 707, 752, and 788 °C and with the YSZ-LSM electrodes sintered at (a) 1100 °C; and (b) 1200 °C. Cell potential difference scan rate = 20 mV s^{-1}.	157
Figure 74	Nyquist plots for SOERs at OCPD operating with H_2 at 707, 752, and 788 °C; YSZ-LSM electrode sintered at (a) 1100 °C; and (b) 1200 °C. Filled markers indicate order of magnitude frequency intervals over the range 0.1 – 10^5 Hz.	157
Figure 75	Effect of current density on cell potential differences for SOERs with a YSZ-LSM electrode sintered at (a) 1100 °C; and (b) 1200 °C, operating with a CO/CO_2 ratio of 1/9, at 707, 752, and 788 °C. Potential difference scan rate was 60 mV s^{-1}.	159
Figure 76	SEM photomicrographs of a SOER after testing showing (a) 'beaded' droplets of Ag on the surface of the electrolyte; and (b) Ag present near both electrode – electrolyte interfaces.	160
Figure 77	SEM photomicrographs of YSZ pillars on Ni-YSZ substrate. (a) Pillar array at 60° tilt; (b) misplaced droplet (red zone); (c) pillar array at 30° tilt; and (d) showing missing pillars as red circles. Reproduced with permission from (145)	165
Figure 78	SEM photomicrographs of YSZ square scaffolds, with decreasing magnification from (a) – (c). (a) and (b) reproduced with permission from (145).	166
Figure 79	SEM photomicrographs of (a) broken; (b) an array; and (c) high-magnification array YSZ pillars.	166
Figure 80	Variation of the ratio of electrode area to projected area with pillar geometry, for a hexagonal lattice pillar array.	169
Figure 81	(a) Geometry of a pillared electrode; and (b) meshed, on Comsol Multiphysics.	170
Figure 82	Cross section of simulated (symmetrical) SOER geometry.	171
Figure 83	FEA simulations of (a, d) overpotential; (b, e) local current density; and (c, f) oxygen mole fraction under cathodic (a-c) and anodic (d-f) polarisation of |0.3 V|, T = 737 °C.	174
Figure 84	Simulated output current densities with varying pillar height and WE-RE potential difference, under (a-c) cathodic; and (d-f) anodic polarisation for l_p = 30 (a, c, d, f) or 50 μm (b, e), at T = 737 (a, b, d, e) or 826 °C (c, f).	175
Figure 85	Simulation results showing how current density varies with pillar height and l_s/l_p at 826 °C, l_p = 30 μm, under (a) cathodic; and (b) anodic polarisations of |0.25 V|.	176
Figure 86	Schematic of O_2 evolution into non-percolating pores (red shade) during electrolysis.	181
Figure 87	Top-down view photograph of inkjet printed pillar array, before sintering.	184
Figure 88	SEM photomicrographs of the (a) electrolyte; (b) pillar array; and (c) broken pillar.	184
Figure 89	SEM photomicrographs of the pillared oxygen-electrode array with LSM sintered at 1000 °C, post electrochemical characterisation.	185
Figure 90	SEM photomicrographs of the pillared oxygen-electrode array with LSM sintered at 1100 °C, post electrochemical characterisation.	185
Figure 91	Effect of current density on power densities for cells operating with H_2 at 707, 752, and 788 °C with the YSZ-LSM electrodes sintered at (a) 1000 °C; and (b) 1100 °C. Cell potential difference scan rate = 20 mV s^{-1}.	187

Figure 92	Nyquist plots for reactors at open circuit potential and operating with H_2 at 707, 752, and 788 °C. LSM electrode sintered at (a) 1000 °C; and (b) 1100 °C. Filled markers indicate order of magnitude intervals in frequency over 0.1 – 10^5 Hz.	188
Figure 93	Effect of current density on cell potential differences for SOERs with LSM sintered at (a) 1000 °C; and (b) 1100 °C, operating with CO/CO_2.	189
Figure 94	Nyquist plots for cells at OCPD and operating with CO/CO_2 at 707, 752, and 788 °C; LSM electrode sintered at (a) 1000 °C; and (b) 1100 °C. Filled markers indicate order of magnitude intervals in frequency over 0.1 – 10^5 Hz.	190
Figure 95	Simulated LSM phase potential for anodic polarisation at 788 °C, net current density 0.4 A cm^{-2}.	192
Figure 96	SEM photomicrographs of the printed LSM electrode after sintering and electrochemical characterisation (a) side; and (b) surface views. Dr. Tao Li, Imperial College London, performed the SEM experiments in this instance, (JEOL JSM-5610LV, Japan, 20 kV beam).	197
Figure 97	Nyquist plots showing impedance variation (a) with time during NiO reduction at 707 °C; and (b) with temperature. Filled markers denote decade intervals in frequency over 0.1 – 10^5 Hz.	197
Figure 98	Schematic of TPB length decrease during NiO reduction.	199
Figure 99	Effect of current density on power densities for cells operating with H_2 at 707, 752, and after 4 hours of chrono-potentiometry at 10.4 mA cm^{-2}, at 788 °C; scan rate was 10 mV s^{-1}.	200
Figure 100	(a) Effect of applied current density on cell potential difference over time; and (b) Nyquist plots taken after each chrono-potentiometry measurement at OCPD (showing cumulative time) at 788 °C.	200
Figure 101	Photograph of the SOER mounted on an alumina tube for testing, with LSM electrode exposed.	202
Figure 102	Variation of interaction energy with inter-particle separation between pairs of YSZ, CGO, and NiO particles.	226
Figure 103	The RCF required to separate aggregates from a dispersion for two maximum particle sizes, r_p < 400 nm, and r_p < 200 nm. As expected, larger particles require a lower RCF for a given centrifugation duration than smaller particles.	227
Figure 104	Relationship between surface tension and aqueous Natsurf 265 (Croda, UK) concentration. Data from (334).	230
Figure 105	Variation of the typical viscosity – shear rate plot.	232
Figure 106	Zeta potential variation with (a) pH; (b) Duramax 3005 concentration at pH 6.8 – 8; and (c) solubility of the constituent elements with varying pH (10^{-2} mol dm^{-3} KCl). Reproduced with permission from (337).	233
Figure 107	(a) Zeta potential variation of LSCF particles with varying dispersant concentration and pH: Dispex Ultra FA 4416 (no-fill markers) and Duramax D3005 (filled black markers); and (b) PSD of the LSCF particles.	235
Figure 108	Viscosity – shear rate relationship for LSCF and composite CGO-LSCF inks.	236

Figure 109	Surface-view photographs of the sintered CGO-LSCF layer.	236
Figure 110	Cross-sectional SEM photomicrograph of the NiO-YSZ|YSZ|CGO|CGO-LSCF SOER.	238
Figure 111	(a) Cell potential difference variation with current density and temperature; and (b) Nyquist plots at OCPD at each operating temperature, filled markers indicate decade intervals in frequency.	239
Figure 112	Electrochemical characterisations of SOFCs with inkjet printed YSZ-LSM electrode sintered at 1100 °C (a,b), and 1200 °C (c-f). Each set of results was obtained from a different SOFC.	241
Figure 113	Bode plots for cathodes sintered at (a) 1100; and (b) 1200 °C at OCPD and varying operating temperature.	242
Figure 114	Effect of current density on SOER potential difference, for 20 and 60 mV s^{-1} cell potential difference scan rate.	243
Figure 115	Predicted decrease in O^{2-} ion oxidation reaction overpotential with local O_2 pressure.	244
Figure 116	Fuel cell / electrolysis mode power / current densities for different SOERs with LSM sintered at 1100 °C, together with corresponding Nyquist plots at OCPD, where decade intervals are denoted by filled markers between $0.1 – 10^5$ Hz.	245
Figure 117	Surface view photographs of the pre-sintered CGO film (a) 1; (b) 5; (c) 10; and (d) 20 layers thick. Reproduced with permission from (343).	248
Figure 118	SEM micrographs of the sintered 5-layer CGO film at (a, b) 1300; and (c, d) 1500 °C.	249

Nomenclature, Abbreviations, and Acronyms

Symbol	Definition	SI Units
a_i	Activity of species i	kmol m^{-3}
A	Electrode projected area	m^2
A_{des}	Pre-exponential factor for hydrogen desorption kinetics	s m^2 mol^{-1}
A_H	Hamaker constant	J
AM	Additive manufacturing	-
BET	Brunauer–Emmett–Teller Theory	-
Ca	Capillary number	1
C_d	Cure depth (laser sintering)	m
CGO	Gadolinium-doped ceria	-
c_p	Polymer concentration	kmol m^{-3}
C_p	Constant pressure molar-specific heat capacity	J mol^{-1} K^{-1}
$C_{p,m}$	Constant pressure mass-specific heat capacity	J mol^{-1} K^{-1}
D_K	Knudsen diffusion coefficient	m^2 s^{-1}
D_i	In-flight droplet diameter	m
$D_{i/j}$	Binary diffusion coefficient or gases i and j	m^2 s^{-1}
D_m	Droplet splat diameter on substrate	m
d_p	Average pore diameter	m
D_p	Parameter for laser sintering	m
DPB	Dual phase boundary	-
e	Electronic charge	A s
e^-	Electron	-
$\dot{E}$	Rate of evaporation	m s^{-1}
E_a	Process activation energy	J mol^{-1}
E_c	Threshold energy required for polymerisation (laser sintering)	J
EDX	Energy-dispersive X-ray Spectroscopy	-
E_{des}	Activation energy for hydrogen desorption	J mol^{-1}
E_{eq}	Equilibrium potential difference	V

E_{in}	Energy into a system	kJ s^{-1}
E_l	Laser energy (laser sintering)	J
E_{out}	Energy out of a system	kJ s^{-1}
E_{tn}	Thermoneutral potential difference	V
E_∞	Electric field	V m^{-1}
f_k	Dimensionless fugacity coefficient of gas k	1
F	Faraday constant	A mol^{-1}
FIB	Focused Ion Beam	-
g	Acceleration due to gravity	m s^{-2}
G	Gibbs energy	kJ $kmol^{-1}$
G_S	Shear modulus	Pa
h	Height	m
H	Enthalpy	kJ $kmol^{-1}$
H_{crit}	Critical cracking thickness	m
H_l	Printed layer thickness	m
h_p	Planck's constant	m^2 kg s^{-1}
I	Current	A
I_s	Ionic strength	kmol m^{-3}
j	Current density	A m^{-2}
j_0	Exchange current density	A m^{-2}
j_0^{ref}	Reference exchange current density	A m^{-2}
k	Rate constant	m^{-3} mol^{-1} s^{-1}
k_B	Boltzmann constant	m^2 kg s^{-2} K^{-1}
L	Characteristic length, *i.e.* nozzle diameter	m
l_h	Pillar height	m
l_p	Pillar diameter	m
l_s	Pillar centre-to-centre spacing length	m
LSCF	Lanthanum Strontium Cobalt Ferrite	-
LSM	Lanthanum Strontium Manganite	-

M_i	Relative molecular mass of species i	kg kmol^{-1}
N_i	Flux of species i	mol m^{-2} s^{-1}
N_A	Avogadro's constant	mol^{-1}
Oh	Ohnesorge number	1
OCPD	Open Circuit Potential Difference	V
P	Pressure	Pa
P_d	Voltage pulse duration to piezoelectric printhead	s
P_D	Power density	W m^{-2}
Pe	Peclet number	1
P_{eq}	Equilibrium vapour pressure	Pa
p_i	Partial pressure of gas i	Pa
PSD	Particle Size Distribution	-
P_t	Local, total electrode pressure	Pa
Q	Heat flow	kJ s^{-1}
Q_s	Colloid surface charge	C
R	Gas constant	J kmol^{-1} K^{-1}
RCF	Relative Centrifugal Force	-
RCP	Random Close Packing	-
Re	Reynolds number	1
S	Entropy	J kmol^{-1} K^{-1}
SEM	Scanning Electron Microscopy	-
SOE	Solid Oxide Electrolyser	-
SOER	Solid Oxide Electrochemical Reactor	-
SOFC	Solid Oxide Fuel Cell	-
SSZ	Scandia-stabilised Zirconia	-
t	Thickness	m
T	Temperature	K
TGA	Thermogravimetric Analysis	-
T_m	Melting point	K

TPB	Triple Phase Boundary	-
r_p	Particle radius	m
u	Velocity	m s^{-1}
u_0	Droplet ejection velocity	m s^{-1}
u_s	Sedimentation velocity	m s^{-1}
U	Cell potential difference	V
U^i	Internal energy	kJ
V	Volume	m^3
V_p	Voltage applied to piezoelectric printhead	V
W	Work done on a system	J
We	Weber number	1
W_e	Electrostatic inter-particle interaction energy	J
W_{ex}	Depletion inter-particle interaction energy	J
W_{vdw}	van der Waals inter-particle interaction energy	J
y_i	Local mole fraction of gas i	1
YSZ	Yttria-stabilised Zirconia	-
z	Exponent	1
Z	Pre-exponential factor of Arrhenius rate constant	m^{-3} mol^{-1} s^{-1}

Greek Letters

α_i	Charge transfer coefficient of reaction i	1
γ	Surface tension	N m^{-1}
γ'	Surface energy	J m^{-2}
γ_0	Sticking probability of hydrogen adsorption kinetics	1
Γ	Surface site density for hydrogen	mol m^{-2}
Δ	Polymer size (length)	m
ε	Electrode porosity	1
ε_0	Permittivity of a vacuum	F m^{-1}
ζ	Exponent in j_0 expression	1

ζ_p	Poisson ratio	1
η	Overpotential	V
θ_e	Equilibrium contact angle	radians
Θ	Colloidal stability ratio	1
κ^{-1}	Debye length	m
λ	Refractive index	1
Λ_s	Particle surface potential	V
μ	Viscosity	Pa s
ν_i	Stoichiometric coefficient of species i	1
ξ	Zeta potential	mV
ρ	Density	kg m^{-3}
σ	Conductivity	S m^{-1}
τ_i	Tortuosity of phase i	1
ϑ_p	(Dispersed) particle volume fraction	1
$\vartheta_{p,T}$	Maximum particle volume fraction	1
φ	Particle packing density in film	1
ϕ	Electric potential	V
χ	Dielectric constant	1
ψ	Photon frequency	s^{-1}
ω_a	Number of particles in an aggregate	1
ϖ	Particle coordination number	1

Subscripts

B	Binary	-
e	Electron	-
el	Electronically-conducting phase	-
a	Anodic	-
c	Cathodic	-
in	Into a system	-

max	Maximum	-
out	Out of a system	-
p	Polymer	-
K	Knudsen diffusion	-
r	Relative to the zero-solids case	-
R	Species that becomes reduced	-
rev	Reversible process	-
ref	Reference conditions	-
conc	Concentration polarisation	-
act	Activation polarisation	-
inlet	Reactor inlet conditions	-
IR	Ohmic polarisation	-
O	Species that becomes oxidised	-
io	Ionically-conducting phase	
	Superscripts	
eff	Effective, *i.e.* adjusted for medium properties	-
pc	Phase Change	-
o	Standard conditions	-
pos	Positive electrode	-
neg	Negative electrode	-
t	Transition state	-

1. Introduction

Chapter Summary

The transition in electrical energy generation from conventional fossil fuels to renewable, intermittent resources, primarily solar and wind, necessitates flexible grid-scale energy storage. The most promising option for long term (> day) and high power (GW) energy storage is 'power-to-gas', where surplus electrical energy is stored in chemical bonds, as a fuel. The most understood fuels, with respect to production, handling, and storage, typically contain C-H, C-O, C-C, and H-H covalent bonds, therefore a critical challenge is the production of these fuels using electrical energy, instead of fossil fuels. The most promising technologies to accomplish this are electrochemical reactors, specifically high-temperature, reversible solid oxide electrochemical reactors.

1.1. Grid-scale Energy Storage

The diversity of energy sources into the UK electricity grid is increasing, as shown in **Figure 1**. This is a result of external pressures, including commitments to reduce emissions of CO_2 and other pollutants, diminishing fossil fuel stocks, an aversion to nuclear power, and energy security concerns (1, 2). The offshore wind potential for the UK by 2030 is predicted to be *ca*. 25 GW (80 % of average UK power demand), and the relative area of the UK land mass required to completely meet power demands from solar generation, at present photovoltaic efficiencies is < 2% (3-5). Therefore, it is unsurprising that these domestically available, non-polluting, and inexhaustible resources are highly desirable future sources of energy.

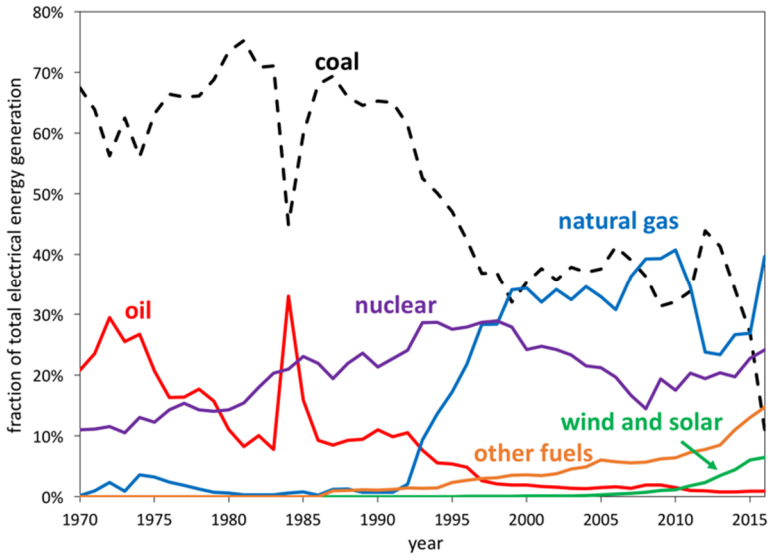


Figure 1. Electrical energy source, and its fraction of the total power generation in the UK, from 1970 - 2016. Data taken from reference (6).

However, both wind and solar are intermittent resources, *i.e.* their generation is independent of power demand (**Figure 2a**), and is irreproducible due to a weather-dependence including cloud cover and wind speed, which invariably means that generation is lower than installed capacity (**Figure 2b**). Therefore, as electrical energy generation becomes more reliant on wind and solar energy, power balancing will become increasingly challenging.

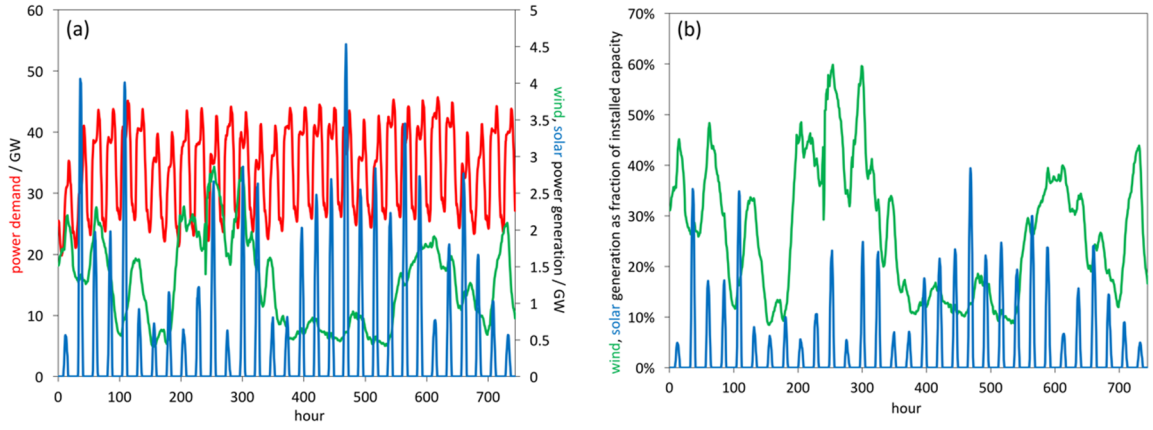


Figure 2. January 2017 data for (a) power generation in England and Wales; and (b) wind and solar generation as a fraction of their total installed capacities. Data taken from reference (3).

There are two immediate solutions to the intermittency problem, either to match power demand with supply, or vice versa; the latter option being impractical, as explained above. The former solution, also known as Demand Response (DR), has the potential to increase overall efficiency and is currently active globally, through policies and consumer incentives (7). However, due to a lack of pricing information available to consumers and demand inelasticity, the effect of DR has been limited. Furthermore, DR is not expected to reduce total electricity use and peak demand by more than 2.8 % and 1.3 %, respectively, in the UK (8, 9). Therefore, a power balancing technology that can cope with supply / demand fluctuations is required to solve this problem, *i.e.* energy storage at a grid-scale. To balance electrical power supply and demand, grid-scale energy storage should have a sufficiently high power and capacity; the specific requirements are explored in Section 1.2.

1.2. Energy Storage Technologies

There are several forms in which energy can be stored, the most common are mechanical (including kinetic and potential energy), thermal, electrochemical, and chemical (power-to-gas) (10). Each energy storage technology operates over different characteristic time scales, conventionally defined as the re/discharge duration of the device, which can range from seconds, to days and more. Therefore, depending on the duration and magnitude of the power demand / supply fluctuation, different technologies can be more effective. The most common energy storage technologies are summarised, according to their capacity and power, in **Figure 3a**.

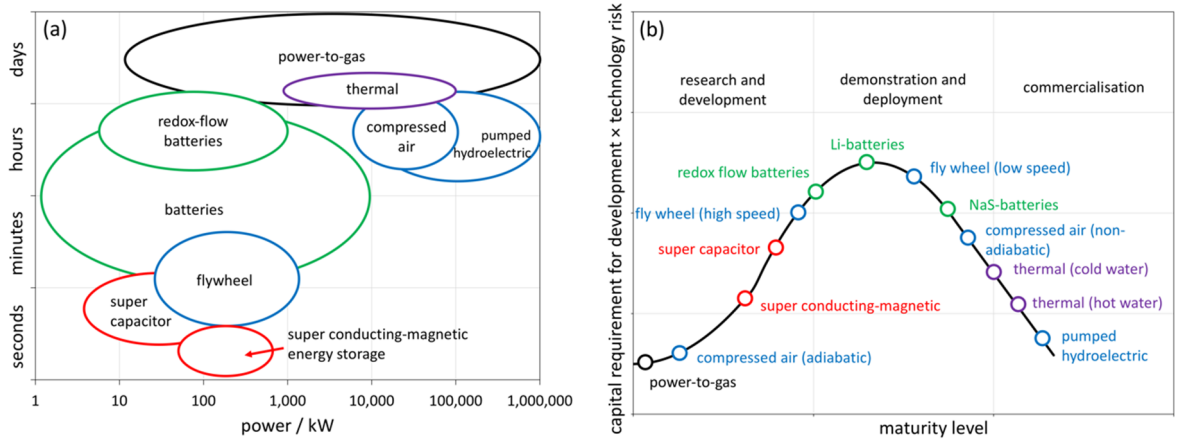


Figure 3. (a) Summary of energy storage technologies with characteristic timescales and powers, highlighted by type: electrical (red), mechanical (blue), electrochemical (green), thermal (purple) and chemical (black). Data from (11-14); and (b) maturity of energy storage technologies. Reproduced with permission from (15).

To meet long-term (≥ days), high power (GW) energy storage requirements (**Figure 2a**) where thermal storage is inefficient (*i.e.* non-equatorial), the most promising technologies are pumped hydroelectric storage (PHES) and power-to-gas. The relative maturities of the different energy storage technologies in **Figure 3a** are shown in **Figure 3b**, with PHES being the most established. However, major drawbacks of PHES include that it is location inflexible, *i.e.* is constrained by geography and climate, has comparatively high installation costs (*e.g.* £425M for the Dinorwig Plant (Wales), constructed in 1984 (16)), and is usually environmentally destructive, requiring vast areas to be flooded to increase storage capacity. Furthermore, as shown in **Figure 4**, most PHES installations are geographically distant from large population centres, requiring expensive electricity transmission lines that are generally opposed by the general public and landowners (17, 18).

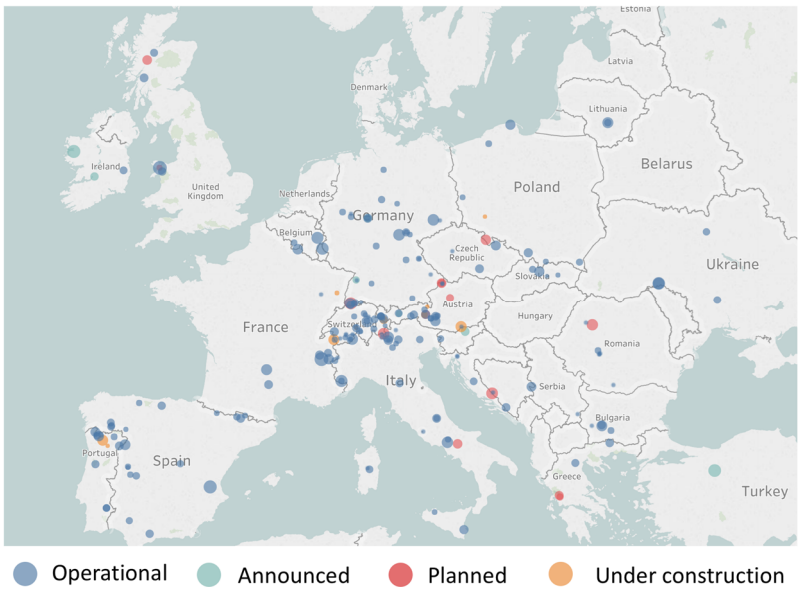


Figure 4. Map of hydroelectric facilities in Europe with > 1 MW power. Reproduced from (19).

Conversely, power-to-gas, defined as the conversion of electrical energy into chemical energy, *i.e.* electrolysis of H_2O to H_2, is highly location flexible, does not require centralisation, and is environmentally benign, neglecting the sourcing of raw materials and source of net energy into the system. Therefore, despite the high risk and capital cost required to develop commercial power-to-gas technologies, they should provide the most practical solution for the future.

1.3. Power-to-gas

The prospect of storing surplus electrical energy in chemical bonds was identified as early as the 19th century, when in 1874, Jules Verne (1828 – 1905), recognising the finite coal supply, and noting that hydrogen gas (discovered in 1766 (20)) could be produced electrolytically (21), announced that "water will be the coal of the future" (22). However, 144 years later, we are still searching for ways to make this a reality, albeit equipped with a larger selection of energy carriers, and improved electrolysis technologies.

Selection of the chemical ('gas') into which surplus electrical energy can be converted is a compromise between the relative difficulties of production, storage, and handling. The most realistic candidates are outlined in **Table 1**.

Table 1. Physical and chemical properties for power-to-gas energy storage materials. IDLH (immediately dangerous to life or health) concentrations are shown. Specific energy is for complete combustion at 298 K (23-27).

Carrier	Specific energy / MJ kg^{-1}	Vapour pressure (293 K) / bar	IDLH / ppm	Flammability limits (in air) / %
CH_4	50	-	-	5.3 - 15
CO	10.1	-	1200	12 - 75
H_2 (g)	141.7	-	-	4.0 - 75
Hydrazine	18.6	$1.40x10^{-2}$	50	4.7 - 100
Methanol	19.7	0.13	6000	6.0 - 36
NH_3 (l)	13.1	8	300	-
Petrol (octane)	44-46	0.047	750	1.0 - 7.6

1.3.1. Conventional Gas Production Techniques

The conventional synthesis routes of different carrier fuels in **Table 1** vary, and are shown by the reactions described in the remainder of this Section.

Hydrogen gas is produced typically by the water – gas shift reaction (1), with hydrocarbons by steam reforming (the most economical process when using methane (28)), shown in reaction (2), by the autothermal reforming reaction (3), or by hydrocarbon pyrolysis, shown in reaction (4) (29, 30).

$$CO + H_2O \rightleftharpoons CO_2 + H_2 \quad (1)$$

$$CH_4 + H_2O \rightleftharpoons CO + 3H_2 \quad (2)$$

$$C_nH_m + {}^1/_2\, nH_2O + {}^1/_4\, nO_2 \rightleftharpoons nCO + {}^1/_2\,(n+m)H_2 \quad (3)$$

$$C_nH_m \rightleftharpoons nC + mH_2 \quad (4)$$

Carbon monoxide is synthesised industrially by the Boudouard and water gas shift reactions (5) - (7).

$$C + O_2 \rightleftharpoons CO_2 \quad (5)$$

$$CO_2 + C \rightleftharpoons 2CO \quad (6)$$

$$C + H_2O \rightleftharpoons CO + H_2 \quad (7)$$

Methanol is produced synthetically via the Fischer-Tropsch reactions using synthesis gas, as shown in equation (8). This can also be used to produce hydrocarbons with higher molecular weights, *e.g.* octane.

$$CO + 2H_2 \rightleftharpoons CH_3OH \quad (8)$$

Synthetic methane is produced typically by the Sabatier reaction (9).

$$CO_2 + 4H_2 \rightleftharpoons CH_4 + 2H_2O \quad (9)$$

Ammonia is produced almost exclusively by the Haber-Bosch process, using reaction (10).

$$N_2 + 3H_2 \rightleftharpoons 2NH_3 \quad (10)$$

Several routes exist to synthesise hydrazine, all using ammonia as a raw material. However, due to cost and abundance, the only realistic ammonia oxidants are Cl_2, O_2, and H_2O_2. These reaction routes are shown in equations (11) - (13) (31). Due to the additional oxidant requirement and hydrazine's comparatively high toxicity, it is an impractical grid-scale energy storage chemical (although may find utility as a transport fuel (32)), so will not be considered further.

$$NaClO + 2NH_3 \rightleftharpoons N_2H_4 + NaCl + H_2O \quad (11)$$

$$2(CH_3)_2 + NH_3 + NH_2Cl + NaOH \rightleftharpoons N_2H_4 + NaCl + 3H_2O + 2CH_3COCH_3 \quad (12)$$

$$2NH_3 + H_2O_2 \rightleftharpoons N_2H_4 + 2H_2O \quad (13)$$

Notably, the primary raw materials required for the synthetic processes above are C, CH_4, N_2, and H_2O, which are used to produce CO and H_2. While H_2O and N_2 are abundant, inexhaustible and non-polluting feedstocks, C and CH_4 are finite and highly polluting. Therefore, it is essential that alternative production routes are established for CO and H_2, that use the surplus generation of electrical energy.

Figure 5 shows a possible route to synthesise the common fuels using CO and H_2 that are produced using renewable energy. As the surplus energy is supplied electrically, the most appropriate reduction and oxidation technologies are electrochemical (*i.e.* electrolysers and fuel cells), minimising the number of process steps and maximising conversion efficiencies.

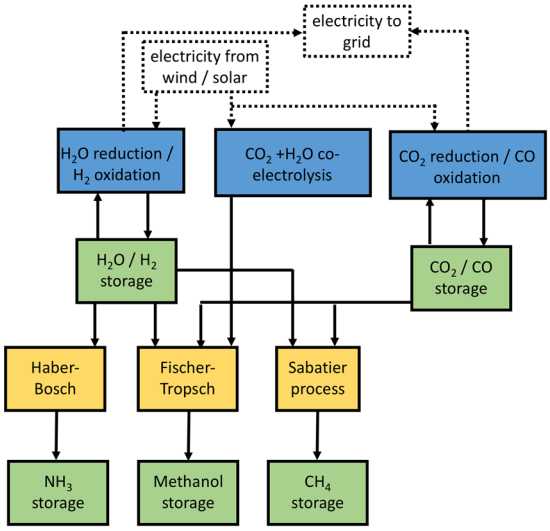


Figure 5. Technology routes to produce common fuels (green) with well-established industrial processes (yellow), without the requirement for fossil fuels. Electrochemical conversion processes are shown in blue. Abundant and environmentally benign raw material inputs are omitted.

1.3.2. Electrochemical Production of H_2 and CO_2

There are a number of operational power-to-gas plants worldwide that utilise low-power (< 1 MW) alkaline or polymer exchange membrane (PEM) water electrolysers (33), frequently combined with a battery to smooth supply from a solar or wind source to produce H_2 (34), as shown in **Figure 6**. These power-to-gas applications fulfil a niche role, and are uneconomical for general electrical grid service at present electricity prices. Furthermore, neither PEM with conventional materials nor alkaline electrolyser technology has the capability to reduce CO_2 electrochemically (CO poisons the catalyst (35)), so an intermediary chemical reaction would be required to produce hydrocarbons, resulting in a decrease in overall efficiency and increase in cost; therefore, it is preferable to deploy an electrochemical conversion technology that can reduce CO_2 directly.

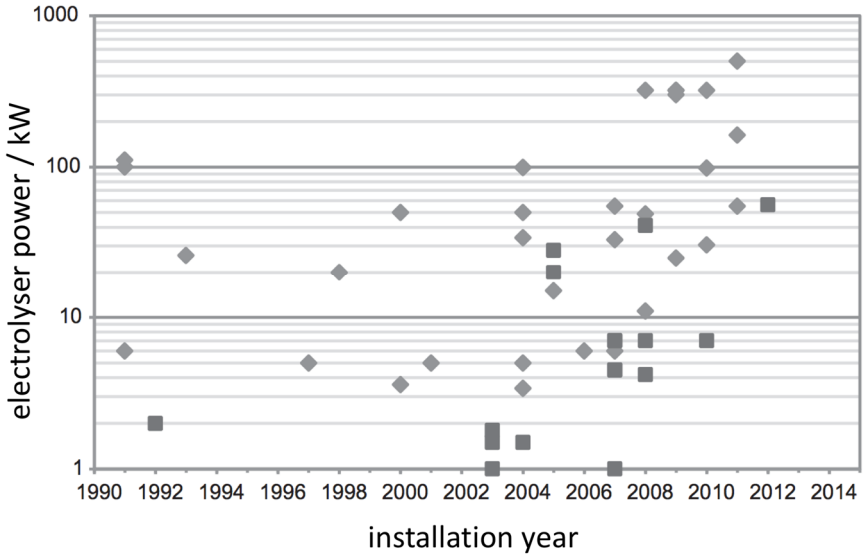


Figure 6. Electrical power of alkaline (diamond) and PEM (square) electrolysers installed in operational power-to-gas plants worldwide. Reproduced with permission from (33).

Fuel cell and electrolyser technologies that have been developed are summarised in **Table 2**, differing in operating temperature, materials, feedstocks, and products. The maturation level, and hence developmental risk, of each technology is different. A limited selection of alkaline fuel cells and electrolysers (36), PEM fuel cells and electrolysers (37), and molten carbonate fuel cells (38) are presently available commercially, but are not economically viable for grid-scale power-to-gas energy storage.

There are two operational temperature regimes in which to reduce CO_2 electrochemically: low (*ca.* 25 °C) and high (600 - 1000 °C). A preferable system should:

- Minimise complexity
- Minimise cost
- Maximise yield (*i.e.* CO selectivity)
- Maximise electrical energy conversion efficiency

Therefore, high-temperature CO_2 reduction has several fundamental advantages compared to low-temperature alternatives, due to lower electrical energy requirements (higher efficiency) for electrolysis (39, 40), higher product selectivity and current densities (> an order of magnitude) (41, 42), and a non-requirement for precious metal catalysts (capital cost). Therefore, the high-temperature electrolysis options are molten carbonate (MCER), solid oxide (SOER), and proton ceramic (PCER) electrochemical reactors.

The feasibility of CO_2 reduction has been demonstrated in molten carbonate electrolysers, but the kinetics were limited by low O^{2-} ion diffusion and material instabilities (43, 44). Furthermore, H_2O electrolysis cannot be performed using molten carbonate electrolytes, unlike in SOERs and PCERs, so molten carbonates have less utility to produce energy storage carriers via the routes shown in **Figure 5** than the alternatives.

The primary difference between SOERs and PCERs concerns ion transport through the electrolyte, the former conducting oxide ions (O^{2-}) and the latter protons (H^+). Both systems have proven rapid kinetics for fuel cell and electrolyser modes (> 1 A cm^{-2}); however, due to the H^+ conduction in the latter case, CO product selectivity is decreased and hydrogen-containing materials are produced (*i.e.* H_2, H_2O, CH_4) (45). Therefore, SOERs are more suited to CO / CO_2 storage than PCERs. An advantage of PCERs over SOERs operating in electrolyser mode is that they can produce dry H_2, as opposed to a pure O_2 stream in the latter case (46), allowing greater fuel utilisation. However, the main drawback with PCERs is that an acceptable compromise between electrolyte stability and conductivity has not been found (47-49). In contrast, conventional SOER materials are highly stable over thousands of hours operating with CO, CO_2, H_2, and H_2O (50, 51). Consequently, the focus of this Thesis concerns the advancement of SOER technology by engineering and fabrication methodologies, using conventional materials throughout.

Table 2. Classification of different fuel cell / electrolyser technologies with details of operation, materials, and maturity. Reproduced and modified from (52).

Classification	Operating Temperature / °C	Electrolyte	Feed*	Products*	Maturity	Comments	References
Alkaline – aqueous	40 - 90	KOH	H_2O	H_2 only	Mature	Commercially available	(36, 53)
General aqueous electrolysis	25	H_2O + salt	H_2O CO_2	H_2, CO, formic acid, formate, alcohols, hydrocarbons (highly electrode material dependent)	R & D	Limited by low O^{2-} ion conductivity	(54-57)
Organic Solvent	25	Organic solvents *i.e.* methanol	CO_2	Hydrocarbons, CO, formic acid	R & D	Relatively high CO_2 solubility, limited characterisation of anode reactions	(58, 59)
PEM	20 - 200	Polymer *i.e.* Nafion	H_2O CO_2	H_2 (some hydrocarbons and CO detected)	Mature for H_2O, R & D for CO_2	Commercially available, low charge yields for CO_2 reduction, commercial PEM requires Pt (expensive), catalyst poisoning	(37, 60-63)
Molten carbonate	450 - 900	Molten salt *i.e.* Li_2CO_3	CO_2	C (s), CO, or CO_2 (temperature dependent)	R & D	High-temperature material corrosion, fuel cells are commercialised, thermodynamically-complex	(38, 43, 64)
Solid oxide	600 - 1000	Ceramics *i.e.* Yttria-stabilised zirconia	H_2O CO_2	H_2 CO	R & D	Degradation-limited, fuel cells have been commercialised, can operate with *ca*. 90 % CO_2 feed	(65, 66)
Proton ceramic electrolyser	500 - 600	Ceramics *i.e.* Y-doped $BaZrO_3$	H_2O CO_2	H_2 (CO and CH_4 have been reported)	R & D	Reported CO_2 reduction products are questionable / unproven	(45, 67-69)

* For electrolysis mode, columns are reversed for fuel cell mode.

2. Theory and Literature Review

Chapter Summary

This Chapter begins by introducing the fundamental thermodynamics and kinetics that govern electrochemical systems and solid oxide electrochemical reactors (SOERs). The limitations of conventional SOER fabrication techniques are explained, and the different additive manufacturing technologies that have been used to fabricate ceramic components are reviewed. The fundamentals of inkjet printing are introduced, and finally, the present state of inkjet-printed SOERs is reviewed, covering ink formulation, printer settings, printed deposit treatment, and electrochemical characterisation.

Note: Figures from the literature have been inserted with their original resolution.

2.1. Electrochemical Theory

2.1.1. A Select History of Electrochemistry

Electrochemistry, the branch of physical chemistry in which electricity is the outcome or cause of a chemical change, was first identified by the Italian professor of physics at the University of Pavia, Alessandro Volta (1745 – 1827) in 1800, with his invention of the modern battery, called the voltaic pile, in conjunction with the observations by Luigi Galvani of electrical energy evolved from the connection of two dissimilar metals connected by a moist conductor (frog's leg). The voltaic pile was a series of Cu-Zn pairs, using brine as the electrolyte, and separated by a non-conducting porous 'felt' material, as shown in **Figure 7**. Even today, the voltaic pile design is the most common geometry for 'stacking' individual electrochemical reactors to scale overall current / potential difference.

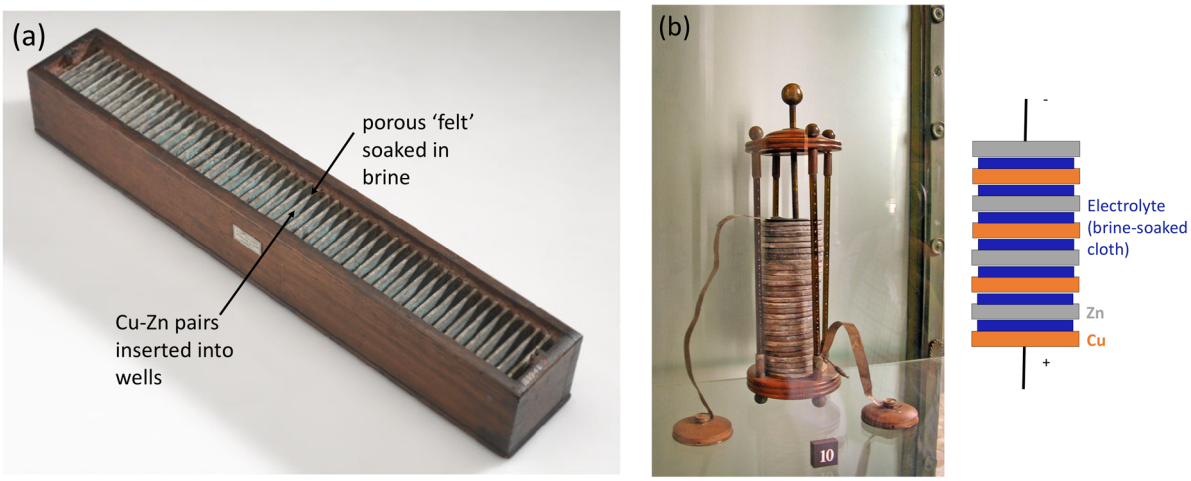


Figure 7. (a) Voltaic pile (1801 design, R & G Knight, London, England, 1801-1838). Reproduced with permission from (70); and (b) Volta's voltaic pile on display at the Tempio Voltiano Museum, Como, Italy.

British scientist Sir Humphry Davy (1778 – 1829) experimented with the voltaic battery at the Royal Institution in London, and observed that electricity production was due to chemical reactions, which he subsequently used to discover many of the first and second group metals of the periodic table. In 1806, Davy published his electrical theory of chemical affinity, discovering that electricity could overcome the forces holding molecules together. His student and successor, the prolific experimentalist Michael Faraday (1791 – 1867), established the relationship between electricity and magnetism, with the invention of the electric motor (1821) and dynamo (1831). Observing that the electricity generated from magnetism and other methods has the same effect, in 1834 he published his two laws of electrochemistry, cumulating

in a relationship to predict product yield from current, a process he called 'electrolysis' (71, 72). Shortly after, in 1839, the Swiss scientist Christian Friedrich Schoenbein (1799 – 1868) conceptualised the H_2 / O_2 fuel cell (73), which was demonstrated experimentally by British scientist William Robert Grove (1811 – 1896) (74), confirming the technical feasibility of a fuel cell (27).

2.1.2. Thermodynamics

Considering a thermodynamically-open system at steady state, the energy balance on the electrochemical reactor shown in **Figure 8** may be used to derive equation (14).

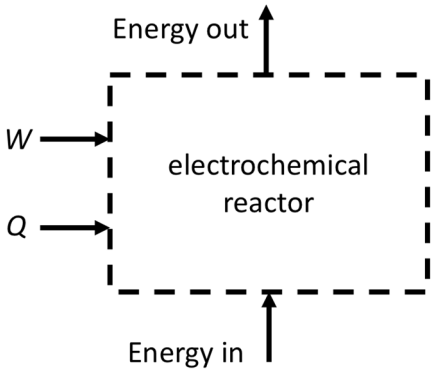


Figure 8. Energy balance on an electrochemical reactor.

$$0 = \sum_{\forall \text{ inputs}} \left[{U^i}_{\text{in}} + m\left(\frac{{u_{\text{in}}}^2}{2} + g h_{\text{in}}\right)\right] - \sum_{\forall \text{ outputs}} \left[{U^i}_{\text{out}} + m\left(\frac{{u_{out}}^2}{2} + g h_{\text{out}}\right)\right] + Q - W_{\text{elec}} + \sum_{\forall \text{ inputs}} PV_{\text{in}} - \sum_{\forall \text{ outputs}} PV_{\text{out}} \quad (14)$$

Where U^i represents internal energy, m represents mass, u, velocity, g, gravitational acceleration, h, the height at inlet (in) or outlet (out) conditions; P and V represent the pressure and volume changes, respectively, so their product is expansion work. Q and W_{elec} are heat and maximum work (other than expansion work, *i.e.* the electrical work) on the electrochemical reactor. Defining a positive volume change to be work done by the system, the sign convention for W_{elec} is negative, *i.e.* work done by the system. Inserting the definition of enthalpy given in equation (15), the incremental reaction enthalpy change (*i.e.* $\delta H = H_{\text{products}} - H_{\text{reactants}}$) may be derived for isobaric conditions, and is shown in equation (16).

$$H = U + PV \quad (15)$$

$$\delta H = \delta Q - \delta W_{\text{elec}} \quad (16)$$

The Gibbs energy change of the reaction at isothermal and isobaric conditions is defined by equation (17).

$$\delta G = \delta H - T\delta S \quad (17)$$

Where δS is the incremental reaction entropy change. Substituting equation (16) into (17) gives a relationship for Gibbs energy change (18).

$$\delta G = \delta Q - \delta W_{\text{elec}} - T\delta S \quad (18)$$

Assuming the system is at steady state and processes are reversible, substituting the second law of thermodynamics, given in equation (19), into (18), we obtain equation (20) (75), *i.e.* the Gibbs energy change of a process is equal to the work done by the system.

$$\delta Q_{\text{rev}} = T\delta S \quad (19)$$

$$\delta G = -\delta W_{\text{elec}} \quad (20)$$

For a galvanic cell, work is performed by transporting a charge over an (electric) potential difference ($\Delta\phi$), as the result of a chemical reaction. Therefore, transporting δn moles of ions through potential difference $\Delta\phi$, we obtain equation (21) for electrical work.

$$\delta W_{\text{elec}} = \nu_{\text{e}} F \Delta\phi \cdot \delta n \quad (21)$$

Where ν_{e} represents the electronic stoichiometric coefficient, and F is the Faraday constant. Substituting equation (21) into (20), taking the limit $\delta n \rightarrow 0$, and integrating for the transportation of 1 mole of ions, we obtain the molar Gibbs energy change of the reaction (ΔG) given in equation (22).

$$\Delta G = -\nu_{\text{e}} F \Delta E_{eq} \quad (22)$$

ΔE_{eq} is the cell equilibrium potential difference. Therefore, at standard conditions (reference T, P) where the Gibbs energy change is known, the equilibrium cell potential difference may be calculated as shown in equation (23).

$$\Delta E^{\text{o}}{}_{eq} = -\frac{\Delta G^{\text{o}}}{\nu_{\text{e}} F} \quad (23)$$

Where the '°' denotes properties at standard conditions.

2.1.2.1 Effect of Temperature on Cell Equilibrium Potential Difference

The Gibbs energy change, defined in equation (17), depends on the reaction enthalpy and entropy changes, which may be adjusted from standard (*i.e.* T^{o}) to non-standard conditions (*i.e.*

T) using the relationships in equations (24) and (25), accounting for any phase changes (pc) where appropriate. The mass-specific, constant pressure, heat capacity variation with temperature ($C_{p,m}(T)$) may be approximated using the Shomate equation, as shown in equation (26), where the coefficients (c_i) have been found empirically and published (76). The molar-specific, isobaric, heat capacity (C_p) can be calculated by multiplying $C_{p,m}$ by the relative molecular mass.

$$\Delta H = \Delta H^{\circ} + \int_{T^{\circ}}^{T^{\mathrm{pc}}} C_p(\hat{T}).d\hat{T} + \Delta H^{\mathrm{pc}} + \int_{T^{\mathrm{pc}}}^{T} C_p(\hat{T}).d\hat{T} \quad (24)$$

$$\Delta S = \Delta S^{\circ} + \int_{T^{\circ}}^{T^{\mathrm{pc}}} \frac{C_p(\hat{T})}{\hat{T}}.d\hat{T} + \frac{\Delta H^{\mathrm{pc}}}{T^{\mathrm{pc}}} + \int_{T^{\mathrm{pc}}}^{T} \frac{C_p(\hat{T})}{\hat{T}}.d\hat{T} \quad (25)$$

$$C_{p,m}(T) = c_0 + c_1(T \times 10^{-3}) + c_2(T \times 10^{-3})^2 + c_3(T \times 10^{-3})^3 + \frac{c_4}{(T \times 10^{-3})^2} \quad (26)$$

2.1.2.2 Effect of Concentration (or Pressure) on Cell Equilibrium Potential Difference

Standard conditions are typically at unit activities for all species (k) (*i.e.* $a_{\mathrm{k}} = 1$). Therefore, to adjust the equilibrium potential for non-unit activities, the Nernst equation (27) is used, where R is the gas constant and 'i' and 'j' denote products and reactants, respectively.

$$\Delta E_{eq} = \Delta E^{\circ}{}_{eq} - \frac{RT}{\nu_e F} \ln\left(\frac{\prod_{\forall i} {a_i}^{\nu_i}}{\prod_{\forall j} {a_j}^{\nu_j}}\right) \quad (27)$$

For gaseous reactants and products, the activity coefficient (a_{k}) is equal to the partial pressure (p_{k}) of the gas multiplied by its dimensionless fugacity coefficient (f_{k}), as shown in equation (28).

$$a_{\mathrm{k}} = f_{\mathrm{k}} p_{\mathrm{k}} \quad (28)$$

Fugacity coefficients can be found experimentally, or are often approximated using an equation of state. Alternatively, the 'ideal gas' approximation may be taken, where $f_{\mathrm{k}} = 1$.

2.1.3. Kinetics

The analysis in Section 2.1.2 is valid only for equilibrium conditions. To drive an electrochemical reaction in a specific direction, an overpotential (η) is required, as shown in **Figure 9**. Therefore, the cell potential difference (U) for electrolyser and fuel cell modes is given in equation (29).

$$U = \begin{matrix} \text{electrolyser} \\ \mp \\ \text{fuel cell} \end{matrix} \left(\Delta E_{\mathrm{eq}} \pm |\eta^{\mathrm{pos}}| \pm |\eta^{\mathrm{neg}}| \pm \sum \frac{I t_i}{A_i \sigma_i}\right) \quad (29)$$

Where I, t, A and σ are the current, thickness, area, and conductivity of conductive layer i, respectively.

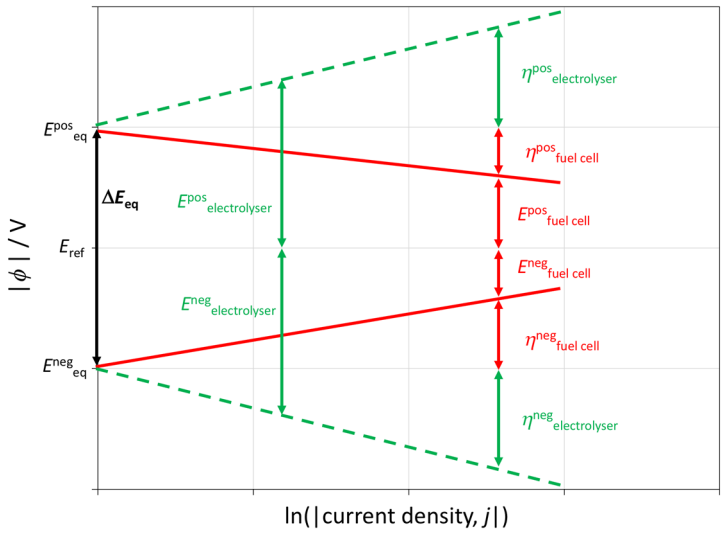


Figure 9. Schematic showing definitions of overpotential and electrode potential for 'positive' (pos) and 'negative' (neg) electrode potentials for electrolyser and fuel cell operation.

This idealised system does not account for potential losses that occur within the cell when non-negligible current flows, as for real systems. Consequently, current is not expected to increase exponentially indefinitely with increasing overpotential. There are three classes of potential losses (inefficiencies):

i) Charge transfer losses, termed 'activation polarisation' (η_{act});

ii) Ohmic losses due to Ohm's law ($\Delta\phi_{IR}$);

iii) Mass transfer losses due to diffusion, termed 'concentration polarisation' (η_{con}).

Accounting for these losses, equation (29) can be rewritten, and used to calculate the overall cell potential difference ($\Delta E_i \equiv U$) as in equation (30).

$$U = \begin{matrix} \text{electrolyser} \\ \mp \\ \text{fuel cell} \end{matrix} \left(\Delta E_{eq} \pm |\eta^{pos}| \pm |\eta^{neg}| \pm \left|\eta^{pos}{}_{act}\right| \pm \left|\eta^{neg}{}_{act}\right| \pm \left|\eta^{pos}{}_{con}\right| \pm \left|\eta^{neg}{}_{con}\right| \pm |\Delta\phi_{IR,total}|\right) \quad (30)$$

The consequences of these losses on fuel cell and electrolyser current densities are shown schematically in **Figure 10**. The current density (j) is equal to the reactor current (I) divided by a characteristic electrode area (A), which is conventionally the projected area of the electrode. The causes and mechanisms of these potential losses are explored in greater detail in the remainder of this sub-section.

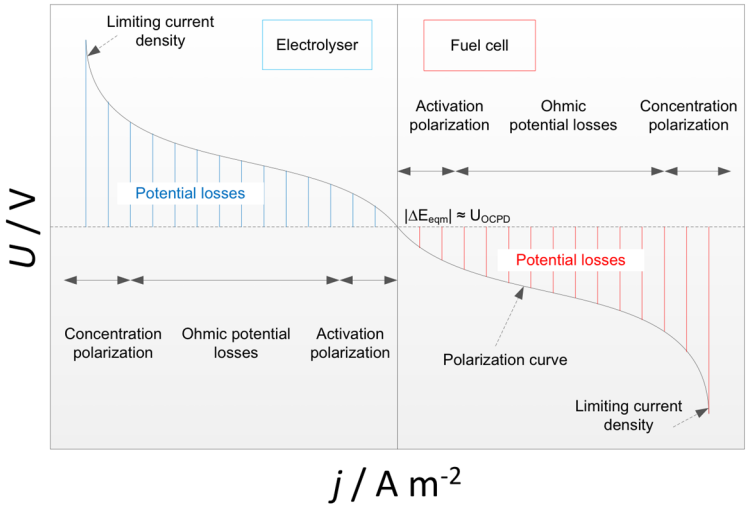


Figure 10. Typical fuel cell and electrolyser performance, showing the regimes under which different polarisation loss mechanisms dominate. Reproduced with permission from (52).

2.1.3.1 Activation Polarisation

Electron transfer processes have an activation energy, which at low current densities dominates reactor inefficiencies. The system may be understood by considering the schematic in **Figure 11** (Marcus theory), which shows the reaction coordinate for the (single) electron transfer process between an identical reactant and product.

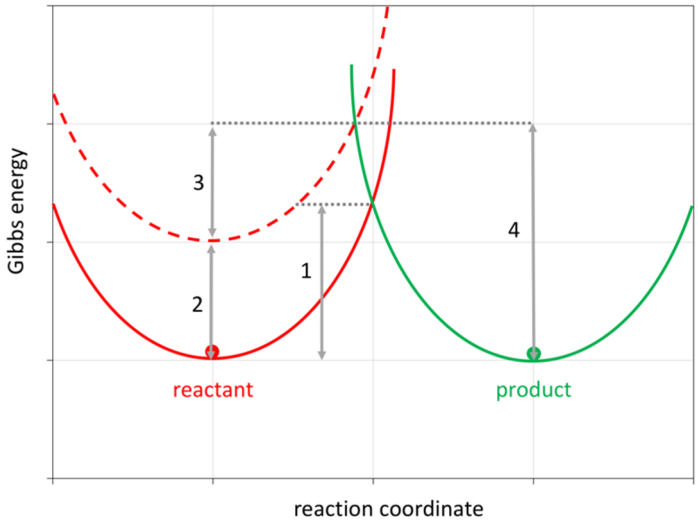


Figure 11. Schematic of the Gibbs energy relationship between an identical reactant (red) and product (green), and after application of a potential difference (dashed).

The rate constant for the electron transfer process (k_e) follows the Arrhenius-type relationship shown in equation (31), where ΔG^t is the Gibbs energy of the transition state, and Z indicates the intrinsic electron transfer rate and probability of crossing through the transition state

(intersection of parabolae), to product, for a single reaction direction. The activation energy for this process is responsible for activation polarisation, *i.e.* '1' on the schematic.

$$k_{\mathrm{e}} = Z\exp\left(\frac{-\Delta G^{\mathrm{t}}}{RT}\right) \qquad (31)$$

Application of a potential (difference) raises (or lowers) the Gibbs energy of the reactants ('2'), as shown by the dotted parabola. Therefore, the activation energy for the forward reaction decreases ('3'), and the activation energy for the reverse reaction increases ('4'). The relative changes for the forward and backward processes are encompassed by a parameter called the 'charge transfer coefficient', the sum of which is equal to the number of electrons transferred (equation (32)).

$$\alpha_{\mathrm{a}} + \alpha_{\mathrm{c}} = \nu_e \qquad (32)$$

Where α_{a} and α_{c} are the charge transfer coefficients for the anodic (oxidation) and cathodic (reduction) processes for the electrochemical reaction, respectively. Substituting equation (23) into (31), and including both forward and backward reactions, the overall reaction kinetics occurring at an electrode can be described using the Butler-Volmer equation, which relates activation overpotential (η_{act}) with current density (j), shown in equation (33) (77).

$$j = j_0\left[\exp\left(\frac{\alpha_a F}{RT}\eta_{act}\right) - \exp\left(-\frac{\alpha_c F}{RT}\eta_{act}\right)\right] \qquad (33)$$

Where j_0 is the exchange current density, and is viewed as the intrinsic idle current across the reaction interface at equilibrium (*i.e.* when $\eta = 0; j = j_0$) (27).

2.1.3.2 Ohmic Potential Losses

At intermediate current densities in electrochemical reactors, losses due to Ohm's law dominate, and because electrochemical systems have multiple functional layers (electrodes and electrolyte), individual material conductivities must be included. Therefore, ohmic potential losses are usually calculated according to equation (34).

$$\Delta\phi_{\mathrm{IR,total}} = I\sum_{\forall \mathrm{i}}\frac{t_i}{\sigma_{\mathrm{i}}A_{\mathrm{i}}} \qquad (34)$$

Where t_{i} and σ_{i} are the thickness and conductivity of functional layer i, respectively. This equation applies only when concentration changes are negligible. The electrodes of many electrochemical reactor systems are porous, and therefore the layer thickness underestimates

the actual conductive path length. Consequently, thickness is adjusted, or more frequently the conductivity is adjusted, to account for porosity and tortuosity (see Section 2.2.5.4).

2.1.3.3 Concentration Polarisation Losses

The Butler-Volmer equation (33) assumes that mass transfer kinetics are rapid, *i.e.* not rate limiting; however, at high current densities, mass transport rate limitations often become significant. Therefore, the Butler-Volmer equation can be modified to include species concentrations, as shown in equation (35). As current density becomes limited by Fick's law, the limiting current density can be calculated using equation (36). Preferably, the concentration dependence can be included in the overpotential term, which is adjusted according to the Nernst equation (27), and inserted into the standard Butler-Volmer equation (1 dimension).

$$j = j_0 \left[\left(\frac{C_{\mathrm{R},x=0}}{C_{\mathrm{R},x=\mathrm{bulk}}} \right) \exp\left(\frac{\alpha_a F}{RT} \eta_{act} \right) - \left(\frac{C_{\mathrm{O},x=0}}{C_{\mathrm{O},x=\mathrm{bulk}}} \right) \exp\left(-\frac{\alpha_c F}{RT} \eta_{act} \right) \right] \quad (35)$$

$$\text{So as } j \cong -\nu_e F D_{\mathrm{q}} \frac{\partial c_{\mathrm{q}}}{\partial x}, \frac{C_{\mathrm{R},x=0}}{C_{\mathrm{R},x=\mathrm{bulk}}} = \frac{j_{L,R} - j_R}{j_{L,R}} \text{ and } \frac{C_{\mathrm{O},x=0}}{C_{\mathrm{O},x=\mathrm{bulk}}} = \frac{j_{L,O} - j_O}{j_{L,O}} \quad (36)$$

Where C_{i} is the concentration of either the species that becomes reduced (R), or oxidised (O) by the electron transfer and D_{q} is the diffusion coefficient of species q in the electrolyte. Calculation of C_{q}, which is often distributed spatially, and D_{q}, depends on reactants, products, electrode microstructures, local current densities, and operating conditions (T, P).

2.2. Solid Oxide Electrochemical Reactors

2.2.1. A Brief History of Solid Oxide Electrochemical Reactors

Henry Cavendish (1731 – 1810) is generally credited with the first observation of solid state electrochemistry through his findings on the temperature-dependent conductivity of glass in 1774 (78); the electrolytic nature of this glass was published less than 100 years later (79, 80). The most significant event in history for solid oxide electrochemical reactors (SOERs) occurred in 1899, when Walther Nernst (1864 – 1941) discovered the so called 'Nernst mass' of a conducting ceramic containing 85 mol% ZrO_2 and 15 mol% Y_2O_3 (81), which is still the most common electrolyte material for solid oxide electrochemical reactors (SOERs), albeit with a Y_2O_3 concentration of 8 mol%, which is the minimum amount required to stabilise the cubic lattice structure.

The conceptual solid oxide fuel cell (SOFC) was first demonstrated in 1937 using a doped-zirconia electrolyte, Fe_3O_4 cathode, and C anode (82). Understandably, these electrode materials where poorly-suited to SOFCs due to their instability with the reactant and product

gases. Shortly after, German scientist Carl Wagner (1901 – 1977) proved that the conductivity of doped-zirconia electrolytes resulted from the presence of oxygen vacancies that were mobile under an oxygen partial pressure gradient (83), so is considered the founder of solid state chemistry (84). In 1957, Wagner published a subsequent paper that laid out the theoretical foundation for SOFCs (85). Several additional important discoveries were made in the 20th century that significantly improved the performance of SOERs:

- The discovery of rare-earth transition metal perovskites that provided enhanced oxygen oxidation / reduction kinetics, particularly doped-lanthanum manganite, which has an equivalent thermal expansion coefficient to doped-zirconia, and therefore good adhesion, post sintering.
- The use of Ni metal as the electronically-conducting phase within composite anodes, that provided favourable electrochemical kinetics in the fuel-electrode, and remains the standard electronically conducting material in SOERs today (86).
- The co-sintering of composite anodes with the electrolyte at high temperatures, which improved the gas-tightness of the electrolyte and reaction site density, dramatically increasing electrochemical performance and facilitating lower-temperature operation (87). The oxygen-electrode could then be applied subsequently, and sintered at a lower temperature, preventing its chemical reaction with the electrolyte.

2.2.2. Theory of Operation

Solid oxide electrochemical reactors operate at 600 – 1000 °C, at which the electrolyte materials are sufficiently conductive to O^{2-} ions. At these temperatures, both products and reactants are gaseous. Notably, at these temperatures, the hydrocarbon reforming process is activated (in the presence of catalysts), as shown by equation (2), so that SOERs can operate with most hydrocarbons. Furthermore, if waste heat generated from fuel cell operation is used *e.g.* for industrial or domestic heating, overall system efficiencies can be *ca*. 85 – 90 % (27).

There are three types of mobile species in SOERs:

- Gaseous products and reactants
- Ionic charge carriers, *i.e.* O^{2-} ions
- Electrons (e^-)

Each type of species is transported through a different phase, or void for gases. Therefore, reactions occur at so called 'triple phase boundaries' (TPBs), *i.e.* the intersection of electronically-conducting phase | ionically-conducting phase | pore. As the solid phase is neither consumed nor produced, TPBs are usually distributed spatially within a three-dimensional porous electrode, maximising their density. There are two types of electrodes in SOERs: the 'oxygen-electrode', which is typically exposed to (static) air, and where O_2 / O^{2-} reduction / oxidation occurs; and the 'fuel-electrode' that is exposed to the mixture containing a fuel (*i.e.* H_2, CO) and any oxidised fuels (H_2O, CO_2).

The schematic in **Figure 12** shows the principle of operation of SOERs, which is summarised qualitatively below for fuel cell operation with H_2:

1. O_2 diffuses into the porous cathode,
2. O_2 adsorbs dissociatively at a TPB
3. O is reduced to an O^{2-} ion (may be a single or multi-step process)
4. O^{2-} travels across the electrolyte
5. H_2 diffuses into the anode
6. H_2 adsorbs at a TPB
7. H_2 is oxidised to H_2O, releasing 2 electrons, which are transported to the cathode through an external electrical circuit
8. H_2O desorbs from the TPB and diffuses to the bulk gas stream

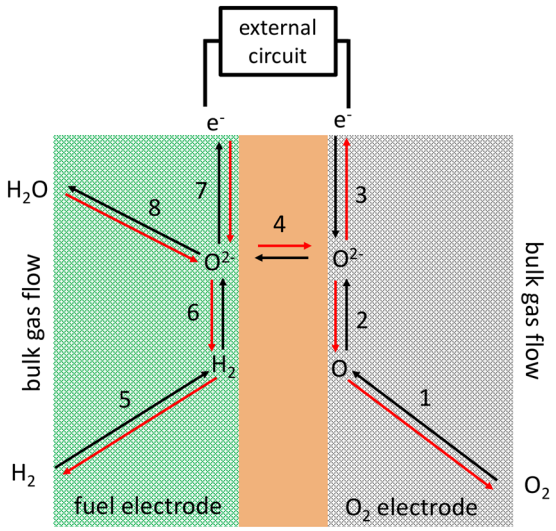


Figure 12. Schematic showing the principle of operation for an SOFC (black arrows) or SOE (red arrows) operating with H_2 / H_2O and O_2. The electrolyte is shown in orange.

The reactions occurring within the porous electrodes for both fuel cell (SOFC) and electrolyser (SOE) modes, along with CO_2/CO operation, are shown by equations (37) - (39).

Oxygen-electrode reaction:

$$O_2 + 4e^- \underset{\text{SOE}}{\overset{\text{SOFC}}{\rightleftarrows}} 2O^{2-} \quad (37)$$

$$CO_2 + 2e^- \underset{\text{SOFC}}{\overset{\text{SOE}}{\rightleftarrows}} CO + O^{2-} \quad (38)$$

Fuel-electrode reactions:

$$H_2O + 2e^- \underset{\text{SOFC}}{\overset{\text{SOE}}{\rightleftarrows}} H_2 + O^{2-} \quad (39)$$

2.2.3. Materials for Solid Oxide Electrochemical Reactors

Solid oxide electrochemical reactors are characterised by having an O^{2-} ion-conducting metal-oxide electrolyte, sandwiched by electronically-conducting, porous, positive and negative electrodes, whereby the reactants / products are supplied / removed, respectively through the pores. The most common SOER materials used given in **Table 3**.

Table 3. The most common materials for the functional layers of SOERs, showing conducted species and chemical formulae (88-93). The abundance of each element in the Earth's crust is also specified for context (94).

Functional layer	Material	Species conducted	Chemical formula	Element abundance / ppm*
Electrolyte	Scandia-stabilised zirconia (SSZ)	O^{2-}	$(Sc_2O_3)_{0.1}(ZrO_2)_{0.9}$	Zr = 165 Sc = 22
	Yttria-stabilised zirconia (YSZ)		$(Y_2O_3)_{0.08}(ZrO_2)_{0.92}$	Y = 33
	Gadolinium-doped ceria (CGO)		$Gd_{0.2}Ce_{0.8}O_{1.95}$	Ce = 60 Gd = 5.4
	Samarium-doped ceria (SDC)		$Sm_{0.2}Ce_{0.8}O_{2-x}$	Sm = 6
	Lanthanum strontium gallium magnesium oxide (LSGM)		$La_{0.8}Sr_{0.2}Ga_{0.8}Mg_{0.2}O_{3-x}$	La = 30 Ga = 15 Mg = 2.33
Oxygen-electrode	Lanthanum strontium manganite (LSM)	e^-	$(La_{0.8}Sr_{0.2})_{0.95}MnO_{3-x}$	Sr = 375 Mn = 950
	Lanthanum strontium cobalt ferrite (LSCF)	e^- and O^{2-}	$(La_{0.6}Sr_{0.4})_{0.95}Co_{0.2}Fe_{0.8}O_{3-x}$	Co = 25 Fe = 5.6×10^4
Fuel-electrode	Nickel	e^-	Ni	Ni = 75
	Copper		Cu	Cu = 55

* For comparison, the abundances of Ag, Au, and Pt are 0.07, 0.004, and 0.004 ppm, respectively (95).

Depending on the electrode and electrolyte materials, an 'interlayer' may be required to prevent their chemical reaction at high temperatures (> 1000 °C during sintering), or to bridge a difference in their thermal expansion coefficients. Examples include CGO between YSZ and LSCF, and SDC between YSZ and barium strontium cobalt ferrite ($Ba_{0.5}Sr_{0.5}Co_{0.75}Fe_{0.25}O_{3-\delta}$, BSCF), to prevent undesirable solid-state reactions (96). For a comprehensive list of electrolyte, anode, and cathode materials, the reader is directed to reference (97).

2.2.4. Thermodynamics

2.2.4.1 Gas Mixtures

Due to the oxidising / reducing nature of gas mixtures at the fuel-electrode (H_2O / H_2, CO_2 / CO) and the dependence of Gibbs energy on the operating temperature, the operating conditions should be selected carefully to maintain materials' stabilities and favourable reaction kinetics. At reactor start-up, reduction of NiO to Ni in the fuel electrode is typically required, due to the oxidation of Ni in air during SOER fabrication. **Figure 13** shows the equilibrium potential difference of the H_2O/H_2, CO_2/CO, and Ni/NiO reaction pairs with varying operating temperature, with the oxygen-electrode exposed to air at 0.1 MPa. For the initial NiO reduction process, H_2 (> 99 %) is typically used, which is highly-reducing at all temperatures. For electrolysis, the onset of mass transport control can be mitigated by increasing the concentration of the oxidised species; however, it is critical that the gas mixture does not become oxidising to Ni. Notably, at $T < ca.$ 800 °C, the H_2O / H_2 gas mixture has the greater oxidising potential, and at $T > ca.$ 800 °C, the CO_2 / CO has the greater oxidising potential, suggesting that each gas mixture is favourable at different operating temperatures.

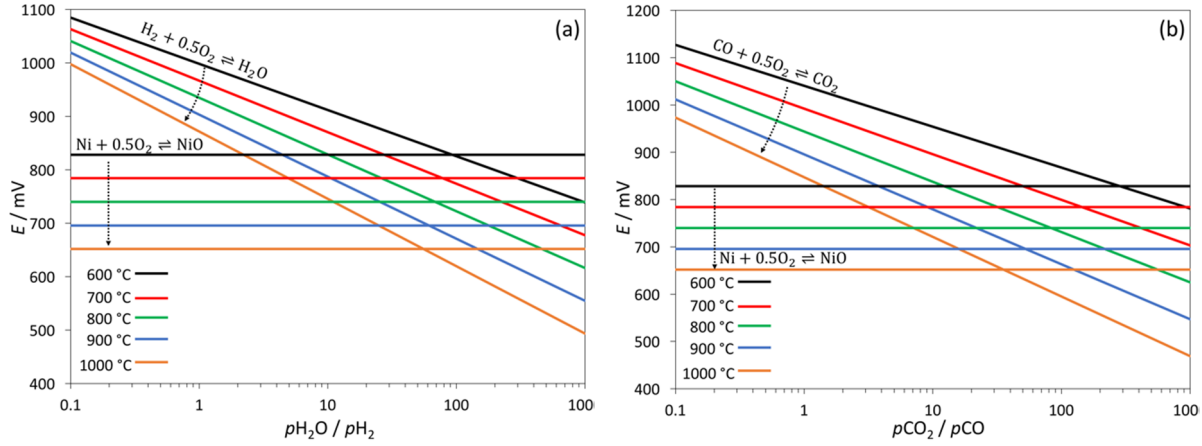


Figure 13. Potential difference variation with temperature and concentration for reaction (37) coupled with reaction: (a) (39); and (b) (38). Ni/NiO oxidation / reduction potential difference with reaction (37) is shown at equivalent temperatures. Data taken from (98).

2.2.4.2 Thermoneutral Potential Difference

During electrolysis, the preferred operational cell potential difference is the point at which no net heat is generated by the reactor, maximising energy conversion efficiency. This is referred to as the 'thermoneutral potential difference' (ΔE_{tn}), which can be calculated using equation (40) (99).

$$\Delta E_{tn} = \frac{-\Delta H(T,P)}{\nu_e F} \quad (40)$$

Where ΔH represents the reaction enthalpy which depends on temperature (T) and pressure (P). ν_e represents the electron stoichiometry of the overall cell reaction, and F is the Faraday constant. **Figure 14** shows the variation of the thermoneutral potential difference for CO_2 and H_2O electrolysis (for gaseous reactants and products), at 0.1 MPa. Evidently, CO_2 electrolysis can operate at a higher potential difference before heat loss inefficiencies.

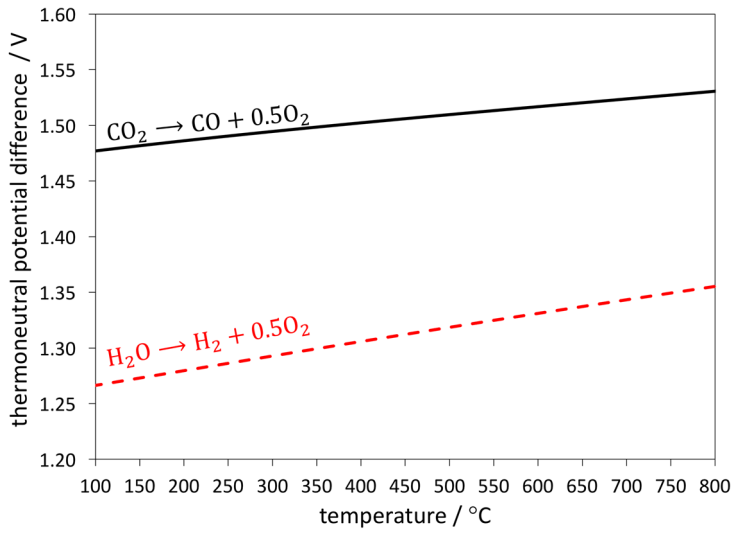


Figure 14. Effect of temperature on thermoneutral potential difference for CO_2 and H_2O (g) electrolysis. Thermodynamic data from (27).

2.2.5. Kinetics

Due to the three-dimensionality of SOER electrodes, reactant / product concentrations are distributed spatially within the electrode, and therefore the most appropriate kinetic model for SOER electrodes is the Butler-Volmer relationship (equation (35)) in which the overpotential is adjusted appropriately to account for local concentrations. Consequently, overpotential, and hence current density, are also predicted to be distributed spatially, so that it is not possible to determine electrochemical kinetic parameters reliably, *i.e.* the exchange current density and charge transfer coefficients, from conventional electrode performances. Therefore, it is necessary to perform experiments on electrode geometries of known TPB length and overpotential, the results against which the Butler-Volmer equation can be fitted and kinetic parameters extracted. These are typically referred to as 'patterned' electrodes, and comprise a 2D (*i.e.* independent of height) structure of electronically-conducting material with a known length, adhering to the electrolyte material. The potential difference between each phase and a reference electrode (of the same material), and hence overpotential, can be controlled precisely.

Considering these factors, the published literature on kinetic parameters for the oxygen- and fuel-electrodes are reviewed in Sections 2.2.5.1 and 2.2.5.2, respectively, for the conventional SOER materials: Ni, YSZ, and LSM.

2.2.5.1 Oxygen-electrode Electrochemical Kinetics

Operating with air (p_{O2} = 21 kPa) and the conventional YSZ-LSM oxygen-electrode materials, electrochemical kinetics can be considered to follow the Butler-Volmer equation where reactions occur at (and are confined to) TPBs. The exchange current density (j_0) varies with temperature (T) and gas partial pressures. Measurements on patterned LSM on a YSZ electrolyte with a LSM reference electrode and Pt counter electrode at 945 °C (T^{ref}) determined that at high cathodic overpotential, an activation process dominated, and at low overpotentials, a O transfer process competed with a charge transfer process (100, 101). Assembling these mechanisms into a kinetic model, equation (41) describes the exchange current density for the oxygen-electrode reaction.

$$j_0 = {j_0}^{\mathrm{ref}} \exp\left(\frac{-E_{\mathrm{a,O}}}{R}\left(\frac{1}{T} - \frac{1}{T^{\mathrm{ref}}}\right)\right)\left(\frac{P_{\mathrm{t}} y_{O2}}{{p_{O2}}^{\mathrm{ref}}}\right)^{\zeta} \qquad (41)$$

Where ${j_0}^{\mathrm{ref}}$ represents an empirical exchange current density at reference conditions, P_t the pressure locally within the electrode, and T^{ref} and ${p_{O2}}^{ref}$ represent reference temperature and oxygen partial pressure, respectively. ζ is constant, and y_{O2} represents the local O_2 mole fraction. E_a represents the activation energy for the oxygen electrode (O). Many values for ${j_0}^{ref}$ have been published; however, most reports used A m^{-2} units for j_0, indicating that a fundamental TPB property has been omitted, namely that TPBs are localised along a line, *i.e.* units are A m^{-1}. Therefore, any reported exchange current densities in A m^{-2} are unreliable (102-105). Consequently, the only reliable exchange current density was obtained from patterned LSM-YSZ electrode experiments, and is reported in **Table 4** (106).

The charge transfer coefficients under anodic and cathodic polarisations differ, due to the different mechanisms (transition states and phases) for O_2 reduction / O^{2-} oxidation (107). Therefore, most reports which predict equal forward and backward charge transfer coefficients, are unreliable. The charge transfer coefficients for O_2 reduction, measured with a patterned LSM-YSZ electrode were 0.75 and 0.25, for the forward and backward reactions, respectively. However, these values failed to reproduce experimental results from other studies when incorporated into a simulation framework. Therefore, the most suitable values for the charge transfer coefficients under cathodic polarisation were taken from a comprehensive review and

comparison publication (108), fitted against multiple sets of experimental data, and are given in **Table 4**. The patterned LSM-YSZ study extended anodic polarisation overpotentials to ≤ |100 mV|, which was insufficiently high to extract kinetic parameters. In the absence of reliable studies, charge transfer coefficient values under anodic polarisation of 0.5 have been included in **Table 4** (109, 110); however, these are inaccurate.

Table 4. Values of constants and the kinetic parameters for the oxygen-electrode. SOE and SOFC denote overall cell operation, *i.e.* anodic and cathodic electrode polarisation, respectively.

Parameter / unit	Value	Reference
$\alpha_{SOE,a}$, $\alpha_{SOE,c}$, $\alpha_{SOFC,a}$, $\alpha_{SOFC,c}$ / 1	0.5, 0.5*, 0.4, 0.1	(108, 111, 112)
j_0^{ref} / A m^{-1}	2.5×10^{-4}	
$E_{a,O}$ / J mol^{-1}	1.4×10^{5}	
T^{ref} / K	1218	(113)
p_{O2}^{ref} / 10^5 Pa	0.21	
ζ / 1	0.375	

*Charge transfer coefficients of 0.5 are inaccurate; however, in the absence of any published literature, these values are assumed.

The overpotential expression to use in the Butler-Volmer equation that accounts for local concentration distributions is given by equation (42).

$$\eta = \phi_{\text{io}} - \phi_{\text{el}} - \frac{RT}{2\nu_e F}\ln\left(\frac{P_{\text{t,inlet}}y_{\text{O2,inlet}}}{P_{\text{t}}y_{\text{O2}}}\right) \quad (42)$$

Where ϕ is the potential of the ionically-conducting (io) or electronically-conducting (el) species, *i.e.* YSZ and LSM, respectively; 'inlet' indicates conditions at the reactor inlet. y_{O2} accounts for local concentration differences, as in Section 2.2.5.3.

2.2.5.2 Fuel-electrode Electrochemical Kinetics

Electrochemical kinetics at the conventional Ni-YSZ fuel-electrode follow the Butler-Volmer relationship, in which overpotential is adjusted for local concentrations, as for the oxygen-electrode. Patterned Ni-YSZ electrode experiments with hydrogen identified the exchange current density dependency on hydrogen concentration and temperature, resulting in equation (43) (106, 113, 114).

$$j_0 = {j_0}^{\mathrm{ref}} \exp\left(\frac{-E_{\mathrm{a,F}}}{R}\left(\frac{1}{T}-\frac{1}{T^{\mathrm{ref}}}\right)\right)\frac{\left(\frac{P_{\mathrm{t}}y_{\mathrm{H2}}}{{p_{\mathrm{H2}}}^{\mathrm{ref}}}\right)^{0.35}\left(\frac{P_{\mathrm{t}}(1-y_{\mathrm{H2}})}{1.013\times10^{5}}\right)^{0.6\ 5}}{1+\left(\frac{P_{\mathrm{t}}y_{\mathrm{H2}}}{{p_{\mathrm{H2}}}^{\mathrm{ref}}}\right)^{0.5}} \quad (43)$$

Where the reference hydrogen partial pressure ($p_{\mathrm{H2}}^{\mathrm{ref}}$) varies with temperature, and is given by equation (44).

$${p_{\mathrm{H2}}}^{\mathrm{ref}} = \frac{A_{des}\Gamma^2\sqrt{2\pi RTM_{\mathrm{H2}}}}{\gamma_0}\exp\left(\frac{-E_{\mathrm{des}}}{RT}\right) \quad (44)$$

A_{des}, E_{des}, Γ, and γ_0 represent the hydrogen desorption pre-exponential factor, activation energy, surface site density, and adsorption 'sticking' probability, respectively. M_{H2} is the relative molecular mass of H_2, *i.e.* 2.016 kg kmol^{-1}.

To find values for the kinetic parameters, *i.e.* j_0^{ref} and the charge transfer coefficients, results of measurements with patterned electrodes of Ni on YSZ provided the only reliable data. For identical reasons outlined in Section 2.2.5.1, exchange current densities calculated using composite 3D electrodes with units A m^{-2} were considered unreliable. Furthermore, the effect of gas mixture on kinetic parameters at the fuel-electrode was much greater than for the oxygen-electrode, *e.g.* the presence of H_2O in the H_2 fuel inlet increases the rate of electrochemical hydrogen oxidation (115) by modifying the mechanism, in addition to the hydrogen concentration. Experimental results with patterned electrodes indicated that the charge transfer coefficient varied with temperature (116). Therefore, sets of charge transfer coefficients and process activation energies are presented alongside the constants for equations (43) and (44) in **Table 5**. Notably, the results are inconsistent between different research groups, reflecting the endemic problem of reproducibility across the field.

Table 5. Values of constants and kinetic parameters for the fuel-electrode operating with H_2 / H_2O mixtures.

Parameter / unit	Value	Reference
$\alpha_{SOFC,a}$, $\alpha_{SOFC,c}$ (750 – 850 °C, 33 % H_2, 4 % H_2O, 63 % Ar) / 1	0.27, 0.73	
$\alpha_{SOFC,a}$, $\alpha_{SOFC,c}$ (750 °C, 17 % H_2, 4 % H_2O, 79 % Ar) / 1	0.19 – 0.23, 0.81 – 0.77	(116)
$\alpha_{SOFC,a}$, $\alpha_{SOFC,c}$ (750 °C, 8 % H_2, 4 % H_2O, 88 % Ar) / 1	0.23 – 0.18, 0.77 – 0.82	
$E_{a,F}$ / J mol^{-1}	9.16×10^{4}	
T^{ref} / K	1012	
$\alpha_{SOE,a}$, $\alpha_{SOE,c}$, $\alpha_{SOFC,a}$, $\alpha_{SOFC,c}$ (700 °C) / 1	0.9, 0.1, 0.65, 0.35	
j_0^{ref} / A m^{-1}	4.092×10^{-2}	(108, 113, 114, 117)
T^{ref} / K	973	
$E_{a,F}$ / J mol^{-1}	1.2×10^{5}	(104)
A_{des} / s m^2 mol^{-1}	5.59×10^{15}	
E_{des} / J mol^{-1}	8.812×10^{4}	(114)
Γ / mol m^{-2}	1.2×10^{-5}	
γ_0 / 1	0.01	

The overpotential in the fuel-electrode, adjusted for local H_2 concentration, is given in equation (45).

$$\eta = \phi_{\mathrm{el}} - \phi_{\mathrm{io}} - \frac{RT}{2F}\ln\left(\frac{y_{\mathrm{H2,inlet}}}{y_{\mathrm{H2}}}\frac{1-y_{\mathrm{H2}}}{1-y_{\mathrm{H2,inlet}}}\right) \qquad (45)$$

2.2.5.3 Gas Transport

Figure 15 shows the microstructure, obtained by Focused Ion Bean-Scanning Electron Microscopy (FIB-SEM), of a real oxygen-electrode fabricated by conventional powder-mixing techniques; the microstructure of the fuel-electrode is similar. Notably, the void structure comprises a tortuous network of pores of various sizes, so both molecular and Knudsen diffusion mechanisms occur simultaneously. Consequently, the most appropriate model for (open pore) diffusion within the electrodes is the 'Dusty Gas Model', which accounts for frequent collisions between the gas molecules and with the porous media (118).

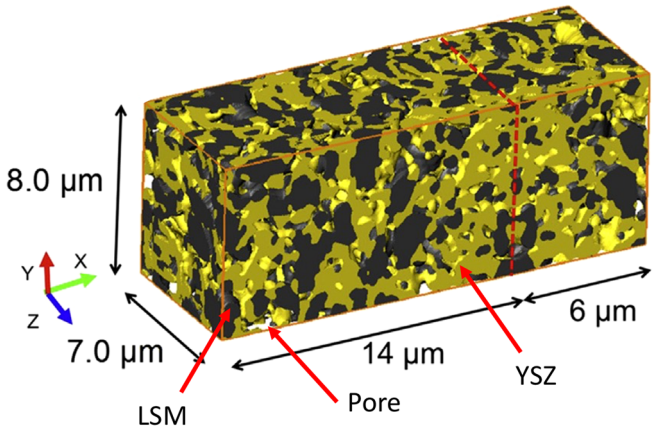


Figure 15. 3D reconstructed FIB-SEM image of composite YSZ-LSM electrode. Reproduced with permission from (112).

Equation (46) describes the Dusty Gas model for a binary gas mixture of i / j (*i.e.* O_2 / N_2, H_2 / H_2O, CO / CO_2, *etc.*), assuming ideal gas behaviour which is appropriate due to the high temperature and low pressure of the reactor (119).

$$N_i\left(\frac{1}{D^{\text{eff}}{}_{\text{K,i}}}+\frac{1-y_\text{i}}{D^{\text{eff}}{}_{\text{B,i/j}}}\right)=\frac{y_\text{i}}{D^{\text{eff}}{}_{\text{B,i/j}}}N_\text{j}-\frac{P_\text{t}}{RT}\nabla y_\text{i}-\frac{y_\text{i}}{RT}\left(1+\frac{\varepsilon/\tau\, {d_\text{p}}^2}{32D^{\text{eff}}{}_{\text{K,i}}}\frac{P_\text{t}}{\mu_{\text{i/j}}}\right) \quad (46)$$

Where N_i represents the flux density of species i, D is the effective (eff) binary (B) or Knudsen (K) diffusion coefficient, d_p is the (average) pore diameter, ε and τ are the (open pore) porosity and tortuosity of the porous phase within the electrode, respectively, and $\mu_{\text{i/j}}$ is the viscosity of the binary gas mixture. The effective Knudsen and binary diffusion coefficients that account for microstructure can be calculated using the Bruggeman correction, as shown in equations (47) and (48), respectively (120, 121).

$$D^{\text{eff}}{}_{\text{K,i}}=\frac{1}{3}\frac{\varepsilon}{\tau}d_p\sqrt{\frac{8RT}{\pi M_i}} \quad (47)$$

$$D^{\text{eff}}{}_{\text{B,i/j}}=\frac{\varepsilon}{\tau}D_{\text{B,i/j}} \quad (48)$$

$D_{\text{B,i/j}}$ is the binary diffusion coefficient for the gas mixture i / j, which varies with temperature, and can be approximated, for varying temperature and pressure, using equation (49).

$$D_{\text{B,i/j}}=\frac{0.0143T^{1.7\ 5}}{P_\text{t}(a^{1/3}+b^{1/3})^2}\sqrt{\frac{{M_i}^{-1}+{M_j}^{-1}}{2000}} \quad (49)$$

Where a and b are empirical constants unique to the gas mixture, equal to 6.12 and 13.1, respectively, for H_2 / H_2O, and 16.3 and 18.5, respectively, for O_2 / N_2. M_k is the relative

molecular mass of species k (122). The viscosity of a binary gas mixture can be estimated using equation (50) (122). Individual, measured values for viscosity (μ_i) at T can be found in the literature (123, 124), or estimated using equation (51), where the coefficients (b_q) for H_2, H_2O, CO, CO_2, O_2 and N_2 are tabulated in the literature (122).

$$\mu_{i/j} = \frac{y_i \mu_i {M_i}^{0.5} + y_j \mu_j {M_j}^{0.5}}{y_i {M_i}^{0.5} + y_j {M_j}^{0.5}} \quad (50)$$

$$\mu_i(\text{Pa s}) = \sum_{\forall q} b_q \left({}^{T}/_{1000}\right)^{q} \quad (51)$$

2.2.5.4 Ionic-species Transport

Doping the cubic (fluorite) ZrO_2 lattice with another metal oxide, *i.e.* Y_2O_3, creates vacancies in the lattice structure, as shown in **Figure 16**.

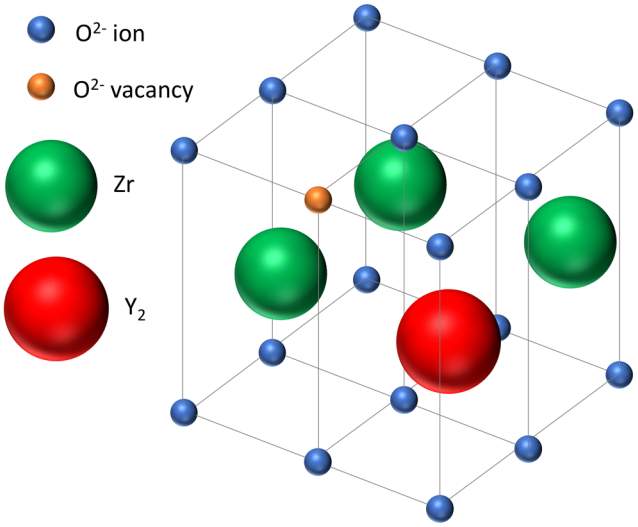


Figure 16. Schematic of the ZrO_2 lattice doped with Y_2O_3, and the creation of an oxygen vacancy.

The doping metal oxide has a lower oxidation state, *i.e.* Y^{III} or Sc^{III} compared to the Zr^{IV}; therefore, to balance overall charge, (mobile) oxide ion vacancies are created within the lattice, and hence O^{2-} ionic conductivity results. It is desirable to optimise dopant concentration for maximum conductivity, given in **Table 6**.

Table 6. Common doping oxides for zirconia, and the required concentration for full stabilisation (125).

Doping oxide	Concentration for full stabilisation / mol%
CaO	12 - 15
Y_2O_3	8 - 9
Sc_2O_3	8 - 9
R_2O_3*	8 - 12

* 'R' represents other rare-earth metals with oxidation state +3.

The transport of charged species 'k' of charge q_s (O^{2-} ions or e^-, with charges -2 and -1, respectively) within these materials ('i') due to a potential gradient is determined by the phase conductivity (σ), as shown in equation (52), where 'eff' denotes 'effective', *i.e.* adjusted for microstructure using the tortuosity (53), or with the Bruggeman approximation when tortuosity is unknown (54), for nominally spherical constituents (120, 121).

$$\nabla N_{\mathrm{k}} = -\frac{{\sigma_i}^{\mathrm{eff}}}{q_s F}\nabla\phi_i \qquad (52)$$

$${\sigma_i}^{\mathrm{eff}} = \frac{\varepsilon}{\tau}\sigma_i \qquad (53)$$

$${\sigma_i}^{\mathrm{eff}} = \sigma_i \varepsilon^{3/2} \qquad (54)$$

Where ε and τ, in this instance, refer to the volume fraction and tortuosity of the conductor network, respectively. The pure-phase conductivities for conventional SOER materials are given in **Table 7**.

Table 7. Conductivity expressions for varying T, for conventional SOER materials (126).

Material	σ / S m^{-1}
Ni	3.37×10^6-1065.3T
YSZ	$3.34\times10^4\exp(-10300/T)$
LSM	$8.855\times10^7\exp(-1082.5/T)/T$

2.3. Literature Review

2.3.1. Conventional SOER Fabrication Processes and their Limitations*

Three types of processes have been reported for fabricating the functional layers of solid oxide electrochemical reactors: (i) chemical methods, (ii) physical methods, and (iii) powder mixing processes, which are most common (127). Conventional powder processing methods involve mixing the constituent phases, as powders, with a sacrificial pore-forming phase where porosity is desirable, to form 'pastes' that are tape cast or screen printed into films, then subsequently dried and sintered (128, 129). Due to the similarity in sintering temperatures of the electrolyte (*e.g.* YSZ) and fuel-electrode (*e.g.* NiO-YSZ), they are typically co-sintered, minimising electrolyte porosity and mitigating gas leakage through the electrolyte. Oxygen-electrodes (*e.g.* LSM or LSCF) typically require a much lower sintering temperature, and therefore a minimum of two sintering steps are necessary.

Both tape casting and screen printing rely on random particle mixing within the electrode pastes to create high densities of triple phase boundaries (TPBs) (130), which are the intersections of individually percolated pores, electronically-conducting and ionically-conducting phases, at which reactions occur (131). Alternatively, for mixed-conducting materials (*i.e.* LSCF) reactions occur at dual phase boundaries (DPBs), which are the intersection of pores and the mixed conductor. Such techniques result in poorly reproducible microstructures, porosities, and TPB densities, as shown in **Figure 15** and **Figure 17**, for the oxygen- and fuel-electrodes, respectively, on which the electrode performance depends critically (132), particularly for the oxygen-electrode which typically accounts for the majority of the total SOER resistance (133). Furthermore, a significant fraction of TPBs are non-percolating, limiting reactor performance (134), as shown for a Ni-YSZ electrode in **Figure 17**, in which only *ca*. 60 % of TPBs percolate. Similarly, for the YSZ-LSM electrode, microstructural investigations have found that up to 25 % of LSM particles within the bulk electrode are non-percolating, resulting in *ca*. 1/3 of the TPBs being inactive (135, 136). However, no reports have been published of investigations of the composite electrode microstructural properties close to the electrolyte | electrode interface, which is where most electrochemical reactions occur.

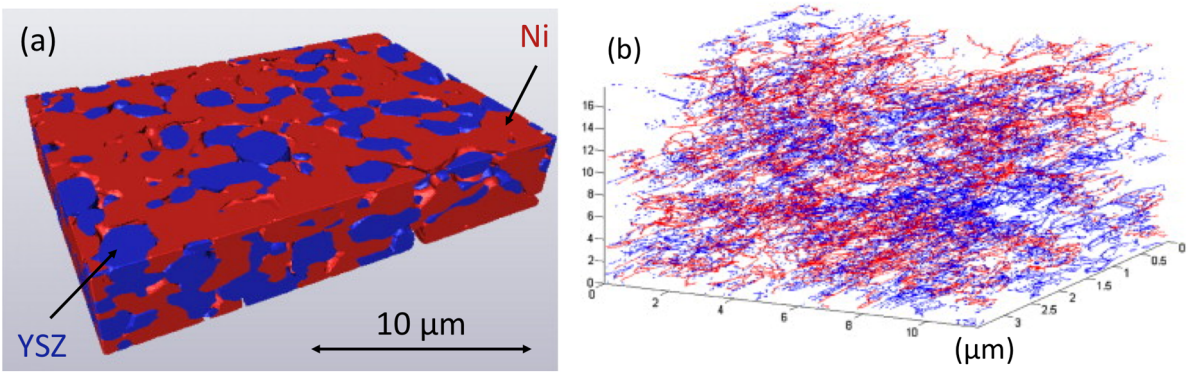


Figure 17. Real Ni-YSZ electrode reconstruction by FIB-SEM showing (a) phases; and (b) percolating (blue) and non-percolating (red) TPBs. Reproduced with permission from (137).

Hence, microstructural engineering is critically important to improve SOER electrochemical performance (138). Infiltrated-scaffold techniques with higher percolating TPB densities and control over porosity are being developed (139-141), the scaffolds being fabricated by tailored sintering of the electrolyte phase mixed with a pore-forming phase (142), or by mining 'trenches' in pre-densified ceramic films with an excimer laser (143). The former process requires many (*ca*. 20) time consuming steps to add sufficient solids into the scaffold to ensure percolation of the electronically-conducting phase and for a high TPB density, so it is widely considered unsuitable for manufacturing. The latter process is subtractive, and therefore inferior to additive methods which have less material waste.

Furthermore, tape casting and screen printing suffer from significantly greater minimum electrolyte layer thicknesses compared to those produced by more complex and expensive technologies, such as chemical vapour deposition (CVD) or pulsed laser deposition (PLD) (127, 144). Consequently, for conventionally fabricated SOERs, the ohmic resistance remains high, which cannot be decreased using the conventional techniques.

*Section text partially reproduced from Farandos et al., 2016 (145).

2.3.2. Introduction to Additive Manufacturing

Additive manufacturing (AM) technologies began to be developed in the 1980s (146, 147), and are highly versatile, rapid prototyping techniques that have been applied to graphics output (148), displays (149), plastic electronics (150, 151), biomaterials (152, 153), ceramic (148), carbon fibre, and metal components (154). There are several classifications of scalable AM technologies, including laser-assisted technologies such as stereolithography or laser sintering / melting, (micro-)extrusion, and 3D inkjet printing (155). The desired resolution (*i.e.* minimum lateral feature size) and the fabrication time required to deposit a specific volume varies

between different AM processes, as shown in **Figure 18**. Evidently, to manufacture SOER electrode microstructures that have a useful feature length of *ca*. 10 µm (130), selective laser consolidation, micro-extrusion, and direct stereolithography are > 1 order of magnitude too large, in their present development. Indirect stereolithography is too slow to be compatible with manufactured components.

With inkjet printing, it is possible to print structures of 10 - 50 µm resolution with *ca.* 30 pL droplet volumes at acceptable printing speeds for manufacturing (145). More recently-developed printheads are able to eject droplets with *ca*. 1 pL volume; hence, resolutions of < 10 µm should be achievable (156). Therefore, inkjet printing is the most suitable technology with which to manufacture SOER electrodes; the other AM technologies may find utility fabricating auxiliary cell components including supports and interconnects. The remainder of this section reviews the application of different AM technologies for ceramic parts manufacture, particularly for conventional SOER materials.

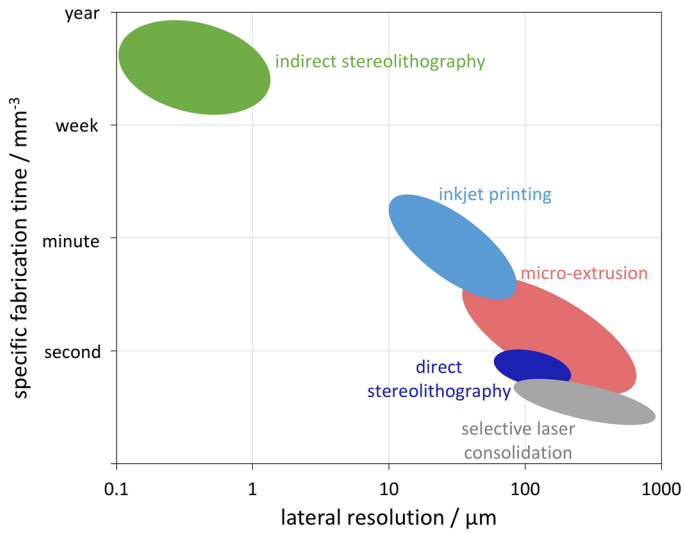


Figure 18. Variation of fabrication time (per mm^3) and lateral resolution for different AM technologies, as of 2017, that have been used to fabricate ceramic components (145, 157-170).

2.3.3. Laser Lithography

The term 'laser-assisted' AM encompasses a wide range of technologies that are differentiated on the basis of whether the phase of the precursor bed is a powder (Section 2.3.3.1) or liquid (Section 2.3.3.2). The general principle of operation involves application of a thin layer of the precursor phase into a suitable container, and exposing select regions of the precursor to a laser beam, which causes sintering locally. Successive layers of the precursor phase are added and treated identically, eventually to produce 3D structures, as shown schematically in **Figure 19**.

For multi-material structures, separate precursor beds would be required, increasing fabrication time, cost, and probability of contamination.

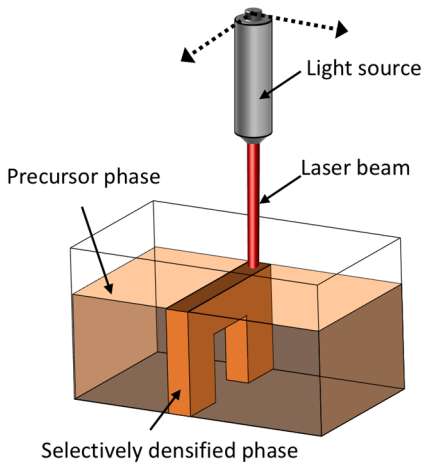


Figure 19. Schematic of the operating principle of laser lithography printers.

2.3.3.1 Selective Laser Consolidation

Selective laser consolidation, which includes both sintering and (partial) melting, employs a particulate bed, in which laser light is used to facilitate sintering or melting of the (ceramic) particles (171). The achievable resolution of printed structures is determined primarily by the laser spot diameter. In contrast, the microstructure and density of the fabricated components depend on the thickness and packing density of the powder layer, the laser beam energy, and exposure duration (158).

Resolutions of 520 µm for selectively-sintered YSZ have been demonstrated, but its effective density was only 56 % of its bulk value, due to a low powder packing density in the precursor bed (158), which was spread and homogenised using a roller. Variations of 'conventional' roller or blade depositions include slurry or spray depositions, which can increase packing densities (171).

Layers of $La_{0.9}Sr_{0.1}Ga_{0.8}Mg_{0.2}O_{3-\delta}$ (LSGM), an intermediate-temperature SOER electrolyte material, have been produced by laser melting, resulting in higher ionic conductivity than layers prepared by solid-state sintering routes. The stoichiometry of a LSGM electrolyte was influenced by laser power and duration; greater laser power and lower scan speed decreased the formation of secondary phases, with optimum conditions being *ca.* 1100 W at 1 mm s^{-1}. The feasibility of electrolyte layer fabrication, with a 98.5 % density, has been demonstrated. However, achieving higher resolution microstructures was not attempted (172).

Laser sintering has been used to fabricate 100 µm width Ni-patterned electrodes on pre-sintered YSZ, demonstrating how the laser sintering parameters affected the sintered substrate (157). Laser energy densities > 0.05 J mm^{-1} sample length resulted in fracture of the YSZ pellets, requiring greater laser writing speeds. Despite greater speeds, thermal shock caused surface micro-cracking, which could lead to lower long-term durability in an operational SOER.

2.3.3.2 Laser Stereolithography

Laser stereolithography employs a liquid precursor bed, containing a heat or light-curable monomer (thermo- or photo-resist, respectively). Direct lithography additionally includes (ceramic) particles dispersed in the resist, that are sintered after combustion of the polymerised precursor, creating the ceramic component. In contrast, indirect (sacrificial) lithography first builds a polymer template, which is coated subsequently by the desired material, *i.e.* a ceramic, before the polymer is removed, increasing fabrication complexity, duration, and cost.

For direct lithography, a high volumetric loading of the ceramic particles in the precursor dispersion is essential to achieve high sintered densities. Typically, layers of 25 - 250 µm thickness are applied, so optimising suspension rheology is essential to achieve homogenous components. Fabrication speed depends on laser write speeds, which are determined by the laser power and the minimum polymerisation energy, as well as dispersion re-coating speeds. The achievable cure depth, C_d, is defined for a specified laser energy (E_l), as shown in equation (55).

$$C_d = D_p \ln\left(\frac{E_l}{E_c}\right) \qquad (55)$$

Where D_p represents a parameter related to the laser attenuation length, and E_c represents the threshold energy required to induce polymerisation. Hence, a range of suitable laser powers or layer thicknesses can be determined (173).

Lateral resolutions of 125 - 200 µm have been reported for printed alumina structures, for which the vertical height was 25 µm. The precursor dispersion was illuminated using LEDs through the bottom of a transparent container, whereby the entire building plane (43.2 mm × 76.8 mm) could be cured in one step. After polymerisation, the sample was drawn out, the dispersion layer refreshed, the sample subsequently returned to the dispersion, and the process repeated. After polymer burn-out and sintering, densities of 99.3% of theoretical values were achieved (159, 160). Rather than illumination of the entire building plane, when a single UV beam was used to cure the polymer, smaller feature sizes of *ca.* 200 and 100 µm were possible, respectively,

for aqueous and non-aqueous precursors (174), with single layer heights of *ca.* 20 µm. Conventional, 'single-photon' polymerisation occurs when the photoresist is illuminated by photons with energies exceeding E_c. However, if two (or more) photon beams, with identical or different frequencies corresponding to energies lower than those required for single-photon polymerisation, are focused into a small volume and absorbed simultaneously, the energy difference between the lower and upper molecular states is equal to the sum of the energies of the two photons, so could exceed the energy threshold for inducing polymerisation, as shown in equation (56).

$$\sum_{1}^{n} h_p \psi_n > E_c \qquad (56)$$

Where ψ_n represents the incident photon frequency, and h_p is Planck's constant. Multi-photon polymerisation can achieve a higher resolution, as higher energy densities are required to facilitate sufficient multi-photon absorptions, *e.g.* squared intensity for two-photon laser lithography; hence, the resolution can be increased (175-177).

The feasibility of fabricating inorganic components (silicon carbon nitride) has been demonstrated, by functionalising the photoresist, achieving feature sizes of 150 nm (178). ZrO_2-substitution into the polymer structures has also been achieved at resolutions of *ca.* 50 nm. However, the ZrO_2 loading was < 14% and the supporting polymer had not been removed, so would not be applicable as a SOER component (29).

In contrast to single-photon polymerisation, no ceramic dispersions have been used for two-photon polymerisations. However, stable and free-standing ceramics can be fabricated using indirect two-photon lithography, whereby the microstructure is first written in a standard photoresist. This template is then covered using *e.g.* atomic layer deposition and the polymer etched out, *e.g.* using O_2 plasma. Al_2O_3 lattices of *ca*. 1 µm resolution with 5 - 200 nm thicknesses have been fabricated using this technique (161, 162). This sacrificial method could potentially also be used to fabricate the electrode or current collection components, as metallic (*i.e*. gold) deposition on these polymer templates has already been demonstrated at the 300 - 500 nm feature size resolution range, with the gold deposition achieved either by sputter coating (179), or electroplating (180). However, without significant improvements in writing speed and post-processing to decrease fabrication time, adoption of sub-micrometre laser lithography for large-scale manufacture of solid oxide electrochemical reactor components is unlikely.

2.3.4. Micro-extrusion

Micro-extrusion, also called robocasting, fabricates structures by extruding a ceramic dispersion continuously from a syringe, as shown schematically in **Figure 20**. The precursor has shear-thinning rheology, so that objects with structural rigidity are produced after extruding 'filaments' that exhibit solid-like behaviour after deposition (181). Alternatively, solidification can be achieved by evaporation of the primary solvent in the ink. Additional, secondary solvents may be added to facilitate filament deformability to establish interconnectivity between individual deposited filaments. One study fabricated a microstructure with 100 - 500 μm resolution for a wide range of metal (oxides) including nickel-based structures (163). These types of structures, theoretically, could serve as porous substrates onto which finer micro-structured functional electrodes could be deposited. Preliminary work on SOFC fabrication using micro-extrusion technology has been attempted, but not yet published after peer-review (182). Ceramic components made of alumina (Al_2O_3) with 100 μm resolution have been fabricated using hydrogels; extension of this technique to YSZ should be possible by substituting the Al_2O_3 for YSZ and modifying the heat treatment procedure appropriately (164). The main challenge for ceramic robocasting is obtaining high solids volume fractions to ensure structural integrity during post-printing treatment (sintering). Presently, most extruded inks have a high polymer content (*ca.* 25%) required to provide structural integrity during printing (**Figure 20**), but high ceramic densities have been reported, after sintering.

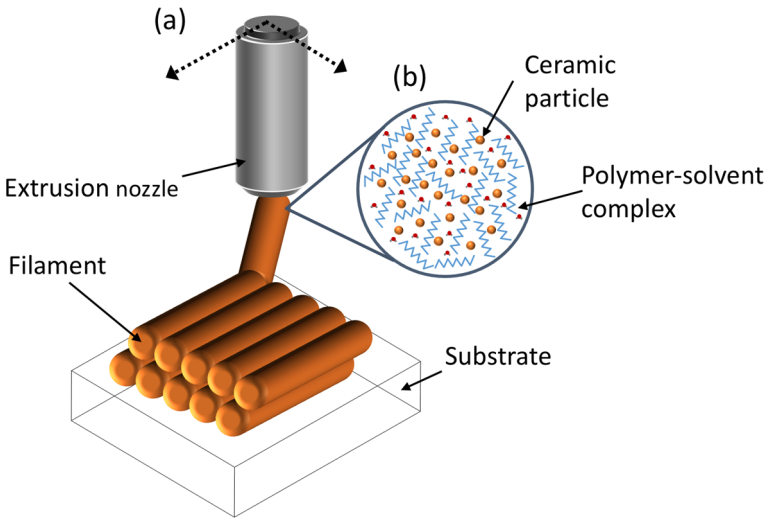


Figure 20. Schematic of a 3D single-nozzle micro-extrusion printer, showing the process of solids deposition and the composition of the precursor dispersion.

2.3.5. Inkjet Printing

A precursor colloidal ceramic dispersion ('ink') can be deposited using either a continuous, electromagnetic, electro-hydrodynamic, thermal drop-on-demand (DOD), or piezoelectric DOD system, the latter being the preference of industrial inkjet printing technologies (148). For continuous inkjet printers, droplets are produced by Rayleigh-Plateau instability within a liquid jet at a particular wavelength, resulting in a stream of droplets with consistent geometry. The droplets are charged and deflected towards a substrate by an electric field; many miss the target and may be recycled, or frequently are wasted (183). Unlike continuous printing, discrete droplets with a precise volume, typically of the order pL (10^{-15} m^3, although femtolitre droplets have been reported (184)), are ejected individually at pre-determined locations with a DOD printer (**Figure 21a**). Deposited droplets may coalesce on the substrate, before drying, and form 1D 'line' structures, which in turn can coalesce to form 2D planar sheets; over-pinning of these sheets forms 3D structures. Droplets are formed by generating pressure waves in an ink-filled channel behind an orifice (printhead nozzle). Ejection occurs when the kinetic energy transferred to the droplet exceeds the surface energy required to form the droplet, and upon ejection, a 'finger' of fluid is released. Above a critical pressure, which depends on the rheological properties of the ink, nozzle geometry and ejection pressure, the finger breaks off, forming a spherical droplet (185).

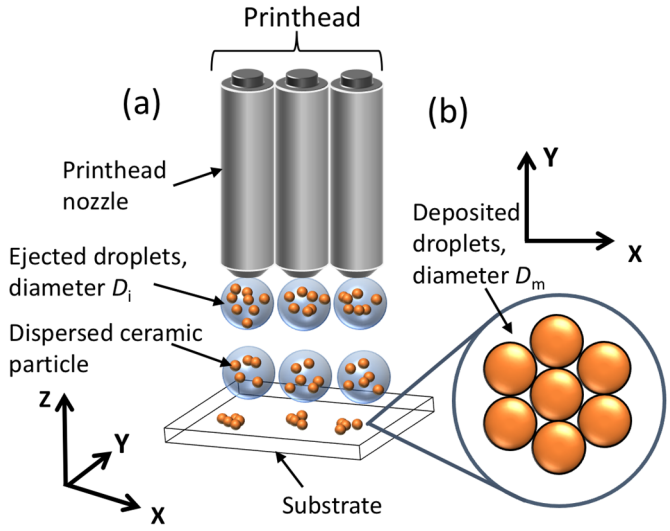


Figure 21. (a) Schematic of a 3D, multi-nozzle, DOD printer; and (b) the appearance of a monolayer of dried deposited droplets in a hexagonal lattice with no inter-droplet overlap.

After the droplets impact and settle on the surface of a substrate, solidification occurs, typically by evaporation, leaving a layer of solid deposit (**Figure 21b**) with a customisable droplet deposition pattern. However, other solidification techniques, including interfacial 'curing' reactions, are possible. The 'resolution' of printed structures, defined as the minimum lateral feature size, is determined by the droplet impact, settling, and coalescence processes, which depend on the droplet size and rheology, the substrate, and printer settings including ejection pressure and pulse duration (186).

The pressure that causes ejection within a piezoelectric DOD inkjet printhead results from an expansion and contraction of a piezoelectric crystal in each printhead nozzle (187). In thermal DOD inkjet printing, the pressure is caused by either the nozzle thermal expansion or vaporisation of a fraction of the ink by application of a current to a heating coil within the nozzle; this causes pressure to increase within the nozzle, ejecting the ink. The latter has a lower capital cost than the former, as expensive piezoelectric crystals are not required (188), but the inks typically require a volatile species and its evaporation results in solids accumulation within the nozzles, and hence reduced lifetime and reproducibility. In addition, studies have shown that predicting printability for thermal DOD inkjet printing is more difficult than piezoelectric systems (148), possibly due to differences in the actuation between piezoelectric and thermal DOD droplet generators (189).

Zirconia inks have been developed for dental applications using thermal DOD printers (165, 166). However, the resolution requirements are not as stringent as for micro-structured electrodes, and the addition of high concentrations of additives such as alumina or volatile

organic compounds to facilitate ejection, would impact electrochemical performance and make the ink less environmentally benign for manufacturing processes.

Fabrication of microstructures with a lateral resolution of 110 - 140 μm, and vertically 1.7 μm thickness have been reported, but the ink was resin-based, which is less environmentally suitable compared to aqueous inks (167).

Unlike alternative AM technologies, 3D inkjet printing has already been applied successfully to fabricate SOERs (Section 2.3.7). Its main advantages include full automation and compatibility with manufacturing, and precise control over layer thickness, which is essential for fabricating functional layers with < 10 μm thickness (168, 170) and tailored electrode microstructures (145); it is also a non-contact, and so non-destructive technique (*c.f.* how laser sintering affects the substrate, leading to micro-cracks or fracture) (157, 190). An additional advantage is that multiple materials can be printed simultaneously, analogous to different colours in conventional desktop-printers, using multiple printheads.

2.3.6. Inkjet Printing Ceramics

High-resolution fabrication of ceramic components using a 3D inkjet printer involves three steps:

i) formulating a suitable ink;

ii) optimising the printing technique with respect to droplet ejection and resolution;

iii) sintering printed structures.

The physical properties of the ink are constrained by 'printability' limits, which are outlined in Section 2.3.6.1, and colloidal stability to aggregation, which is outlined in Section 2.3.6.2. For a specific ink formulation, the resolution and avoidance of defects depends critically on the printer settings and droplet evaporation (191), which are covered in Sections 2.3.6.3 and 2.3.6.4. Due to the non-general nature and material dependence of the third factor, it is covered in detail elsewhere (192, 193).

2.3.6.1 Ink Physical Properties

The formation and behaviour of liquid droplets is controlled by surface tension, inertia, and viscosity; consequently, the printability of an ink can be characterised by the dimensionless Reynolds (Re) and Weber (We) numbers, defined in equations (57) and (58), respectively. The Re and We numbers can be combined into additional dimensionless relationships; the Ohnesorge (Oh) and Capillary (Ca) numbers, defined in equations (59) and (60), respectively,

which indicate the constraints of 'printability' (148). Printability is defined as the reproducible ejection of droplets with a consistent geometry across all nozzles, and is essential for printing reproducible structures without defects.

$$\mathrm{Re} = \frac{\rho u_0 L}{\mu} \quad (57)$$

$$\mathrm{We} = \frac{\rho {u_0}^2 L}{\gamma} \quad (58)$$

$$\mathrm{Oh} = \frac{\sqrt{\mathrm{We}}}{\mathrm{Re}} = \frac{\mu}{\sqrt{\gamma \rho L}} \quad (59)$$

$$\mathrm{Ca} = \frac{\mathrm{We}}{\mathrm{Re}} = \frac{\mu u_0}{\gamma} \quad (60)$$

Where ρ represents the ink density, u_0 droplet ejection velocity (typically between 1 - 5 m s^{-1}), L the characteristic length, conventionally the diameter of printer nozzles (typically 20 - 70 µm), μ ink viscosity, and γ the ink / air surface tension (185). The predicted constraints of printability differ between sources, as shown in **Table 8**.

Table 8. Dimensionless number constraints for printability and printed deposits without defects.

Physical properties range	Constraint	Reference
$2 < \mathrm{Ca}$	Printability	(194)
$1 < \mathrm{Oh}^{-1} < 10$	Printability	(195)
$4 < \mathrm{Oh}^{-1} < 14$	Printability	(196)
$\mathrm{We} > 4$	Minimum flow for ejection	(197)
$\mathrm{We}^{0.5}\mathrm{Re}^{0.25} < 50$	Avoid splashing	(198)
$\mathrm{Re} < 5$	Avoid satellite formation	(199)
$\mathrm{We} > 9$	Avoid satellite formation	(200)

The Oh number is independent of driving conditions (*i.e.* u_0) and closely corresponds to a nozzle jet, so is an appropriate parameter for DOD printing conditions (201). When Oh^{-1} is insufficiently high, viscous forces dominate and prevent droplet ejection. When Oh^{-1} is too high, satellite drops form, as shown in **Figure 22**. In addition to printability, dimensionless number relationships have been proposed for the minimum flow required for droplet ejection, avoidance of splashing after substrate impact, and mitigating the formation of satellite droplets, which are also given in **Table 8** (202).

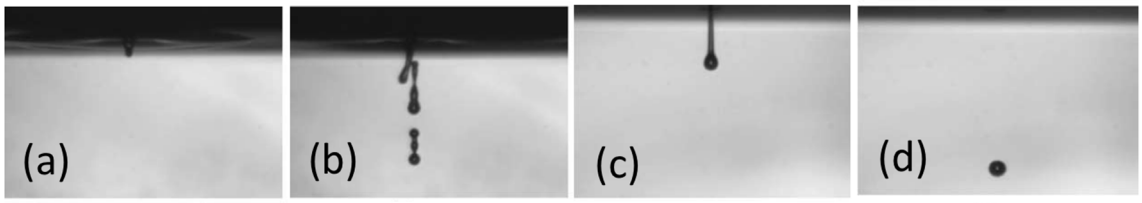


Figure 22. Photographs of droplet ejection and flight for (a, b) $Oh^{-1} > 10$; and (c, d) $1 < Oh^{-1} < 10$. Reproduced with permission from (203).

The inequalities in **Table 8** define a set of possible Re and We numbers for stable droplet formation and ejection, and the constraints of the most commonly accepted relationships are shown in **Figure 23**.

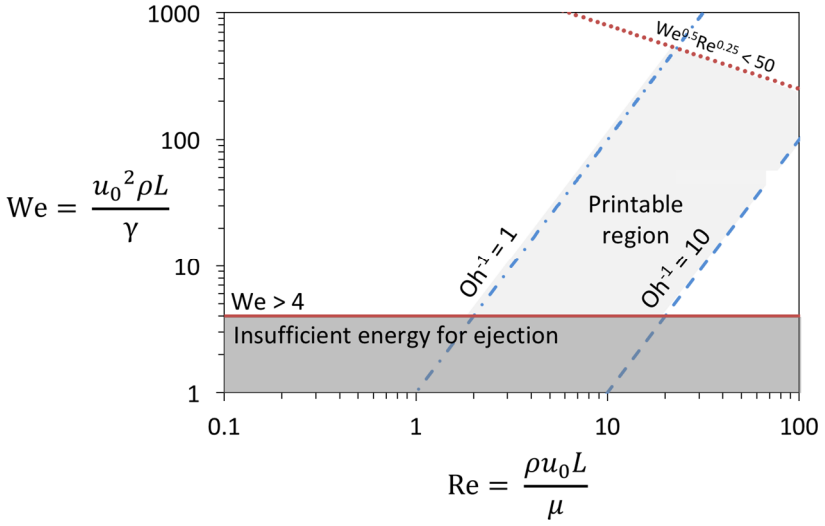


Figure 23. Graph showing the constraints of printability.

Notably, the droplet formation process is independent of the particle radius (r_p), on which the stability of the ink depends critically. However, the viscosity of the dispersion is strongly correlated to the volume fraction of particles (ϑ_p), for which many relations exist; several are given in **Table 9**.

Table 9. Correlations between relative viscosity (μ_r) and intrinsic viscosity ($[\mu]_1$), for ϑ_p in the range $0 \leq \vartheta_p \leq \vartheta_{p,T}$.

Model	Equation	Reference
Einstein	$\mu_r = 1 + 2.5\vartheta_p$	(204)
Krieger Dougherty	$\mu_r = \left(1 - \frac{\vartheta_p}{\vartheta_{p,T}}\right)^{-[\mu]_1 \vartheta_{p,T}}$	(205)
Mooney	$\mu_r = \exp\left(\frac{[\mu]_1 \vartheta_p}{1 - \vartheta_p/\vartheta_{p,T}}\right)$	(206)
Eilers	$\mu_r = \left[1 + \frac{1}{2}[\mu]_1 \left(\frac{\vartheta_p}{1 - \vartheta_p/\vartheta_{p,T}}\right)\right]^2$	(207)
Quemada	$\mu_r = \left(1 - \vartheta_p/\vartheta_{p,T}\right)^{-2}$	(208)
Robinson	$\mu_r = 1 + [\mu]_1 \left(\frac{\vartheta_p}{1 - \vartheta_p/\vartheta_{p,T}}\right)$	(209)

Note: μ_r is the relative viscosity, *i.e.* the ratio of dispersion to solvent viscosity; $[\mu]_1$ is the first term in a Taylor expansion of μ_r, of which the Einstein relation represents the dilute limit. The empirical intrinsic viscosity term for colloidally-stable dispersions varies depending on the viscometer type, but is always approximately 2.5 (210).

2.3.6.2 Colloidal Stability

The colloidal stability of an ink refers to the rate of dispersed particle aggregation, and subsequent sedimentation; greater stability implies a lower rate of aggregation. To quantify colloidal stability, Derjaguin – Landau – Verwey – Overbeek (DLVO) Theory is typically used; particles are assumed to be spherical, and equally-sized for the remainder of this Section.

Several inter-particle interactions determine colloidal stability, the most significant of which can be categorised into two groups: (i) attractive van der Waals (W_{vdW}) and depletion potentials (W_{ex}), and (ii) repulsive electrostatic potentials (W_e), as defined in equations (61) - (63), and (64), respectively (211-213).

$$W_{\mathrm{vdw}}(P_s) = -\frac{A_H}{6}\left(\frac{2r_p}{(P_s + 2r_p)^2 - 4{r_p}^2} + \frac{2{r_p}^2}{\left(P_s + 2r_p\right)^2} + \ln\left(\frac{(P_s + 2r_p)^2 - 4{r_p}^2}{\left(P_s + 2r_p\right)^2}\right)\right) \quad (61)$$

Attractive W_{vdw} interactions decrease with increasing inter-particle separation (P_s), and depend on particle radius (r_p), and solvent properties, which are encompassed by the Hamaker constant, A_H. The Hamaker constant can be evaluated using simplified Lifshitz theory, between a pair of

particles (i = 1, 2) and a solvent (i = 3) using the relationship in equation (62).

$$A_H = \frac{3}{4}k_B T\left(\frac{\chi_1-\chi_3}{\chi_1+\chi_3}\right)\left(\frac{\chi_2-\chi_3}{\chi_2+\chi_3}\right) + \frac{3h_p\psi_n}{8\sqrt{2}}\left(\frac{(\lambda_1{}^2-\lambda_3{}^2)(\lambda_2{}^2-\lambda_3{}^2)}{\sqrt{(\lambda_1{}^2+\lambda_3{}^2)(\lambda_2{}^2+\lambda_3{}^2)(\lambda_1{}^2+\lambda_2{}^2)+\sqrt{(\lambda_2{}^2+\lambda_3{}^2)}}}\right) \quad (62)$$

Where χ_i and λ_i represent the dielectric constant (relative permittivity) and refractive index of phase i, respectively. k_B is the Boltzmann constant and ψ_n represents the photon frequency at which the refractive index was measured (214, 215). Additional attractive depletion potentials arise when particles are sufficiently close to prevent the passage of (spectator) dissolved species (usually polymers) from entering between them (213). This causes an attractive osmotic pressure between the particles due to a concentration difference, and depends on polymer concentration (c_p), relative molecular mass (M_p) and length (Δ), as shown in equation (63).

$$W_{\mathrm{ex}}(P_s) = -k_B T N_A {M_p}^{-1} c_p \frac{\pi}{12}\left(2r_p+\Delta-(P_s-2r_p)\right)^2\left(4r_p+2\Delta+(P_s-2r_p)\right); 2r_p < P_s < \Delta \quad (63)$$

N_A represents Avogadro's constant. Repulsive electrostatic potentials arise from layers of ions within the solvent that assemble around the particle in response to the surface charge of the particle. Therefore, the ions are oppositely charged to the particle surface, and equally charged, so mutually repellent. The magnitude of this electrostatic repulsion depends on particle surface potential (Λ_s), the relative permittivity of the solvent (χ) and the Debye length (κ^{-1}), as shown in equation (64) (216).

$$W_{\mathrm{e}}(P_s) = \pi\chi\varepsilon_0 r_p {\Lambda_s}^2 \ln\left(\frac{1+\exp(-\kappa P_s)}{1-\exp(-\kappa P_s)}\right) \quad (64)$$

Where ε_0 represents the permittivity of a vacuum. Notably, electrostatic repulsion is proportional to r_p; hence, dispersions of smaller particles are more difficult to stabilise electrostatically. The Debye length is given in equation (65), where 'e' represents the electronic charge, and I_s the ionic strength; hence diffuse double layers that are responsible for inter-particle repulsion collapse with increasing (root of) ionic strength.

$$\kappa^{-1} = \sqrt{\frac{\chi\varepsilon_0 k_B T}{2N_A e^2 I_s}} \quad (65)$$

Predicting particle surface potential is challenging, and is generally not attempted. Therefore, a parameter called the 'zeta potential' (ξ) is usually measured experimentally by electrophoresis measurements (217), using the Henry equation (66), and the Smoluchowski approximation (218), which is suitable for aqueous solvents with ionic strengths *ca.* 10^{-3} kmol m^{-3}, as shown (219, 220).

$$\xi = \frac{3u}{2E_\infty}\frac{1}{\varepsilon_0\chi}\mu\frac{1}{f(\kappa, r_p)} \approx \frac{u}{E_\infty}\frac{1}{\varepsilon_0\chi}\mu \quad (66)$$

Where u represents the particle velocity under applied electric field E_∞. Greater zeta potential indicates greater repulsion between the double layers of adjacent particles, producing a higher energy barrier to aggregation, increasing dispersion stability. It is generally accepted that in the range -20 mV < ξ < +20 mV dispersions have low stability, so for stable dispersions, the magnitude of zeta potential should exceed these values (221). To evaluate the electrostatic interaction energy, the zeta potential is converted to particle surface charge (Q) using the semi-empirical Loeb equation (67) (222, 223).

$$Q = 8\pi\chi\varepsilon_0\frac{k_B T}{ne}\kappa {r_p}^2\left(\sinh\left(\frac{ne\xi}{2k_B T}\right) + \frac{2}{\kappa r_p}\tanh\left(\frac{ne\xi}{4k_B T}\right)\right) \quad (67)$$

Where n represents valence of ions in the diffuse double layer. Particle surface potential can then be calculated using equations (68) or (69), depending on the value of the left-hand side term.

$$\frac{Qne}{4\pi\chi\varepsilon_0 r_p k_B T} \leq \ln\left(1/\vartheta_p\right) \rightarrow \Lambda_s = \frac{Q}{4\pi\chi\varepsilon_0 r_p} \quad (68)$$

$$\frac{Qne}{4\pi\chi\varepsilon_0 r_p k_B T} \geq \ln\left(1/\vartheta_p\right) \rightarrow \Lambda_s = \frac{k_B T}{ne}\ln\left[\frac{1}{6\vartheta_p\ln\left(1/\vartheta_p\right)}\left(\frac{ne}{k_B T}\right)^2\left(\frac{Q}{4\pi\chi\varepsilon_0 r_p}\right)^2\right] \quad (69)$$

The half-life of the dispersion, *i.e.* the time required to reduce the number of distinct dispersed particles by half through aggregation ($t_{1/2}$), can be calculated from the stability ratio (Θ) in equation (70), often evaluated numerically, and with equation (71) (224, 225).

$$\Theta = 2r_p\int_0^\infty \frac{\exp\left(\sum_{\forall i} W_{\mathrm{i}}(\hat{P}_s)\right)}{\left(\hat{P}_s + 2r_p\right)^2}.d\hat{P}_s \quad (70)$$

$$t_{1/2} = \Theta \frac{3\mu}{4k_B T N_0} \quad (71)$$

Where N_0 represents the number of particles in the dispersion at time t_0. Notably, dispersions of higher particle concentrations have shorter half-lives.

Several strategies may be employed to induce inter-particle repulsion, and are classified as electrostatic, stearic, or electro-stearic. The most common methods of inducing surface charge for electrostatic repulsion are varying the pH, for aqueous solvents (226), and / or adding charged dispersants that adsorb on particle surfaces. Typically, the charged dispersant adsorbs on particle surfaces, imparting charge (electrostatic), or is sufficiently large to prevent dispersed particles becoming sufficiently close together that aggregation occurs (stearic), or a combination of both (electro-stearic). Therefore, the dispersant should be soluble in the selected solvent and have an affinity for the dispersed particles' surface to ensure sufficient surface coverage for stabilisation. Additional dispersant properties that increase colloidal stabilities are polymeric chain lengths > 10 nm and the presence of double bonds in the chain structure, facilitating polarisation and decreasing the Hamaker constant (227), which decreases inter-particle attractive potentials, according to equation (61).

2.3.6.3 Resolution

Two factors determine the resolution of printed structures: (i) the maximum 'splat' (spreading) diameter of the droplet after impact with the substrate (D_m); and (ii) the diameter of the in-flight droplet (D_i), which is the therefore the minimum splat diameter after impact, in the absence of super-hydrophobic substrates. D_m is influenced by the impact process and D_i is controlled by nozzle diameter and droplet ejection parameters.

Understanding the processes governing droplet interaction with the substrate is a prerequisite for optimising resolution. After a droplet has been ejected, the following processes can be generalised into two distinct stages:

i) an impact driven stage, in which droplet kinetic energy is dissipated; and

ii) a surface energy driven stage, in which droplets interact with the surface to reach an equilibrium position.

The resolution of the features of printed layers depends critically on these stages for a droplet of given in-flight diameter, so it is important to understand the droplet and printer parameters that influence droplet behaviour during each stage. There are two time scales of phase change from a liquid to a solid deposit that influence D_m (186):

i) Rapid phase change, *i.e.* a chemical reaction such as polymerisation;

ii) Slow phase change, *i.e.* evaporation.

Due to the relatively high velocities of droplets ejected from inkjet printers (*ca.* 1 - 5 m s^{-1}), the kinetic energy upon impact will dissipate and force the droplet to spread to a greater diameter that its equilibrium diameter, as determined by surface tension alone (228). Spreading stops when all kinetic energy has been dissipated (229). Several models for this process have been developed by considering the kinetic energy dissipation, increase in surface energy, and viscous dissipation during spreading for different surfaces and impact properties, as described in equations (72) - (75) (229-234).

$$D_m = D_i\left(\frac{\mathrm{We}+12}{3(1-\cos(\theta_e)+4(\mathrm{We}/\mathrm{Re}^{0.5})}\right)^2 \approx D_i\mathrm{Re}^{0.25} \quad (72)$$

$$D_m = 0.61D_i\left(\frac{\mathrm{We}}{\mathrm{Oh}}\right)^{0.166} \quad (73)$$

$$[0.2\mathrm{Oh}^{0.33}\mathrm{We}^{0.65}+0.25(1-\cos(\theta_e))]\left(\frac{D_m}{D_i}\right)^2+\frac{2}{3}\left(\frac{D_m}{D_i}\right)^{-1}=\frac{\mathrm{We}}{12}+1 \quad (74)$$

$$\frac{D_m}{D_i} = 1+0.48\mathrm{We}^{0.5}\exp(-1.48\mathrm{We}^{0.115}\mathrm{Oh}^{0.21}) \quad (75)$$

D_i is a function of the physical properties of the ink, the printhead nozzle diameter, and the printing parameters. D_m typically ranges from 1.23 - 5D_i for droplet impact without splashing; θ_e represents the equilibrium contact angle between droplets and substrate surface, and is usually measured experimentally. Neglecting capillary effects, equation (72) can be simplified as shown (235). The distance between the printhead nozzles and the substrate is typically *ca.* 0.5 mm, so for simplicity, the dimensionless groups in equations (57) - (60) can be evaluated at ejection conditions, as droplet conditions immediately above the substrate and at the nozzle are approximately identical (acceleration due to gravity can be neglected). These models have limited utility due to the requirement of having to predict droplet ejection properties (*i.e.* u_0), and therefore it is typically easier to measure resolution empirically.

The ratio D_m / D_i is determined by the physical properties of the ink and substrate surface; however, the ejection process can be optimised to maximise resolution by minimising D_i by changing printer settings, which for a piezoelectric inkjet printer are typically pulse duration (P_d), voltage amplitude (V_p), and frequency. Operating at the velocity maximum (defined as the optimal ejection velocity), which occurs when acoustic waves in the printhead resonate (**Figure 24a**), reduces variation in unknown (and unpredictable) changes in the driving

parameters, so is favourable (236). In addition, resonance maximises the amplitude of the acoustic wave, facilitating lower V_p, and hence a lower droplet volume as the piezoelectric is deformed less. For a given fluid, increasing V_p above the critical minimum, below which ejection does not occur, increases droplet volume and velocity linearly, as shown in **Figure 24b**. The printing frequency is equal to the droplet ejection frequency and is defined as the frequency of applied voltage pulses, which determines print time for a given object. Higher frequencies reduce print time, but the droplet ejection process becomes more chaotic, as the acoustic waves in the cavity from previous pulses are not yet fully damped (**Figure 24c**). The damping of the pressure waves increases with increasing ink viscosity, and therefore also particle loading (as shown in **Table 9**), which should be considered for frequency optimisation; the onset of instabilities is typically established experimentally.

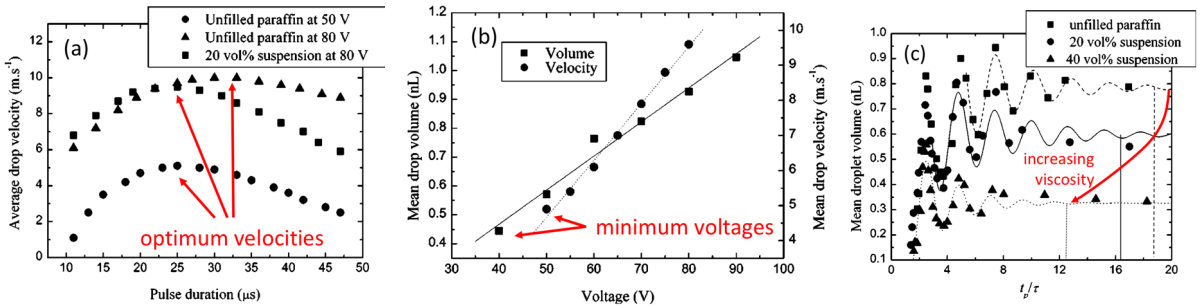


Figure 24. Effect of (a) P_d on u_0 (at 10 kHz); (b) V_p on droplet volume and u_0 at P_d = 30 μs, 10 kHz; and (c) the droplet volume relationship with reciprocal of frequency (t_p), for a study with paraffin solvent (236), normalised by the optimal P_d (= τ) = 30 μs. Reproduced, with annotations, with permission from (185).

2.3.6.4 Coffee Staining Effect

As the deposited droplet contains dispersed particles, the solidification process differs from that of a pure liquid droplet, as the solvent phase does not evaporate uniformly. At low contact angles, the rate of evaporation at the droplet edges is greater than the droplet centre so a ring of particles is deposited at the droplet circumference. These deposited particles 'pin' (immobilise) the droplet contact line, resulting in a receding contact angle and increased mass transport of particles in the droplet outwards radially. This phenomenon is known as the coffee stain effect and requires both: (i) a 'pinned' contact angle, although this has been disputed (237), and (ii) solidification primarily via evaporation (238). The consequence of this effect is that D_m defines the diameter of the solid deposit after drying. There are several approaches to mitigate coffee staining, other than non-evaporative solidification, such as counteracting it with a Marangoni

flow (239, 240), manipulating the atmospheric solvent partial pressure (humidity for water) (240), droplet spacing (241), droplet impact velocity (203), and substrate temperature (242).

2.3.7. Inkjet Printed Solid Oxide Electrochemical Reactors

Inkjet printing has been deployed to fabricate the functional layers of SOERs with a range of materials and printer settings, reviewed below, for both green (un-sintered) and sintered structures. A summary of printed materials, with ink solvent, substrate material, sintering temperature profile, resolution, and whether the deposits were characterised electrochemically is given in **Table 10**, and reviewed in detail over the remainder of this Chapter.

Table 10. Summary of Inkjet-printed SOER layers.

Printed Material	Solvent	Substrate	Sintering temperature profile (hold time)	D_m / μm	Electrochemical performance reported	Ref.
YSZ	α-terpineol	Sintered NiO-YSZ	1400 ºC	360 (pre-sintered)	YES	(243)
CGO	Propionic acid and 1-propanol	Sintered NiO-YSZ	1100 ± 50 ºC (2 h)	500 (pre-sintered)	NO	(244)
CGO	α-terpineol-MeOH	Sintered NiO-YSZ	1400 ºC (4 h)	1000 (pre-sintered)	NO	(245)
YSZ	H_2O-EtOH	Green NiO-YSZ	Firing at < 700 ºC for 48 h to remove organics, 1300 ºC (6 h)	170 (post-sintered)	YES	(168)
YSZ-SDC	H_2O	Sintered NiO-YSZ	1400 ºC (5 h), 5 ºC min^{-1} ramp rates	Reported as 600 dpi but not measured	YES	(170)
CGO	Unspecified	Sintered LSM	1300 ºC (2 h)	Unreported, but > 200 μm	NO	(246)
YSZ	α-terpineol	Sintered NiO-YSZ	1375 ºC (2 h) Co-sintered at 950 ºC	Unreported	YES	(247)
NiO-YSZ	α-terpineol	Green NiO-YSZ				
NiO-CGO	α-terpineol-MeOH	Stainless steel 430L	Co-sintered at 1350 ºC	1500	YES	(248)
CGO		Green NiO-CGO				
LSCF	H_2O and 1,5 -pentanediol	Sintered CGO	950 ºC (2 h) in air	Reported as 600 x 300 dpi but not measured	YES	(249)
LSCF	α-terpineol	Glass	Unsintered	80 (for ten overlapped splats)	NO	(250)
LSCF-CGO	H_2O	Sintered CGO	1000 ºC (2 h)	150 (pre-sintered)	YES	(251)

LSM-YSZ	α-terpineol	Sintered YSZ	Co-sintered at 1200 ºC (1 h)	Unreported	YES	(252)
LSM	α-terpineol	Green LSM-YSZ				
YSZ	α-terpineol	Green 3mol% YSZ	Co-sintered at 1450 ºC with a burnout stage at 300 ºC	Unreported	NO	(253, 254)
NiO						
SLT						(254, 255)
NiO-YSZ			1450 °C for 1 hour	Unreported	NO	(255)

2.3.7.1 Printed 2D Layers

Several different materials have been inkjet printed onto green, or sintered, NiO-YSZ composite electrode supporting substrates. In one case (243), a YSZ ink was prepared by dispersing ball-milled and subsequently filtered YSZ particles in α-terpineol. Initially 20 - 40 μm aggregates of YSZ particles were milled to 400 nm average diameter to prevent printhead nozzles blocking, because of the empirically-defined size constraint of $r_p < L / 50$, where r_p represents the particle radius and L printer nozzle diameter. However, ball milling cannot ensure all particles have $r_p < 400$ nm from an initial nominal diameter of *ca*. 1 μm. After dispersing the particles, ink viscosity was reduced by diluting with methanol (MeOH) for YSZ concentrations of 5 and 15 wt%, to 2.7 and 4.1 mPa s, respectively. To increase YSZ colloidal stability, the plasticiser bis(2-ethylhexyl)phthalate and binder ethyl cellulose were added in equal parts by weight, but the quantities were unspecified. This gave stability times, inferred as the absence of visible sedimentation, of 72 and 24 hours for the 5 and 15 wt% YSZ formulations, respectively.

The inkjet printer used was a modified Domino MacroJet electromagnetic (solenoid valve) printer with $L = 90$ μm, with an un-sintered NiO-YSZ substrate positioned 4 mm below the nozzle. No nozzle blocking was observed with trial print runs, and droplet ejection was reproducible, over the duration of observation. The printing optimisation process consisted of varying the droplet ejection time (P_d) from 375 to 550 μs and ejection pressures of 39 - 78 kPa. At $P_d < 375$ μs, droplets were not ejected, and at a pressure of 39 kPa droplets were ejected only at $P_d > 400$ μs. Over the range 59 - 78 kPa, droplets were ejected at all other ejection times within the range. It was expected that the ejected droplet volume would be linearly proportional to the opening time when ejection does occur, so at > 550 μs, droplet volume was too large to be useful. Droplet capillary action resulting in adhesion to the nozzle plate was responsible for non-ejection; the adhering droplets collected until gravitational effects caused them to drop as a single large droplet. A square surface of side length 57 mm was printed, with a minimum $D_m = 360$ μm. The inter-droplet overlap within a single printed layer to provide complete coverage, *i.e.* continuous layers ignoring defects, was found to be 25 %, as defined by the ratio of lateral droplet overlap to splat diameter. A 5 μm thick electrolyte was produced (243).

The same inkjet printer was used to deposit a $Ce_{0.9}Gd_{0.1}O_{1.95}$ (CGO) electrolyte layer onto a sintered NiO-YSZ substrate (244). The ink was prepared by dissolving Ce^{III} acetate hydrate and Gd^{III} acetate hydrate in propionic acid at 120 ºC. The solution was cooled and filtered to remove particles with $r_p > 150$ nm to prevent nozzle blocking. Viscosity was adjusted to the printable

region by adding propan-1-ol at a concentration of 0.75 kmol m^{-3} for printability, resulting in dispersion stability for 24 hours, as inferred by the absence of aggregation and sedimentation. Printer settings were a printing height of 10 mm, ejection pressure of 60 kPa, and P_d = 350 µs, resulting in complete, crack-free coverage with D_m = 500 µm with a 20 % diameter overlap, onto a substrate heated to 100 ºC to reduce drying stresses and mitigate crack formation (although this is disputable, as explained in Section 5.1). An intermediate heat treatment process was used between printing layers (10 in total) to dry the previously printed layer by placing the substrate-layer structure on a hot plate at 400 ºC, which also combusted residual organics, although this was unconfirmed by thermogravimetric analysis (TGA) measurements. Removal and replacement of the printed structure between each layer precludes the fabrication of high-resolution microstructures due to the difficulty of replacing the structure to within 5 µm accuracy of its previous position. After printing, the green structure was heated at 5 ºC min^{-1} to 650 ºC at which it was held for 1 h to combust any remaining organics, and then heated at 5 ºC min^{-1} to 1100 °C, which resulted in CGO structures with > 98 % theoretical density. However, this seems to be a very low densification temperature for CGO, so the authors claims are questionable.

The process of formulating and printing a CGO ink was further optimised to avoid the coffee stain effect (245), using 10 mol% CGO particles with r_p = 200 nm, ethyl cellulose as the dispersant, and MeOH solvent, in which ethyl cellulose was soluble. The formulation process involved firstly creating a colloidally-stable dispersion, subsequently adjusting physical properties for printability, and finally studying the droplet ejection behaviour. To maximise the printed electrolyte layer density, dispersant concentrations should be minimised to avoid structural porosity and potentially delamination from the substrate during sintering, while maintaining colloidal stability. The minimum concentration of ethyl cellulose was found to be 10 wt% with respect to the ceramic powder mass. Without reporting the minimum concentration with respect to particle surface area, reproducing these experiments with different CGO particles would be challenging.

Viscosity at 5 wt% CGO with the minimum dispersant concentration was varied by dispersing CGO in varying α-terpineol-MeOH mixtures (245), and investigating whether Marangoni flow could mitigate the coffee staining effect. CGO dispersed in α-terpineol-MeOH mixtures with varying compositions were inkjet printed, and the droplets investigated with respect to printing pressure and P_d; the optimal vol./vol. ratio was established as 50/50 – 40/60 α-terpineol / MeOH for jetting and colloidal stability. The optimum ejection settings for minimising droplet volume

to increase the density of the printed layer were found as 40 kPa ejection pressure and P_d = 450 µs, resulting in 8.6 nL volume droplets, with u_0 = 2.2 m s^{-1}. The coffee stain effect was mitigated for all formulations between 50/50 and 40/60 α-terpineol / MeOH at optimal ejection settings, due to capillary draining in the substrate (tape casted and sintered porous NiO-YSZ) occurring over a time scale an order of magnitude faster than that for evaporation and Marangoni flow, due to the high porosity (25 %) and thickness (500 µm) of the substrate. YSZ, NiO, and LSM inks were developed with the same formulation and were stable against aggregation for > 2 h, inferred by the absence of sedimentation, not by quantifying particle zeta potential or size distributions (PSDs).

A study investigating the optimal printer settings for an electromagnetic printer (L = 100 µm) used to fabricate the electrolyte and electrodes of SOFCs determined the effects of P_d and ejection pressure on droplet volume and velocity, and how this also impacted the shape of printed deposits (roundness and circularity) (248). α-terpineol-based inks with a binder were prepared, with added MeOH (1:1 volume ratio) to reduce viscosity and facilitate higher solids loadings (reasoning for the latter was not given). A 5 wt% YSZ ink with added binder was inkjet printed onto a sintered NiO-YSZ cermet, heated to 120 °C, to form a 57 mm x 57 mm square cell, with a hexagonal droplet deposition array (D_m = 1.5 mm, P_d = 400 µs), resulting in a gas-tight layer *ca*. 6 µm thick, after sintering at 1400 °C. The same procedure was used to deposit composite NiO-CGO and CGO inks. The dispersed particles were ball milled for 10 h, resulting in average particle diameters and viscosities of 443 nm, 7.2 mPa s, and 129 nm, 7.5 mPa s, for NiO and CGO, respectively. The inks were filtered with a 3 µm glass fibre filter prior to loading, printed onto a stainless-steel substrate (SS430 L), and sintered at 1350 °C.

Aqueous-based inks are environmentally preferable compared to primarily organic-based inks, and consequently several formulations have been developed. A YSZ electrolyte layer of 1.2 µm thickness was fabricated by inkjet printing using an aqueous-based ink (168). YSZ particles with average radius 25 nm were dispersed in a mixture of ethanol / H_2O at weight ratio 20/80. Two inks were formulated:

i) ‘concentrated’ ink with 20 wt% YSZ;

ii) ‘dilute’ ink with 6 wt% YSZ.

Both inks were stabilised by a polyvinylpyrrolidone (PVP)-ethanol dispersant mixture (53 wt% PVP) at a concentration 8 mg m^{-2} of (unreported) particle surface area. The μ, γ, ρ, and

Oh^{-1} values were: 4.28 mPa s, 36.4 mN m^{-1}, 1.14 g cm^{-1}, 6.73, and 2.63 mPa s, 36.2 mN m^{-1}, 1.01 g cm^{-1}, 10.28 for the concentrated and dilute inks respectively; u_0 was unreported. The stability was measured over 100 days and validated by r_p(100 days) = 50 nm (*i.e.* $t_{1/2}$ = 100 days). A HP Deskjet 1000 printer (L = 20 μm) was used to print electrolyte layers onto a green NiO-YSZ substrate (volume ratios of 2:3) with both inks at a resolution of 600 × 300 dpi. The coffee stain effect was not observed after printing single droplets. Gas-tight layers were not achieved after sintering the dilute ink deposit, but were achieved after sintering five printed layers of the concentrated ink, with 15 s print intervals to allow for drying between subsequently printed layers (168, 256).

Another aqueous-based ink formulation was used to print electrolyte layers using a thermal inkjet printer (HP Deskjet 2668 printer, USA, estimated L = 21 μm) (170). YSZ (r_p = 37 nm) at 20 wt% was dispersed by ultrasonication for 30 minutes in distilled water with added polyethylene glycol with a molecular weight of 4000 kg $kmol^{-1}$ (PEG-4000) at 25 wt% relative to the YSZ particle mass. At 25 ºC, the values of μ, γ, ρ, and Oh^{-1} were measured as 5.13 mPa s, 56.5 mN m^{-1}, 1.2 g cm^{-3}, and 7.4, respectively. The ink was inkjet printed onto a porous, sintered NiO-YSZ substrate tape with sufficient porosity to avoid the coffee stain effect. 1.5 μm thick layers were printed with 30 s drying intervals. Due to some Ni contamination originating from the anode substrate, a residual electrolyte electronic conductivity was detected, which was more significant with fewer printed layers, as expected. Consequently, the anode substrate was printed with four YSZ layers, as shown in **Figure 25a**, onto which LSM was wet-sprayed subsequently.

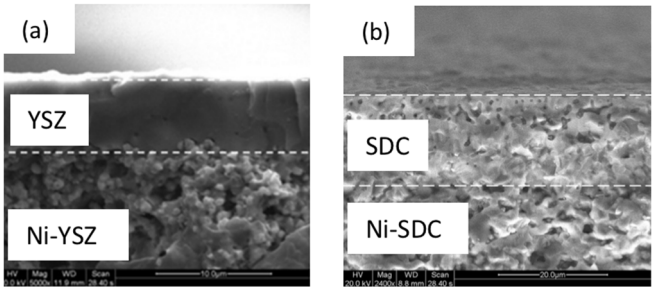


Figure 25. SEM photomicrographs showing inkjet printed and sintered (a) YSZ on Ni-YSZ; and (b) SDC on Ni-SDC. Reproduced with permission from (170).

Reactor electrochemical performance was increased by inkjet printing a $Sm_{0.2}Ce_{0.8}O_{1.9}$ (SDC) buffer layer, from an ink with composition 10 wt% SDC, 50 wt% PEG-4000 relative to the SDC, and triethanolamine at 10 wt%, relative to the SDC. The resulting ink properties μ, γ, ρ, and Oh^{-1} were equal to 6.7 mPa s, 70 mN m^{-1}, 1.1 g cm^{-3} and 5.9, respectively, and no

aggregation was observed over 5 days. However, D_m and u_0 were unreported, so predictions of resolution, satellite formation and / or splashing were omitted. The SDC was more challenging to sinter than YSZ, as evidenced by the porosity present in the electrolyte shown in **Figure 25b**. To form a complete SOER, a SDC barrier layer was printed directly onto a printed YSZ layer, but required a greater time interval for drying due to the decreased solids content (although the reason for this is unclear). Finally, a $Ba_{0.5}Sr_{0.5}Co_{0.8}Fe_{0.2}O_{3-\delta}$ (BSCF) oxygen-electrode was wet-sprayed onto the SDC barrier layer (170).

An aqueous-based CGO / $La_{0.6}Sr_{0.4}Co_{0.2}Fe_{0.8}O_{3-\delta}$ (LSCF) ink was formulated for printing oxygen-electrodes (251). The stability to aggregation of CGO / LSCF in water was determined by measuring particle zeta potential (ξ) over a pH range (unreported ionic strength), using aqueous NH_3 to increase pH, with 1 wt% (relative to the solids content) of copolymer A-6114 dispersant (Toa Gosei Co., Japan). It was determined that at pH 10 (ξ_{CGO} = -45 mV, ξ_{LSCF} = -20 mV), a dispersion with CGO / LSCF ratio of 50/50 - 40/60 was suitable for inkjet printing. The PSD of the composite ink was bimodal, with diameters of 80 and 230 nm. Despite large ξ values for CGO, its sedimentation was observed 48 h after formulation, however, LSCF particles were stable for up to a month, due to the electro-stearic effect of the dispersant at pH 10, which adsorbed on particle surfaces via the carboxylic group. To prevent sedimentation, the dispersing process was optimised by staged addition of the CGO after the LSCF had been dispersed, although the authors do not explain why this increased colloidal stability, for equivalent zeta potentials. The ink at pH 10, 40/60 (vol%) CGO / LSCF and 5 wt% solids had μ = 1 mPa s; Oh^{-1} was unreported, and hence printability was undetermined.

The CGO-LSCF ink was printed onto a sintered NiO-CGO|CGO substrate (preparation outlined elsewhere (257)) (50 and 600 µm thick layers, respectively) using a Pico Jet-1000 inkjet printer (Microjet Co. Ltd., Taiwan) with L = 50 µm. Droplet volume was 50 pL, and the solid deposits had a diameter of 150 µm and exhibited the coffee staining effect. The thickness of the printed cathode layer was *ca*. 2 µm, as shown in **Figure 26**. CGO-LSCF electrode porosity was low, supposedly due to the nominally small particles, so gas permeation to TPBs was hindered significantly (251).

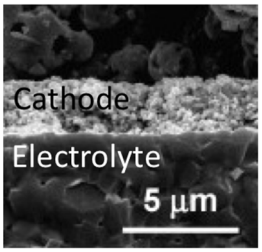


Figure 26. SEM photomicrograph of the cross section of the inkjet printed CGO|CGO-LSCF structure layer. Reproduced with permission from (251).

The printability of colloidally-dispersed $La_{0.6}Sr_{0.4}Co_{0.2}Fe_{0.8}O_3$ (LSCF) for oxygen-electrode layers was investigated using a Dimatix DMP 2831 piezoelectric DOD inkjet printer (Fujifilm, USA, $L = 21.5$ µm) (258). The LSCF inks were α-terpineol-based and the composition of solids and a polymeric ethyl cellulose dispersant were varied in the range 3.5 - 12 wt% ($r_p < 1.6$ µm) and 0.03 - 0.4 wt%, respectively. The dispersant promoted colloidal stability and provided mechanical strength to the green printed films. After dispersing the LSCF by ball milling for 1 week, the different compositions resulted in a surface tension of 34 mN m^{-1} and a temperature-dependent viscosity of $2 < \mu < 10$ mPa s at $40 < T < 60$ ºC ($3 < Oh^{-1} < 24$). At $T < 40$ ºC, the viscosity was too high for ejection and at $T > 60$ ºC, drying occurred at the nozzle, resulting in blockage. Layers were printed onto dense YSZ pellets (50 µm thick); V_p = 10 - 50 V and P_d = 2.64 - 30 µs, at a droplet ejection frequency of 2 kHz were varied to increase u_0 up to a maximum of 9 m s^{-1}; hence, the Weber number (We) varied in the range $0 < We < 57$. We was a significant parameter in determining printability, and at $We > 35$ satellite droplets and splashing were observed. At $We < 35$ and $Oh^{-1} \leq 24$, reproducible droplets were observed, which indicated a different printability constraint to what is conventionally assumed; however, this is not believed to apply generally, unlike the printability relationships given in **Table 8**. These settings resulted in a resolution of 400 dpi with a feature resolution of 60 - 90 µm and a droplet volume of 7 pL. Multiple layers were printed, supposedly each with a thickness of 100 nm, which appears to be impossibly low considering the particle sizes were *ca*. 10 times larger. Three or more printed layers were required for a defect-free surface, as one layer produced a surface coverage of 90 %; however, information on droplet overlap and lattice spacing were omitted. A porous LSCF structure facilitating gas diffusion resulted, suitable for SOERs.

Green structures of $Sm_{0.5}Sr_{0.5}CoO3$ (SSC) and $Sm_{0.2}Ce_{0.8}O_{1.9}$ (SDC) were inkjet printed to form a porous structure suitable for the oxygen-electrode (190). The SSC / SDC powders were mixed in a mass ratio of 70/30 with particle sizes of 0.5 - 0.7 µm and dispersed in water at a concentration of 5 wt% by ultrasonicating directly with a probe for 30 minutes. PEG-4000 was

added as a pore former at 2.5 wt %; polyacrylic acid and glycerine were added at 0.75 wt% and 1.25 wt%, respectively, to modify viscosity and increase colloidal stability (no sedimentation was observed over 3 days). The physical properties of the ink were ρ = 1.05 g cm^{-3}, γ = 71.50 mN m^{-1}, and μ = 8.74 mPa s, the resulting Oh^{-1} = 4.54. A modified HP Deskjet 2668 inkjet printer (USA) with a resolution of 600 dpi was used to print 45 layers with total thickness of 15 µm onto a pre-fabricated half-cell with a NiO-YSZ anode and YSZ electrolyte, with an SDC interlayer.

A LSCF film was inkjet printed with a resolution of 600 × 300 dpi using a HP Deskjet 1010 (USA) onto a 200 nm thick CGO barrier layer produced by pulsed laser deposition (PLD) onto a pre-sintered NiO-YSZ|YSZ substrate (249). However, neither nozzle diameter or particle mass fraction within the ink were reported, and hence ink density and Oh^{-1} were undetermined. The ink was prepared by ball milling commercial LSCF powder (Kceracell Co., Ltd, Republic of Korea) for 36 h and then filtering out larger particles with a sieve (no specifications provided). The resulting powder was mixed with water, DISPERBYK-2012 dispersant (BYK-Chemie GmbH) and 1,5, pentanediol at a concentration of 20 wt%. When the concentration of 1,5, pentanediol was < 20 wt%, 'fault lines' were observed in the printed layers, suggesting that the physical properties of the formulations lay outside of the Oh^{-1} printable range. The dispersed LSCF particles had r_p = 100 nm, as determined by dynamic light scattering (DLS); little change occurred over 34 days indicating colloidal stability.

The (Newtonian) viscosity of the ink was 2.93 mPa s, suggesting that the particle loading was low. In addition, γ, P_d, V_p and ejection frequency were unreported. To vary the LSCF layer porosity, the 'greyscale' (leaving gaps between deposited droplets) setting for printed layers was adjusted from a luminosity of 50 - 200 inclusive, in increments of 50, where 0 represented 'black' (unreported droplet overlap), and 255 'white'. The number of printed layers for each was 40, 80, 160, and 200, with corresponding porosities of 10.2 %, 12.7 %, 13.6 % and 16.2 %, respectively; drying times between each layer were unreported. The printed structures were dried at an unspecified temperature for 24 h, then sintered at 950 °C for 2 h. Cracking was observed in films with luminosities 50, 100, and 150, as shown in **Figure 27**, and was attributed to relatively slow rates of evaporation of the solvent at higher particle concentrations. However, this is unverifiable as evaporation rates were not reported. Furthermore, lower evaporation rates actually increase the ability of a printed film to resist capillary stresses that arise during drying of printed films (as explained in Section 5.1), increasing film resistance to cracking. The printed layer thicknesses decreased from 0.11 to 0.02 µm, the latter seeming impossibly low for a

reported 100 nm particle diameter) for luminosity values from 50 - 200, so cracking may have been mitigated at high luminosities because film thicknesses were lower than the critical cracking thickness. The sintered LSCF films were *ca*. 5 µm thick. Porosity in the printed layers was controlled by varying luminosity, so the reproducibility of the 'microstructures' is questionable.

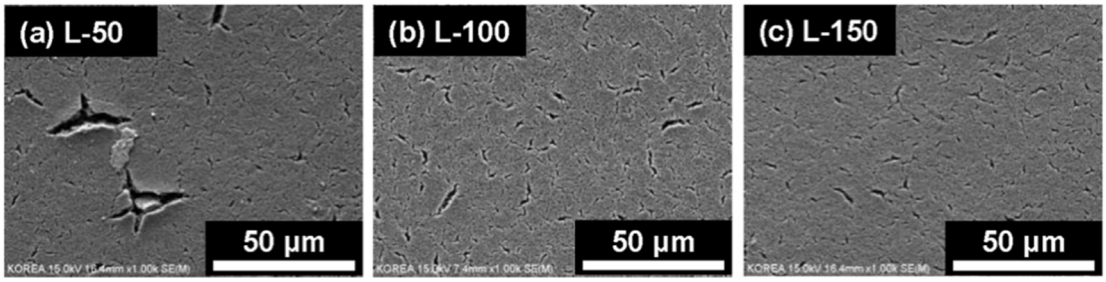


Figure 27. SEM photomicrographs showing cracking in the sintered LSCF layers at a luminosity setting of (a) 50; (b) 100; and (c) 150. Reproduced with permission from (249).

An α-terpineol-based LSCF ink was inkjet printed onto glass substrates to investigate the effect of substrate roughness, printing distance, inter-layer drying time and ambient temperature on the deposited LSCF (250). A Dimatix DMP 2831 piezoelectric DOD printer (16 nozzles, L = 22 µm, nominal droplet volume 10 pL) (Fujifilm, USA) was used to deposit the LSCF stabilised by ethyl cellulose, with a LSCF solids loading of 12 wt%, above which nozzle blocking occurred, suggesting the colloidal stability of the dispersion was low. The ink was prepared by ball milling the particles in α-terpineol for > 1 week to break up aggregates, then filtered with a 1 µm syringe filter. It was claimed, but not proven, that this would remove all particles > 200 nm in diameter, which is unlikely given the aperture size of 1 µm, which would explain why nozzle blocking was encountered at > 12 wt% solids. The droplet ejection frequency was 2 kHz, but P_d and V_p were unreported, besides a rise and fall time of 1 µs to and from V_p, u_0 = 6 m s^{-1}, and a back pressure (meniscus) of 127 mm H_2O to prevent free flow of ink from the reservoir.

After varying the printing height over 0.25 - 1.5 mm, the drying time between printing passes 0 - 240 s (the duration of a printing pass was 10 s), the substrate smoothness, and ink temperature between 25 - 60 °C, the most favourable conditions were found to be 0.7 - 1 mm, no additional drying time (*i.e.* actual drying time was 10 s), a smooth substrate, and a 50 °C ink temperature. The resulting droplet after settling on the substrate had a volume of 2 µL, θ_e = 17 °, and a surface coverage of LSCF of 60 %; consequently, ≥ 2 layers were required for complete coverage. The diameters of a single splat and of overlaid splats were 59 µm, and 80 µm (droplet overlap of 36 %), respectively. D_i was *ca*. 25 µm, therefore D_m / D_i was

ca. 2.4. The vertical height of a single printed layer was 100 nm. Unfortunately, μ and γ were unreported, so the Oh^{-1} number and hence printability were not determined. The printed deposits were not sintered, which was required to validate this ink formulation for fabricating SOERs, as this is often a challenging step to achieve a useful microstructure, due to challenges with adhesion of the electrolyte to a substrate, porosity, *etc*. Coffee staining in the deposits was significant, as shown in **Figure 28**; it was proposed that the resulting microstructures could enhance gas diffusion and electrical conduction for SOERs, although this was not validated, either experimentally or by simulations.

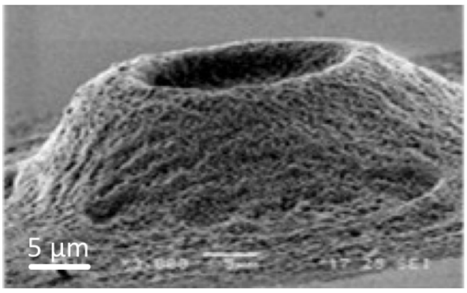


Figure 28. SEM photomicrograph showing significant coffee staining for an un-sintered inkjet printed LSCF deposit. Reproduced with permission from (250).

Dual functional layers of a composite NiO-YSZ electrode with a YSZ electrolyte were inkjet printed sequentially (247). The two inks were prepared separately, and the properties optimised for inkjet printing. Both inks were α-terpineol-based and contained polyvinyl butyral (PVB), butyl benzyl phthalate (BBP), and polyalkalyne glycol (PAG) at 0.1 wt%. Two NiO-YSZ inks were formulated, containing YSZ particles (r_p = 200 nm) and NiO particles (r_p = 15 nm and r_p = 150 nm) at 3 wt% each. The electrolyte ink contained YSZ (r_p = 200 nm) at 6 wt%. At room temperature, and at 47 ºC, the ink viscosities were measured as 73 mPa s and 6.5 mPa s, respectively; inks were stable to aggregation and for jetting over > 25 days, although this was not validated by zeta potential or PSD measurements.

A Dimatix DMP 2831 printer with Dimatix 11610 cartridges (Fujifilm, USA), with a nominal 10 pL droplet volume, was used to print the structures, although droplet volume was not measured experimentally (247). The diameter of the printhead nozzles was not mentioned or used to calculate Oh^{-1}, but is known to be 21 µm, reported elsewhere (156). Consequently, printability, or the presence / absence of satellites formation was not acknowledged, nor was the ejection velocity measured to predict whether satellite droplets or splashing were probable. 10 layers of the NiO-YSZ were printed onto a supporting, pre-sintered, NiO-YSZ substrate (60/40 wt% ratio, respectively) with a stable droplet ejection rate of 3 kHz with V_p = 32 V and

P_d = 2.94 µs. D_m was unreported, but a 15 µm droplet overlap (square deposition lattice) was used, and described as 'substantial'. The supporting substrate was heated to 80 ºC to increase the drying rate. 20 layers of the electrolyte layer were printed on top of the printed NiO-YSZ, with identical printer settings. Both inkjet printed NiO-YSZ layers were 12 µm thick, and the electrolyte was 6 µm thick. After sintering, the printed layers could be distinguished by SEM, and differed depending on the NiO particle size in the ink, as shown by **Figure 29**. Furthermore, the layers fabricated using the r_p = 150 nm particles had a non-uniform porosity, attributed to aggregate formation.

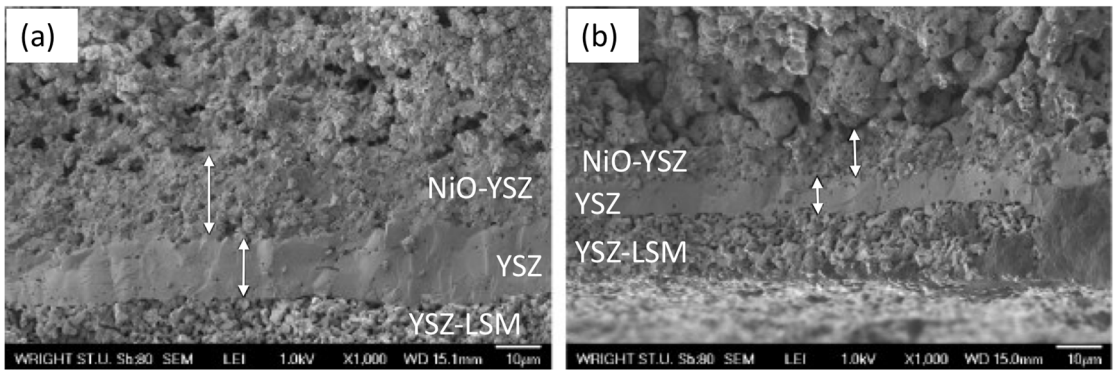


Figure 29. Cross sectional SEM photomicrographs of layers produced using NiO particles (a) r_p = 15 nm; and (b) r_p = 150 nm. Reproduced with permission from (247).

This research was developed further to print complete SOFCs by printing four functional layers sequentially on top of a tape-casted NiO-YSZ support layer (55/45 wt% respectively): a NiO-YSZ anode interlayer, a YSZ electrolyte, a LSM-YSZ composite cathode, and a LSM current collection layer (252). Each required a separate ink, and contained the binders and plasticisers PVB, BBP and PAG at 0.1 wt%. The solid contents of each ink were 2.8 wt% NiO and YSZ in the composite anode ink, 10.7 wt% YSZ in the electrolyte ink, 1.45 wt% YSZ and LSM in the YSZ-LSM ink, and 10.7 wt% LSM in the current collector ink. The viscosities of the inks were 58 - 63 mPa s and were essentially Newtonian at room temperature. At 58 ºC, viscosities decreased to 4 - 12 mPa s and displayed shear thickening behaviour, attributed to the α-terpineol. The single-species inks were stable for 2 - 3 weeks, the composite NiO-YSZ ink was stable for 3 - 4 weeks, but the LSM-YSZ composite ink required regular homogenising to prevent aggregation, in spite of the comparatively low solids loading, suggesting colloidal instability. No zeta-potential or PSD measurements were taken to validate this claim.

The same Dimatix DMP 2831 printer was used to print each layer with V_p = 32 V, P_d = 2.944 µs, a slew rate of 0.93 V µs^{-1}, and a droplet ejection frequency of 3 kHz. 10 layers of the NiO-YSZ anode ink were printed onto the substrate at 80 ºC, followed by partial sintering

at 950 ºC. 12 layers of the YSZ ink were then printed onto the composite NiO-YSZ layer, with the ink reservoir temperature at 48 ºC. The YSZ layer was then sintered at 1400 ºC for 2 h. 20 layers of the LSM-YSZ ink were printed onto the YSZ, with the ink reservoir temperature at 58 ºC. The temperature of the electrolyte 'substrate' was raised to 100 ºC to rapidly dry the LSM-YSZ deposits. 30 layers of the LSM ink were then printed to complete the cell at an ink temperature of 48 ºC.

The substrate temperature for this step was critical for drying behaviour; when the temperature was too low (40 - 70 ºC), the ink spread beyond the cell periphery, whereas when the temperature was too high, coffee staining resulted (contrary to predictions that higher evaporation rates mitigate this effect); the optimum temperature was 100 ºC. After sintering, the electrochemical performance in fuel cell mode was measured and compared to another cell in which the cathode layers were pasted rather than inkjet-printed; the performance with the printed cathode was lower, which was attributed to non-optimised cathode layer ink formulation, but not explained. SEM microstructural inspection revealed smaller pores with the printed cathode than the pasted cathode, and no clear interface between the LSM-YSZ and LSM layers. This comparative study highlighted the need for optimised ink formulation, printing parameters, and sintering processes to fully exploit 3D printing for SOER applications. Again, D_m and the lattice patterning for droplet deposition were unreported, despite being critical parameters in determining individual layer thicknesses and the number of layers required for fully densified structures (252).

Dense layers of NiO, YSZ, and lanthanum-doped strontium titanate (SLT) were deposited using a Dimatix DMP 2831 printer (Fujifilm, USA) onto a green, 3 mol% YSZ substrate for a segmented-in-series fuel cell architecture (254). Particle sizes were all < 1 μm, but PSDs were unreported. Particles were dispersed in α-terpineol and colloidally stabilised with Solsperse 13940 at 2 wt% relative to the particles mass, for all species, by ball milling with zirconia beads for 24 h. The viscosities of the NiO and YSZ inks were *ca*. 27 and 46 mPa s (unreported temperature), respectively, so the temperature of the printhead was raised to 50 °C to decrease the viscosities to the recommended range of 10 - 12 mPa s. The inks were printed onto each other sequentially, heated to 300 °C to combust organics, and subsequently co-sintered at 1450 °C, to form the arrangement YSZ|SLT|NiO|YSZ with an approximate thickness of 15 μm for each layer. A patent application (253) was filed for the above inks composition that also reports a stable cell potential difference for the fabricated SOER over *ca.* 20 h with a H_2/H_2O mixture in the molar ratio 97/3 at 800 °C.

A NiO-YSZ ink, colloidally stabilised by Solsperse 13940 and incorporating PMMA pore-forming beads was developed to print porous electrodes for a catalyst coking sensor for fuel reforming systems (255). The mass ratio NiO / YSZ / Solsperse 13940 / PMMA / α-terpineol in the ink was 3.8 / 11.6 / 1.3 / 5.7 / 77.6 wt%, respectively. A SLT ink was formulated to the same composition specified above and used to provide electrical contacts to the electrode sensor (254). Both inks were deposited onto a green 3 mol%-YSZ substrate, and co-sintered at 1450 °C for 1 h.

2.3.7.2 Printed 3D Structures

Basic, tailored SOER microstructures have been fabricated by printing CGO electrolyte films onto a LSM substrate with an appropriate microstructure. The CGO ink was prepared by Afit Corp., Japan, with CGO particles of r_p = 150 nm at 4 wt% loading. μ and γ were *ca.* 7 – 8 mPa s, and 28 mN m^{-1}, respectively. A piezoelectric DOD inkjet printer (KE-GON-M3, Afit Corp., Japan, unspecified *L*) was used to print the CGO layer with ejected droplets of 42 pL volume. A porous, dense LSM honeycomb-structure substrate was used as an oxygen-electrode layer, and square and hexagonal patterns of CGO were printed, with a post-sintering depth of 12 µm. Twenty printed layers were required for complete densification, as shown in **Figure 30a, b** (246). However, as the substrates were hexagonal and square lattices, it was difficult to determine the printing resolution; the ink had overflowed the confines of the substrate, as shown by **Figure 30c**, so the resolution was > 200 µm.

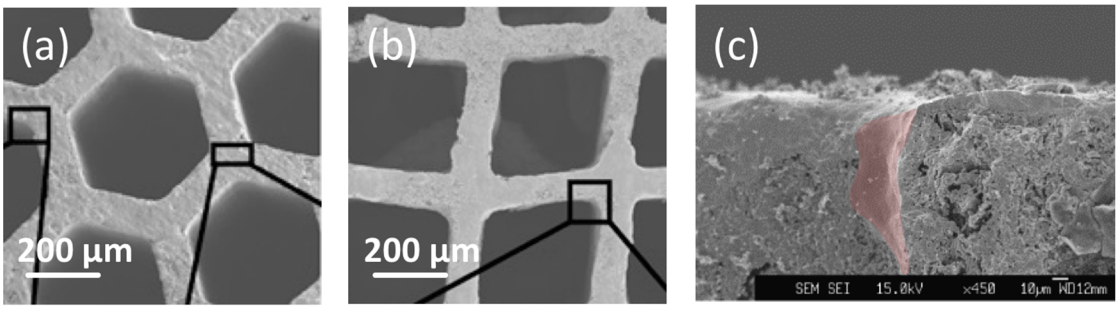


Figure 30. SEM photomicrographs of (a) the hexagonal; (b) square CGO microstructures; and (c) cross-sectional view of the CGO layer on the square LSM substrate. The red shaded region shows where the printed CGO layer exceeded the confines of the substrate. Reproduced with permission from (246).

2.3.8. Electrochemical Characterisation

This section reviews the electrochemical characterisations of the inkjet printed functional layers (where applicable), differentiated based on which functional layer was printed, for the conventional SOER materials.

2.3.8.1 Inkjet Printed YSZ Electrolyte

The practical operating temperature for SOERs with a YSZ electrolyte is 700 – 800 °C; therefore, only electrochemical measurements at these temperatures are reported here. **Figure 31** shows fuel cell mode peak power densities for the NiO-YSZ|YSZ (printed)|YSZ-LSM cells with the thickness for each electrolyte, between 700 – 800 °C. Operating with H_2, the open circuit potential difference (OCPD) ranged from 0.95 – 1.15 V for all reactors, indicating that the printed electrolytes were essentially gas tight. For the measurement series across all temperatures, there was a clear trend of increasing performance with decreasing electrolyte thickness, and with increasing temperature, as expected. Three of the measurements were incomplete across the operating temperature range, in one instance because the reactor failed at high temperature (247), probably due to structural failure within the anode. In the other instances of incomplete data series, only the peak power results, which were achieved at 800 °C were reported.

One of the SOFCs (green diamond series in **Figure 31**) was also tested with an SDC interlayer (2 µm thick) and a BSCF cathode fabricated conventionally (170). The peak power densities at 700, 750, and 800 °C were 400, 700, and 1040 mW cm^{-2}, respectively. The increase in performance was attributed to the superior performance of the BSCF cathode; however, the best performing printed SOFCs used the conventional YSZ-LSM cathode (168).

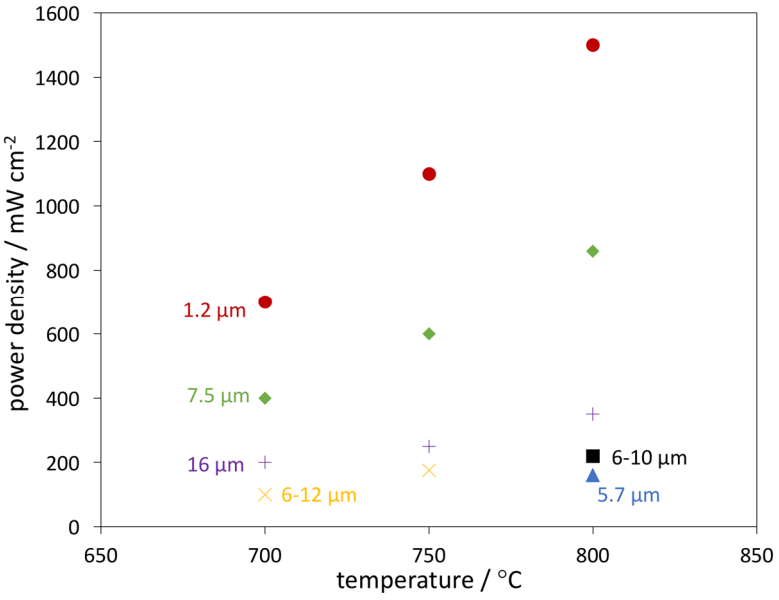


Figure 31. Variation of reported fuel cell mode peak power densities with temperature and inkjet printed YSZ electrolyte thickness. Cross markers indicate testing in dry H_2 at the anode,

otherwise humidified H_2 was used; all cathodes were exposed to air. Data from (168, 170, 243, 247, 248, 252).

2.3.8.2 Inkjet Printed Electrode

Only three studies from the literature electrochemically characterised an inkjet printed oxygen-electrode for SOFC operation, and each had a different composition:

i) YSZ-LSM composite (252);

ii) CGO-LSCF composite (251);

iii) LSCF (249).

In the first instance, the electrochemical performance of an inkjet printed YSZ-LSM cathode was compared to a (conventionally) pasted YSZ-LSM cathode, both produced from the same dispersion, and 47 μm thick. The electrochemical performances of the inkjet printed and pasted YSZ-LSM SOFCs are shown in **Figure 32**. The peak power density achieved with the inkjet printed electrode was *ca*. 40 % lower than the pasted electrode, despite both having identical compositions. Electrochemical impedance spectroscopy revealed a much higher impedance at low frequencies for the inkjet printed electrode compared to the pasted electrode. This indicated an increased gas-transport resistance, and therefore the loss of performance was attributed to a sub-optimal microstructure.

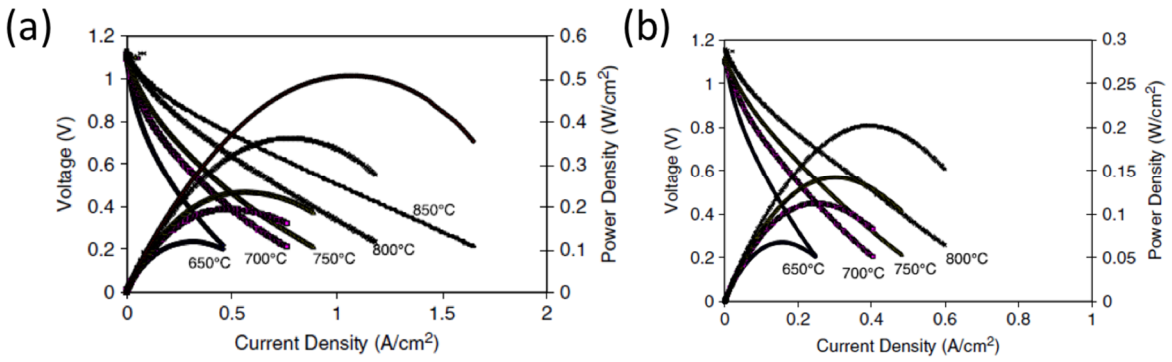


Figure 32. Effect of current density on SOFC potential difference and power density for (a) hand-pasted; and (b) inkjet printed cathode. Reproduced with permission from (252).

In the second instance, with inkjet printed CGO-LSCF, the OCPD was only 0.43 V, the cause of which was not identified, and consequently, the electrochemical results are not considered for review here. However, microstructural studies revealed that the outer surface of the CGO-LSCF layer was highly dense, *i.e*. very low porosity. This would have significantly limited gas diffusion into the cathode, and consequently would lower the threshold current density for mass

transfer control, which was also the most probable cause for the loss of performance for the inkjet printed YSZ-LSM cathodes described above.

The inkjet printed LSCF cathode with a CGO electrolyte and Ni-YSZ anode achieved peak power densities at 700, 750, and 800 °C of 79, 118, and 377 mW cm^{-2}, respectively, using humidified H_2 as the fuel, and air as the oxidant; the OCPD was 1.04 – 1.14 V for all measurements (249). Maximising porosity and pore size increased the peak power density, which was limited by gas transport as evidenced by electrochemical impedance spectroscopy. The maximum porosity achieved was 16.2 % (determined from SEM analysis). Therefore, by increasing the porosity further, performance could increase.

2.4. Conclusions

Inkjet printing has been used successfully to fabricate electrolytes and barrier layers of SOERs with competitive electrochemical performances compared to cells fabricated conventionally. Gas-tight, highly-dense YSZ electrolytes have been fabricated with < 2 μm thickness, by inkjet printing, which is smaller than is reliably practical using conventional tape casting or screen printing techniques. In addition, composite LSM-YSZ, CGO-LSCF, and LSCF oxygen-electrodes have been fabricated by inkjet printing. However, their electrochemical performance was limited by the microstructure of the printed deposit, which had a 'skin' of low-porosity at the electrode | bulk gas interface. Consequently, cathodes prepared by conventional pasting methods had a superior performance to the inkjet printed electrodes. In addition, only electrochemical characterisation in fuel cell mode using H_2 has been attempted. For a more versatile energy storage device, CO oxidation, as well as electrolysis of H_2O and CO_2 are also desirable reactions; therefore, the performance of inkjet printed SOERs should be established for these additional electrochemical reactions.

Furthermore, most inks were organic-based, using α-terpineol as the solvent, or partially aqueous-based (H_2O with alcohol), which are less environmentally preferable than predominantly aqueous inks, that are also easier to understand and to predict colloidal-stability, which is essential for practical inks with a long shelf-life.

Therefore, to maximise the impact inkjet printing can have on SOERs, advancements are needed in:

i) ink formulation, *i.e.* transition to aqueous inks;

ii) improving lateral resolution, to allow fabrication of tailored microstructures;

iii) optimising microstructure of inkjet printed electrodes to increase electrochemical performance.

3. Project Objectives

Chapter Summary

The project's aim was to validate inkjet printing as an effective, scalable, and environmentally-benign fabrication method for solid oxide electrochemical reactors with enhanced performances compared to those of conventionally-fabricated reactors. This Chapter outlines the project's objectives, and corresponding tasks, which if completed, would satisfy the aim.

3.1. Research Objectives Introduction

Due to the relatively mature developmental status of SOER materials, all methods considered and developed in this research project are applicable to manufacturing, and concern the conventional SOER materials: Ni, YSZ, LSM, CGO. The objectives to achieve the aim, are outlined in the remainder of this Chapter, highlighting the most challenging tasks involved for each. A holistic approach was required throughout, as printed (micro-)structures were highly dependent on ink formulation.

3.2. Aqueous Inks Formulation

The challenge of transitioning from organic to aqueous ink formulations, which are environmentally preferable and easier to understand scientifically, is twofold. Firstly, the colloidal stability of the inks must be ensured, to prevent particle aggregation which would block printhead nozzles. This can be achieved by applying the predictive capabilities of DLVO theory, as outlined in Section 2.3.6.2. However, electrostatic / stearic stabilisers at variable pH for the conventional SOER materials dispersed in water were undefined, so needed to be found. Secondly, the printability of the inks must be ensured. This is more challenging with aqueous than organic solvents due to their lower inherent viscosity (*ca*. 1 mPa s) and high surface tension (*ca*. 70 mN m^{-1}), which need to be increased and decreased, respectively, without compromising the stability of the colloids, or affecting the morphology of the printed deposit (156, 259).

3.3. Improving Lateral Resolution

Improving inkjet printing resolution would facilitate the sequential deposition of SOER materials, facilitating microstructures with a tailorable architecture that cannot be achieved using conventional fabrication methods. Resolution depends primarily on the ejected droplet diameter (D_i). To decrease D_i, a smaller printhead nozzle diameter and more sensitive piezoelectric crystals are required than have been used previously (reviewed in Section 2.3.6.3). The challenge of using printhead nozzles with smaller diameters are that:

i) Particle size distribution (PSD) needs to be optimised to prevent nozzle blocking, which requires highly-stable dispersions of small particles (*ca*. 200 nm). New techniques are required to refine PSDs at this scale. Alternatively, printing liquid (nitrate) precursors and producing ceramic phases *in-situ* could be a possibility to mitigate practical difficulties resulting from instability of the colloidal dispersions and reduced droplet volume. However, the maximum concentration of salts, and

hence solids, is very low, so this technique is unsuitable for manufacturing and will not be considered further.

ii) Smaller absolute D_i values result in smaller droplet spread diameters on the substrate that dramatically increases the printing duration and probability of defects for a given film size. Therefore, significantly more detailed ink characterisations than those reported in the literature (Section 2.3.7) are required, to ensure the inkjet printing is effective and reproducible.

3.4. Electrochemical Performance Validation

Most published studies concerning inkjet printing to-date, as reviewed in Section 2.3.7, deposited only the electrolyte, and where electrodes were inkjet printed, the electrochemical performance was either low, or insufficient detail concerning the experimental method was provided, rendering the studies irreproducible. Therefore, an objective of this research project was to address the limitations encountered within the literature, to fabricate SOERs reproducibly with superior electrochemical performances than those previously reported in Section 2.3.7. This requires first the electrochemical performance of inkjet printed electrolytes to be validated, before progressing to inkjet printed electrodes.

3.5. Printing 3D Microstructures

Hitherto, the porosity within printed electrodes has been too low for adequate rates of mass transport of reactants and products to / from TPBs. Furthermore, TPB percolation within electrode microstructures fabricated using composite inks is not expected to exceed conventionally-fabricated electrodes, as previous inkjet printed electrodes have also relied on random powder mixing to create high TPB densities.

There are two routes to increase porosity:

i) inclusion of a pore-forming material template which is removed subsequently by combustion (260);

ii) optimisation of particle ordering during deposition and drying.

The first option requires the introduction of an additional species into the ink, increasing complexity of formulation, interaction with the substrate, and the combustion / sintering process. Therefore, the latter process is preferable.

Fabricating electrode microstructures using inkjet printing has the potential to increase TPB percolation and therefore maximise performance, by sequential deposition (non-composite

inks) of each material, which avoids reliance on random powder mixing. Therefore, to achieve this objective, there were two tasks:

i) predict which microstructures result in the greatest electrochemical performance, using finite element simulations to model spatial distributions of overpotential, current densities, and reactant / product concentrations, governed by the equations reported in Chapter 2;

ii) validate experimentally the predictions of electrochemical performance of optimised inkjet printed electrode microstructures (fuel cell and electrolysis modes).

3.6. Conclusions

The Objectives of this project were to:

i) optimise inks by developing aqueous formulations;

ii) improve lateral resolution compared to what has been reported in the literature;

iii) validate experimentally the electrochemical performance of inkjet printed solid oxide electrochemical reactors;

iv) fabricate optimised 3D electrode microstructures, with the overall aim of enhancing the electrochemical performances of inkjet printed solid oxide electrochemical reactors, compared to those fabricated by conventional techniques.

4. Experimental Equipment

Chapter Summary

This Chapter describes the experimental equipment and procedures used throughout the following chapters of this thesis to avoid repetition, as many of the methods are repeated throughout. Details concerning ink formulation, deposition, and electrochemical characterisation of inkjet printed solid oxide electrochemical reactors are provided.

4.1. Ink Formulation and Characterisation

The experimental particle handling procedures and characterisations, with the equipment used in this research project are given in **Table 11**.

Table 11. Ink formulation and characterisations, with corresponding equipment and experimental procedures.

Outcome	Equipment and Procedure
Mass-specific surface area	300 mg particle samples were degassed at 200 °C for *ca*. 24 hours, followed by N_2 adsorption using a Micrometrics 3Flex machine (Canada). Specific surface area was then calculated using Brunauer-Emmett-Teller (BET) theory.
Particle size distribution (PSD)	Particles were dispersed at low concentrations in the continuous dispersion medium (solvent) and particle diameter was determined by dynamic light scattering (DLS) at constant temperature (25 °C) using a Zetasizer μV instrument (Malvern, UK), as the average of 7 individual measurements. To ensure high quality results, concentration was varied iteratively, and size re-measured at each concentration, until the result became independent of concentration.
Zeta potential	Particles were dispersed in water with a spectator KCl salt concentration of 10 mol m^{-3}. Where applicable, pH was raised and lowered using NH_3 (aqueous) and nitric acid (0.1 mol dm^{-3}), respectively, both from Sigma Aldrich, USA. Electrophoresis measurements were taken using a Zetasizer μV instrument (Malvern, UK), as the average result from 7 runs of 20 measurements. Zeta potential was calculated subsequently using the Smoluchowski approximation, shown in equation (66). The measurement error was taken to be the standard deviation between the averages of each run.
pH	A pH meter and probe (Jenway 3510, UK, and Mettler-Toledo, USA, respectively) were used to quantify pH throughout.
Determination of solids mass fraction / rate of combustion	All combustibles were removed by a thermogravimetric analysis (TGA) treatment, using a Netzsch TG 209F1 Libra (USA), temperature ramp rate 4 °C min^{-1} in air with a 50 cm^3 min^{-1} flow rate. Initial sample mass was 30 mg per measurement.
Viscosity	After stirring dispersions for 24 hours, a DV-E concentric cylinder viscometer (Brookfield, UK) was used to measure viscosity at room temperature by varying the rotation rate of the inner cylinder. Torque readouts were converted to shear stresses, to normalise results.
Density	The density of dispersions was measured by weighing a sample of known volume (pipette) using a Mettler-Toldeo PK-300 (USA) balance.
Surface tension*	A tensiometer (Model 250-U1, Ramé-hart, USA) was used to measure the equilibrium contact angle of the inks against a Teflon syringe, and subsequently converted to surface tension. For each droplet, 7 readings were taken, and the reported surface tension was the average measurement for 3 droplets of each ink.

Particle dispersion	Particles were dispersed in the solvent by direct ultrasonication using a probe (Q55, 20 kHz, 6 mm Ti alloy tip, QSonica, USA) by 3×3 minute bursts, with 3 minute cooling intervals, at 60 % power.
Refining the PSD	Dispersions were centrifuged at varying relative centrifugal force (RCF) depending on solvent and particle properties, using an Eppendorf 5810 R centrifuge (Germany) at 21 °C. The centrifuge tubes were made by Fisher Scientific, USA (polypropylene sterile, disposable centrifuge tubes, 50 cm^3). The remaining dispersions were filtered with an 800 nm syringe filter (Cole-Parmer, USA), unless specified otherwise.
Sintering behaviour*	Dilatometry was analysed in a dilatometer Netzsch model DIL 402C (USA) in static air, heating the samples to 1500 °C at 5 °C min^{-1}, dwelling the samples for 10 hours, followed by cooling to room temperature.

* Dr. Tao Li (Imperial College London) conducted all surface tension and dilatometry measurements.

4.2. Inkjet Printing

Details of the inkjet printer, and its features that facilitated characterisation of the droplets (in-flight) and printed deposits are given in **Table 12**.

Table 12. The experimental inkjet printing equipment and characterisation procedures.

Outcome	Equipment and Procedure
Inkjet Printing	A Ceradrop X-serie piezoelectric inkjet printer (France) was used to deposit the inks, at is offered superior resolution (5 μm droplet placement accuracy) and characterisation facilities than alternatives. Drying occurred at 18 – 25 °C, unless stated otherwise. The printer could accommodate 3 separate printheads, and therefore deposit 3 phases simultaneously. They were: 1. Fujifilm Dimatix Q-class (USA), 256 nozzles with a nominal droplet size of 30 pL, droplet ejection frequencies > 5 kHz. 2. Fujifilm Dimatix DMC series (USA), 16 nozzles, with nominal droplet diameters of 10 pL or 1 pL, droplet ejection frequencies < 1 kHz. 3. Konica Minolta (Japan) printhead, 1024 nozzles, nominal droplet diameter 13 pL, droplet ejection frequencies *ca*. 20 kHz, for UV-curable monomer inks.
Structure design	Ceradrop 'CeraSlice' computer aided design software (Ceradrop, France) was used to produce all inkjet printed designs
In-flight diameter (D_i), ejection velocity, active nozzles	An in-built camera that faced ejected droplets (away from printed structures) was used to observe droplets in-flight, using a strobe light with customisable durations between images. This facilitated measurement of D_i and u_0, and the number of active nozzles.
Splat diameter (D_m)	A co-axial camera with the printheads, facing the substrate, was used to capture optical images of droplets on each substrate, separated from each other so they could be distinguished individually. An in-built measurement tool was used to measure the diameter of > 10 dried droplets on each substrate, and the average was taken as D_m.
Ensure nozzle activity	To ensure nozzle activity during printing, nozzle 'purging' was necessary, after *ca*. 5 minutes of printing. A purging procedure with customisable pressure and duration was used, and nozzles were subsequently wiped with a lint-free cloth. To avoid damaging the piezoelectric crystals, a 30 kPa ejection pressure with a duration of 0.3 – 1 second was typical.
Avoiding contamination	The ionically-conducting materials were deposited using the Dimatix Q-class printhead, and the electronically-conducting materials were deposited using the Dimatix DMC series printheads. The Dimatix Q-class printheads were irreplaceable due to cost, therefore, to mitigate contamination, *ca*. 500 cm^3 of water with surface tension reduced with Natsurf 265 (0.2 mg cm^{-3}) was flushed through the nozzles after each print run. Different Dimatix DMC printheads were used for each electronically-conducting material ink formulation.

4.3. Solid Oxide Electrochemical Reactor Characterisation

The experimental equipment used for imaging, mounting SOERs for testing, and electrochemical characterisations, with the corresponding procedures, are outlined in **Table 13**.

Table 13. Equipment used for producing and electrochemically characterising SOERs in this research project.

Outcome	Equipment and Procedure
Sintering	SOER materials were heated in a furnace (Elite Thermal Systems furnace, UK) with a material-dependant temperature profile.
Microstructural imaging	Scanning electron microscopy (SEM) was performed at 20 kV, 15 mm working distance with 10 mm chromium coating (JSM 6400, JEOL, USA) for microstructures reported in Chapter 8. The surface and cross-sections of the inkjet printed SOERs were imaged using a Hitachi TM3030 SEM at 15 kV accelerating voltage.
Reactor current collection	Current collection from the electrodes was via silver paste (Alfa Aesar, USA) brush coated directly onto the periphery of the electrodes, followed by addition of a silver mesh (80 mesh, woven from 0.115 mm diameter wire, Alfa Aesar, USA), completed with a silver wire (0.25 mm diameter, 99.9% purity, annealed, VWR International, UK), unless specified otherwise. Either 2 or 4-electrode (probe) measurements were taken, as outlined in the relevant sections.
Reactor sealing	The SOERs were cemented to an alumina tube 15 cm long (Almath Crucibles Ltd., UK) with outer diameter 26 mm, and inner diameter 20 mm, using a ceramic sealant (Aron Ceramic D, Aron Alpha Toagosei, USA). The sealant was cured, *in-situ*, by raising the temperature to 96 °C for 2 h, then 250 °C for 2 h, and finally to the SOER operating temperature.
Gas supply	Gases (BOC, UK) were supplied and extracted via a stainless-steel end-cap (fabricated by the workshop at the Department of Chemical Engineering, Imperial College London, UK) sealed with Viton O-rings (Polymax, UK) against the alumina tube on which the cell was mounted, using Swagelok (USA) stainless steel fittings. Gas flow rates were controlled by automated mass-flow controllers (Bronkhorst, UK).
Cell heat treatment	SOERs were tested at high temperatures. To achieve this, the mounted cells were inserted into a tubular furnace (Elite Thermal Systems Ltd., UK), which had a temperature profile that could be tailored to the SOER under test.
Electrochemical characterisation	A potentiostat / galvanostat capable of electrochemical impedance measurements, using a frequency analyser (FRA) 4.9 module with test procedures created in the Nova 1.10.2 software (PGSTAT302N, Metrohm Autolab B.V., Netherlands) was used for all electrochemical characterisations.

5. Inks Formulation

Chapter Summary

This Chapter describes the formulation of colloidally-stable and printable inks for the inkjet printing the functional layers of solid oxide electrochemical reactors. Inks to fabricate the electrolyte (YSZ), barrier layer (CGO), and electrodes (LSM and NiO) were developed. Their printability and the effect of their composition on structural features observed in deposited films is evaluated.

Note: sections of this Chapter are partially reproduced from Farandos et al., 2016; and Farandos et al., 2018 (145, 280).

5.1. Yttria-stabilised Zirconia Ink

Yttria-stabilised zirconia (YSZ) is the most common electrolyte material for solid oxide electrochemical reactors (SOERs), so has been researched widely. To stabilise YSZ colloids in water, the surface charge must be sufficiently high to prevent aggregation. **Figure 33** shows the variation of zeta potential (ξ) of 4 commercially-available YSZ powders with pH in water; the pH was varied using HCl or NaOH, for acidic or basic conditions, respectively (261). Notably, the variation in results with particles from different manufacturers is large, probably due to the introduction of impurities in the manufacturing process (262), and that the isoelectric point of YSZ is *ca*. pH 7. Therefore, to stabilise YSZ colloids in water, the addition of a dispersant and / or variation of pH was required.

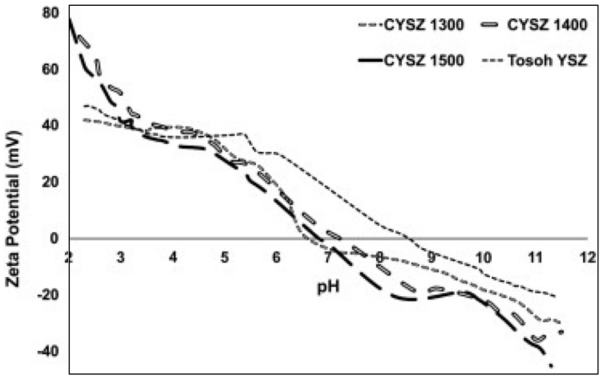


Figure 33. Variation of zeta potential with pH of 4 commercially-available YSZ powders in water. Reproduced with permission from (261).

The approximate zeta potential required for colloidal stability is > |20 mV|, so acidic / basic conditions would be required to stabilise YSZ through pH alone. This was undesirable due to the printhead materials used in this research project and that yttrium is predicted to dissolve at pH < *ca*. 6 (263), so stabilisation with a dispersant species at neutral conditions is preferable (156). **Table 14** shows the relative binding affinities to YSZ of common electrostatic dispersant functional groups; the most effective being the carboxylic acid group. Additional properties that increase stability are the presence of double C=C covalent bonds in the chain structure, as it facilitates polarisation and reduces the Hamaker constant (Section 2.3.6.2), and a chain length > 10 nm (227). The dispersant should not contain metal ions as these would not be removed during the downstream combustion and sintering process, resulting in possible detrimental electronic conductivity in the electrolyte.

Ammonium polyacrylic acid salts ($-COO^-(H^+)$ and NH_4^+ functional groups) have been used as effective dispersants for YSZ (264), and an appropriate ammonium polyacrylic acid dispersant

with a native basic pH = 8 is Dispex A40 (anionic, molecular weight is 10000 kg $kmol^{-1}$) (BASF, Germany), which is effective at low concentrations.

Table 14. The YSZ binding affinity of common dispersant functional groups (227).

Functional Group	Binding affinity
-OH	Low
$-NH_2$	Low*
-COOH	High

* Can cause a significant change in pH, altering colloidal stability

5.1.1. Materials and Methods

5.1.1.1 Colloidal Stability

$(Y_2O_3)_{0.08}(ZrO_2)_{0.92}$ (YSZ) particles purchased from two suppliers (Sigma Aldrich (SA), USA, and Fuel Cell Materials (FCM), USA) were stabilised colloidally in deionised water with Dispex A40 (BASF, Germany), added with varying concentrations relative to the mass-specific particle surface area, to determine the concentration required for maximum stability. Measurements for both particles were recorded.

5.1.1.2 Printability

After colloidal stabilisation, particles size distributions (PSDs) were determined by DLS, and were narrowed by centrifugation at 1350 RCF for 2 minutes, and 1000 RCF for 5 minutes, for the SA and FCM particles, respectively. Post-refinement PSDs of the filtrate were subsequently re-measured to ensure printhead nozzle blocking would not occur. Polyethylene glycol with molecular weight 35,000 kg $kmol^{-1}$ (PEG 35000) (Sigma Aldrich, USA) was added to the filtrate at varying concentrations and allowed to dissolve for 24 h. Immediately prior to printing, the alcohol ethoxylate Natsurf 265 (Croda Chemicals, UK) was added at a concentration of 0.2 mg cm^{-3} of the total volume of the ink, beyond which further decrease in surface tension was not expected, see Appendix 4: Natsurf 265 Surface Tension. Five different ink compositions were formulated for preliminary printing experiments.

5.1.1.3 Substrate Fabrication*

A NiO-YSZ slurry was prepared by mixing the constituent powders at 60:40 wt% ratio of NiO:YSZ (Inframat Advanced Materials, USA), respectively, with polyethersulfone (PESf) (Radel A-300, Ameco Performance, USA) as a binder and polyethyleneglycol 30-

dipolyhydroxystearate (Arlacel P135, Uniqema, USA) dispersant in dimethyl sulfoxide (Sigma Aldrich, USA), using a planetary miller at mass ratios 200:25:2:100 of NiO-YSZ, binder, dispersant, and solvent, respectively. The substrate was then fabricated via a phase inversion-assisted tape casting process, with an adjustable casting knife gap. The resultant sheets were soaked in an external coagulant (water) bath for 24 h to allow the phase inversion to complete, and subsequently flattened and dried.

Differently sized NiO particles were trialled, to achieve the closest possible sintering match to the YSZ printed layer (see Section 5.1.2.4).

* Substrate fabrication method and experimental procedure was developed and carried out by Dr. Tao Li, Imperial College London.

5.1.1.4 Preliminary Printing Experiments

A Dimatix Sapphire QS-256/30 AAA printhead (Fujifilm, USA) was used to deposit the dispersions onto the NiO-YSZ substrate. The optimal ejection pulse (Ink 1) was recorded as V_p = 80 V and P_d = 13 μs, including a rise and fall time of 2 and 5 μs, respectively. Droplet ejection frequency was 2.8 – 5 kHz.

The drying time between each printed layer was 240 s at an ambient temperature of 26 – 28 °C. The droplet deposition pattern was a square lattice (*i.e.* a coordination number of 4 for each droplet) for all printed structures; however, droplet overlap (diameter overlap between coordinated pairs) varied between 20 – 40%.

5.1.1.5 Sintering*

To determine an effective, and non-destructive sintering profile, dilatometer studies were conducted. Nanometre and micrometre-sized NiO particles (NiO(nm) and NiO(μm), respectively) (Inframat Advanced Materials, USA) and nanometre-sized YSZ particles (Inframat Advanced Materials, USA and Sigma Aldrich, USA, YSZ(I) and YSZ(S), respectively) were individually, and as 60:40 wt% mixtures, compressed into cylinders of *ca.* 3–4 mm height using a tablet press with a 1700 kg cm^{-2} load (Gamlen Tableting Ltd., UK) for dilatometry measurements. These results were used to match shrinkage rates and lengths as closely as possible in the final sintering profile.

* Dilatometry measurements were carried out by Dr. Tao Li, Imperial College London.

5.1.1.6 Microstructural Characterisation

The surfaces and cross section of the printed YSZ layers were imaged using a Hitachi TM3030 SEM (Japan) at 15 kV accelerating voltage. Cross sectional imaging was destructive, requiring the YSZ sample to be fractured prior to mounting for imaging.

5.1.2. Results and Discussion

5.1.2.1 Colloidal Stability

The mass-specific surface area of the SA and FCM YSZ particles were measured as 9.2 and 10.8 $m^2 g^{-1}$, respectively.

The variation of zeta potential with pH for SA particles in water is shown in **Figure 34a**, the result at pH 7 is believed to be erroneous and probably a consequence of the particles having negligible surface charge, invalidating the measurements through aggregation. At pH > 10 and < 3, colloidal stability is predicted; however, these pH values lie outside of the materials' stability of the inkjet printer printheads. Furthermore, yttrium is predicted to dissolve at even mildly acidic pHs (263, 265). Therefore, stabilisation at neutral conditions by a dispersant species is preferable. The zeta potential for both SA and FCM particles with varying Dispex A40 concentration is shown in **Figure 34b**. Unsurprisingly, particles were charged negatively by the adsorption of Dispex A40 which contains the (dissociated) carboxylic acid functional group. Evidently, maximum stability occurred at 0.2 mg m^{-2} YSZ surface area for both SA and FCM particles. Notably, the isoelectric point of both populations of YSZ particles was less than pH 7, due to the relatively high zeta potential of the particles in the absence of Dispex A40. However, the magnitude of zeta potential close to the point of stability (*ca*. |20 mV|) was unreliable, due to aggregation of the particles during the measurement.

Stability against aggregation was confirmed by the absence of sedimentation over a period of weeks, and agreed with DLVO theory predictions (see Appendix 1: DLVO Theory).

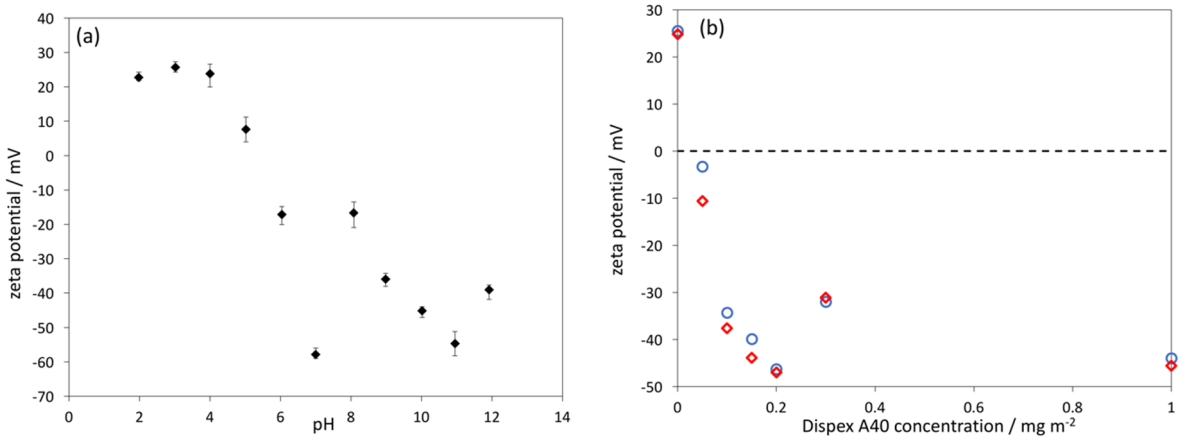


Figure 34. Zeta potential variation of (a) SA particles in water with varying pH; and (b) SA (blue circle) and FCM (red diamond) YSZ particles with Dispex A40 concentration at neutral conditions.

5.1.2.2 Printability

PSDs were determined for both particles after centrifugation and filtration, stabilised colloidally in water without any additional additives. The PSDs are shown in **Figure 35**; both were smaller than the threshold for nozzle blocking (*ca*. *L*/50). The FCM PSD was narrower and had a lower average size of 115 nm than the wider SA PSD centred about 194 nm, due to differences in the original (prior to centrifugation) PSDs.

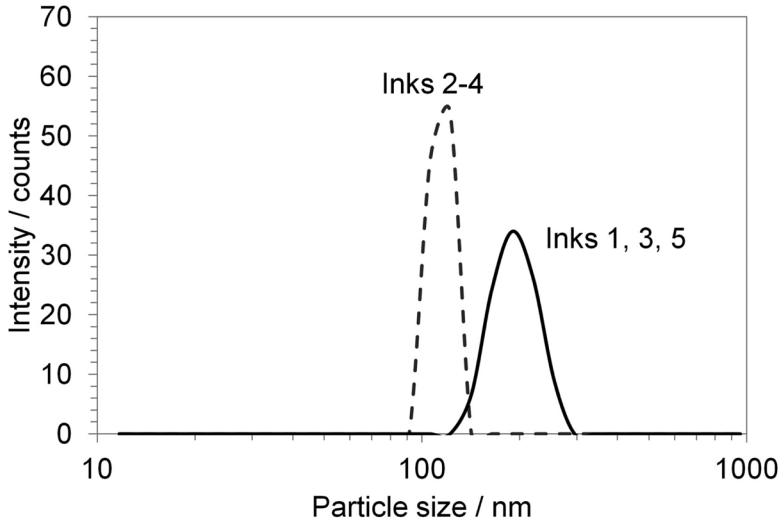


Figure 35. PSDs of the SA (Inks 1, 3, 5) and FCM (Inks 2, 4) particles. Reproduced with permission from (145).

Five different aqueous inks were formulated, varying the solids fraction, PSDs and PEG concentration, with formulations reported in **Table 15**, to investigate the effect of ink

composition on printed structures. The physical properties of all formulations lay within the printable range (148).

Table 15. Physical properties of the ink formulations, with corresponding printing parameters.

Ink #	Supplier	μ / mPa s	γ / mN m^{-1}	Oh^{-1} / 1	YSZ loading / wt%	PEG 35000 concentration / mg cm^{-3}	Particle diameter / nm	Droplet volume / pL	u_0 / m s^{-1}	D_m/D_i / 1
1	SA	4.7[a]	24	8.5	24	25	194	29	4.5	1.6
2	FCM	4.1[b]	24	9.1	20	25	115	30	4.5	1.7
3	SA	8.8[a]	25	4.4	10	40	194	29	4.5	1.8
4	FCM	7.5[a]	25	5.1	10	40	115	27	4.5	2.7
5	SA	4.2[a]	28	9.2	3	30	194	20	2.8	2.8

[a] Newtonian Viscosities; [b] Shear thinning behaviour observed, viscosity of 4.1 mPa s was at an 'infinite' shear rate.

5.1.2.3 Preliminary Printing Experiments

Thin layers of each ink were printed onto the substrate to assess their ability to resist cracking, which would otherwise create gas leaks in any sintered electrolyte layer or mechanical failure in complex microstructures. In the pre-sintered films, cracks form during drying in response to a capillary pressure gradient throughout the film, due to evaporation-driven flows that result from the relatively high surface tension of water (266). Inks 1 and 5 resulted in planes that did not crack; however, Inks 2 – 4 cracked, as shown in **Figure 36** (post sintering), which is explained in the remainder of this section.

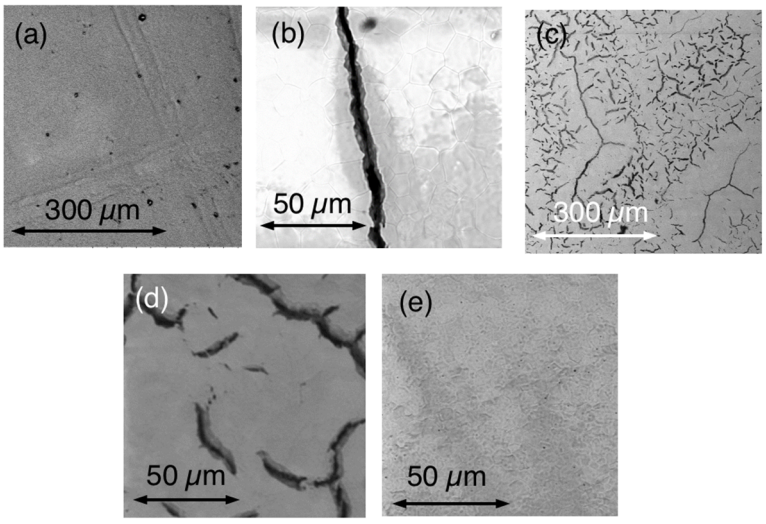


Figure 36. SEM surface view photomicrographs of sintered planar structures fabricated with (a) 12 layers of Ink 1; (b) 25 layers of Ink 2; (c) 16 layers of Ink 3; (d) 40 layers of Ink 4; and

(e) 20 layers of Ink 5. Droplet overlap was 40 % for Ink 1, and 20 % for Inks 2–5. Reproduced with permission from (145).

The critical cracking thickness (H_{crit}), defined as the film depth below which cracking does not occur, depends on the effective shear modulus of the YSZ particles (G_S), the particle packing density (φ), coordination number (ϖ), particle radius (r_p), effective Poisson's ratio (ζ_p), and the surface tension of the ink (γ), according to equation (76) (267).

$$\frac{H_{\text{crit}}}{r_p} = 0.050\left(\frac{G_S \varpi \varphi r_p}{2\pi(1-\zeta_p)\gamma}\right)^{2/3} \qquad (76)$$

It was essential that the thickness of a single dried printed layer (H_l) < H_{crit}, as when printing isolated droplets (*i.e.* narrow structures in the x-y plane), the rate of evaporation ($\dot{E}$) is high, so the ability to mitigate cracking is determined by the condition: $H_l < H_{crit}$. At low $\dot{E}$, cracking may be avoided at $H_l > H_{crit}$. Assuming the particles were spherical and assembled in a random close packing (RCP) arrangement in the printed film (*i.e.* $\varpi = 9$, $\varphi = 0.64$ (268)), this would indicate that the critical cracking thickness for Inks 1 – 5 was 24, 9, 22, 9, and 21 μm, respectively, using models to predict G_S and ζ_p (269) (see Appendix 5: Critical Cracking Thickness).

In reality, H_{crit} would be expected to differ from the theoretical values for some formulations for four reasons:

i) particles were non-spherical and their average size did not represent all particles in the distribution;

ii) strong inter-particle interactions may cause aggregation, decreasing the particle packing fraction and coordination number;

iii) coordination number may not be uniform, and aggregated particles with lower coordination number are less resistant to cracking;

iv) for printed layer number n, where $n > 1$, the 'substrate' is a previously printed layer, and consequently it may be possible for cracks to enter the substrate, decreasing the structure's potential to withstand cracking, *i.e.* $H_{crit}(n > 1) < H_{crit}(n = 1)$ (270).

However, it was also evident that packing arrangement ($\varpi.\varphi$) varied with organic additive composition, as cracking behaviour was inconsistent for constant r_p. This can be explained by considering the processes that occur during droplet drying. As the water evaporates, the particles (and polymer) are concentrated within the printed film. If the particles are brought

sufficiently close together, they may overcome electrostatic repulsion, and aggregate (irreversibly). In addition, if there is a free polymer present in the drying droplet, a depletion potential may be induced if its concentration is sufficiently high, and inter-particle separation sufficiently low (*i.e.* excluded volumes). The packing density within these aggregates ultimately determines the packing density within the printed films, provided inter-particle potentials exceed the capillary pressure during drying. As polymer concentration is increased further during drying, a stabilisation potential is induced, locking the particles in their existing arrangement, as shown schematically in **Figure 37**.

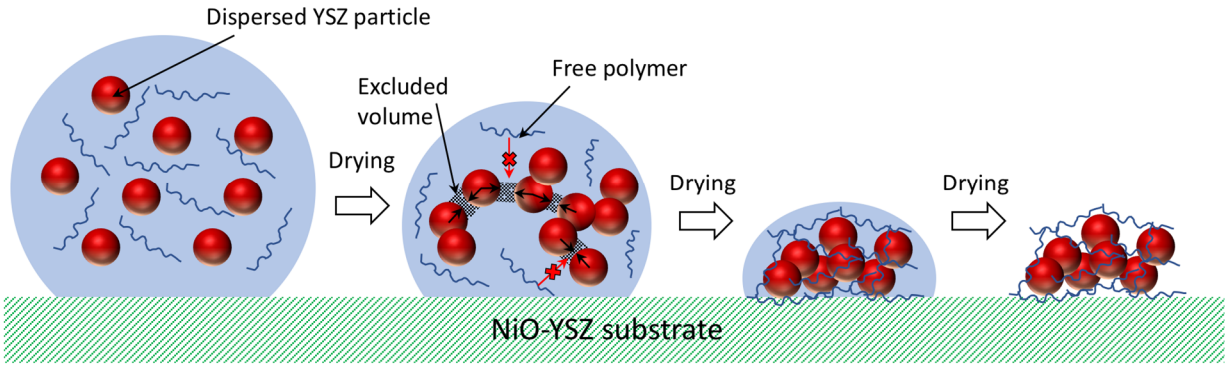


Figure 37. Schematic of the inter-particle depletion potential inducing a destabilisation potential as drying progresses. Reproduced with permission from (145).

Inks 1 and 2 both had a concentration of 25 mg cm^{-3} PEG 35000, and similar surface coverage per printed layer (7.5 and 7.0 monolayers equivalent, respectively, see Appendix 3: Particle Surface Coverage); however, Ink 2 cracked and Ink 1 did not. This was attributed to the smaller YSZ particle size in Ink 2, which decreased H_{crit} by *ca.* 60 %. In addition, as the droplet overlap for Ink 1 was 40 %, rather than 20 % for Ink 2, the volume of deposited ink was approximately 90 % greater in the former case for a given printed area, so the surface area to volume ratio was approximately 50 % lower than for the case of Ink 2, which decreased $\dot{E}$, so even $H_l > H_{crit}$ could be tolerated. However, the condition $H_l > H_{crit}$ was unlikely for Ink 1 as un-sintered printed pillars of *ca.* 60 µm diameter, *i.e.* a single splat, did not crack (see Section 8.3.1). The packing density of particles in Ink 1 was 64 %, corresponding to RCP, so it can be inferred that the rate and extent of particle aggregation during drying was insufficient to decrease the packing density.

Inks 3 and 4 had an increased free polymer concentration of 40 mg cm^{-3} and decreased surface coverage per printed layer (2.3 – 1.7 monolayer equivalent). They also had lower YSZ particle mass fractions, which would suggest lower rates of aggregation than Inks 1 and 2, so would form denser aggregates upon drying; however, this was not the case, as cracking was observed

for both inks. Therefore, it is proposed that the increase in concentration of the polymer during drying contributed to an increased (attractive) depletion potential between the particles, inducing aggregation, and that this progressed sufficiently to decrease $\varpi.\varphi$ (*i.e.* ($\varpi.\varphi$) < 9 × 0.64). When the stabilisation potential was induced as drying progressed, the aggregates became locked in a kinetically immobile state, so the overall packing density was lower than for Inks 1 and 2. This state could resist deformation due to residual capillary pressures, so the particles did not rearrange into a closer-packed state. Notably, the depletion potential was greater for the larger YSZ particles (Ink 3) as shown in equation (63), so the factor $\varpi.\varphi$ was lower for Ink 3 than Ink 4. The absolute value of $\varpi.\varphi$ is difficult to predict due to the combination of aggregation kinetics and evaporation-driven flows.

Alternatively, cracking in Inks 3 and 4 could have been due to the lower surface coverage than for Inks 1 and 2 as *ca*. 3 - 3.5 times as many layers were required to form a film of equivalent thickness. Hence, particles that were deposited in subsequently printed layers interacted with particles that had been deposited in previously printed layers to form aggregates with low packing densities. However, this can be excluded as the surface coverage for Ink 5 was 25 % monolayer equivalent, *i.e.* approximately 30 times the number of layers were required to fabricate a structure of equivalent thickness to Ink 1 and cracking was not observed. As the deposited solid was 25 % monolayer equivalent for Ink 5, particle separation upon deposition was sufficiently large to neglect attractive depletion potentials, so a RCP structure resulted. This also meant that previously deposited polymer was not re-dispersed by subsequently (wet) printed layers, so it is also unlikely that cracks can enter the NiO-YSZ substrate.

The We, Re, and $We^{0.5}Re^{0.25}$ for Ink 1 were 58, 66, and 22 respectively. Therefore, although Re > 5, which predicts that satellites would form during ejection, these were not problematic as they re-combined with the primary droplet before impact, and the condition We > 9 was satisfied. Splashing was not predicted to occur as the condition $We^{0.5}Re^{0.25}$ < 50 was satisfied. This is important as Ink 1 can be used to fabricate microstructures without defects caused by splashing, which is unpredictable (demonstrated in Chapter 8).

5.1.2.4 Sintering

The dilatometer results for the FCM, SA, and the particles used to fabricate the substrate, are shown in **Figure 38**. Evidently, the NiO (both nano- and micro-sized) and YSZ particles were inherently thermally-mismatched; however, by combining both nano- and micro-sized NiO particles with YSZ in the substrate, the final shrinkage behaviour of the NiO-YSZ composite

could be modified. The results show that the closest sintering behaviour match to the FCM and SA particles was achieved using only the micro-sized NiO particles in the substrate.

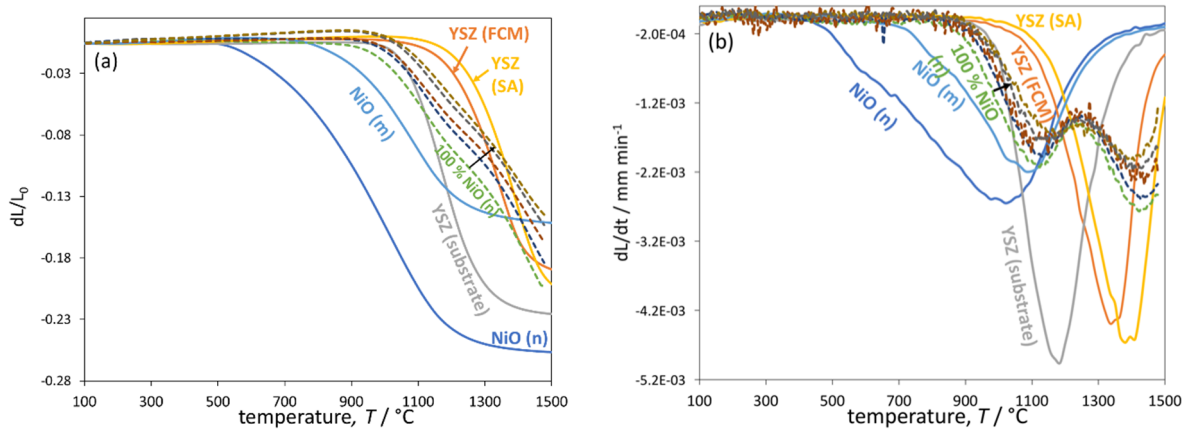


Figure 38. Sintering behaviour with varying temperature of the particles (solid lines) and substrate compositions (dotted lines) used in this study, with respect to (a) original length; and (b) time.

To achieve sintered structures with minimal stresses due to sintering behaviour, the printed structures were heated at a rate of 4 °C min^{-1} to 600 °C, at which they were held for 6 h in air, then heated at a rate of 15 °C min^{-1} to 1500 °C, at which they were held for 10 h, before being cooled at 4 °C min^{-1} to room temperature. This resulted in dense YSZ structures well-adhered to the NiO-YSZ substrate, suitable for electrolyte use, as shown in **Figure 39**. Each printed layer was *ca*. 2 µm thick, post-sintering.

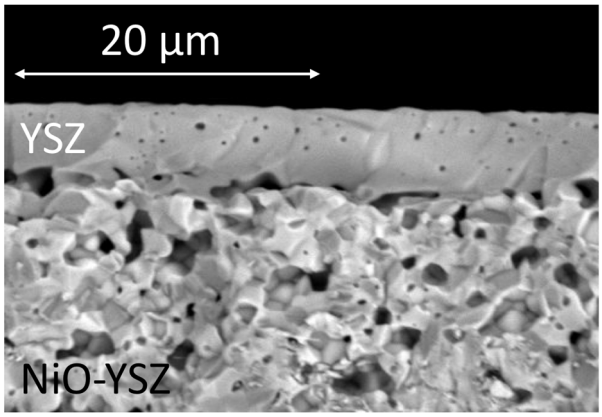


Figure 39. Cross sectional SEM photomicrograph of a co-sintered, inkjet printed YSZ layer on NiO-YSZ.

5.1.3. Conclusions

Planar YSZ films for SOER electrolytes were fabricated by inkjet printing aqueous-based inks, electrostatically-stabilised by the ammonium salt of a polyacrylic acid. The effects of ink composition on crack formation, resulting from capillary effects during drying within the printed films, was investigated by varying particle size, solids loading, and the viscosity by varying the polymer additive concentration. It was established that the added polymer content significantly influenced crack formation by inducing attractive depletion potentials between adjacent particles through drying, decreasing the particle packing density, which reduced their ability to resist cracking. Further, it was essential to allow sufficient drying time between sequentially printed films to ensure that layer height did not exceed the critical cracking thickness of the film.

5.2. Gadolinium-doped Ceria Ink

Gadolinium-doped ceria, $Ce_{0.8}Gd_{0.2}O_{2-x}$, (CGO) has greater O^{2-} ion conductivity than YSZ, however, at high temperature and under highly-reducing conditions, CGO becomes electronically conductive due to the partial reduction of cerium ($Ce^{IV} \rightarrow Ce^{III}$) at low oxygen partial pressures (271, 272), making it a challenging electrolyte material with which to work. Therefore, CGO is frequently employed as a 'boundary' layer between YSZ electrolytes and the oxygen-electrode material: lanthanum strontium cobalt ferrite $La_{0.6}Sr_{0.4}Co_{0.2}Fe_{0.8}O_{3-x}$ (LSCF) (273), to prevent chemical reaction between YSZ and LSCF (274).

A single study investigating colloidal CGO in water has been published (275); dispersions were optimised for a dip-coating process, which is very different to inkjet printability (276, 277). The isoelectric point of CGO particles (Fuel Cell Materials, USA) was found to be *ca*. pH 7, as shown in **Figure 40a**, and varying the pH away from neutral conditions was found to dissolve Ce^{IV} and Gd^{III}, as shown in **Figure 40b**. Therefore, pH-assisted colloidal stabilisation for CGO is impractical, so an effective dispersant was required.

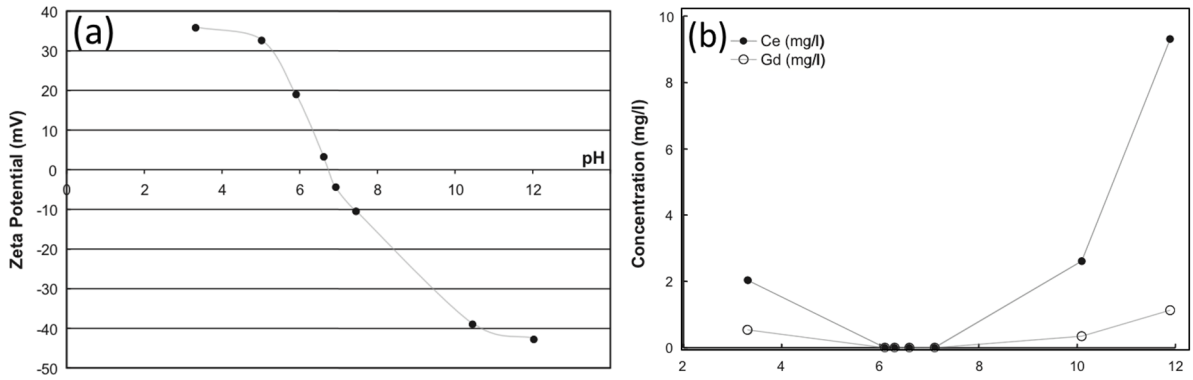


Figure 40. (a) Zeta potential – pH relationship for CGO particles dispersed in water; and (b) equilibrium concentration of dissolved Ce^{IV} / Gd^{III} with varying pH. Reproduced with permission from (275).

To stabilise CGO particles in water, the polyacrylic acid ammonium salt Duramax D3005 (Rohm & Hass, PA, USA) was used, the optimal concentration being 3.0 wt%. However, preliminary experiments undertaken at Imperial College to reproduce this colloidal stability from (275) failed, as shown in **Figure 41**, showing almost all dispersed species had aggregated and sedimented after *ca*. 3 hours.

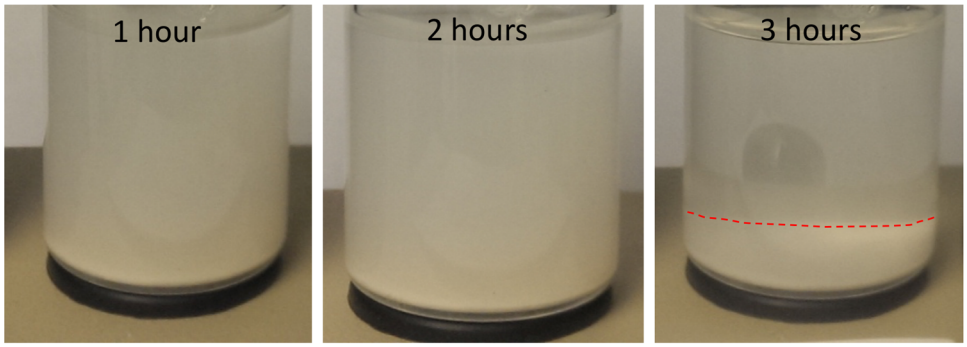


Figure 41. Photographs of dispersed CGO with Duramax D3005 (3 wt%) over 3 hours, sediment level is shown with dotted red line.

5.2.1. Materials and Methods

5.2.1.1 Colloidal Stability

$Ce_{0.8}Gd_{0.2}O_{2-x}$ (CGO) particles (Fuel Cell Materials, USA) were stabilised in de-ionised water with Dispex A40 (BASF, Germany), added at varying concentrations relative to the mass-specific particle surface area, to determine the concentration required for maximum colloidal stability.

5.2.1.2 Printability

After colloidal stabilisation, centrifugation at 1350 RCF for 2 minutes, and syringe filtration, the PSD was determined by DLS to ensure printhead nozzle blocking would not occur.

Polyethylene glycol with molecular weight 35000 kg $kmol^{-1}$ (PEG 35000) (Sigma Aldrich, USA) was added to the filtrate at 25 mg cm^{-3} and allowed to dissolve over *ca*. 24 h. Immediately prior to printing, the alcohol ethoxylate Natsurf 265 (Croda Chemicals, UK) was added at a concentration of 0.2 mg cm^{-3} of the total volume of the ink.

5.2.1.3 Substrate Fabrication*

CGO was inkjet printed on both a NiO-CGO substrate, for an electrolyte application, and onto a pre-inkjet printed YSZ substrate, for a barrier layer application.

In the former case, CGO and NiO (Inframat Advanced Materials, USA) were mixed with dimethyl sulfoxide (DMSO, VWR, USA) and polyethersulfone (PESf, Radel A-300, Ameco Performance, USA), and milled for 48 h (JARMILL, Gladstone Engineering Ltd, UK). Poly(ethylene glycol) 30-dipolyhydroxystearate (Arlacel P135, Uniqema) was added, and mixing continued for an additional 48 h. The final composition contained the above compounds in the ratio 60:90:100:20:2, respectively. The dispersion was degassed under vacuum, with stirring, subsequently cast onto a plate with a casting knife height of 0.5 mm and then submerged into an external coagulant bath to complete the phase inversion process. The substrate precursor was kept in a coagulant bath overnight to completely exchange the solvent, before being dried and flattened.

In the latter case, 8 layers of the YSZ 'Ink 1' formulation, reported in Section 5.1, were inkjet printed as outlined in Section 5.1.1.4 onto a NiO-YSZ substrate fabricated as reported in Section 5.1.1.3. CGO was deposited on top of this un-sintered structure.

* The composite NiO-CGO substrate fabrication method described above was developed and completed by Dr. Tao Li, Imperial College London.

5.2.1.4 Preliminary Printing Experiments

A Dimatix Sapphire QS-256/30 AAA printhead (Fujifilm, USA) was used to deposit the CGO dispersions onto the NiO-CGO, or a pre-printed, unsintered NiO-YSZ | YSZ substrate. The drying time between each printed layer was 240 s at an ambient temperature of 26 – 28 °C. The droplet deposition pattern was a square lattice (*i.e.* a coordination number of 4 for each droplet) with a droplet overlap of 40 % for all printed structures.

5.2.1.5 Sintering and Microstructural Characterisation*

To determine an effective, and non-destructive sintering profile, dilatometry measurements were taken; this was essential for co-sintering NiO-CGO|CGO and NiO-YSZ|YSZ|CGO structures successfully. The results were used to match shrinkage rates and lengths as closely as possible in the final sintering profile. The printed and sintered microstructures were characterised as described in Section 5.1.1.6.

* Dr Tao Li, Imperial College London, conducted the dilatometry measurements.

5.2.2. Results and Discussion

5.2.2.1 Colloidal Stability

The mass-specific surface area of the CGO particles was measured as 13.8 m^2 g^{-1}. **Figure 42a** shows the zeta potential variation with pH; many of the data points near to the isoelectric point were inaccurate due to aggregation of the particles during the measurements. CeO_2 and Gd_2O_3 were predicted to dissolve in water in mildly acidic or basic conditions (265, 278), therefore, to ensure thermodynamic stability, the pH of the solution was neutral. **Figure 40b** shows the variation of zeta potential with Dispex A40 concentration for the CGO particles in water at pH 7; the maximum stability was achieved at *ca*. 0.8 mg m^{-2} of CGO.

Colloidal stability of the ink was verified by the absence of aggregation and sedimentation over a period of weeks, which agreed with stability predictions from DLVO theory (see Appendix 1: DLVO Theory for Aqueous Dispersions).

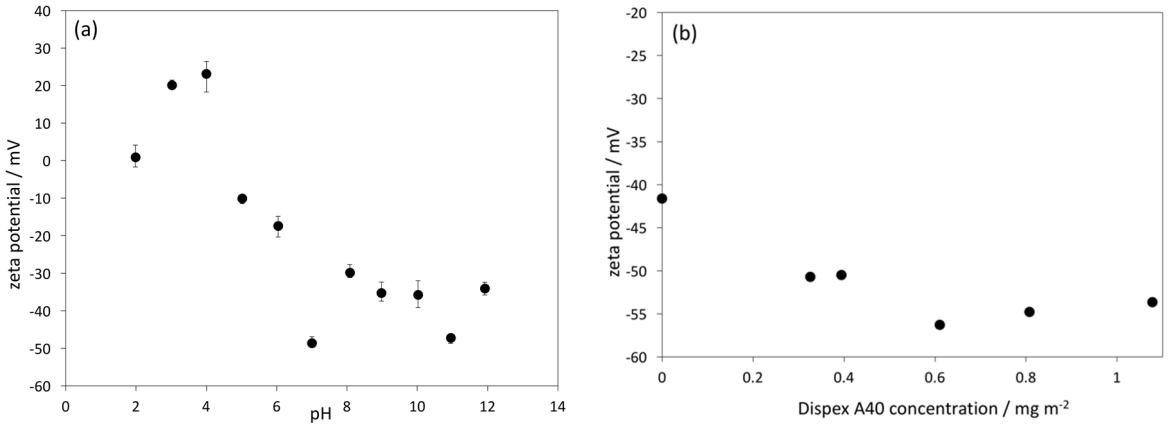


Figure 42. Effects on zeta potential of (a) pH; and (b) Dispex A40 concentration at pH 7 for CGO particles in water with 10^{-2} kmol m^{-3} KCl.

5.2.2.2 Printability

CGO PSD was determined for centrifuged and filtered particles stabilised in water by Dispex A40 at 0.8 mg m^{-2} concentration, without any additional additives, as shown in **Figure 43**. By intensity counts, the average particle size was measured as 165 nm, which was sufficiently low to avoid nozzle blocking.

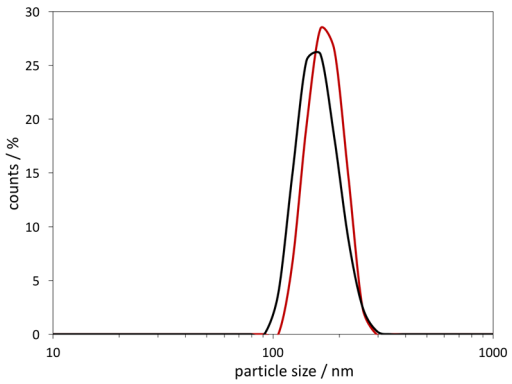


Figure 43. PSD of the filtered CGO particles in water, by intensity (red) or volume (black) counts.

To ensure rapid deposition of CGO, and also mitigate cracking by keeping layer height below the critical cracking thickness, the mass fraction of CGO was set as 13 wt%, at which no sedimentation was observed over a period of weeks. The final ρ, μ, γ, and Oh^{-1} were 1.148 g cm^{-3}, 4.95 mPa s, 28 mN m^{-1}, and 8.25, respectively. The viscosity of the ink was shear thinning, as shown in **Figure 44**, so the viscosity reported above is at an infinitely-high shear rate, evaluated graphically, as shear rates in the printhead nozzle were high (see Appendix 6: Evaluating Infinite Shear Rate Viscosity).

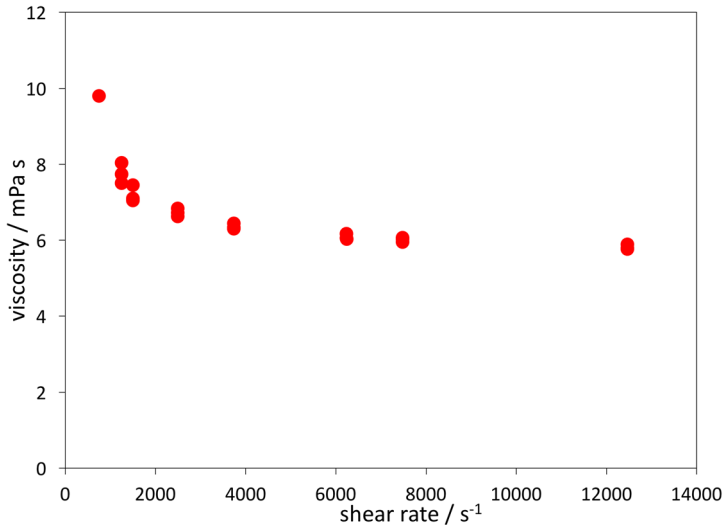


Figure 44. Viscosity – shear rate relationship for the aqueous CGO ink.

5.2.2.3 Preliminary Printing Experiments

The optimal printing parameters (determined as outlined in Section 2.3.6.3) were V_p = 100 V and P_d = 15 μs, including a rise and fall time of 1.5 and 3.5 μs, respectively. The ejection velocity of the CGO ink was measured as 4 m s^{-1}. Therefore, the resulting Weber number was 34, predicting no satellite droplet formation. The corresponding Re number was 48, so the splashing condition $We^{0.5}Re^{0.25}$ = 15 was also satisfied. The thickness of each printed CGO layer was measured as 775 nm, and D_m was measured as 80 μm.

5.2.2.4 Sintering and Microstructural Characterisation

The dilatometry results for the CGO particles are shown in **Figure 45**. The difference between the YSZ, CGO, and NiO-CGO sintering behaviour was large, so sintering with minimal stresses was challenging for the case of un-sintered substrates.

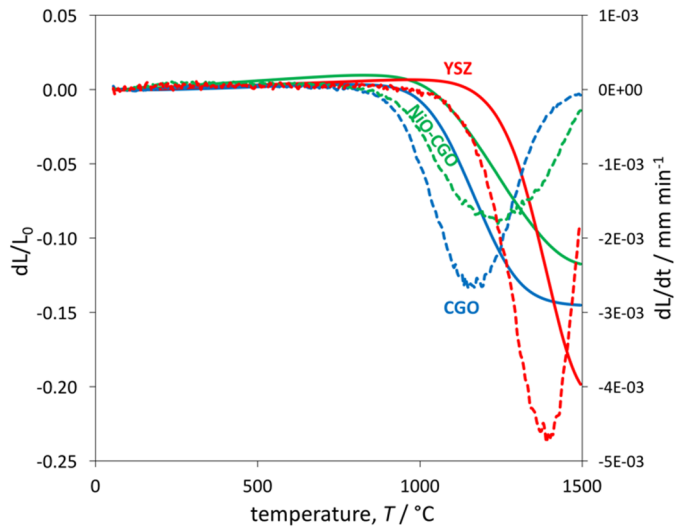


Figure 45. Dilatometry results for CGO (blue), NiO-CGO (green), and YSZ (red) powders used for the substrate and electrolyte, in terms of length change (solid lines) and rate (dashed lines).

Applying the YSZ sintering profile described in Section 5.1.2.4 to the inkjet printed CGO resulted in sintered structures with large cracks, and delamination between the electrode, and electrolyte (and barrier layer). Therefore, an intermediate temperature dwell step was added to reduce thermal stresses, after a combustion step at 600 °C (4 °C min^{-1}, 6 h). Raising the temperature to 1300 °C at 15 °C min^{-1}, holding for 2 h, at which the shrinkage rates of the NiO-CGO substrate, CGO electrolyte, and the CGO and YSZ particles, were similar, subsequently heating to 1500 °C for 10 h at 15 °C min^{-1}, and cooling to room temperature at 2 °C min^{-1}, crack-free CGO layers attached to the substrate resulted, as shown in **Figure 46**. The sintering match of the CGO and NiO-CGO phases was close, so a highly-dense, gas-tight electrolyte layer was achieved, as shown in **Figure 46a**. However, the CGO did not shrink as much as YSZ at these temperatures. Therefore, achieving both dense YSZ and CGO layers was not possible using the particles in this study, without bending of the deposit and substrate. Consequently, comparatively large pores remained in the CGO barrier layer, as shown in **Figure 46b**.

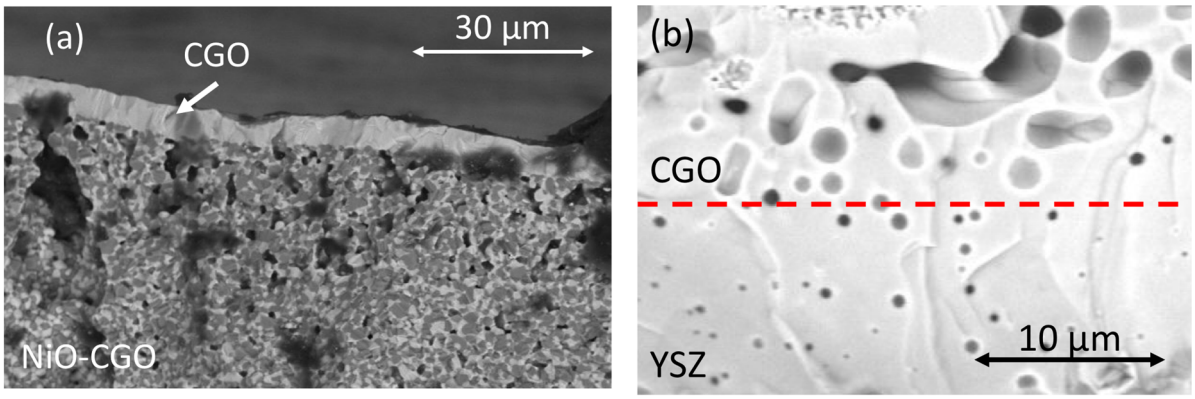


Figure 46. SEM photomicrographs of (a) sintered CGO electrolyte; and (b) co-sintered YSZ electrolyte and CGO boundary layer.

To reduce porosity within the CGO barrier layer, the particle packing fraction within the pre-sintered inkjet printed films should be increased, by optimising particle assembly during evaporative droplet drying. Presuming the packing density of CGO particles in the barrier layers was RCP, *i.e.* $\varphi = 0.64$, it could be increased to a maximum of *ca.* $\varphi = 0.74$, corresponding to a hexagonally-packed microstructure, which is significantly greater, suggesting porosity could be reduced. Strategies to achieve this include inducing an attractive force between the dispersed particles and the droplet | air interface during evaporative drying, which has previously resulted in highly-dense gold films derived from toluene dispersions (279), and altering the rate of evaporation. These effects are explored in further detail in Section 5.3.2.4, and suggest that with larger particles, a faster rate of evaporation (without causing film cracking) and a higher ink viscosity (without compromising printability or colloidal stability) would be preferable.

To minimise the detrimental effects of porosity in the CGO barrier layer, the layer thickness should be reduced, as only a thin contiguous CGO film is required to prevent reaction between YSZ and the oxygen-electrode material. This is easily accomplished by reducing the number of printed layers, the CGO mass fraction in the ink and / or decreasing droplet overlap on the substrate. Preliminary electrochemical characterisations of inkjet printed CGO barrier layers are reported in Appendix 8: Preliminary Electrochemical Characterisation of Inkjet Printed CGO Functional Layers.

5.2.3. Conclusions

A colloidally-stable and printable aqueous-based CGO ink was developed, and preliminary inkjet printing experiments were undertaken to deposit CGO electrolytes and boundary layers, to form the arrangements: NiO-CGO|CGO, and NiO-YSZ|YSZ|CGO, respectively. YSZ and

CGO had significantly different dilatometry behaviour, so to prevent their mutual delamination during sintering, an intermediate heating step was required at 1300 °C, at which their shrinkage rates were coincidental, before additional sintering at 1500 °C. However, even after mitigating layer delamination, it was not possible to densify the CGO completely on the YSZ, the former remaining relatively porous. Increasing the CGO particle packing density in the pre-sintered films could reduce porosity, and thinner CGO films would reduce the significance of detrimental porosity effects on reactor performance.

5.3. Lanthanum Strontium Manganite Inks

Conventionally, solid oxide electrochemical reactors (SOERs) are mechanically supported by a thick (> 300 μm) fuel-electrode, frequently the NiO-YSZ cermet. Inkjet printing is well suited to fabricating thin-films, so can be used to fabricate the electrolyte (and barrier layer where required), and oxygen-electrode, sequentially. Sections 5.1 and 5.2 outlined printable ink formulations for the electrolyte and barrier layers, respectively. Therefore, this chapter concerns the development of an ink suitable for inkjet printing the oxygen-electrode.

Deploying a YSZ electrolyte without a barrier layer, lanthanum strontium manganite (LSM) is the typical oxygen-electrode material, due to its thermal and chemical compatibility with YSZ, and high activity for O_2 / O^{2-} reduction / oxidation. A study into formulating aqueous LSM dispersions has been published, and optimised for tape casting (281). Investigations into the variation of zeta potential with pH identified the isoelectric point at *ca*. pH 3, as shown in **Figure 47a**. However, even at highly-basic conditions, the zeta potential was insufficiently large in magnitude for colloidal stability. Furthermore, as shown in **Figure 47b**, the solubility of all LSM elemental constituents in water was found to be higher under mildly acidic conditions, whereas all were insoluble under basic conditions. Therefore, a dispersant was required to stabilise the LSM colloid; Duramax D3005 was trialled and found to be ineffective ≤ 24 h after addition.

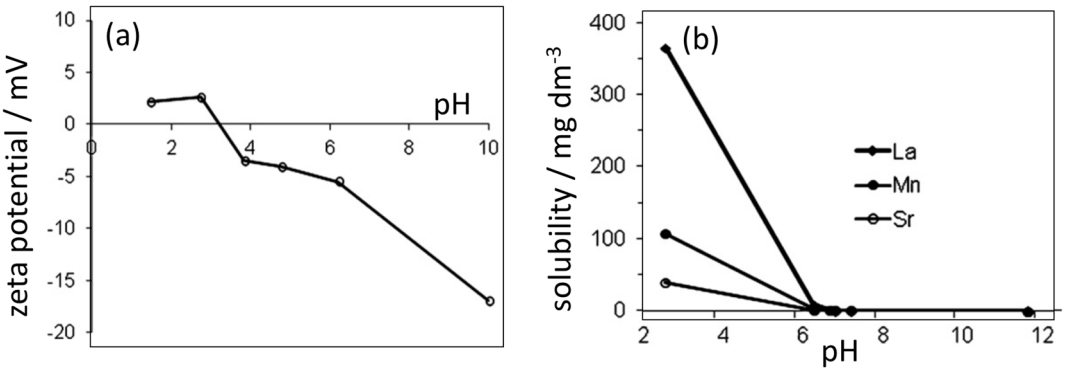
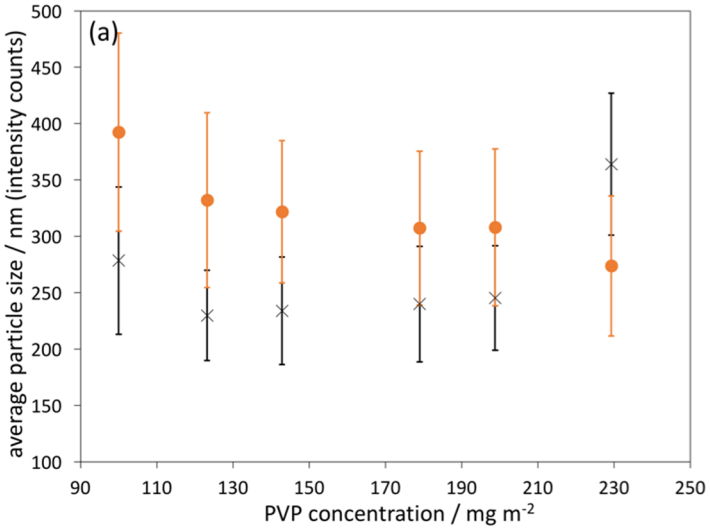


Figure 47. Effect of pH on LSM: (a) zeta potential; and (b) constituent elements' aqueous solubilities. Reproduced with permission from (281).

An additional study into aqueous-based LSM particle dispersions, optimised for brush coating, used Poly(N-vinylpyrrolidone) with a molecular weight of 40000 kg kmol^{-1} (PVP 40000) as the dispersant species, at 3.7 wt% relative to the LSM powder (282). However, as shown in **Figure 48a**, an impractically high *ca*. 200 mg m^{-2} PVP 40000 concentration was required to maintain a constant PSD over 3 days. Furthermore, screening experiments with PVP 360000, which is larger and therefore potentially a more effective stearic dispersant, found that a concentration of *ca*. 50 wt%, compared to the LSM mass, was required to prevent LSM aggregation and sedimentation over 1 h, as shown in **Figure 48b**. At this concentration, the viscosity of the dispersion was too high for inkjet printing, with any practical LSM solids loading. Therefore, a more effective dispersant for aqueous LSM dispersions, optimised for inkjet printing, was required.



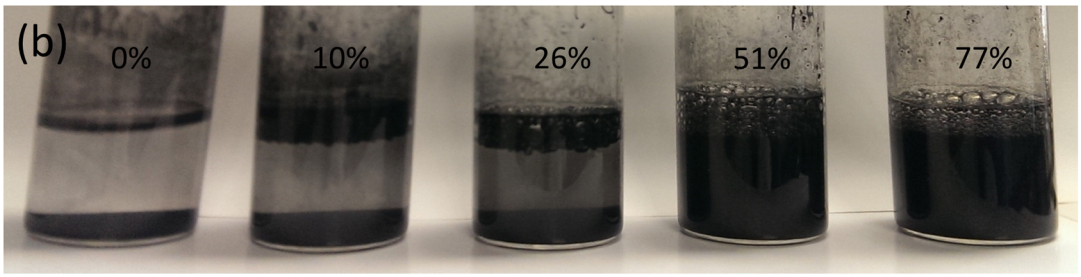


Figure 48. (a) Effect of PVP 40000 concentration on average LSM particle size, after initially dispersing (black cross) and after 72 h (orange circle); and (b) photographs of LSM dispersions stabilised with different mass fractions (relative to LSM) of PVP 360000 after standing for 1 h.

The oxygen-electrode in SOERs is typically a YSZ-LSM composite; consequently, there are two printing options:

i) formulate a composite YSZ-LSM ink; or

ii) formulate separate YSZ and LSM inks, and deposit sequentially to produce the electrode.

In the first instance, YSZ and LSM need to be co-dispersed, so the particles must not hetero-coagulate, *i.e.* should have like surface charge (negative). Printing this ink would give a comparable microstructure, and therefore comparable electrochemical performance, to that achieved from conventional powder mixing methods, validating inkjet printing as an alternative manufacturing route for SOERs.

In the second instance, by depositing the YSZ and LSM sequentially, they can be highly localised within the electrode, so the microstructure could be tailored and reproducible. However, due to the present limits of inkjet printing resolution, the triple phase boundary (TPB) density would be expected to be lower, compared to co-printing YSZ and LSM; however, all TPBs should be percolating. This technique presents a route to fabricating advanced microstructures for the next generation of oxygen-electrodes, as inkjet printing resolution is expected to improve in the future. Therefore, both composite YSZ-LSM and LSM inks would have practical utility. The remainder of this Chapter describes how these inks were formulated for inkjet printing. Their deployment for oxygen-electrode fabrication and electrochemical characterisation is the subject of later Chapters in this Thesis.

5.3.1. Materials and Methods

5.3.1.1 Colloidal Stability

$La_{0.8}Sr_{0.2}MnO_3$ (LSM) particles purchased from Fuel Cell Materials (USA) were dispersed in both water at pH 10 (aqueous formulation), adjusted with aqueous NH_3 to maximise the particle surface charge, and butanol (BtOH, organic formulation), to investigate which solvent would be most effective for inkjet printing. The electrostatic dispersants shown in **Table 16** were trialled for aqueous LSM dispersions, by addition at varying concentrations relative to the particle specific surface area.

The only dispersant to adsorb on LSM particles, and to reduce their rates of sedimentation was Aluminon, which was therefore taken forward for further zeta potential measurements. All other dispersants had no effect on dispersion stability.

Table 16. List of electrostatic dispersants, with their chemical description and manufacturer, trialled for aqueous, colloidal LSM.

Dispersant	Description	Manufacturer
Duramax D-3005	ammonium salt of an acrylic polymer	Rohm and Haas, USA
Dispex A40	ammonium salt of a polyacrylic acid	BASF, Germany
Ammonium citrate	ammonium salt of citric acid	Sigma Aldrich, USA
Darvan C	poly methyl methacrylate	Vanderbilt Minerals, USA
Tiron	sodium salt of a sulfonic acid	Sigma Aldrich, USA
Aluminon	aurintricarboxylic acid ammonium salt	Sigma Aldrich, USA

In BtOH, Butvar B98 (polyvinyl butaryl, PVB, molecular weight 70000-100000 kg $kmol^{-1}$, Sigma Aldrich, USA) was added as a dispersant and plasticiser at a concentration of 25 mg cm^{-3}, due to its:

i) 'simple' combustion during the sintering process, *i.e.* non-destructive to the printed structure;

ii) high effectiveness at low-concentrations to increase solvent viscosity, for printability (283).

Due to the low solubility of BtOH in H_2O (*ca*. 68 kg m^{-3} at 25 °C) (284), a BtOH-based YSZ ink was required for a composite YSZ-LSM formulation. YSZ was dispersed in BtOH,

stabilised by PVB; a concentration of 9 mg cm^{-3} was found to be sufficiently high. The solids loading of YSZ was 13 wt%, after centrifugation at 1300 RCF for 4 minutes, and filtering.

5.3.1.2 Printability

After colloidal stabilisation, the LSM PSD was narrowed by centrifugation for 4 minutes at 870 and 1200 RCF, for the aqueous and organic formulations, respectively, and subsequently syringe filtered. The resultant PSD was measured by DLS (in water), and for the YSZ dispersions, the particles used were identical to those in Section 5.1, so their PSD was like that reported previously, in Section 5.1.2.2.

For the aqueous LSM formulation, PEG 35000 (Sigma Aldrich, USA) was added at 25 mg cm^{-3} and allowed to dissolve over *ca*. 24 h. Immediately prior to printing, the alcohol ethoxylate Natsurf 265 (Croda Chemicals, UK) was added at a concentration of 0.2 mg cm^{-3} of the total volume of the ink.

For the BtOH formulation, the viscosity and surface tension of the ink were expected to lie within the printable range, so addition of further organic species was unnecessary.

To make the composite inks, appropriate quantities of each aqueous ink (YSZ ink formulation reported in Section 5.1) were added, for an ultimate LSM:YSZ ratio of 60:40.

5.3.1.3 Substrate Fabrication

The LSM and composite YSZ-LSM inks were inkjet printed onto a pre-sintered NiO-YSZ|YSZ substrate, fabricated as described in Section 5.1.

5.3.1.4 Preliminary Printing Experiments

A Dimatix DMC Series 10 pL nominal droplet volume printhead (Fujifilm, USA) was used to inkjet print the LSM formulations onto the pre-sintered YSZ. The diameter of the printhead nozzles was 21 μm. The drying time between each printed layer was 240 s, at an ambient temperature of 26 – 28 °C.

The droplet deposition pattern was a square lattice (*i.e.* a coordination number of 4 for each droplet) with a droplet overlap of 40 % for all printed structures. Both YSZ and (YSZ-)LSM layers were circular and approximately coaxial. The post-sintering diameter of the YSZ layer was 17 mm, and the diameter of the (YSZ-)LSM layer, was 6 mm.

5.3.1.5 Sintering and Microstructural Characterisation

The (YSZ-)LSM deposits were sintered separately to the pre-sintered electrolyte and supporting layer, and were therefore constrained laterally during sintering by the substrate, which preserved porosity within the oxygen-electrode without requiring a pore-forming template. Consequently, shrinkage of the structure during sintering occurred only vertically.

Due to the presence of organic species in all formulations, an intermediary combustion step at 600 °C (4 °C min^{-1}, 2 h) was used. In the case of the aqueous formulations, this was reduced to 550 °C. To prevent chemical reaction between the YSZ and LSM, sintering was limited to < 1300 °C (285). Therefore, the temperature was raised at 4 °C min^{-1} to 1200 °C, held for 3 h, and finally cooled to room temperature at 4 °C min^{-1}. Printed and sintered microstructures were characterised at high magnification as described in Section 5.1.1.6, and at low magnification optically.

5.3.2. Results and Discussion

5.3.2.1 Colloidal Stability

The mass-specific surface area of the LSM particles was measured as 6.32 m^2 g^{-1}. **Figure 49a** shows the variation of LSM zeta potential with pH, modified using nitric acid or ammonia, for acidic or basic conditions, respectively. The results agree with the trend shown in **Figure 47**, which implied the isoelectric point was *ca*. 3, although at such acidic conditions, dissolution of the constituent elements of LSM occurred, in conjunction with particle aggregation, reducing both accuracy and precision of the zeta potential results. However, at pH > 7, the zeta potential of LSM indicated colloidal stability. Therefore, LSM was dispersed in water at pH 9.5 (maximum zeta potential) at a solid loading of 20 wt%, but surprisingly, aggregation and sedimentation occurred immediately; therefore, a dispersant was required. To maintain thermodynamic stability and maximum surface charge, pH was maintained at 9.5 for all subsequent aqueous formulation experiments.

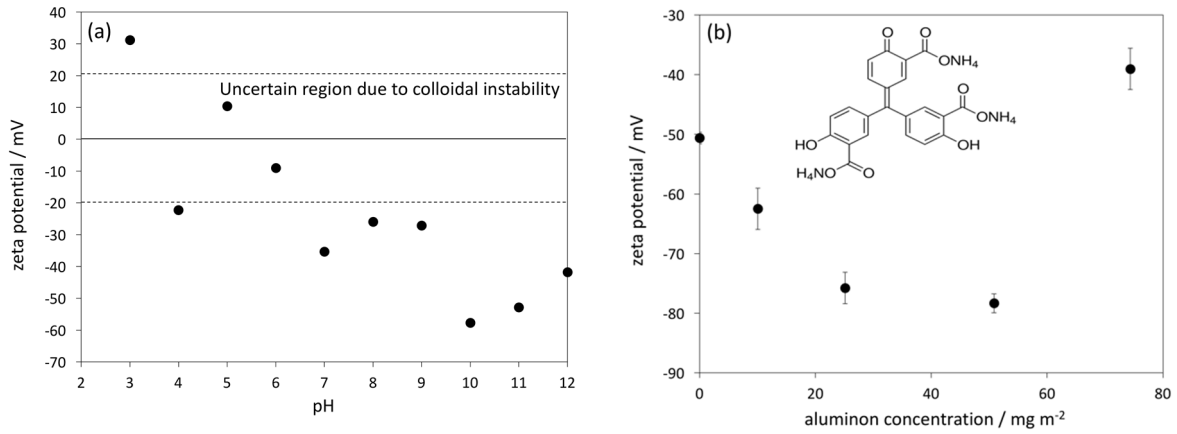


Figure 49. Variation of zeta potential of LSM particles with (a) pH; and (b) dispersed Aluminon concentration (chemical structure shown). Reproduced with permission from (280).

Figure 49b shows the variation of LSM zeta potential with Aluminon concentration in water adjusted to pH 9.5; zeta potential magnitude increased, with the maximum occurring at *ca*. 50 mg m^{-2} of LSM.

5.3.2.2 Printability

After centrifugation and filtration, the average LSM particle size was measured by DLS as 230 nm, as shown in **Figure 50**. The PSD was unimodal, with a standard deviation of 46 nm, which was sufficiently low to prevent nozzle blocking.

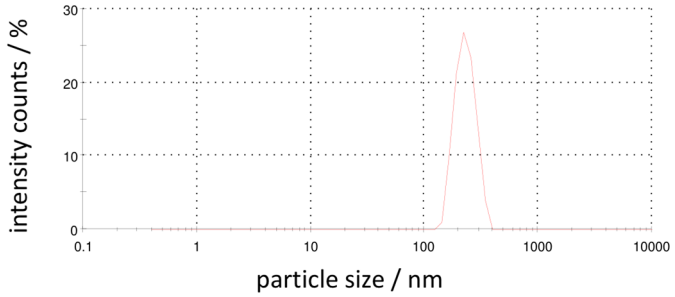


Figure 50. PSD of the LSM particles dispersed in water, after centrifugation and filtering.

To ensure rapid deposition of LSM, its mass fraction in the aqueous ink was adjusted to 5 wt%, post-centrifugation. Adding the PEG 35000 and Natsurf 265, and mixing with an appropriate volume of YSZ ink, the final ρ, μ, γ, and Oh^{-1} were 1.1 g cm^{-3}, 4.1 mPa s, 23 mN m^{-1}, and 5.6, respectively. The viscosity of the ink was mildly shear thinning, as shown in **Figure 51.**

The mass fraction of LSM in the organic formulation was adjusted to 6 wt%. With a PVB concentration of 15 mg cm^{-3}, the ρ, μ, γ, and Oh^{-1} were 1 g cm^{-3}, 7 mPa s, 19.6 mN m^{-1}, and

2.9, respectively. Addition of an appropriate quantity of the YSZ BtOH-based ink changed the physical properties to 0.91 g cm^{-3}, 8.34 mPa s (essentially Newtonian, shown in **Figure 51**), 19.6 mN m^{-1}, and 2.3, respectively. Therefore, the physical properties of all ink formulations lay within the printable range.

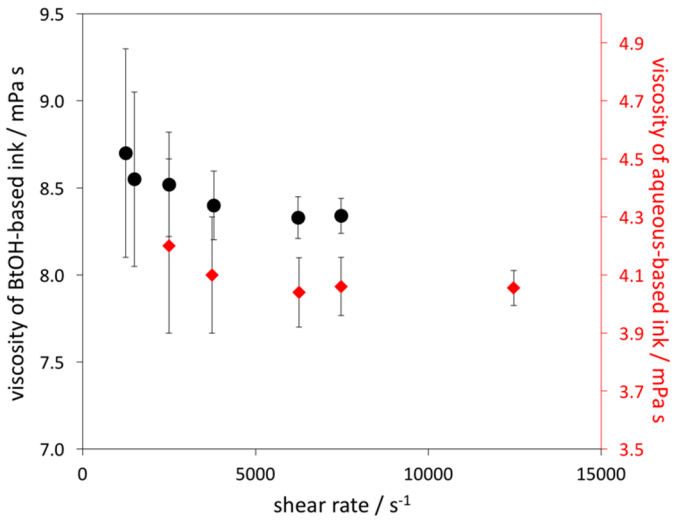


Figure 51. Viscosity variation with shear rate, for the composite YSZ-LSM BtOH (black) and aqueous (red)-based inks.

For the composite BtOH-based YSZ-LSM ink, We, Re, and $We^{0.5}Re^{0.25}$ were 34, 27, and 13, respectively. Satellites droplets were observed, but ultimately recombined with the main droplet, as shown in **Figure 71b**. The condition $We^{0.5}Re^{0.25} < 50$ was satisfied, so splashing was not expected to occur.

5.3.2.3 Preliminary Printing Experiments

The Dimatix DMC 10 pL printheads (Fujifilm, USA) permitted both negative and positive voltages to be applied, *i.e.* an expansion and contraction of the piezoelectric crystals in the printhead, respectively. The optimal voltage pulse profiles for the inks containing LSM are shown in **Figure 52**.

D_m for the aqueous and BtOH-based composite YSZ-LSM inks were measured as 60 and 100 μm, respectively. D_m for the aqueous and BtOH-based LSM inks were measured as 63 and 80 μm, respectively.

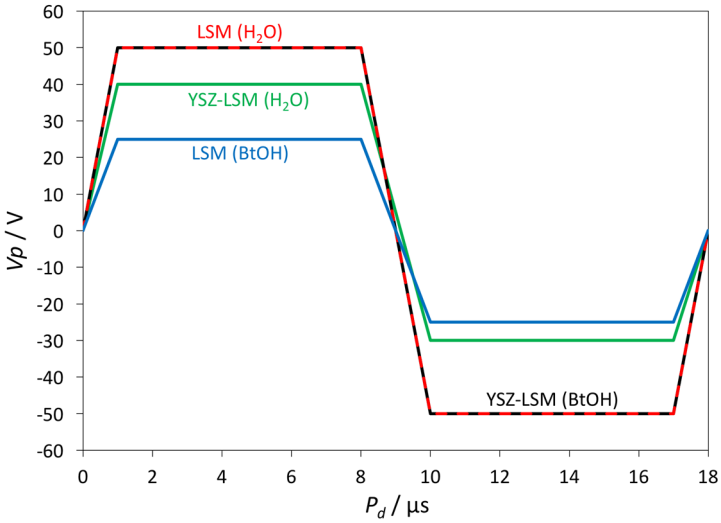


Figure 52. The optimal pulses for the inks containing LSM (blue and red), and YSZ-LSM (green, black), with solvents in parentheses.

5.3.2.4 Sintering and Microstructural Characterisation

After printing 100 layers of the aqueous-based YSZ-LSM ink onto the pre-sintered YSZ substrate, heat treatment resulted in the catastrophic failure of the deposited film, which occurred during the organics' combustion process at < 550 °C, as shown in **Figure 53**. An identical response was observed for the LSM aqueous-based ink.

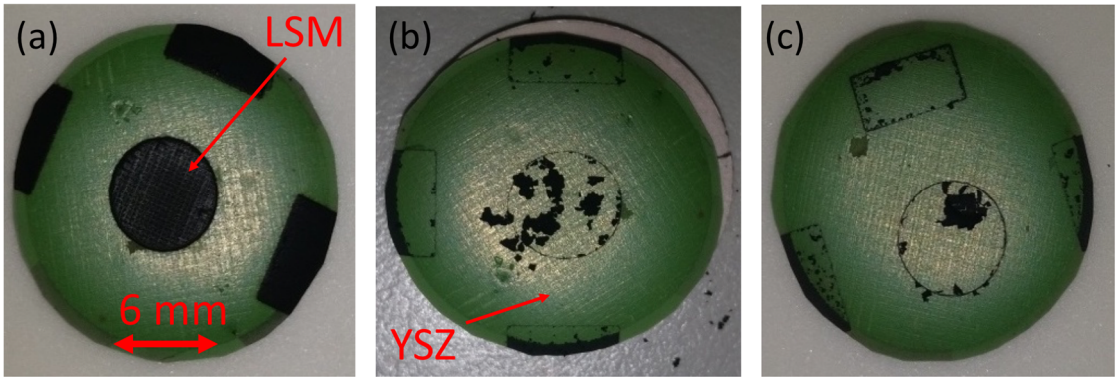


Figure 53. Photographs of the printed LSM-YSZ deposit from the aqueous-based ink (a) before heat treatment; (b) after organic additives combustion at 550 °C at 1 °C min^{-1}; and (c) after sintering at 1200 °C (different sample).

Mitigating the catastrophic failure by reducing the temperature ramp rate from 2 to 1 °C min^{-1} was ineffective; this problem was not due to the rate of loss of Aluminon during combustion (none was expected to be lost via evaporation during drying), as PVB had the greatest rate of loss of mass over temperature, of all effective dispersants, as shown in **Figure 54**, but did not destroy the film in the heat treatment step. Furthermore, the LSM appeared to have sintered

well to itself, upon raising the temperature to 1200 °C, but not to the pre-sintered YSZ substrate, as shown in **Figure 55**.

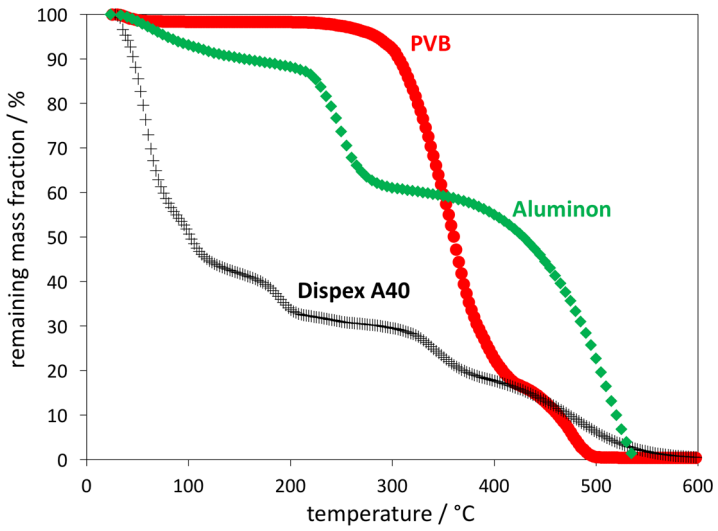


Figure 54. Thermogravimetric analysis (TGA) results of the effective dispersants.

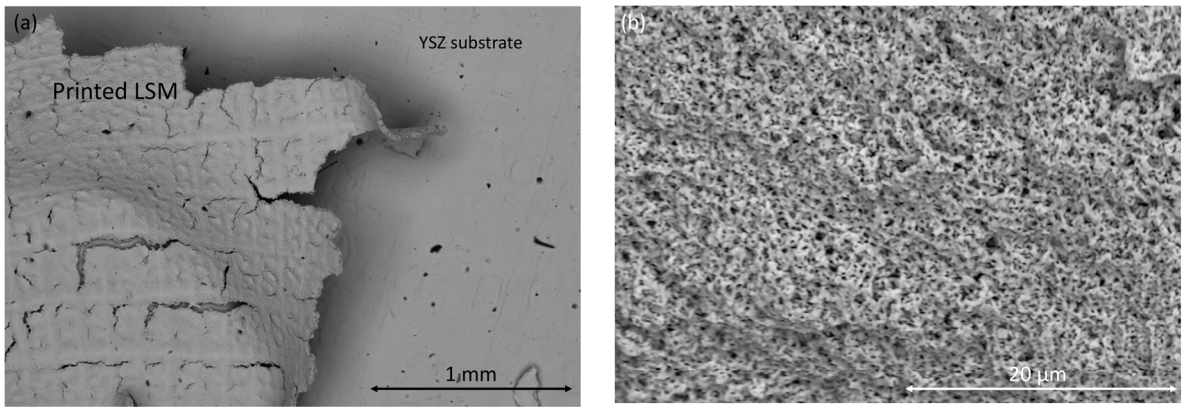


Figure 55. SEM surface photomicrographs of the sintered, aqueous-based LSM ink on printed YSZ at (a) low; and (b) high magnification.

The most significant difference between Aluminon and the other dispersants used was that it is a much smaller molecule, with a much higher density of C=C double bonds; therefore, the enthalpy of combustion may be comparatively greater. However, it could not concluded beyond a reasonable doubt why combustion of Aluminon destroyed the printed YSZ-LSM film. The same effect resulted with the pure LSM aqueous ink. Therefore, to achieve the desired defect-free layers, it was necessary to use the BtOH-based inks, because a suitable dispersant for the aqueous formulations could not be found.

After sintering 100 printed layers of the BtOH-based YSZ-LSM ink at 1200 °C, the structures shown in **Figure 56** resulted. The cross-sectional image shows the YSZ-LSM layer was *ca.* 20

µm thick, indicating that the thickness of a single printed layer was *ca.* 200 nm, *i.e.* a monolayer particle depth, prior to sintering. In addition, the NiO-YSZ and the YSZ-LSM layers appeared to be well-adhered to the YSZ electrolyte, without large defects. The surface SEM image shows that the outer part of the YSZ-LSM layer was highly porous, indicating that the formation of a dense 'skin' had been avoided, which was identified in Section 2.3.8 as the performance limiting feature of previously printed YSZ-LSM electrodes (252). The reasons why the skin formation was avoided are explored in the remainder of this Chapter.

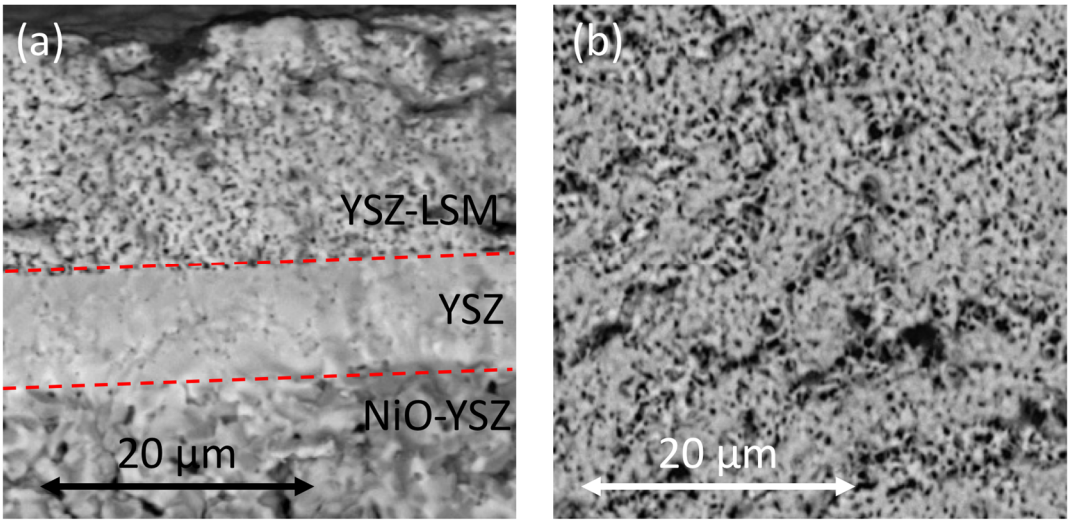


Figure 56. SEM photomicrographs of (a) side view of the sintered NiO-YSZ|YSZ|YSZ-LSM; and (b) surface view of the YSZ-LSM. Reproduced with permission from (280).

The 6 mm diameter of the printed YSZ-LSM electrode was >> D_m (100 µm), so may be considered a large expanse of film. Consequently, lateral flow through the film during drying may be neglected, *i.e.* evaporation is a vertical advection of the solvent, and hence there is a vertical particle flux towards the solvent – air interface, with the flow. Therefore, the diffusivity of particles within the film determined whether or not a skin would form; weak diffusion would result in a skin as advection >> diffusion (286), and consequently the packing density of particles would be expected to be increased, shown schematically in **Figure 57**. As mentioned previously, this effect could be exploited to increase the packing density in inkjet printed CGO barrier layers, as in Section 5.2.2.4.

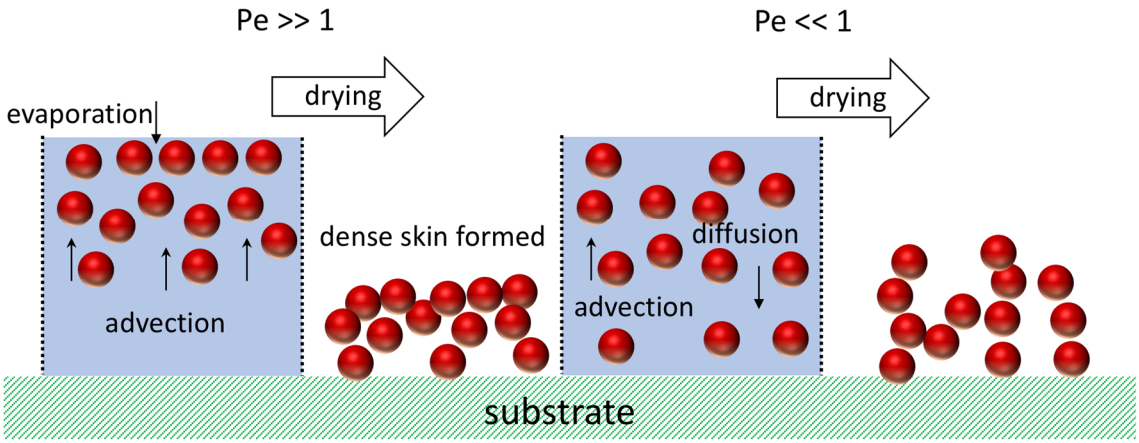


Figure 57. Schematic showing how a 'skin' forms when particle advection dominates.

Whether a skin forms may be predicted by considering the dimensionless Peclet Number (Pe), which is the ratio of particle advective to diffusive transport, and is defined in equation (77). When Pe >> 1, a skin is predicted to form, as particle advection dominates; the opposite is true for Pe << 1.

$$\mathrm{Pe} = \frac{H_{l0}\dot{E}}{D} \approx \frac{6\pi\mu r_p H_{l0}\dot{E}}{k_B T} \qquad (77)$$

Where D represents the particle diffusion coefficient, which can be calculated according to the Stokes-Einstein equation, assuming spherical particles and low Re, as shown. Therefore, r_p represents the particle radius, H_{l0} the initial film depth, $\dot{E}$ the rate of evaporation, μ the solvent viscosity, k_B the Boltzmann constant, and T the temperature of the system. In the previously published study on YSZ-LSM inkjet-printed electrodes (252), α-terpineol was the solvent, with a measured viscosity of 12 mPa s, compared to 8.3 mPa s for the YSZ-LSM ink in this study. Furthermore, although the rate of evaporation was not given, by calculating the equilibrium vapour pressure (P_{eq}) of each solvent at the relevant drying temperature (100 °C and 25 °C, for α-terpineol and BtOH, respectively) it may be inferred that it was greater than in this study (no convection assumed): at 298 K, P_{eq} for BtOH is 884 Pa (287), and at 373 K, P_{eq} for α-terpineol is 1679 Pa (288), *i.e.* α-terpineol is more volatile and expected to have a higher $\dot{E}$ at the reported temperature. r_p and H_{l0} were not given in the previous study, but it is probable that the combination of these effects mitigated film formation in this study by decreasing rates of advection of particles within the drying film. The subsequent sintering step exacerbated the problem by reducing porosity further, so optimising ink formulation is essential to achieve effective microstructures.

5.3.3. Conclusions

Composite and single phase YSZ-LSM and LSM printable inks were formulated for inkjet printing, using two solvents: water and butanol. Water was preferable, due to its environmental compatibility, but inkjet printed YSZ-LSM and LSM structures derived from aqueous-based inks catastrophically failed during sintering. Aluminon, the aqueous electrostatic dispersant for LSM, was responsible for the failure; however, the precise reasons were not identified. Unfortunately, another dispersant effective at stabilising LSM could not be found.

Butanol-based ink formulations, colloidally stabilised with the polymer polyvinyl butaryl, and with physical properties in the printable range, were used successfully to inkjet print YSZ-LSM films suitable for the oxygen-electrode for solid oxide electrochemical reactors, after sintering. The formation of a dense skin at the outer surface of the film (bulk gas interface), that has been reported previously in the literature, was avoided by optimising the ink formulation and drying processes, by ensuring that the dimensionless Peclet number (Pe) << 1. Therefore, these YSZ-LSM films are expected to have an electrochemical performance that exceeds that of inkjet printed electrodes reported previously in the literature, and is the subject of Chapter 7.

5.4. Nickel Oxide Ink

The most commonly used electronically conducting catalyst for solid oxide electrochemical reactor (SOER) fuel-electrodes is nickel due its abundance, high chemical stability, and rapid fuel reduction / oxidation kinetics. However, nickel is thermodynamically unstable when exposed to air at all ambient temperatures, and oxidises to form NiO, as shown by equation (78). Therefore, NiO is the most practical starting material for producing fuel-electrodes in SOERs, due to atmospheric exposure during fabrication. After electrode fabrication, the NiO is typically reduced, *in situ*, immediately prior to SOER electrochemical operation by H_2, or CO, via the reactions shown in equations (79) or (80), respectively. The concentration of CO / H_2 required (thermodynamically) for NiO reduction depends on oxygen mole fraction, H_2 / CO concentration, and temperature, and can evaluated using Ellingham diagrams published in the literature and the thermodynamics diagrams shown in **Figure 13**. The reduction kinetics are pseudo-first order with NiO concentration (289), and also depend on particle size.

$$\mathrm{Ni} + 0.5\mathrm{O_2} \rightarrow \mathrm{NiO} \qquad (78)$$

$$\mathrm{NiO} + \mathrm{H_2} \rightarrow \mathrm{Ni} + \mathrm{H_2O} \qquad (79)$$

$$\mathrm{NiO} + \mathrm{CO} \rightarrow \mathrm{Ni} + \mathrm{CO_2} \qquad (80)$$

Therefore, understanding the properties of dispersed NiO, which inevitably will be the particle surface phase, is more useful for formulating practical inks than Ni metal. A limited number of studies have been undertaken into the aqueous colloidal stabilisation of NiO, due to its difficulty.

A patent published in 2004 reported that it was not possible to find a common dispersant for nickel(II) oxide in water, so that to stabilise the colloidal particles they had to be coated with a material which could have its surface charge modified using a dispersant, *i.e.* ZrO_2 (290). However, this would be unsuitable for SOER electrode fabrication due to the necessity of exposed Ni within the electrodes, to form TPBs. Therefore, it is preferable to disperse NiO particles; **Figure 58a** shows that below *ca.* pH 5, Ni^{2+} dissolves, so pH must be maintained > 5. **Figure 58b** shows that the isoelectric point of NiO lies at *ca.* pH 3.5, so dispersed NiO is negatively charged at all practical pHs compatible with the printhead materials. An additional measurement was made, monitoring how the pH of NiO dispersions changed over time, and found that it would asymptote *ca.* pH 8 – 10 within 7 days. A consequence of this was that, regardless of initial pH, the zeta potential changed over time to become insufficiently large for colloidal stability, as shown in **Figure 58b**, therefore an effective dispersant species was required.

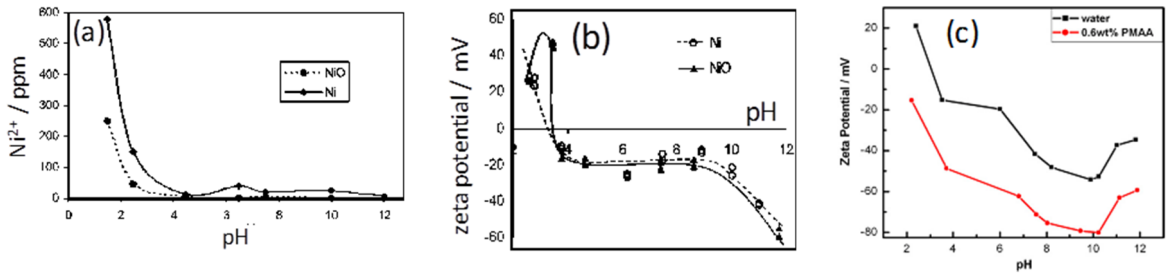


Figure 58. Variation with pH in water of (a) Ni^{2+} concentration; (b) zeta potential for Ni and NiO particles; and (c) NiO zeta potential dispersed with PMAA. (a) and (b) reproduced (adapted) with permission from (291), copyright (2005), American Chemical Society. (c) reproduced with permission from (292).

An effective dispersant was identified as the ammonium salt of a polymethyl methacrylate (PMAA, SD-03, Jiangsu Huagui Hi-Tech Ceramics Co., China). The optimal concentration for colloidal stability was established by determining the minimum viscosity, over a range of solid loadings, at 1.5 wt% PMAA compared to the mass of NiO (292); however, sufficient colloidal stability was achieved at 0.6 wt%, as shown in **Figure 58c**. Therefore, this was the starting point for formulating an aqueous NiO dispersion for inkjet printing. This Chapter considered only NiO dispersions for inkjet printing.

5.4.1. Materials and Methods

5.4.1.1 Colloidal Stability

NiO particles (Sigma Aldrich, USA) were initially dispersed in water, with varying pH (adjusted with nitric acid or aqueous ammonia), to first verify the results shown in **Figure 58b**, and then the zeta potential variation with polymethyl methacrylate concentration (Darvan-C, shown in **Table 16**) was measured. The mass loading of NiO was adjusted to 13 wt% in the inks.

5.4.1.2 Printability

After colloidal stabilisation with Darvan-C, the NiO dispersion was centrifuged at 1350 RCF for 1 minute, and subsequently syringe filtered. The resulting PSD was found by DLS. PEG 35000 was added at a concentration of 25 mg cm^{-3}, to adjust the viscosity, and Natsurf 265 was added at 0.2 mg cm^{-3} to adjust surface tension, immediately prior to printing.

5.4.1.3 Substrate

The substrate used was a pre-sintered YSZ disk 25 mm in diameter (Fuel Cell Materials, USA), *ca*. 250 μm thick.

5.4.1.4 Preliminary Printing Experiments

A Dimatix DMC 10 pL nominal droplet volume printhead (Fujifilm, USA) was used to inkjet print the NiO ink. Drying time between successive layers was 240 s, and the droplet deposition pattern was square (droplet coordination number 4). The droplet diameter overlap within the lattice was 25 % (at > 25 % 'flooding' occurred, *i.e.* flow of ink outside of the desired electrode perimeter).

5.4.1.5 Sintering and Microstructural Characterisation

The dilatometry behaviour of NiO particles was investigated in Section 5.1.2.4, and presented, with increasing temperature in **Figure 38a** and **Figure 38b**, for length change and shrinkage rate, respectively. The greatest rate of length change occurred at *ca*. 1000 °C; however, maximum densification occurred at *ca*. 1300 – 1400 °C. Therefore, the heat treatment profile for the printed NiO deposits included an organics combustion step at 600 °C for 2 h, with ramp rate 2 °C min^{-1}, followed by a sintering step at 1300 or 1400 °C (4 °C min^{-1}) for 3 h, followed

by cooling to ambient temperature at 5 °C min^{-1}. Microstructures were characterised at high magnification as described in Section 5.1.1.6, and low magnification, optically.

5.4.2. Results and Discussion

5.4.2.1 Colloidal Stability

The mass-specific surface area of the NiO particles was measured as 3.7 m^2 g^{-1}. **Figure 59a** shows the variation of NiO zeta potential with pH, in water. The isoelectric point appears to be at *ca*. pH 6 – 7, which is much less acidic than that found previously, as shown in **Figure 58b**. However, the magnitude of the zeta potential at pH 3 – 6 indicated colloidal instability, so these measurements are probably inaccurate, due to particle aggregation during measurements. Furthermore, the 'plateau' in zeta potential between pH 8 – 10 was reproduced, indicating the dominance of –Ni–(OH) surface species, and confirming the surface behaviour of NiO established previously (291). The zeta potential variation with Darvan-C concentration is shown in **Figure 59b**, at both pH 7.7 and 10.2. The zeta potential magnitude was greater at pH 10.2 than 7.7, and maximum stability was achieved at *ca*. 5 mg m^{-2} of the NiO.

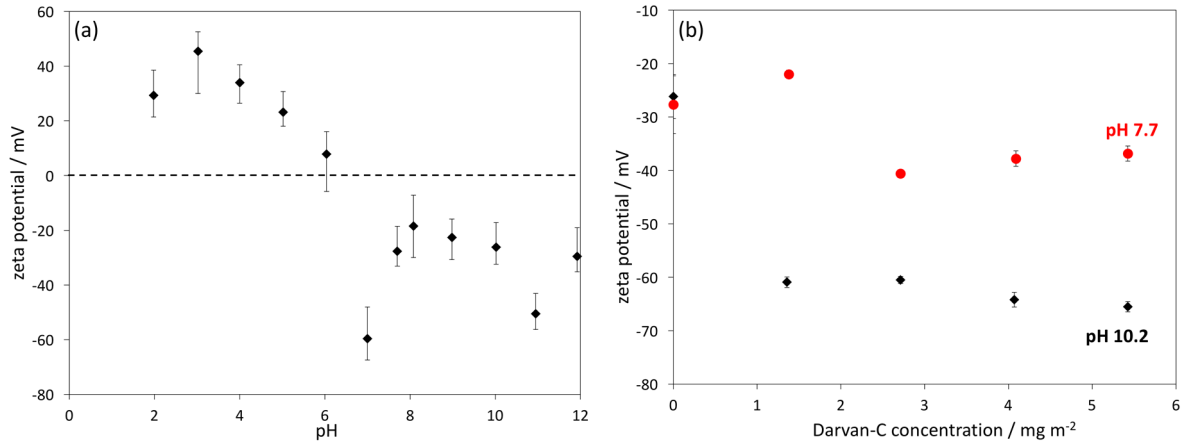


Figure 59. Variation of NiO zeta potential in water with (a) pH; and (b) Darvan-C concentration.

The zeta potential measurement at pH 7 (**Figure 59a**) is probably erroneous, as the isoelectric point was identified at *ca*. pH 7, so aggregation was probably responsible for invalidating that measurement. Hence, repeating the measurement at pH 7.7 (**Figure 59b**) indicated colloidal instability. Therefore, as the zeta potential values were greater in magnitude with Darvan-C, it was added for the final ink formulation. The colloidal stability for the final ink formulation was verified by the absence of aggregation and sedimentation over a period of weeks, and agreed with DLVO theory predictions (see Appendix 1: DLVO Theory for Aqueous Dispersions).

5.4.2.2 Printability

The PSD for the NiO particles was determined with the optimal Darvan-C concentration after centrifugation and filtering, with no other additives, and is shown in **Figure 60**. The PSD was unimodal, with an average particle size of 225 nm and a standard deviation of 20 nm. This was sufficiently low to avoid nozzle blocking.

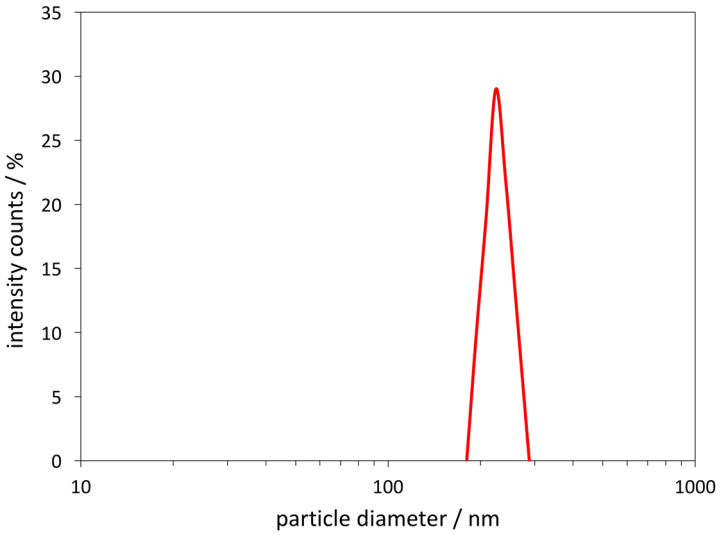


Figure 60. PSD of the NiO particles dispersed in water, by intensity counts.

The mass fraction of NiO was set as 13 wt% to facilitate rapid deposition. The final ρ, μ, γ, and Oh^{-1} were 1.147 g cm^{-3}, 3.4 mPa s (Newtonian, as shown in **Figure 61**), 27 mN m^{-1}, and 7.6, respectively.

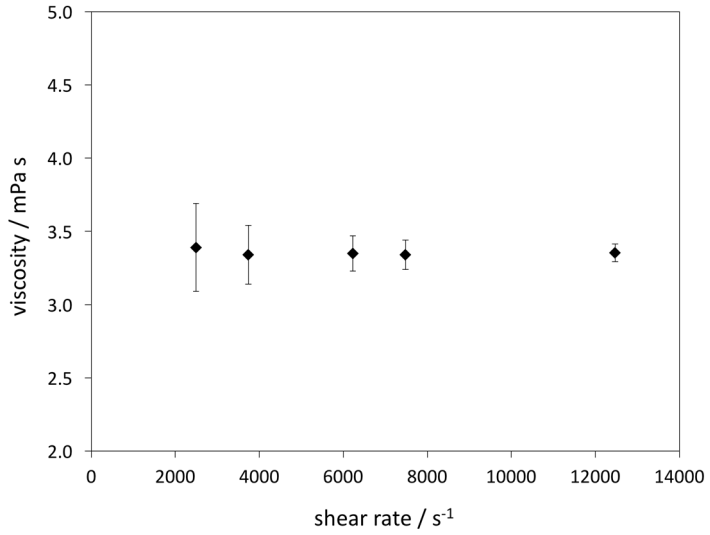


Figure 61. Viscosity of the aqueous NiO ink with varying shear rate.

Droplet ejection velocity was measured as 2.75 m s^{-1}, so We and Re values were equal to 6.7 and 19.4, respectively, violating the satellite droplet conditions in **Table 8**, so predictably

satellite droplets were observed, as shown in **Figure 62**. However, recombination of satellites with the main droplets occurred at *ca*. 150 μm from the nozzle plate, mitigating defect formation in the printing film by setting the printing height to > 150 μm. Splashing was not expected to occur as $We^{0.5}Re^{0.25}$ = 5.4, satisfying the condition in **Table 8**.

5.4.2.3 Preliminary Printing Experiments

The optimal droplet ejection ejection profile for the NiO ink was rise to V_p = 20 V over 1 μs, hold for 7 μs, then change to V_p = -20 V over 2 μs, hold for 7 μs, and finally rise back to 0 V, over 1 μs. The splat diameter of the ink on the YSZ substrate was 45 μm, and diameter overlap was 15 μm. 30 layers were deposited, and the resulting layer thickness (post-sintering at 1300 °C) was 210 nm (**Figure 66b**), *i.e.* a particle monolayer thickness.

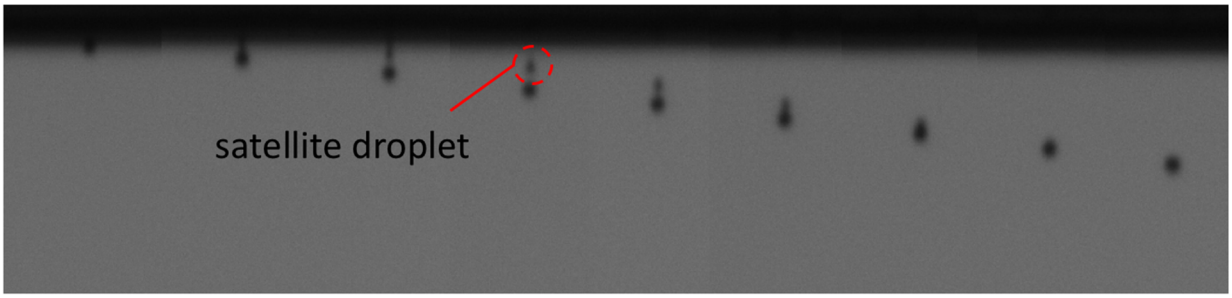


Figure 62. Time-lapse photographs of the NiO ink ejection, with intervals of 5 μs.

5.4.2.4 Sintering and Microstructural Characterisation

Heating the printed NiO deposit to 600 °C, dwelling for 2 h, and cooling to ambient temperature, both at 1 °C min^{-1}, left the printed layer completely intact, indicating clean, and non-traumatic, combustion of the Darvan-C and PEG 35000. Most of the Darvan-C had already evaporated during ink drying as it contained *ca*. 75 % water, as implied by data in **Figure 63**. The evaporation of the water content made it challenging to measure an initial mass reliably, which was the cause of the residual mass error at T > 600 °C, which should be zero.

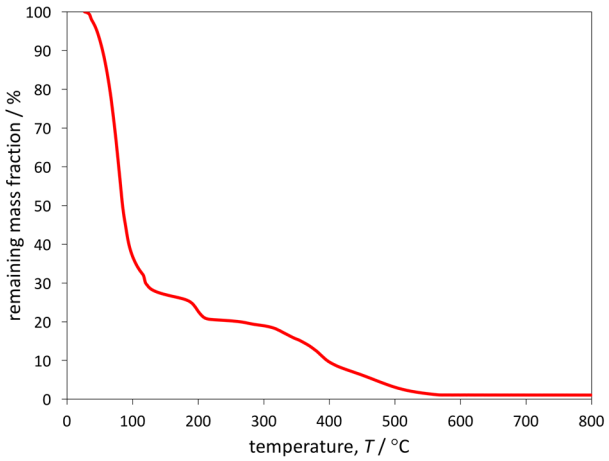


Figure 63. TGA measurements for Darvan-C.

Sintering the inkjet printed NiO films at 1300 and 1400 °C resulted in very different microstructures, as shown in **Figure 64**. At 1400 °C (**Figure 64b**), the NiO microstructure was significantly less porous than at 1300 °C (**Figure 64a**). In both instances, the sintering of NiO to the YSZ substrate was poor; however, the NiO phase appears to be largely contiguous at 1300 °C as shown in **Figure 64c**. Regions where NiO did not sinter to the YSZ would be electrochemically-inactive, and therefore should be avoided.

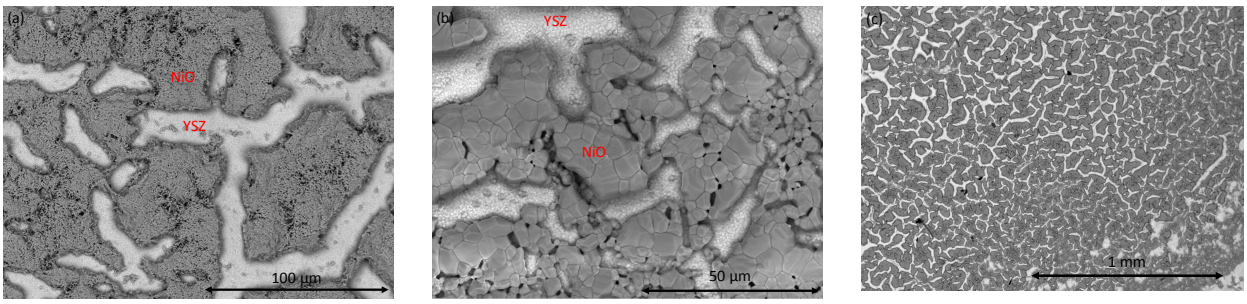


Figure 64. SEM surface view photomicrographs of the printed NiO deposit sintered at (a,c) 1300 °C; and (b) 1400 °C.

The photograph of the sintered NiO shown in **Figure 65a** shows that the outer regions of the printed NiO layer were 'flaky', *i.e.* did not adhere to the YSZ substrate during the sintering process. This indicated that the poor result derived either from the drying of the printed layers, which occurred from the outside radially inwards (observed optically), and / or from changes during sintering. After drying, and prior to sintering, the film was inspected optically and appeared to be defect-free, with the exception of a phase on the surface which was identified by Energy-dispersive X-ray Spectroscopy (EDX) as alumina, which presumably detached from the furnace interior lining, as shown in **Figure 65b**. Therefore, the failure mechanism of the film was expected to occur during sintering.

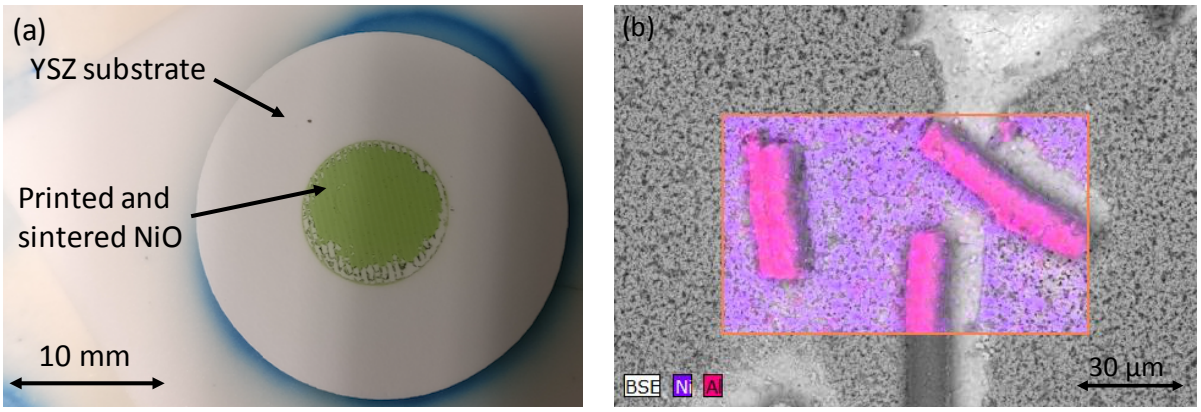


Figure 65. Top-down view (a) photograph of the sintered NiO (1300 °C) film on YSZ; and (b) SEM-EDX result showing alumina (pink) present on the surface.

The surface energy of NiO at 1300 °C (average of its different lattice planes) is *ca*. 2.2 J m^{-2} (293), whereas YSZ is *ca*. 1.25 J m^{-2} (294). Consequently, the primary sintering driving force throughout the (pure) NiO film (assuming that the YSZ phase is immobile) is NiO-NiO sintering, through a surface diffusion mechanism, given that the vapour pressure of NiO is negligible at 1300 °C, and bulk NiO diffusion is *ca*. 3 orders of magnitude lower than surface diffusion (295).

Assuming that during sintering at temperature T, the total change in NiO surface area >> YSZ, which is valid due to the low mobility of YSZ and much greater overall surface area of NiO particles, the work done during sintering (W) can be derived, as shown in equation (81).

$$W(T) = \gamma'_{\mathrm{NiO}}(T) \sum \Delta A_{\mathrm{NiO}} \qquad (81)$$

Where γ'_{NiO} is the surface energy of NiO at temperature T, and ΔA_{NiO} is the average change in surface area of a single NiO particle (*i.e.* summed over all particles). Considering an annulus within the cylindrical NiO printed film, equation (81) can be rewritten in terms of the work done within the annulus during sintering, positioned at radius r, of thickness δr, as shown in equation (82).

$$\delta W(r,T) = \gamma'_{\mathrm{NiO}}(T) \times (N(r)\Delta A_{\mathrm{NiO}}) \qquad (82)$$

Where $N(r)$ represents the number of particles within the annulus. $N(r)$ is equal to the total volume of particles divided by the volume of an individual particle, as shown in equation (83), assuming there is no variation with θ, *i.e.* the film varies radially.

$$N(r) = \frac{\varphi_0 \Delta V}{V_{particle}} = \frac{2\pi r \delta r H_0 \varphi_0}{{}^4/_3 \pi {r_{p,0}}^3} \quad (83)$$

Where φ, H, and r_p represent the particle volume fraction, film depth, and particle radius at pre-sintering conditions ('0'), respectively; ΔV represents the volume of the annulus. Substituting equation (83) into (82) results in equation (84), for the work done in the annulus, as shown.

$$\delta W(r,T) = {\gamma'}_{\mathrm{NiO}}(T).\Delta A_{\mathrm{NiO}}.\varphi_0 \frac{3}{2}\frac{H_0}{{r_{p,0}}^3} r \delta r \quad (84)$$

Taking the limit $\delta r \to 0$, results in equation (85) for the (compressive) force during sintering ($F(r,T)$).

$$\frac{dW(r,T)}{dr} = \mathrm{F}(r,T) = {\gamma'}_{\mathrm{NiO}}(T).\Delta A_{\mathrm{NiO}}.\varphi_0 \frac{3}{2}\frac{H_0}{{r_{p,0}}^3} r \quad (85)$$

Therefore, with increasing radial position, the compressive force that occurs in the NiO film due to particle sintering increases linearly, which could explain the why the printed NiO film lost adhesion to the YSZ substrate at *ca*. r = 4 mm. Therefore, this effect could be mitigated for a given sintering temperature by reducing film thickness (H_0) (*i.e.* fewer printed layers, reduced droplet diameter overlap), or modifying the ink properties to reduce the initial packing fraction (φ_0) *e.g.* by destabilising the dispersion during drying, or increasing the average particle size. Alternatively, increasing the surface area of YSZ, for example, by introducing a microstructure, would remove the assumption of comparatively negligible YSZ area, and significantly reduce the NiO-NiO compressive force resulting from sintering.

To support this hypothesis, two NiO films were printed onto identical YSZ substrates, 10 and 20 printed layers thick (identical ink and droplet overlap), with diameters 5 and 7 mm, respectively, and sintered with an identical temperature profile. No film cracking or flaking was observed in either; the 7 mm film is shown in **Figure 66a**. Both films adhered well to the substrate, post-sintering, (5 mm diameter film shown in **Figure 66b**) and appeared to be distributed uniformly over the YSZ (5 mm diameter film shown in **Figure 66c**). Small alumina particles were present on the NiO surface, as above, so during sintering the samples should be covered within the furnace to prevent this from occurring in the future.

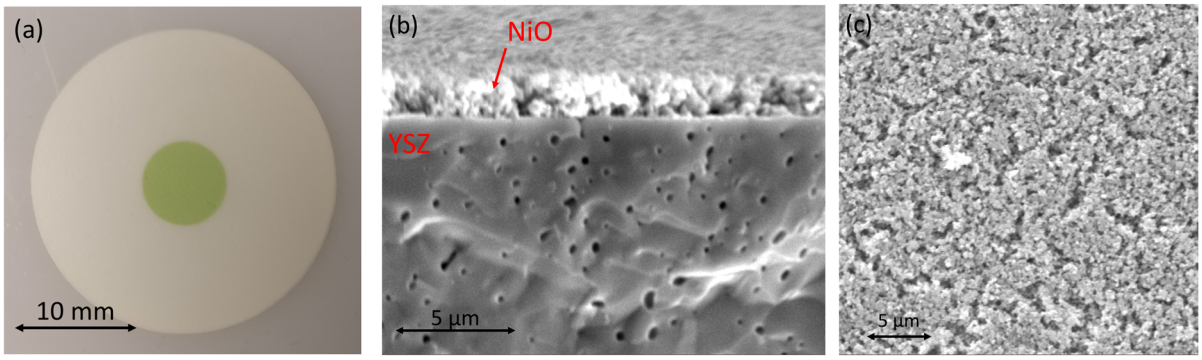


Figure 66. Post-sintering (a) photograph; (b) cross sectional; and (c) surface view SEM photomicrographs of the NiO films. Dr. Tao Li, Imperial College London, performed the SEM experiments in this instance (JEOL JSM-5610LV, Japan, 20 kV beam).

5.4.3. Conclusions

A colloidally-stable NiO dispersion in water was developed, using a polymethly methacrylate electrostatic dispersant, with viscosity and surface tension adjusted by polyethylene glycol and an alcohol ethoxylate, respectively. The aqueous dispersion was inkjet printed onto a pre-sintered YSZ substrate, and subsequently sintered at 1300 and 1400 °C. Increasing the sintering temperature decreased microstructure porosity, which is less favourable for SOER electrodes as the interfacial TPB density would be decreased. As the NiO densified during sintering, it detached from the substrate with increasing radial position. Analysis revealed that detachment occurred because of the significantly higher NiO surface area compared to the YSZ surface area, and consequently, the printed NiO film was constrained in height and radius to prevent this occurring.

6. Inkjet Printed YSZ Electrolyte

Chapter Summary

This Chapter reports inkjet printing results for the optimised aqueous YSZ ink developed in Section 5.1, deployed to fabricate the electrolyte of an electrolyser comprising: NiO-YSZ|YSZ (printed)|YSZ-LSM|LSM, operating with CO/CO_2. The completed solid oxide electrochemical reactor was characterised between 718 – 809 °C, and gave a comparable performance to electrolysers with electrolyte fabricated by conventional methods.

Note Concerning Author Contributions:

Dr. Lisa Kleiminger, while a post-doctoral researcher at Imperial College London, built the experimental equipment and performed the electrochemical characterisation for the SOERs reported in this section, as part of my training on the electrochemical characterisation equipment. I fabricated all SOERs characterised in this section by formulating and printing the YSZ ink, brush coating the YSZ-LSM electrode and LSM current collection layer, and finally sintering the structures. This section is reproduced largely from Farandos et al., 2016 (145).

6.1. Introduction

Having formulated an aqueous, printable YSZ ink ('Ink 1') as described in Section 5.1, the next step was to validate its applicability as an electrolyte for solid oxide electrochemical reactors (SOERs). In this Chapter, YSZ layers were deposited by inkjet printing and used as electrolytes for CO_2 electrolysis. The reactions occurring at the anode and cathode are shown in equations (37) and (38), respectively.

6.2. Materials and Methods

6.2.1. Reactor Fabrication

Twelve layers of Ink 1 (composition reported in Section 5.1.1.5) were inkjet printed onto a NiO-YSZ substrate, fabricated as described in Section 5.1.1.3, using a Dimatix Sapphire QS-256/30 AAA printhead (Fujifilm, USA). The printer settings were $V_p = 80$ V and $P_d = 13$ μs, including an increase and decrease time of 2 and 5 μs, respectively, at a droplet ejection frequency of 2.8 – 5 kHz. The printed layers and substrate were co-sintered, according to the temperature profile described in Section 5.1.2.4.

A composite LSM-YSZ α-terpineol-based paste (Fuel Cell Materials, USA) was brush-coated onto the electrolyte and allowed to dry at *ca*. 20 °C, followed by a coating of a LSM α-terpineol-based paste (Fuel Cell Materials, USA) to aid current collection. After drying, the LSM-YSZ and LSM layers were co-sintered at 1100 °C for 3 h, with temperature ramp rates of 4 °C min^{-1}.

6.2.2. Electrochemical Characterisation

Figure 67 shows schematically the equipment for 4-probe electrochemical characterisation, using the procedures described in **Table 13** to mount the cells. To prepare the fuel-electrode for measurements, NiO was reduced to Ni, as shown by equation (78) at 670 °C in a 25-75 H_2-He gas atmosphere for 2 h after being heated at 4 °C min^{-1} in a pure He atmosphere. After NiO reduction, the SOER was heated sequentially to the operating temperatures: 718, 764, and 809 °C, monitored by a K-type thermocouple. The operational gas feed molar composition was 9/1 CO_2/CO with 40 cm^3 min^{-1} total flow rate. The LSM-YSZ oxygen-electrode was exposed to static air throughout.

To characterise the cells electrochemically, the potential difference response to linearly scanned applied current was measured, as was the electrochemical impedance at open circuit potential difference (OCPD), with a RMS amplitude of 0.01 V over a frequency range 10^5-0.1 Hz.

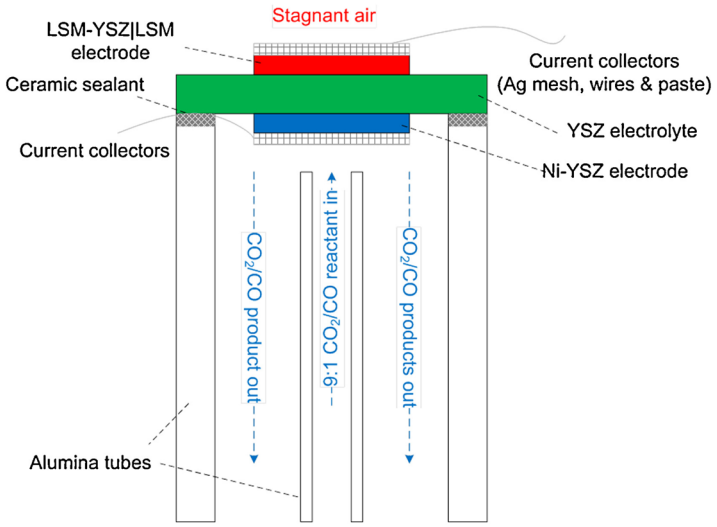


Figure 67. Planar CO_2(-CO)|Ni-YSZ|YSZ|YSZ-LSM|LSM|O_2 cell experimental assembly. Reproduced with permission from (145).

6.3. Results and Discussion

6.3.1. Reactor Fabrication

As shown in **Figure 68**, the printed YSZ electrolyte layer was dense, crack-free, and adhered well to the Ni-YSZ substrate. The shrinkage of the substrate and electrolyte that occurred during (co-)sintering helped to minimise porosity in the electrolyte (*ca*. 30 % shrinkage laterally). After sintering, the total thickness of the printed electrolyte layer was 23 µm, corresponding to *ca*. 2 µm for each of the 12 printed layers; hence, there is scope for decreasing the electrolyte layer thickness, without compromising gas-tightness, so enhancing electrochemical performance.

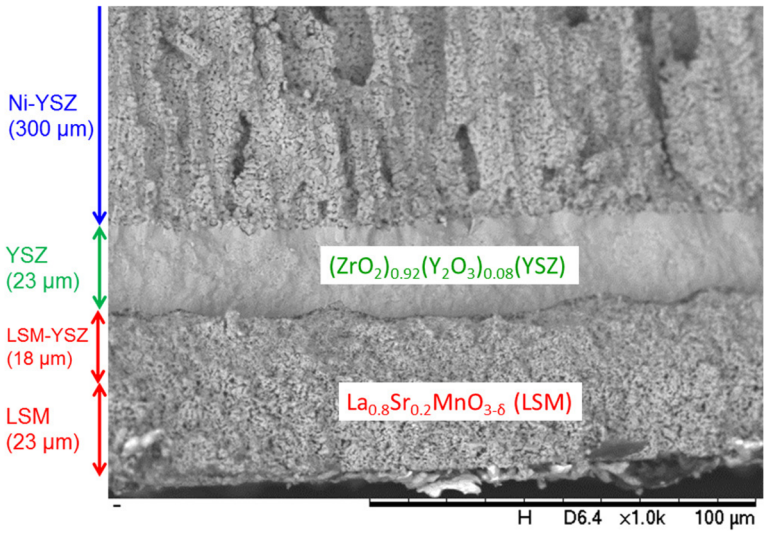


Figure 68. SEM photomicrograph of the cross section of the electrolyser. Reproduced with permission from (145).

6.3.2. Electrochemical Characterisation

The OCPDs were measured as 0.88 - 0.84 V, at 718 °C - 809 °C, respectively, which were close to the theoretically calculated values (296). Current densities achieved at the thermo-neutral potential difference (*ca*. 1.5 V, see Section 2.2.4.2) were between −0.35 and −0.78 A cm^{-2}, as shown in **Figure 69**.

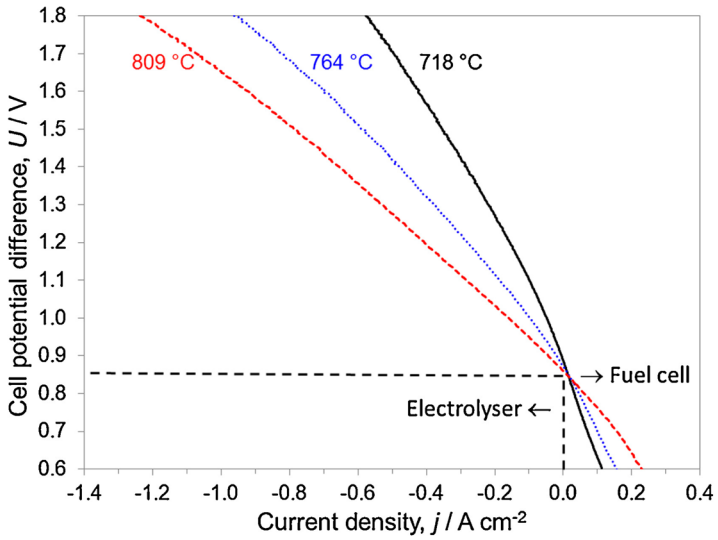


Figure 69. Effects of temperature and applied current density on CO_2(-CO)|Ni-YSZ|YSZ|YSZ-LSM|LSM|air cell potential differences. Reproduced with permission from (145).

As shown in **Figure 70**, the reactor performance, as indicated by the area specific resistance, was dominated by electrode polarisation contributions, due mainly to the tape-casted Ni-YSZ substrate porosity not yet being optimised, so restricting gas diffusion limited current densities.

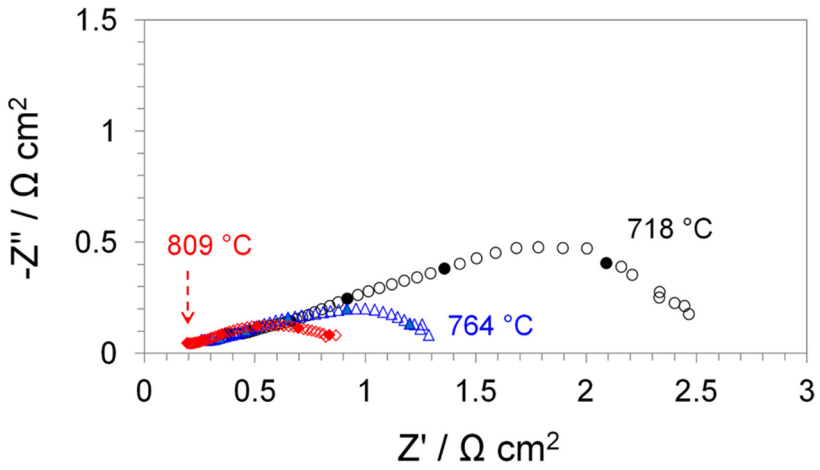


Figure 70. Electrochemical impedance spectra of CO_2(-CO)|Ni-YSZ|YSZ|YSZ-LSM|LSM|air cell at OCPD; filled markers indicate frequency decades (10^5 – 0.1 Hz). Reproduced with permission from (145).

6.4. Conclusions

Planar YSZ electrolyte structures 23 μm thick were fabricated by inkjet printing using the optimised ink formulation and YSZ sintering profile developed and reported in Section 5.1. The SOER was completed by brush coated layers of YSZ-LSM and LSM oxygen-electrode and current collector, respectively. The performance of a Ni-YSZ|YSZ (printed)|YSZ-LSM|LSM electrolyser for CO_2 reduction was determined using a CO_2/CO mixture with a molar ratio of 9/1; at 809 °C, a current density of -0.78 A cm^{-2} was achieved at 1.5 V. Electrolysis performance was dominated by SOER polarisation, primarily due to the microstructure of the fuel electrode support being sub-optimal. Therefore, in the future, the microstructure of the substrate should be improved, and the electrolyte thickness decreased by printing fewer layers.

7. Inkjet Printed YSZ-LSM Electrode

Chapter Summary

This Chapter describes the deployment of the optimised YSZ-LSM ink, developed and reported in Section 5.3, to inkjet print the oxygen-electrode for solid oxide electrochemical reactors with the arrangement: Ni-YSZ|YSZ (printed)|YSZ-LSM (printed)|LSM. Fuel cell and electrolyser mode performances were determined for dry H_2, and CO/CO_2, respectively, between 707 – 788 °C. The effect of oxygen-electrode sintering temperature on microstructure and resulting electrochemical performance was investigated.

Note: this Chapter is largely reproduced from Farandos et al., 2018 (280).

7.1. Introduction

As reported in Chapter 6, an inkjet printed YSZ electrolyte was characterised electrochemically in the solid oxide electrochemical reactor (SOER): Ni-YSZ|YSZ (printed)|YSZ-LSM|LSM in electrolysis mode, operating with CO/CO_2 gas mixtures. The electrolysis performance was comparable to reactors with a YSZ electrolyte fabricated by conventional powder-mixing methods. However, the electrolyte was 23 μm thick, which was larger than other inkjet printed YSZ electrolytes (168, 170, 243, 247), suggesting that by decreasing the electrolyte thickness, ohmic potential losses could be decreased, especially at lower temperatures. Furthermore, printing additional functional layers, *i.e.* the electrodes, can minimise waste during fabrication, and increase the consistency of electrochemical performance between different SOERs, due to the high reproducibility of inkjet printing and long-term ink homogeneity (proven high colloidal stability).

Hitherto, a single study on the electrochemical performance of an inkjet-printed YSZ-LSM composite oxygen-electrode has been reported (252). Notably, the SOER performance was limited by dense film formation at the outer surface of the electrode ('skin'), which decreased the rates of O_2 diffusion to active triple phase boundaries (TPBs) near the electrolyte. If this SOER was adapted to operate in electrolysis mode, the dense film could become particularly problematic by preventing O_2 gas evolved at the anode from escaping, resulting in an increase in O_2 partial pressure within the electrode, diminishing kinetics, and possibly causing catastrophic failure throughout the electrode over operational times required for seasonal energy storage (297).

This Chapter concerns the deployment of the optimised YSZ-LSM ink developed in Section 5.3, to inkjet print the oxygen-electrode of the SOER: Ni-YSZ|YSZ (printed)|YSZ-LSM (printed)|LSM, in which the YSZ-LSM electrode does not have a dense outer skin. The objective was to determine whether SOERs fabricated by inkjet printing could achieve performances, in H_2 fuel cell mode, and when fed with CO/CO_2 in electrolyser mode, that exceeded those produced by conventional powder mixing techniques. The electrochemical reactions for these operations are shown in equations (37) - (39).

7.2. Materials and Methods

7.2.1. Substrate Fabrication*

YSZ and NiO (Fuel Cell Materials, USA) were used as supplied. Polyethersulfone (PESf) (Radal A300, Ameco Performance, USA), 30-dipolyhydroxystearate (Arlacel P135, Uniqema),

and dimethyl sulfoxide (DMSO, HPLC grade, VWR) were used as the polymer binder, dispersant, and solvent, respectively.

The NiO-YSZ substrate was fabricated via a phase inversion-assisted casting process, like that described in Section 5.1.1.3. Firstly, the ceramic powders were mixed with DMSO and dispersant, then milled for 48 h with a planetary roll miller (SFM-1 Desk-top Miller, MTI Corporation, USA). The mixing continued for another 48 h after adding the polymer binder to ensure homogeneity of the dispersion, which had a composition of 24.4 wt% YSZ, 36.7 wt% NiO, 30.6 wt% DMSO, 7.6 wt% PESf, and 0.6 wt% Arlancel P135. Finally, the dispersion was degassed under vacuum, with stirring.

The NiO-YSZ substrate was then prepared by casting the suspension onto a glass plate at *ca.* 20 °C, before being immersed in a coagulation bath of de-ionised water for *ca*. 24 h, and finally air-dried. The casting knife height was set at 1 mm.

* The substrate was produced by Dr. Tao Li, Imperial College London.

7.2.2. Electrolyte Fabrication

It was preferable to fabricate cells with thin electrolytes, to decrease ohmic potential losses, but also to maintain ≥ 4 printed layers (1 in each of the 'positive' and 'negative' x and y printing directions) to increase the probability that defects resulting from missed droplet ejections were covered by droplets in subsequently printed layers. Therefore, the optimised YSZ ink formulation, developed and reported in Section 5.1, was modified by decreasing its mass fraction to 19 wt%. This reduced the ink density to 1.23 g cm^{-3}, decreasing the Oh^{-1} number to 8.2; the surface tension and viscosity were unchanged.

Four layers of this ink were inkjet printed onto the substrate using the Dimatix QS-256/30 AAA printhead (Fujifilm, USA). The splat diameter for the YSZ ink was 60 μm, and a droplet overlap of 20 μm was used, with a square droplet deposition lattice. The ejection pulse V_p = 75 V, with P_d = 11.5 μs, including a rise and fall time of 1.5 and 5 μs, respectively. The droplet ejection frequency and resultant printhead velocity were 5 kHz and 200 mm s^{-1}, respectively.

To co-sinter the substrate and electrolyte, the NiO-YSZ|YSZ structure was heated to 600 °C at 2 °C min^{-1} for 2 h to combust organics, and then ramped at 15 °C min^{-1} to 1450 °C to co-sinter the YSZ particles with the substrate for 5 h, followed by cooling to room temperature at 2 °C min^{-1}. Sintering temperature was reduced from 1500 to 1450 °C as it maintained highly-dense

electrolytes, while reducing the extent of nickel oxide particle coarsening that occurs at high temperatures (298).

To prevent bending due to thermal expansion differences between the composite NiO-YSZ substrate and pure YSZ electrolyte, each sample was constrained above and below by dense, sintered YSZ pellets (25 mm diameter, 250 μm, Fuel Cell Materials, USA).

7.2.3. Oxygen-electrode Fabrication

After co-sintering the NiO-YSZ|YSZ (printed) structure, 100 layers of the optimised BtOH-based YSZ-LSM ink developed and reported in Section 5.3 were printed onto the NiO-YSZ|YSZ structure using the Dimatix DMC 10 pL printhead (Fujifilm, USA) to fabricate the oxygen-electrode, 6 mm in diameter (5 samples in total). Different printheads were used for the YSZ and composite YSZ-LSM inks to mitigate contamination. Printhead selection was a consequence of availability, historical use, and printer compatibility. The splat diameter and droplet overlap were 100 and 50 μm (square droplet deposition lattice), respectively. The optimal droplet ejection pulse was reported in **Figure 52**. The droplet ejection frequency and resultant printhead velocity were 1.5 kHz and 80 mm s^{-1}, respectively. This was lower than that used for the YSZ ink because the QS-256/30 AAA printhead is constructed to a higher quality than the DMC 10 pL printhead, not because of significant differences in ink printability.

The resulting electrode was heated (unconstrained above) to 600 °C at 2 °C min^{-1} for 2 h, then sintered at 1100 or 1200 °C at 4 °C min^{-1} and held for 3 h, and finally cooled to room temperature at 4 °C min^{-1}.

7.2.4. LSM Current Collection Layer Fabrication

On top of the inkjet printed and sintered LSM-YSZ layer, a porous LSM layer was brush-coated on using an α-terpineol-based paste (Fuel Cell Materials, USA). This was left to evaporate in stagnant air at 20 °C, which took approximately 4 h, then heated at a ramp rate of 4 °C min^{-1} to 1100 °C for 3 h.

7.2.5. Electrochemical Characterisation

The SOER was mounted using the procedures described in **Table 13**, and characterised electrochemically using the same equipment as described in Chapter 6, and shown schematically in **Figure 67**. NiO was reduced to Ni for 2 h in a binary He and H_2 mixture at 707 °C (4 °C min^{-1} temperature gradient), at flow rates 30 and 7.5 cm^3 min^{-1}, respectively. Afterwards, the He supply was switched off, and the H_2 flow rate was increased to

20 cm^3 min^{-1} for an additional hour. The O_2 electrode was exposed to static air throughout. Electrochemical characterisation was conducted under both fuel cell mode (pure, dry H_2 at 20 cm^3 min^{-1}), and subsequently electrolyser mode (CO - CO_2 mixture with 4 - 36 cm^3 min^{-1} flow rates, respectively (10 % CO)) at operating temperatures of 707, 752, and 788 °C. Electrochemical impedance spectroscopy (30 mV p-p amplitude) at open circuit potential difference between 10^5 – 10^{-1} Hz, and experiments varying cell potential (20 and 60 mV s^{-1}) were carried out for electrochemical characterisation. The duration for a single SOER electrochemical characterisation was *ca*. 12 hours, after reaching the NiO reduction temperature. This included 3 hours for NiO reduction, and 4.5 hours each for fuel cell and electrolyser tests.

7.3. Results and Discussion

7.3.1. Reactor Fabrication

Figure 71a shows optical time-lapse images of the ejected droplets for the YSZ ink, with intervals of 10 µs. Initially, large satellite droplets formed, and coalesced at *ca.* 570 µm from the nozzle plate to form single droplets 25 pL in volume; droplet ejection velocity was measured as 4.75 m s^{-1}. The working height, *i.e.* the distance from the substrate to the nozzle plate during printing, should be greater than the length at which a single spherical droplet forms; therefore, the working height for printing the electrolyte was 0.6 mm.

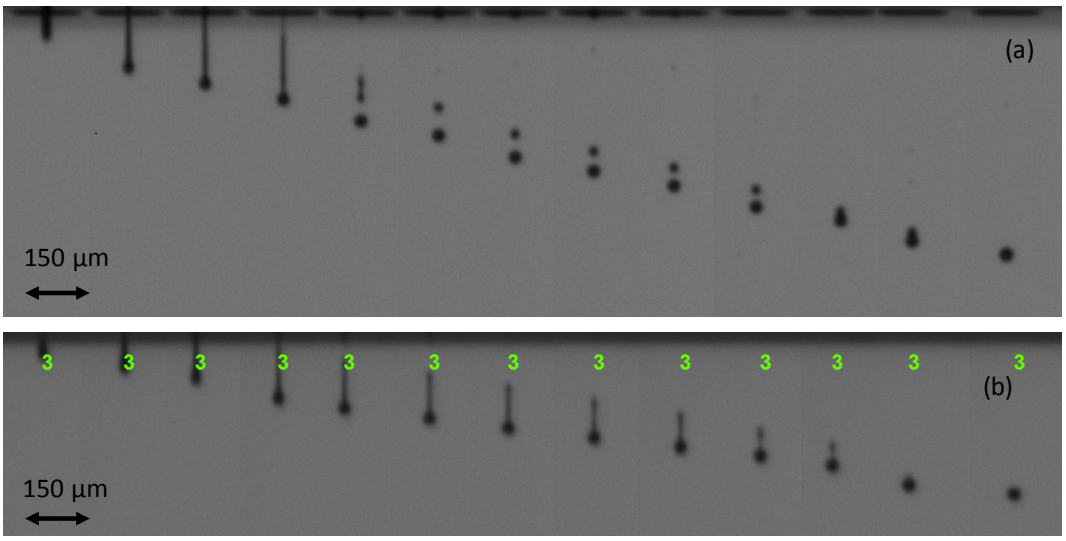


Figure 71. Droplet photographs of the ejected (a) YSZ; and (b) YSZ-LSM inks from a single nozzle, with time intervals of 10 and 5 µs, respectively. Nozzle number ("3") of the printhead

in (b) is shown, and could not be removed from the images. Reproduced with permission from (280).

Figure 71b shows optical time-lapse images of the ejected droplets for the YSZ-LSM ink, with intervals of 5 μs between each droplet. A large filament was observed for 55 - 60 μs after ejection, after which it combined with the main droplet, 10 pL total volume, at *ca.* 350 μm from the nozzle plate. The droplet velocity was measured as 5.9 m s^{-1}. The working height was 0.4 mm.

Figure 72 shows SEM photomicrographs of two SOERs after electrochemical characterisation; one in which the YSZ-LSM electrode was sintered at 1100 °C (a, c), and another sintered at 1200 °C (b, d). Large, finger-like pores penetrated through most of the Ni-YSZ supporting layer, facilitating gas transport. The distance between the top of the finger and the electrolyte was *ca.* 150 μm. It is important to prevent this thickness from being too low (< 100 μm) as the differential in shrinkage rates between the fingers and the rest of the support layer can result in localised bending, resulting in bumps in the electrolyte over the fingers.

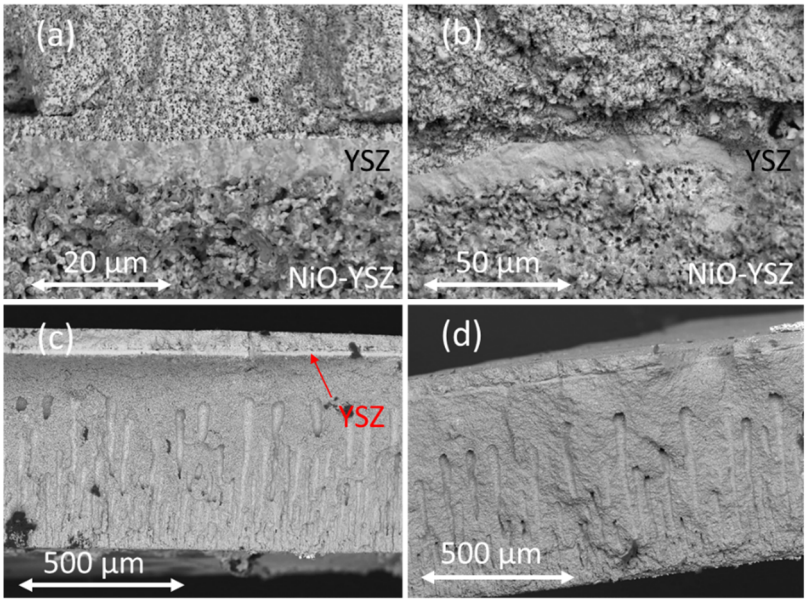


Figure 72. Side view SEM photomicrographs of the SOERs, post-testing; the YSZ-LSM electrode was sintered at 1100 °C (a,c) and 1200 °C (b,d). Reproduced with permission from (280).

The YSZ electrolyte was dense and 9 μm thick, which was comparatively thicker than other inkjet printed electrolytes, but < 50 % of that reported in Chapter 6. Therefore, it is still possible to further decrease the ohmic potential loss due to the electrolyte, by decreasing the electrolyte

thickness, *e.g.* by decreasing solids loading in the precursor ink, and / or droplet overlap during printing.

The LSM current collection layer appears to be well-adherent to the YSZ-LSM layer, so should be effective at providing high lateral electronic conductivity.

7.3.2. Electrochemical Characterisation

7.3.3. Hydrogen – Air Fuel Cell Operation

Dry H_2 was fed to the reactors in fuel cell mode at 707, 752, and 788 °C, with the oxygen-electrode exposed to static air throughout. The measured OCPD at each (ascending) temperature for the SOERs sintered at 1100 °C was 1.075 V, and for the SOERs sintered at 1200 °C was 1.027, 0.98, and 0.965 V, respectively. This indicated that the SOER sintered at 1100 °C was gas-tight, and that the lower than theoretically-predicted OCPD in the latter case was probably caused by a leak originating in the sealant as electrolytes were prepared identically. **Figure 73** shows power density curves, and Nyquist plots for SOERs with YSZ-LSM electrodes sintered at 1100 and 1200 °C are shown in **Figure 74**.

Maximum power densities for cells with the YSZ-LSM electrode sintered at 1100 °C were greater than those for the cells sintered at 1200 °C. Over the range of cell potential differences used, mass transport control was not observed under any conditions on increasing flow rates, so fuel utilisation was non-limiting. YSZ-LSM electrode sintering temperature had a significant effect on the electrode microstructure, with finer particles and pores being expected at lower sintering temperatures, increasing the triple phase boundary (TPB) density (299). For all tested cells, the power densities for the oxygen-electrodes sintered at 1100 °C were greater than those sintered at 1200 °C, as shown in Appendix 9: Electrochemical Characterisation of YSZ-LSM SOERs, probably due to greater TPB densities, as at 1200 °C electrode porosity was lower.

The formation of secondary, insulating, phases due to reaction between YSZ and LSM was not expected to occur at the sintering temperatures and times used (300). Peak power densities of the cells with YSZ-LSM electrodes sintered at 1100 °C and 1200 °C were 0.25, 0.45, 0.69 W cm^{-2}, and 0.16, 0.27, 0.46 W cm^{-2}, at 707, 752, and 788 °C, respectively.

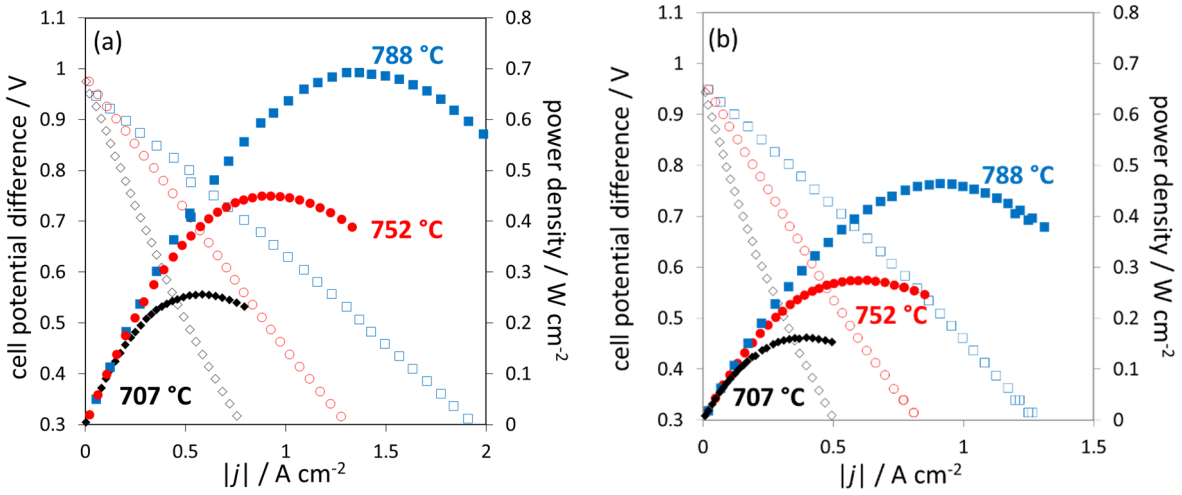


Figure 73. Effect of current density on cell potential difference (hollow markers) and power densities (filled markers) for SOERs operating with H_2 at 707, 752, and 788 °C and with the YSZ-LSM electrodes sintered at (a) 1100 °C; and (b) 1200 °C. Cell potential difference scan rate = 20 mV s^{-1}. Reproduced with permission from (280).

The Nyquist plots in **Figure 74** show that the YSZ-LSM electrode sintered at 1100 °C had a lower polarisation resistance at all temperatures tested, compared to those at 1200 °C, implying higher TPB densities at 1100 °C, as the thickness and composition of both electrodes was identical.

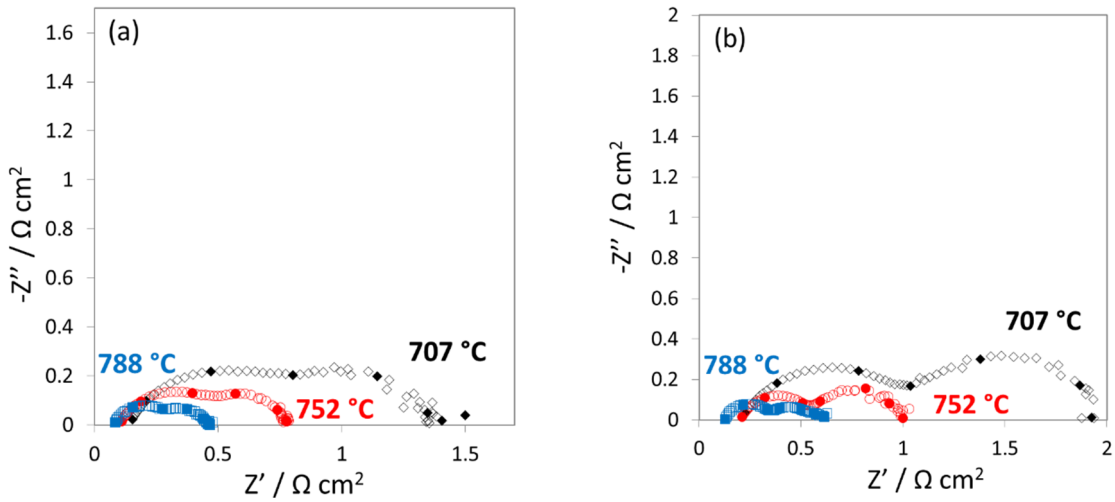


Figure 74. Nyquist plots for SOERs at OCPD operating with H_2 at 707, 752, and 788 °C; YSZ-LSM electrode sintered at (a) 1100 °C; and (b) 1200 °C. Filled markers indicate order of magnitude frequency intervals over the range 0.1 – 10^5 Hz. Reproduced with permission from (280).

Two dominant arcs were present in all Nyquist plots: a high-frequency (1 - 10 kHz) arc, due to charge transfer processes, and a low-frequency (1 - 10 Hz) arc, due to mass transport processes. The anode and electrolyte were identical for both SOERs, so differences in impedance were

attributed to differing YSZ-LSM electrode microstructures. Differences in the high-frequency arc resulted from differing transport of O^{2-} / O intermediates across the LSM | YSZ interface, and (dis-)association processes that are highly microstructure-dependent. The decrease in summit frequencies of the high-frequency arcs with increasing sintering temperature was consistent with results from the literature (301), and are reported in **Table 17**.

Table 17. Approximate high-frequency arc summit frequencies for each operating temperature, for the SOERs with cathodes sintered at different temperatures.

Operating *T* / Sintering *T* (°C)	1100 °C / kHz	1200 °C / kHz
707	3	1
752	5	2
788	6	4

The real impedance of the low-frequency arc was smaller for cathodes sintered at 1100 °C compared to 1200 °C, presumably due to a higher cathode porosity, resulting from a lower sintering temperature. Consequently, the impedance of the cell with cathode sintered at 1200 °C had a greater contribution resulting from mass transport processes compared to the cell with cathode sintered at 1100 °C, which had approximately equal impedance contributions from high and low-frequency processes.

Hence, the performance was competitive with planar solid oxide fuel cells fabricated with identical materials, and exceeded the electrochemical performance of microtubular solid oxide fuel cells operating with similar fuel compositions (302, 303).

7.3.4. Electrolysis with CO/CO_2

After fuel cell-mode experiments with H_2, the gas atmosphere at the Ni-YSZ electrode was changed, and two cells were tested as electrolysers operating with a 1/9 CO/CO_2 mixture, one sintered at 1100 °C and the other at 1200 °C.

Figure 75 shows the effects of current density on cell potential difference at a scan rate of 60 mV s^{-1} and for the operating temperatures: 707, 752, and 788 °C. Current densities at the thermoneutral potential difference (*ca.* 1.5 V, see Section 2.2.4.2) for the cell with the YSZ-LSM electrode sintered at 1100 °C were 0.82, 1.4, and 3.3 A cm^{-2} at 707, 752 and 788 °C, respectively, which were greater than those for the cell with the YSZ-LSM electrode sintered at 1200 °C.

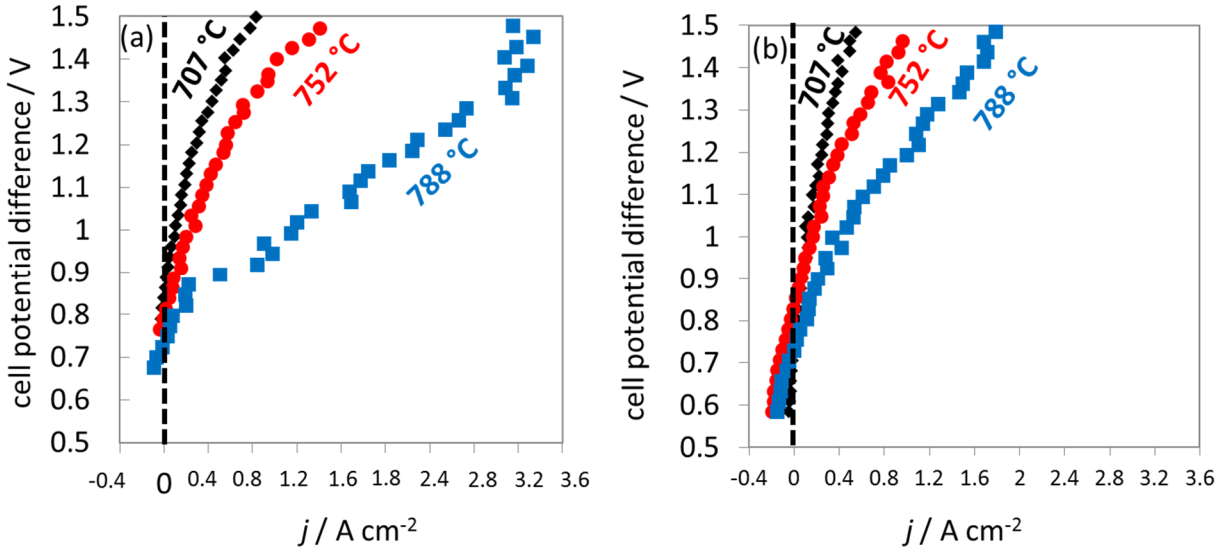


Figure 75. Effect of current density on cell potential differences for SOERs with a YSZ-LSM electrode sintered at (a) 1100 °C; and (b) 1200 °C, operating with a CO/CO_2 ratio of 1/9, at 707, 752, and 788 °C. Potential difference scan rate was 60 mV s^{-1}. Reproduced with permission from (280).

Current densities in electrolysis mode exceeded those achieved in Chapter 6, and were competitive with measurements from the literature with identical materials and similar gas compositions (296, 304, 305), indicating that inkjet-printed electrodes can have a greater electrolysis performance than conventionally-fabricated electrodes (145). The OCPDs were close to the theoretically expected values at 707 and 752 °C (0.896, and 0.870, respectively (306)), but were lower at 788 °C (0.77 V compared to the theoretical 0.849 V) (306), indicating probable failure of the sealant at high temperature.

Current densities corresponding to CO oxidation were also recorded (low overpotentials) for insights into the reversibility and degradation of the SOERs. The higher scan rate in this instance did not violate the condition of pseudo-steady state conditions during scanning, as near-identical measurements were recorded at 20 mV s^{-1} (see Appendix 10: Effect of scan rate on CO_2 reduction measurements).

7.3.5. Electrode Degradation

Figure 76 shows Ag present in the electro-active region of both electrodes, and large (*ca.* 1 – 5 µm diameter), solidified, hemispherical droplet-like deposits on the electrolyte surface near to the YSZ-LSM electrode, presumably due to mobilisation of Ag originating in the Ag paste, after experiments at high (788 °C) temperature and high current densities. Ag mobilisation has been detected previously for YSZ-LSM electrodes at 800 °C (*c.f.* T_m = 961.8 °C) during longer-term experiments, in which electrochemical reactions accelerated the deposition (presumed

condensation) process, so the concentration of Ag within the electrode was greatest at the electrode-electrolyte interface (307).

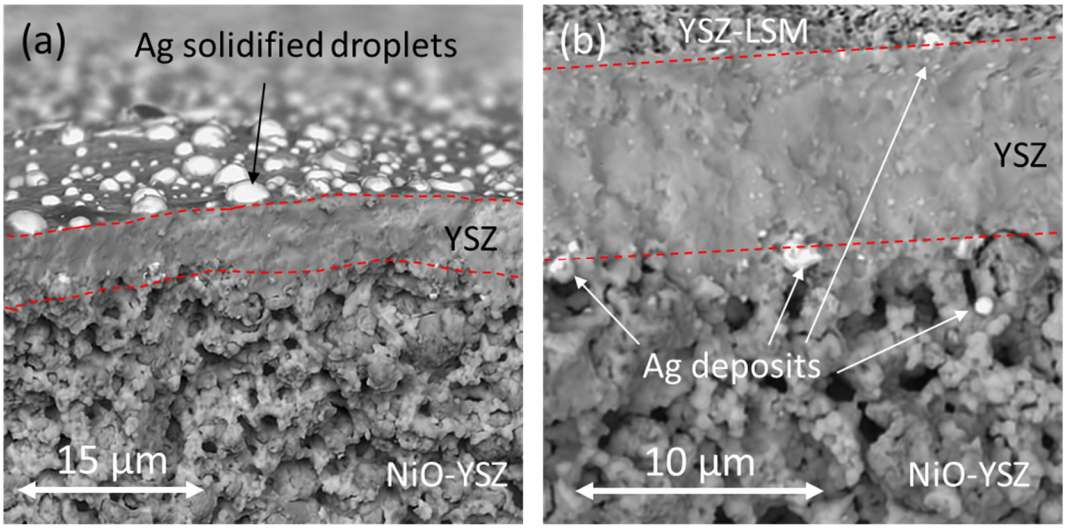


Figure 76. SEM photomicrographs of a SOER after testing showing (a) 'beaded' droplets of Ag on the surface of the electrolyte; and (b) Ag present near both electrode – electrolyte interfaces. Reproduced with permission from (280).

Mobilisation of the Ag to the electrode-electrolyte interface, blocking TPBs and reducing porosity, would cause a decrease in performance over the long operational times required for seasonal energy storage, and may also cause electrical short circuits of the cells if pin holes through the electrolyte were present. Therefore, at the high current densities these electrolysers could achieve, it would be necessary to change the current collecting conductive paste material, and ideally the wire material (**Table 13**), to a metal with a higher melting point, such as platinum or gold, for long-term operation tests.

7.4. Conclusions

The optimised YSZ and YSZ-LSM inks developed in Sections 5.1 and 5.3, respectively, were inkjet printed sequentially onto a NiO-YSZ substrate to fabricate the SOER: Ni-YSZ|YSZ (printed)|YSZ-LSM (printed)|LSM. The SOER was successfully operated reversibly, with dry H_2 and CO/CO_2 for fuel cell and electrolysis modes, respectively. After sintering, the electrolyte and LSM-YSZ electrode were *ca.* 9 and 20 µm thick, respectively. Notably, the formation of a dense 'skin' at the surface of the printed electrode was avoided, which has limited cell performance in previous studies (Section 5.3).

The inkjet printed YSZ-LSM electrodes were sintered at 1100 and 1200 °C, and characterised electrochemically by cycling the cell potential difference, and conducting impedance spectroscopy measurements at OCPD conditions. Electrodes sintered at 1100 °C generated

consistently higher current densities and lower overall cell polarisations due to a higher TPB density. Experiments in fuel cell mode produced peak power densities of 0.25, 0.45, and 0.69 W cm^{-2} at 707, 752, and 788 °C, respectively. Electrolysis experiments produced current densities of 0.82, 1.4, 3.3 A cm^{-2} at the same temperatures, at 1.5 V (thermoneutral) cell potential difference. Therefore, the performance of inkjet-printed SOERs can exceed those fabricated by conventional powder mixing methods.

8. Inkjet Printing Microstructures

Chapter Summary

This Chapter outlines preliminary printing experiments using the optimised aqueous YSZ ink formulation developed and reported in Section 5.1 to fabricate microstructures for the electrodes of solid oxide electrochemical reactors by inkjet printing. Printing and handling challenges to ensure microstructures were reproducible are identified.

8.1. Introduction

Chapter 7 deployed the inks developed and reported earlier in this research project to reproduce microstructures and electrochemical performances of electrodes fabricated by conventional powder-mixing methods, validating the utility of inkjet printing as a fabrication technique for solid oxide electrochemical reactors (SOERs). However, the limitations of these electrodes, including low phase percolation, resulting in inactive triple phase boundaries (TPBs), and high degradation rates, has not been addressed (see Section 2.3.1). This Chapter outlines preliminary experiments using inkjet printing to fabricate tailored electrode microstructures that cannot be produced conventionally.

8.2. Materials and Methods

To ensure percolation of all TPBs within SOER electrodes, it is necessary to separate each phase, *i.e.* deposit each sequentially. As the electrolyte phase required the highest sintering temperature (for conventional materials) of all phases, the microstructural features that can be produced within the ionically-conducting phase determine the effectiveness of the microstructure. Therefore, this Chapter covers only YSZ microstructures.

8.2.1. Ink Formulation

The optimised aqueous YSZ ink developed and reported in Section 5.1 was used to fabricate a variety of microstructures.

8.2.2. Substrate Fabrication

The NiO-YSZ composite, described in Section 5.1.1.3, was used as the substrate.

8.2.3. Inkjet Printed Microstructures

Different microstructures were deposited using an identical printing procedure and ejection settings as described in Section 5.1.1.4, with a reduced droplet ejection frequency of *ca*. 500 Hz, to minimise instabilities within the nozzle (see **Figure 24c**). Different microstructures were fabricated, limited by a minimum feature size (pre-sintering) of a single droplet diameter. The constraining factor limiting the range of printed geometries was that the droplets were ejected vertically, *i.e.* the microstructure cross-section was constant, but could vary vertically.

All microstructures were co-sintered with the substrate according to the optimised sintering profile described in Section 5.1.1.5.

8.3. Results and Discussion

8.3.1. Pillar Arrays

Figure 77 shows pillar arrays, the most effective microstructures in terms of increased surface area, fabricated by inkjet printing. The minimum feature size, *i.e.* resolution, that could be achieved, post-sintering, was 35 μm, which was equivalent to a single droplet splat diameter. **Figure 77a** shows a pillar array, each 50 printed layers tall, with a square coordination lattice. Around the base of each pillar, a defect can be seen, as highlighted in **Figure 77b**; these resulted from an erroneous droplet placement. The droplet placement error was *ca*. 20 μm, which exceeded the manufacturer-specified printer accuracy of 5 μm. Therefore, these defects are caused by droplet ejection instabilities; consequently, to reduce the probability of their occurrance, the droplet ejection frequency should be reduced. **Figure 77b** also shows the presence of very long vertical grains, post sintering, at the pillar base. The reasons for this phenomenon are unknown, but they are not expected to be detrimental to the microstructure electrochemical performance.

In addition, all pillars appear to have a concave top. Presumably, this is due to a mild coffee-staining effect, occurring during drying. **Figure 77c** shows an array of pillars, 180 printed layers thick, with a height of 300 μm, *i.e.* an aspect ratio of *ca*. 8, post-sintering. With a resolution of 35 μm, this was the highest resolution SOER material structure fabricated at the time of publishing (145). **Figure 77d** shows defects that can arise due to inactive nozzles; the red circles show where nozzles have consistently failed to eject ink over the entire printing run. This was primarily due to software issues, and was unavoidable at the time of fabrication. However, since printing these microstructures, software updates resolving this problem have been released by Ceradrop (France).

Some pillars had larger diameters than others, as they were made of two droplets per layer that coalesced into a single droplet before drying. This appeared to be an unavoidable relic caused by the CAD software, which was subsequently avoided by creating CAD files of individual shapes, with a negative droplet overlap (*i.e.* a specified distance between coordinated deposited droplets, no overlap between successive layers) within the structure, rather than specifying the location of individual pillars.

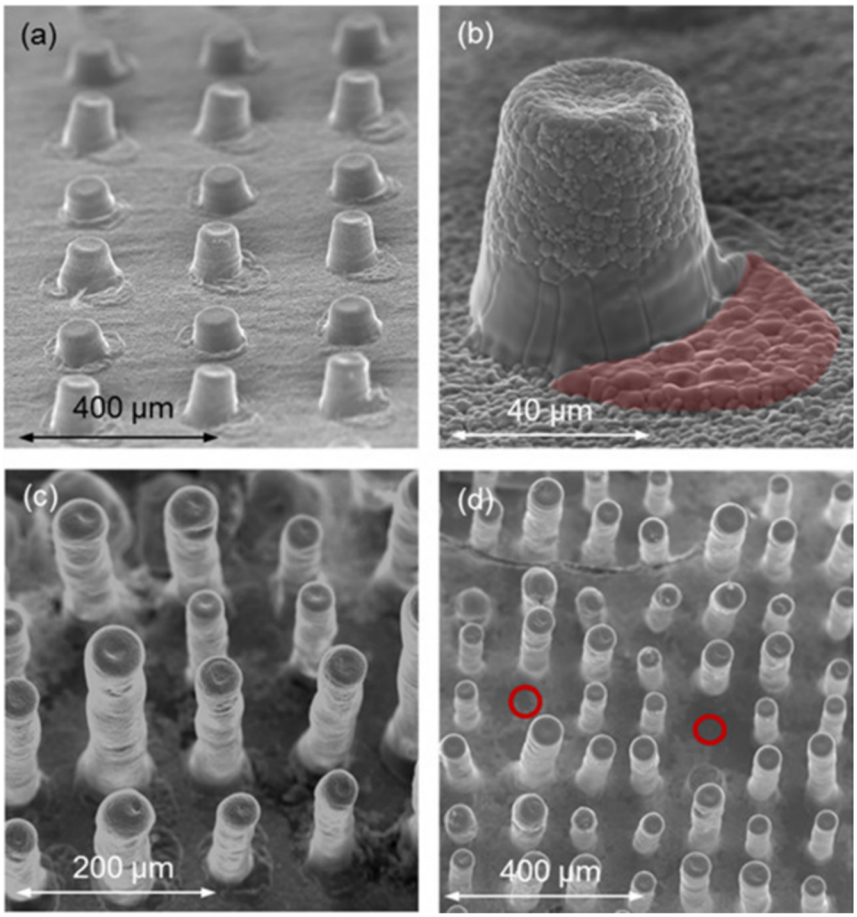


Figure 77. SEM photomicrographs of YSZ pillars on Ni-YSZ substrate. (a) Pillar array at 60° tilt; (b) misplaced droplet (red zone); (c) pillar array at 30° tilt; and (d) showing missing pillars as red circles. Reproduced with permission from (145).

8.3.2. Square Lattice

Another inkjet printed microstructure was a square lattice, shown in **Figure 78**. The minimum feature size was *ca*. 40 µm, post sintering, *i.e.* a single droplet accounting for the accuracy of the printer. Also evident were features due to droplets deposited away from the centre of the structures; this can be avoided in the future by reducing droplet ejection frequency, and hence printhead velocity. **Figure 78c** shows that scaling the microstructure over larger areas was trivial using inkjet printing, which is a necessity for manufacturing SOER electrodes.

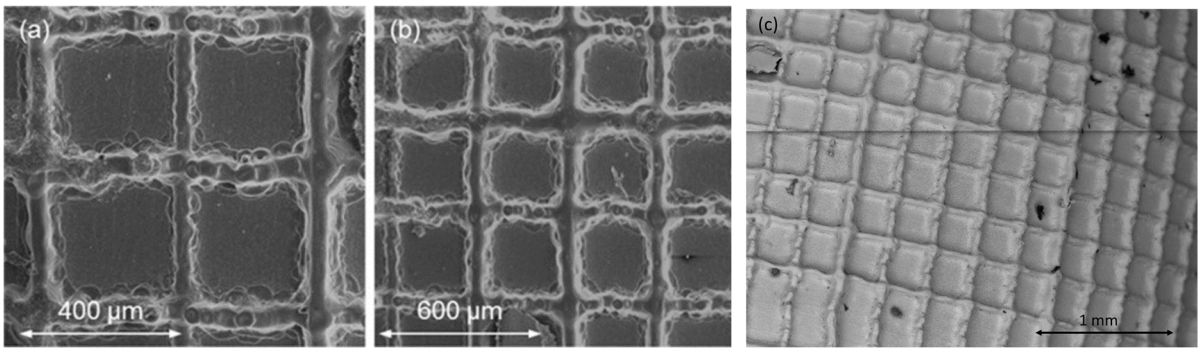


Figure 78. SEM photomicrographs of YSZ square scaffolds, with decreasing magnification from (a) – (c). (a) and (b) reproduced with permission from (145).

8.4. Challenges

Before and after sintering the printed microstructures, they were very fragile and careful handling was required to avoid breakages, as shown in **Figure 79a**. Broken sintered pillars appear to have fractured at their base, indicating that this was the weakest part of the microstructure; at this interface, the difference in substrate and pillar thermal properties during sintering was greatest.

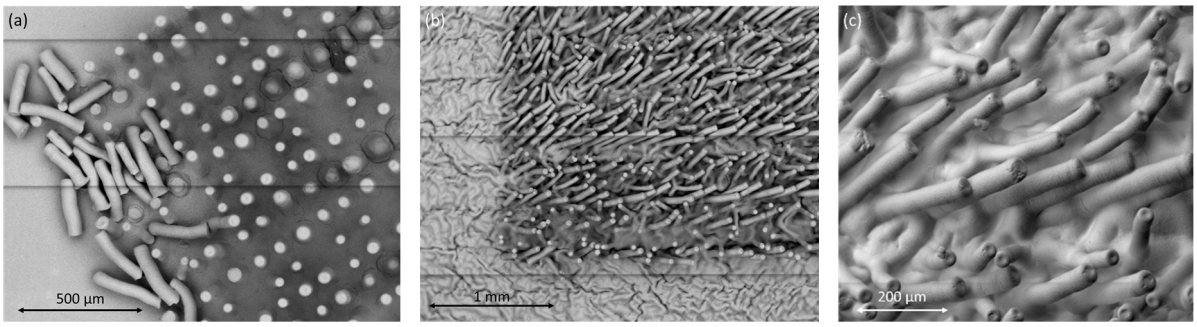


Figure 79. SEM photomicrographs of (a) broken; (b) an array; and (c) high-magnification array YSZ pillars.

Figure 79b shows a pillar array that was printed onto a rough YSZ substrate, and co-sintered at 1500 °C. The pillars do not rise vertically, but at varying angles. The pillars appear to be broken, but on closer inspection, were not, as shown in **Figure 79c**. Therefore, it was essential to have smooth substrates, to avoid these irreproducible microstructures.

8.5. Conclusions

The optimal YSZ ink formulation developed and reported in Section 5.1 was used to fabricate microstructures for SOER electrodes by inkjet printing. Two microstructures were printed: pillar arrays and square lattices. The minimum feature size, *i.e.* resolution, was limited by the

droplet spread diameter on the substrate, post-sintering. Therefore, it was beneficial to co-sinter the microstructure and the substrate, to maximise shrinkage and resolution. Problems encountered were primarily due to the droplet ejection frequency being too high, leading to miss-placed droplets, handling issues that caused the microstructure to break, and a substrate that was insufficiently smooth for reproducible microstructures. However, tailorable and reproducible microstructures were fabricated successfully, validating the utility of inkjet printing for producing microstructures suitable for SOER electrodes.

9. Microstructure Electrochemical Simulations

Chapter Summary

This Chapter describes a finite element analysis multi-physics model created to simulate the electrochemical performance of the printed pillar arrays fabricated in Chapter 8, for use within the oxygen-electrode of reversible solid oxide electrochemical reactors. The transport of gaseous reactants / products, and charged species were combined with electrochemical reaction kinetics, using relationships and parameter values from the literature. The effect of varying pillar geometry, *i.e.* height, diameter, and spacing, on current density was simulated to establish the optimum electrode microstructure, for a range of operating temperatures and potential differences.

9.1. Introduction

Preliminary experiments outlined in Chapter 8 demonstrated that inkjet printing was an effective technique to fabricate YSZ microstructures suitable for SOER electrodes. To maximise electrochemical performances of inkjet printed electrodes, the triple phase boundary (TPB) density should be maximised, which, when constrained by printed phases separately, can be achieved by maximising the interfacial surface area of YSZ|LSM within the electrodes, *i.e.* the ratio of internal electrode area compared to its projected (base) surface area. Therefore, the most effective microstructure to achieve this by inkjet printing is a pillar array, where the relevant geometric variables are the array lattice, pillar height (l_h), diameter (l_p), and centre-to-centre spacing (l_s). For a hexagonal lattice array, the ratio of the electrode area to its projected area is shown in **Figure 80**. Evidently, the electrode surface area to projected area can be increased by maximising l_h, and minimising l_s and l_p.

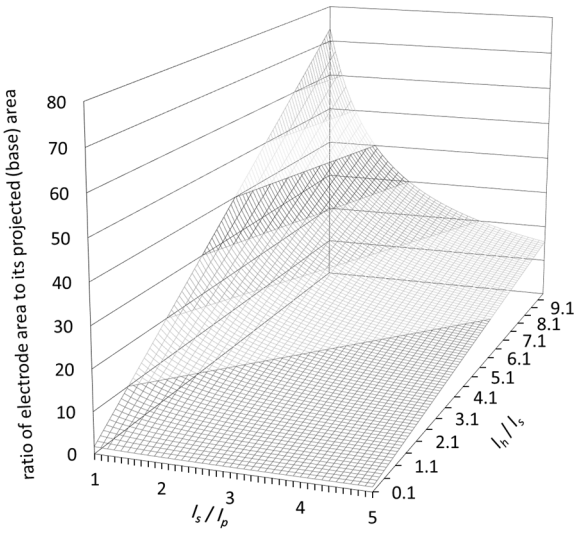


Figure 80. Variation of the ratio of electrode area to projected area with pillar geometry, for a hexagonal lattice pillar array.

However, as Section 2.2.5 explained, electrode performance depends on electrochemical reaction kinetics, gas transport kinetics, and charged-species (O^{2-}, e^-) transport, in addition to the TPB density and operating conditions. Therefore, the increase in electrode area shown in **Figure 80** represents an unobtainable (maximum) increase in performance. Consequently, a multi-physics model was required to simulate how these transport mechanisms interact, to determine current densities. This Chapter describes simulations for the electrochemical performance of the oxygen-electrode under both anodic and cathodic polarisations, *i.e.* electrolyser and fuel cell modes, respectively. The oxygen-electrode was simulated because the reaction kinetics were expected to be slower than at the fuel-electrode (*c.f.* the reference

exchange current densities reported in **Table 4** and **Table 5**), so the greatest performance enhancement resulting from inkjet printing, within present resolution limits, could be achieved.

Before proceeding, it is important to consider the definition of current density because in this unique circumstance of tailored electrode microstructures, the total active area within the electrode is known, *ex ante*. The actual current density, which varies spatially within the electrode, depends on the specific region of the electrode where the reaction occurs. However, when comparing electrodes to determine the best design, it is preferable to conform to the conventional definition of current density for SOERs, which is equal to the total current evolved divided by the projected surface area of the electrode.

9.2. Materials and Methods

9.2.1. Model Software, Setup, and Hardware

Finite element analysis (FEA), multi-physics software (Comsol version 5.2a., Comsol Inc., Sweden) was used to create a model to simulate the electrochemical performance of the pillared (working) electrode, with the 2D axisymmetric geometry shown in **Figure 81a**, using a Macbook Pro (2016 model, Apple, USA), with a 2.7 GHz dual core i5 processor (Intel, USA) and 16 GB RAM.

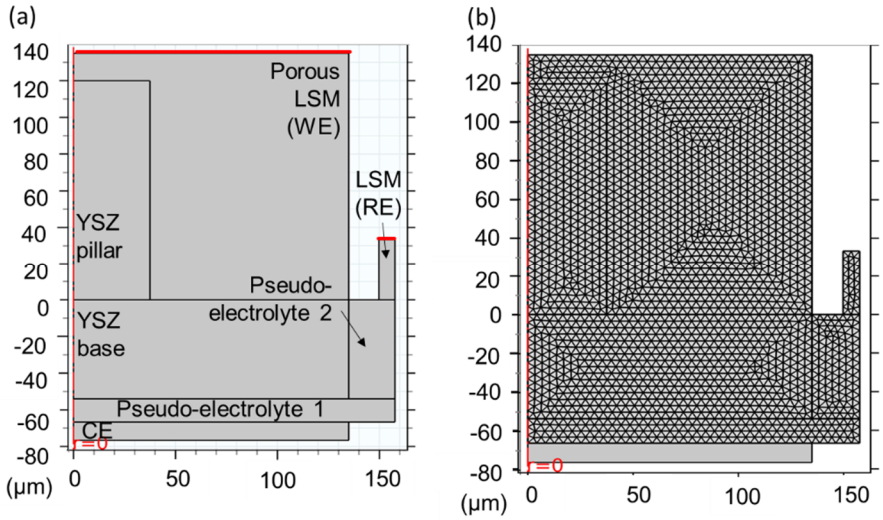


Figure 81. (a) Geometry of a pillared electrode; and (b) meshed, on Comsol Multiphysics.

The working (WE), counter (CE) and reference (RE) electrodes were all LSM, which was necessary to control electrode potential differences directly. 'Pseudo' electrolyte phases, where conductivity and geometry were appropriately scaled, were introduced to simulate a real SOER geometry with a practical element size (accounting for multiple length scales), for a pillar that was in the centre of a (circular) array, *i.e.* far from the reference electrode and edge effects.

Figure 82 shows the dimensions of each phase, corresponding to what could be used in the experimental equipment used in previous Chapters, and shown in **Figure 67**. The additional height of LSM WE over the YSZ pillar was maintained at 15 μm throughout.

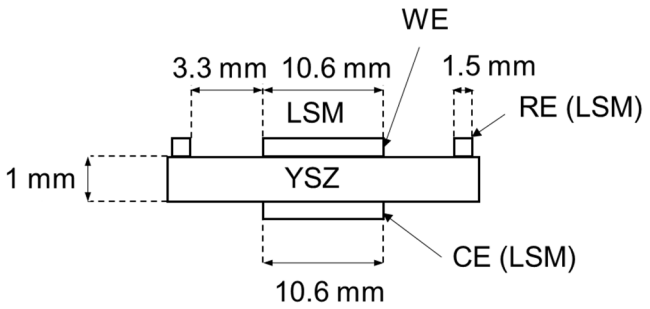


Figure 82. Cross section of simulated (axis-symmetrical) SOER geometry.

The software meshed the geometry ('extra fine') automatically, as shown in **Figure 81b**, constrained by a maximum and minimum element length of 14.2 and 0.6 μm, respectively. For pillar diameters < 50 μm, the maximum element size was reduced to ensure accuracy, down to 0.2 μm. A maximum element growth rate of 1.3, curvature factor of 0.3, and resolution in narrow regions of 1 were specified.

Simulations were conducted under 'stationary' (steady-state) conditions, with a relative solver tolerance of 0.01. A Multi-frontal Massively Parallel sparse direct Solver (MUMPS) was used to compute the simulations. The effects of l_h, l_p, l_s, and the ratio l_s/l_p were investigated, for different operating conditions, and automated using a parametric sweep.

Table 18. Summary of the structural parameters, with values for the porous LSM phase, taken from reference (112).

Parameter / units	Value*
l_{TPB} / μm^{-1}	1.55
ε / 1	0.357
τ_{LSM} / 1	1.43
τ_p / 1	2.22
d_p / μm	1.83

* Notably, these values were for brush-coated LSM on pre-sintered, planar YSZ surface. Values for an inkjet printed layer were undetermined in the literature.

The physical properties of the electrode are shown in **Table 18**, which were evaluated by Focused-Ion-Beam (FIB)-SEM microstructural characterisations into the YSZ|LSM interface

(112). The independent variables were the operating temperature, T, and the potential difference applied between the WE and RE. The former was set as 737, 785, and 826 °C, to approximately match the experimental operating temperatures for set points: 750, 800, and 850 °C, respectively. The latter was varied between -0.3 to +0.3 V. To compare results between simulations, the dependent variable, which was the total output current (j_{out}) was calculated, according to equation (86).

$$j_{\text{out}} = \frac{\int j_{\text{TPB}} l_{\text{TPB}} . dS_{\text{LSM|YSZ}}(r, \theta, z)}{A_{\text{b}}} \quad (86)$$

Where $S_{\text{LSM|YSZ}}$ is the interfacial area between LSM and YSZ, which was a function of radial (r), angular (θ), and vertical positions (z); A_{b} is the projected electrolyte base area for each pillar, which depends on l_p and l_s.

9.2.2. Governing Equations

Equation (37) shows the electrochemical reactions occurring at the oxygen-electrode under anodic and cathodic polarisations. Electrochemical reaction kinetics were assumed to follow the Butler-Volmer relationship given in equation (33), where the exchange current density was calculated using equation (41). Values for the kinetic parameters and the equation for overpotential are given in **Table 4**, and equation (42), respectively. The differential equations governing the flux of charged species within each conducting phase (*i.e.* e^- and O^{2-} ions), and the species involved in electrochemical reactions at the TPBs are given by equations (52) and (87), respectively.

$$\nabla N_k = \frac{\nu_{\text{k}}}{|\nu_{\text{e}}|} \frac{j_{\text{TPB}} l_{\text{TPB}}}{F} \quad (87)$$

Where j_{TPB} and l_{TPB} represent the local current density at the TPB (A m^{-1}) and area-specific TPB density (m m^{-2}), respectively. Stoichiometric coefficients (ν) of O_2 / O^{2-} (k) and electrons (e) are given in equation (37). It was assumed that all electrochemical reactions occurred at, and were confined to TPBs. **Table 7** shows expressions for YSZ and LSM conductivities that were adjusted appropriately for microstructure, shown in equation (53).

Gas transport through pores within the LSM phase was governed by the Dusty Gas Model, given in equation (46), where the effective Knudsen and binary diffusion coefficients were calculated using equations (47) and (48), respectively. The binary diffusion coefficient was calculated according to equation (49), using equations (50) and (51) to approximate the viscosity of an O_2 / N_2 binary mixture.

9.2.3. Boundary Conditions

The governing equations were constrained by appropriate boundary conditions: $P_{t,inlet}$ = 0.1 MPa, and $y_{O2,inlet}$ = 0.21 (*i.e.* ambient air) at the outer limit of the working electrode, and the electric potential at the counter electrode (CE)|bulk gas interface was fixed at 0 V. A specified potential difference between the outer edge of the LSM phase in the RE and WE was used to complete potentiostatic simulations. N_{O2}, N_{O2-}, and N_{e-} were equal to zero across external surfaces (symmetry boundary condition), excluding the outer boundary of the WE and the electric ground at the CE.

9.3. Results and Discussion

9.3.1. Running Simulations

The automating parametric sweep was effective, and > 90 % of cases were solved with the first set of initial conditions (ϕ = 0 V within all phases, y_{O2} = 0.21), which were updated as the solutions to each successive parametric condition. When convergence was unsuccessful, the initial conditions and / or the maximum element size were modified iteratively, and the simulation was re-run until convergence. The average solution time for a single set of parameters was < 2 minutes.

9.3.2. Spatial Distributions

Figure 83 shows spatial overpotential, current density, and oxygen mole fraction distributions within a pillar array (hexagonal lattice, l_p = 30 μm, l_h = 100 μm, l_s/l_p = 2) under an applied potential difference of |0.3 V|, at 737 °C. Under both cathodic and anodic polarisations, the overpotential was predicted to decrease with increasing pillar height, due to the low conductivity of YSZ relative to that of LSM; the potential drop in LSM was negligible. The decrease in overpotential resulted in a decrease in current density with increasing pillar height, in this instance by 13 and 25 %, for cathodic and anodic polarisation, respectively. Therefore, electrode performance can be increased further by increasing the pillar height, as current density at the pillar summit was non-zero.

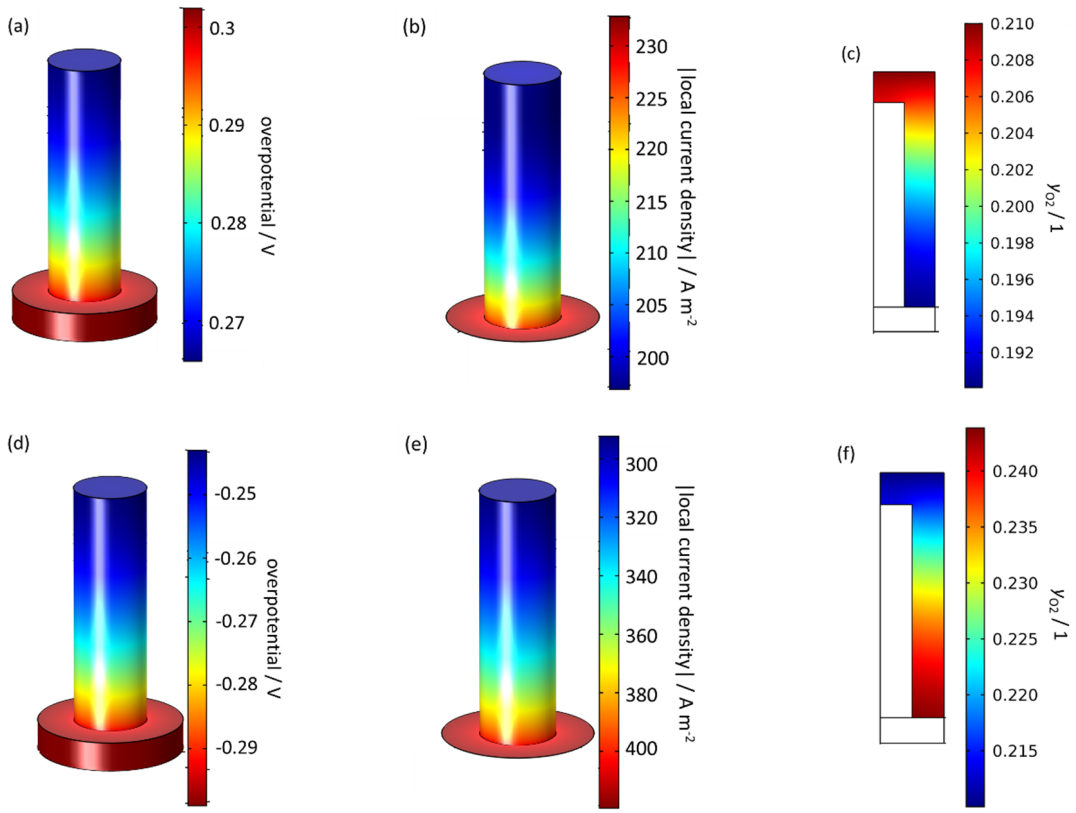


Figure 83. FEA simulations of (a, d) overpotential; (b, e) local current density; and (c, f) oxygen mole fraction under cathodic (a-c) and anodic (d-f) polarisation of |0.3 V|, T = 737 °C.

The mole fraction of oxygen can also limit performance, particularly under cathodic polarisation, as shown in **Figure 83c**. The small change in y_{O2} gradient at the base of the pillar compared to the top suggested that mass transport within the electrode may be limiting under cathodic polarisation for this microstructure geometry; however, analysis of the parametric sweep results was the only reliable way to determine the onset of diffusion control, as shown in Section 9.3.3.

9.3.3. Parametric Sweep Results

Varying l_p from 10 – 100 µm, l_h from 50 – 500 µm, and l_s/l_p from 1 – 3 for both hexagonal and square lattices at each simulated temperature, with small incremental changes in each parameter to aid convergence, resulted in > 5000 unique solutions, too many to report in this Thesis. Therefore, only simulation results that generally aid electrode design and selection of operating conditions, for a hexagonal lattice pillar array, are reported in this Section.

The effect of l_p, l_h, and T, for l_s/l_p = 1.4 (a practical separation) is shown in **Figure 84**. Under both anodic and cathodic polarisations, output current densities were predicted to increase with increasing l_h, due to a greater TPB density. At higher T, performance was predicted to increase,

as expected from the kinetic and thermodynamic relationships governing the model. Notably, under anodic polarisation, mass transport limitations were insignificant, however, under cathodic polarisation mass transport limitations became significant with:

- increasing height, due to the additional resistance to gas diffusion within the porous LSM phase;
- increasing temperature, which evidently increased reaction kinetics to a greater extent than diffusion coefficients;
- increasing potential difference, which increased current densities and therefore increased local depletion of O_2, highlighted by the red shaded zones in **Figure 84** and **Figure 85**.

The predicted onset of mass transport limitations varied with geometry, potential difference, and T.

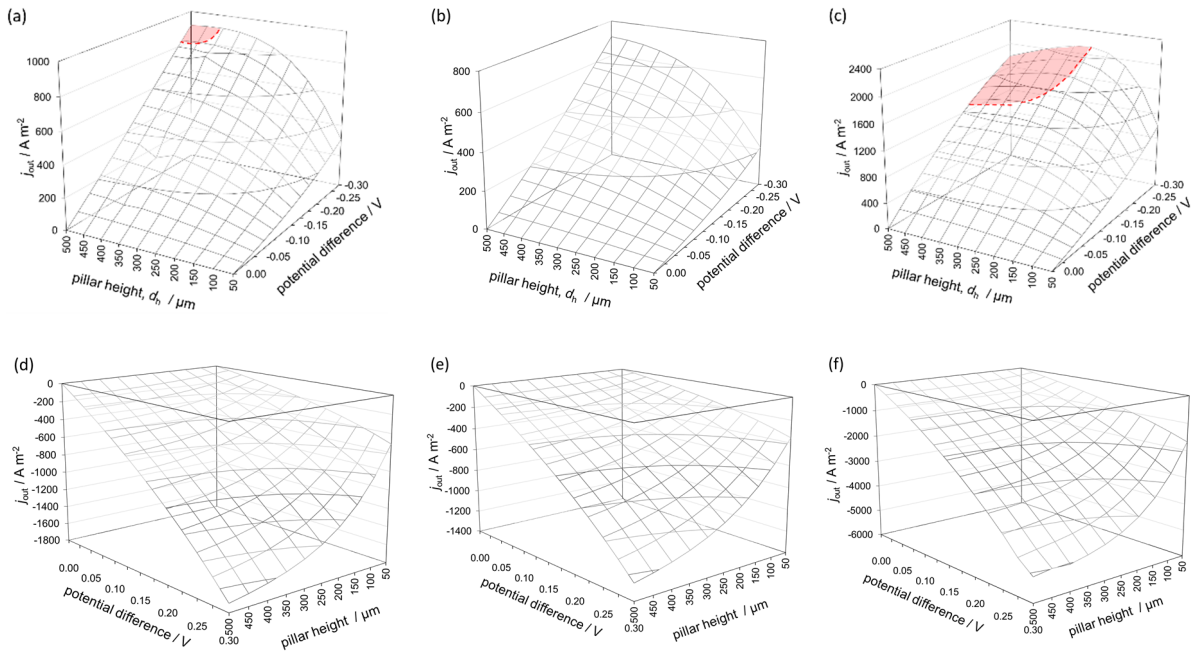


Figure 84. Simulated output current densities with varying pillar height and WE-RE potential difference, under (a-c) cathodic; and (d-f) anodic polarisation for l_p = 30 (a, c, d, f) or 50 µm (b, e), at T = 737 (a, b, d, e) or 826 °C (c, f).

Figure 85 shows the effect of pillar height and spacing / diameter ratio on output current densities, under both anodic and cathodic polarisations (|0.25 V|) for pillars of l_p = 30 µm at 826 °C. Evidently, minimising the ratio increased electrode performance, due to greater TPB densities. However, increasing pillar height did not always increase performance under cathodic

polarisation due to the onset of mass transport limitations, which varied depending on spacing ratio and height, as shown by the red shaded area. Fabricating structures that lie outside of this area would be preferable.

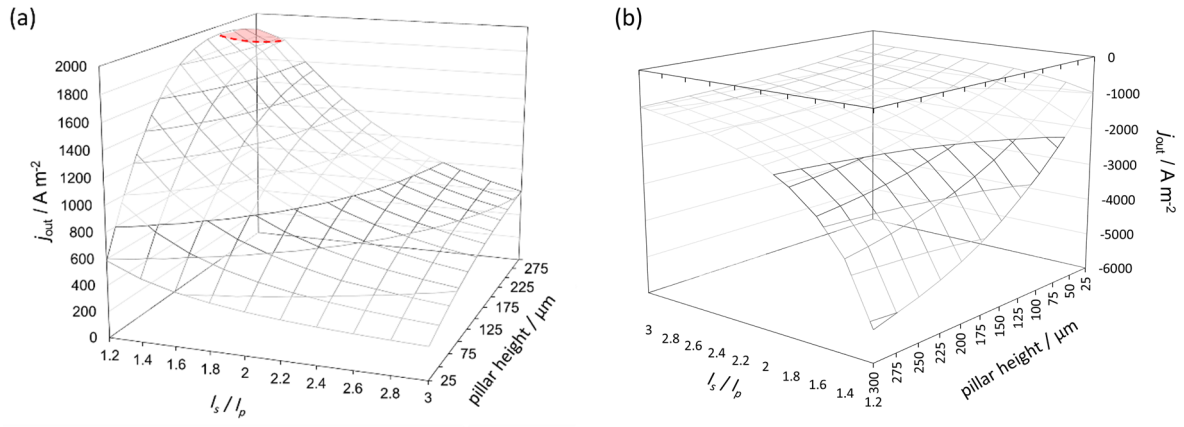


Figure 85. Simulation results showing how current density varies with pillar height and l_s/l_p at 826 °C, l_p = 30 µm, under (a) cathodic; and (b) anodic polarisations of |0.25 V|.

Using these results, the maximum increase in performance with pillars of 30 µm diameter (the approximate resolution of inkjet printing found in Chapter 8), was by factors of *ca*. 3 and 5, under cathodic and anodic polarisations, respectively, compared to the case of no pillars, *i.e.* a 2D YSZ|LSM interface. This was significantly less that the increase in interfacial area of *ca*. 50 times would imply, as shown in **Figure 80**.

9.3.4. Pillar Array Lattice

Compared to body-centred arrays, hexagonally-packed pillar geometries have greater area-specific densities and hence greater TPB densities and increased reactor performances. However, small l_s/l_p ratios, corresponding to long, narrow pore channels, could intensify mass transport limitations, as shown in **Figure 85**, so at a given spacing, the performance is a compromise between pillar lattice, diameter, and height. There are 11 regular circle packings for equivalently sized circles, based on the 11 regular tessellations; the packing densities of each are shown in **Table 19**. As the density within a hexagonal lattice is greatest, for the present resolution achievable using inkjet printing, it is the preferable pillar array lattice.

Table 19. The approximate maximum packing densities (specific to projected area) of the regular tessellations, specified by Schläfli symbols, in descending order of density (308).

Tessellation	Packing density
3, 6 [a]	0.907
$3^2 .4^2$	0.842
$3^2 .4 .3 .4$	0.842
4, 4 [b]	0.785
$3^4 .6$	0.777
3.4 .6 .4	0.729
3.6 .3 .6	0.680
6, 3	0.605
4.8^2	0.539
4.6 .12	0.486
3.12^2	0.391

[a] Hexagonal lattice, [b] Square lattice.

9.4. Conclusions

In this Chapter, a finite element analysis model was developed to predict the electrochemical performance of the printable YSZ pillar microstructures produced in Chapter 8, covered with LSM, for the oxygen-electrode of SOERs. Comsol Multiphysics software was used to run the simulations, and the model included reactant / product mass transport, charged species transport, and electrochemical reaction kinetics, using relationships and parameter values from the literature. The diameter, spacing, and pillar height were varied, within the limits of what was practically printable, to predict the optimised microstructure, *i.e.* maximum current density, for a range of operating temperatures and potential differences. There were several significant outcomes from the simulations:

- As expected, higher operating temperatures increased electrode performance.
- Decreasing pillar diameter and spacing always increased electrochemical performance, by increasing the TPB density.

- Mass transport limitations were predicted to occur under cathodic polarisation, the significance of which depended on potential difference, temperature, and microstructure geometry.
- No mass transport limitations were predicted for anodic polarisations, so increasing the pillar height always increased electrode performance.
- Increases in electrochemical performance by introducing pillars were significantly less than the proportional increase in TPB density; this highlighted the importance of this FEA model to predict actual performance increases for a given set of conditions, and microstructure geometry.

10. Solid Oxide Electrochemical Reactors with Tailored Microstructure

Chapter Summary

This Chapter describes the fabrication of a YSZ electrolyte and pillar arrays for the oxygen-electrode of reversible solid oxide electrochemical reactors SOERs by inkjet printing. The oxygen-electrode was completed by inkjet printing LSM onto the pre-sintered pillars. The resulting SOERs, with structure: Ni-YSZ|YSZ (printed)|YSZ (pillars)|LSM (printed), were electrochemically characterised as fuel cells, operating with dry H_2, and electrolysers, operating with CO/CO_2 (1/1 mixture). The resulting microstructures were imaged by SEM, and the results used to correlate the measured electrochemical performance with the observed microstructure.

10.1. Introduction

10.1.1. Phase Percolation

As reviewed in Section 2.3.1, and highlighted by the microstructural simulations reported in Chapter 9, electrode performance depends critically on both TPB percolation and location within the electrode, *i.e.* proximity to the electrolyte. Therefore, to enhance electrode performance, it is necessary to improve both factors, which requires a transition from conventional composite powder-mixing fabrication techniques, to new methods that facilitate customisable electrode microstructures.

10.1.2. Electrode Degradation

In addition to insufficiently-high power / current densities, poor electrode durability is limiting the widespread deployment of SOERs. Impurities in the reactant mixtures (*i.e.* sulphur) (309), and reactions with the interconnecting and sealant materials in stacks (*i.e.* with Cr and / or Si) (310, 311) can poison the electrodes; however, this may be avoided by pre-cleaning gases, and materials development. Furthermore, the mobility ('coarsening') of Ni in the fuel-electrode during high-temperature operation reduces TPB densities, causing a loss in performance over time (312), which can be mitigated by lowering the operating temperature, reducing moisture in the fuel-stream, and refining the initial particle size distribution (313). However, during long-term electrolysis operation required for seasonal energy storage, a significant degradation mechanism that can result in catastrophic failure of the electrolyser is caused by O_2 evolution into non-percolating pores of < 50 nm in diameter, observed between adjacent YSZ-YSZ and YSZ-LSM particles (297).

Experimental studies in the literature have shown that LSM has two oxygen transport pathways to / from TPBs: a 'surface' route, by which dissociated O atoms are transported across the LSM surface, and a 'bulk' route, by which dissociated O atoms can be incorporated into the LSM phase by a reduction process, facilitated by the variable Mn oxidation state (107). However, it was found that under anodic polarisation, oxygen bulk transport rates were low (314), so it should not be possible for oxygen to escape from non-percolating pores through (saturated) LSM. Therefore, the electrolytic degradation mechanism is shown schematically for a YSZ-LSM composite electrode in **Figure 86**, and the degradation mechanism steps are described below:

1. Transport of O^{2-} to active TPB (percolating electronically and ionically-conducting phases under anodic polarisation);

2. Oxidation of O^{2-}, as shown by equation (37);
3. Removal of e^- through the bulk LSM phase to current collector;
4. Evolution of O_2 (gas) into non-percolating pore (red shade), causing an increase in pressure, eventually resulting in electrode fracture to relieve the pressure.

6

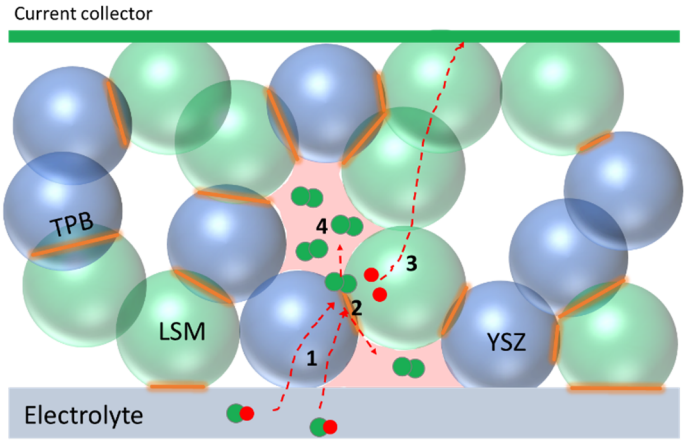


Figure 86. Schematic of O_2 evolution into non-percolating pores (red shade) during electrolysis.

The change in O^{2-} ion oxidation overpotential due to an increase in local O_2 partial pressure is unlikely to be reaction rate-limiting, particularly near the electrode | electrolyte interface (see Appendix 11: Reduction of Oxygen-electrode Overpotential). Consequently, pO_2 can become sufficiently high over time to cause electrode fracture. The mechanically-weakest point within the composite microstructure is at the interface between adjacent YSZ particles, and between YSZ particles in the electrode and the electrolyte / LSM particles, due to the much lower electrode sintering temperature (*ca*. 1000 - 1200 °C (315, 316)) than that required for adequate YSZ sintering (> 1300 °C), as shown in **Figure 38**. Consequently, surface roughness of the YSZ particles in the electrode would be expected to remain, which may be the source of the nano-sized, non-percolating pores. Mitigating this effect is not possible with composite powder electrodes, as the maximum sintering temperature of YSZ-LSM is limited to 1200 – 1300 °C, to avoid chemical reactions between YSZ and LSM.

Therefore, the sequential deposition of YSZ and LSM, at pre-defined locations subject to the predicted optimal electrode microstructures reported in Chapter 9, could mitigate the presence of non-percolating pores by facilitating sequential sintering of each phase at appropriate temperatures, which would lower YSZ surface roughness without favouring chemical reaction.

The fabrication of these microstructures for the oxygen-electrode, the challenges encountered, and their electrochemical characterisation are outlined in the remainder of this Chapter.

10.2. Materials and Methods

10.2.1. Ink Formulation

The optimised aqueous-based YSZ ('Ink 1') ink formulation developed and reported in Chapter 7 was used to inkjet print the electrolyte and pillars. The optimised BtOH-based LSM ink formulation developed and reported in Section 5.3 was used to print the electronically-conducting component of the oxygen-electrode.

10.2.2. Substrate Fabrication

The materials and methods used to fabricate the NiO-YSZ electrode support were outlined previously in Section 7.2.1.

10.2.3. Reactor Fabrication

The electrolyte, pillars, and LSM components of the oxygen-electrode were inkjet printed onto the substrate using the same printheads and ejection profiles as outlined previously for the YSZ and LSM inks, in Sections 5.1.1.4 and 5.3.2.3, respectively. To allow each layer to dry, a 30 second printing interval was taken between successive YSZ and LSM layers.

8 inkjet printed layers of YSZ (square droplet deposition lattice, overlap 20 μm), 4 in each *x* and *y* (perpendicular) directions were used to fabricate the electrolyte at a droplet ejection frequency of 2150 Hz (printhead velocity 80 mm s^{-1}).

A hexagonal array of pillars (single isolated droplets) characterised by a (pre-sintering) pillar diameter, spacing, and height of 60 and 80 μm, and 100 layers, respectively, were printed with a droplet ejection frequency of 336 Hz (printhead velocity 80 mm s^{-1}). Despite the predictions in Chapter 9 suggesting taller pillars would enhance electrochemical performance, the pillars were limited to 100 layers, to ensure the subsequent adhesion between LSM and the entire pillar surface.

100 or 400 layers of the LSM ink were inkjet printed onto the sintered NiO-YSZ|YSZ|YSZ (pillars) structure, and sintered at 1000 or 1100 °C, respectively. The LSM droplet diameter and overlap were 100 and 50 μm, respectively. Droplet ejection frequency was 1500 Hz (90 mm s^{-1} printhead velocity).

10.2.4. Sintering and Microstructural Characterisation

After inkjet printing the YSZ electrolyte and pillars onto the NiO-YSZ substrate, they were co-sintered with an equivalent temperature profile as Section 7.2.2. After inkjet printing the LSM, the structure was heated to 600 °C, held for 2 h, and subsequently sintered at 1000 or 1100 °C for 3 h, rising at 4 °C min^{-1}, and cooling at 5 °C min^{-1}. Microstructures were characterised as in Section 5.1.1.6.

10.2.5. Electrochemical Characterisation

The electrochemical characterisation procedure described in Section 7.2.5 was followed, with the exception that electrolysis measurements were conducted using a CO/CO_2 gas mixture of 1/1, each with a 10 cm^3 min^{-1} flow rate. This increased the reducing potential of the gas mixture, preventing Ni oxidation (**Figure 13b**) locally at high current densities, and still mitigated coking, shown by equations (5) and (6), as the equilibrium CO fraction is 0.7 – 0.91 (52).

10.3. Results

10.3.1. Reactor Fabrication

Figure 87 shows a top-down view photograph of the inkjet printed YSZ pillar array before sintering. There were 3128 pillars, and none were missing, highlighting the high-reproducibility of inkjet printed microstructures.

Inkjet printing introduced artefacts into the un-sintered deposit, as shown by the parallel and perpendicular lines which can be seen across the electrolyte. However, the characteristic length scale of a pillar (*i.e*. diameter) < the length scale of these features; therefore, they did not affect the pillar array during sintering. If necessary, *e.g*. for wider pillars, these features could be removed by introducing an overlap between successive printing 'rasters', *i.e*. printhead sweeps.

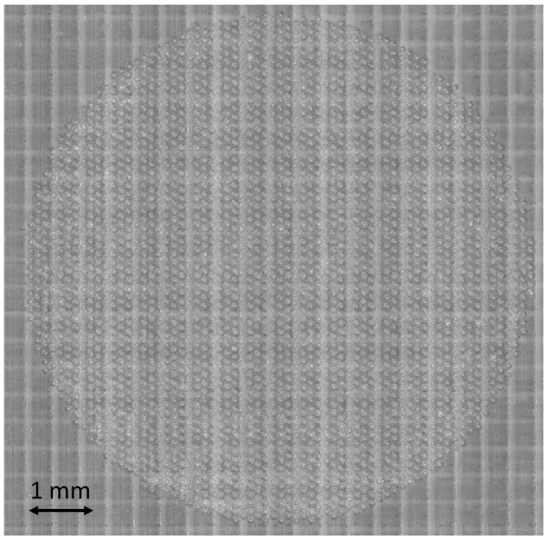


Figure 87. Top-down view photograph of inkjet printed pillar array, before sintering.

SEM photomicrographs of the post-sintering electrolyte, YSZ pillars, and a broken pillar cross section, are shown in **Figure 88a**, **b**, **c**, respectively. The sintered electrolyte was *ca*. 13 μm thick, and appeared to be highly-dense, without obvious defects. The post-sintering diameter, height, and spacing of the pillars were *ca*. 32, 140, and 60 μm, respectively (*i.e.* l_s / l_p = 1.9, aspect ratio = 4.4). As expected from the results in Section 8.3.1, the top of the pillars were concave due to the coffee stain effect. **Figure 88c** shows that internally the pillars were highly dense, so should have high O^{2-} ion conductivity.

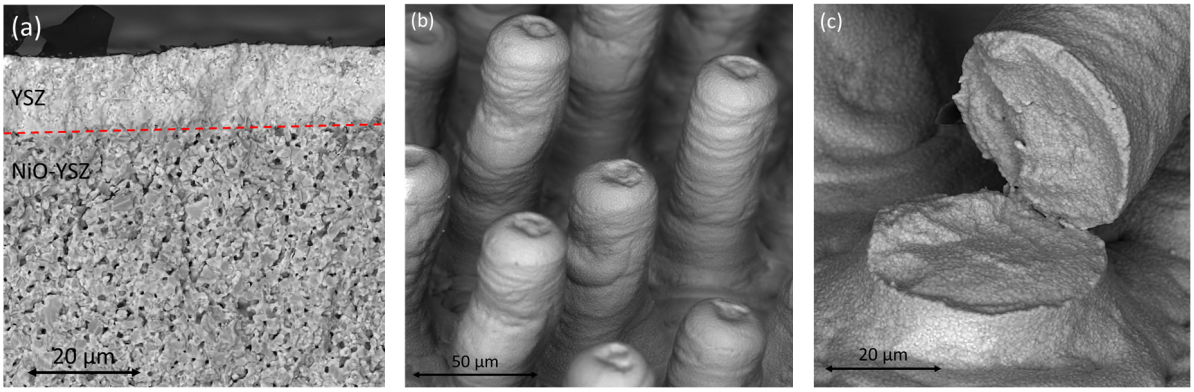


Figure 88. SEM photomicrographs of the (a) electrolyte; (b) pillar array; and (c) broken pillar.

Figure 89 and **Figure 90**, respectively show SEM photomicrographs of the electrochemically characterised SOERs for the LSM sintered at 1000 and 1100 °C. The diameter of the pillars with LSM for the 100 and 400 printed layers were 37 and 46 μm, respectively. Therefore, the thicknesses of the LSM layers surrounding the pillars were 2.5 and 7 μm, respectively, and appeared to be uniform with increasing pillar height.

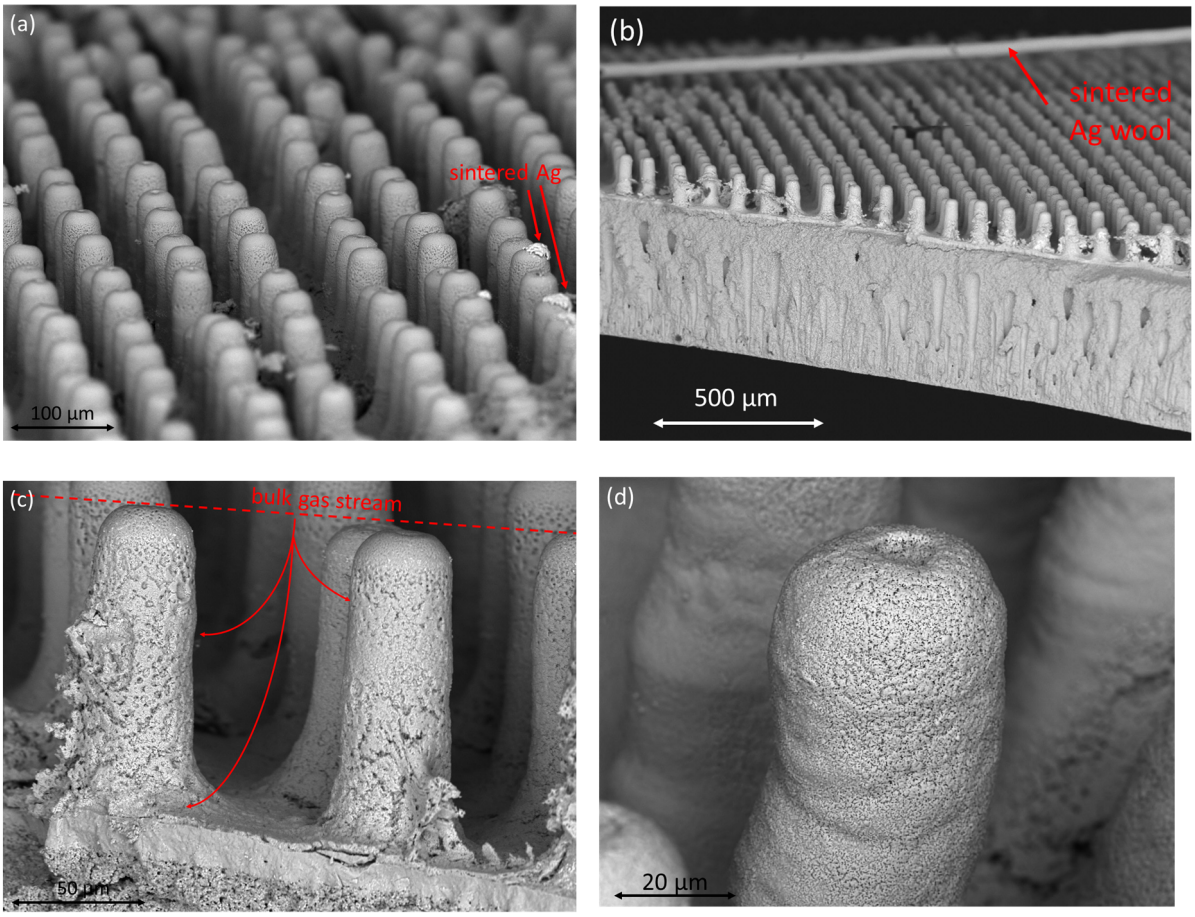
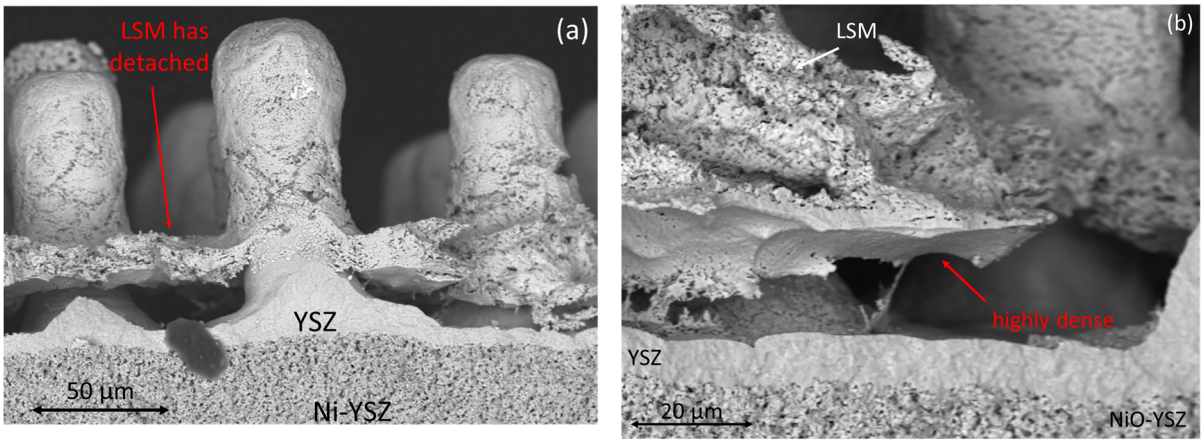


Figure 89. SEM photomicrographs of the pillared oxygen-electrode array with LSM sintered at 1000 °C, post electrochemical characterisation.



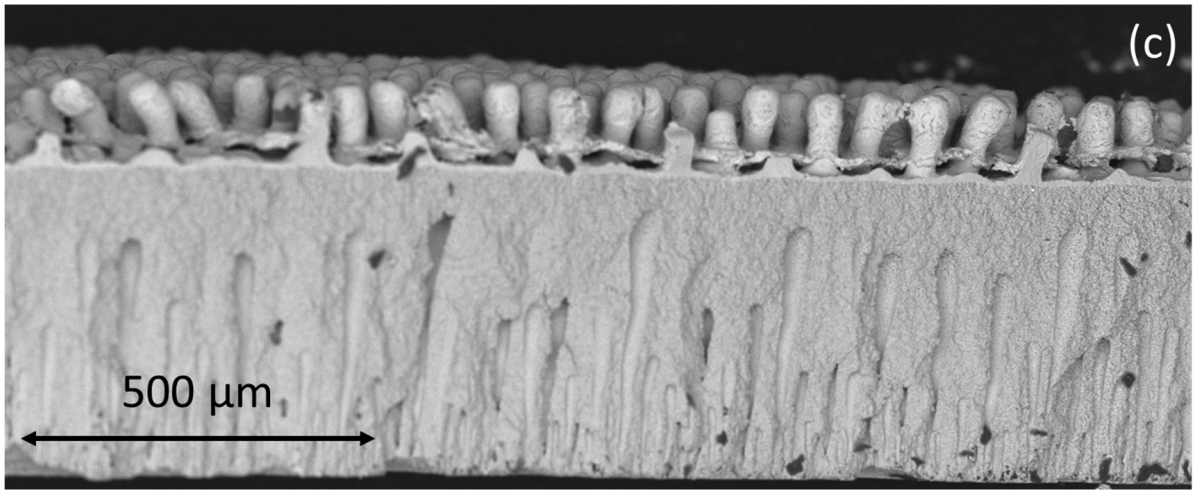


Figure 90. SEM photomicrographs of the pillared oxygen-electrode array with LSM sintered at 1100 °C, post electrochemical characterisation.

Significant microstructural observations were:

- Sintering 100 printed layers of LSM at 1000 °C resulted in a layer of thickness of *ca*. 4 µm, which appeared to completely cover the pillar and electrolyte surface as shown in **Figure 89**.
- Sintering 400 printed layers of LSM at 1100 °C resulted in a layer of thickness of *ca*. 12 µm, which sintered well to the pillars but detached completely from the electrolyte surface, as shown in **Figure 90**. The density of the detached region appeared to be greater than other regions of LSM.
- Contrary to expectations (Chapter 9), large voids within the LSM layer were present between pillars (**Figure 89b**), facilitating un-hindered mass transport of O_2 from the bulk gas stream to the TPBs, for both 100 and 400 layers of LSM. Therefore, the oxygen concentration gradient between pillars predicted in Chapter 9 represents the worst case scenario.
- **Figure 89b** and **Figure 90c** show the porous channels through the NiO-YSZ support layer did not cause bending during NiO-YSZ|YSZ co-sintering, and should facilitate rapid mass transport to the electro-active region from the bulk fuel gas stream.
- The current collecting Ag phase appears to have sintered to the top of the pillars, as shown in **Figure 89a**, which would degrade performance by blocking TPBs.

- The crack present within the electrolyte shown in **Figure 89c** probably occurred during SEM sample preparation, which required the SOER to be fractured, for cross-sectional imaging.

10.3.2. Electrochemical Characterisation

10.3.3. Hydrogen – Air Fuel Cell Operation

Exposing the fuel and oxygen-electrodes to dry H_2 and stagnant O_2, respectively, at 707, 752, and 788 °C, resulted in measured OCPDs of 1.16, 1.15, and 1.15 V, for the LSM sintered at 1100 °C, and 1.12, 1.14, and 1.15 V, for the LSM sintered at 1100 °C. The measured OCPDs were all similar, as expected because each electrolyte was prepared identically, and all indicated gas-tightness, for all operating temperatures. A comparison of fuel cell power densities with varying current density and operating temperature is shown in **Figure 91**. The power densities for all operating temperatures for electrodes with LSM sintered at 1100 °C were greater than those for electrodes with LSM sintered at 1000 °C, by *ca*. a factor of 2.

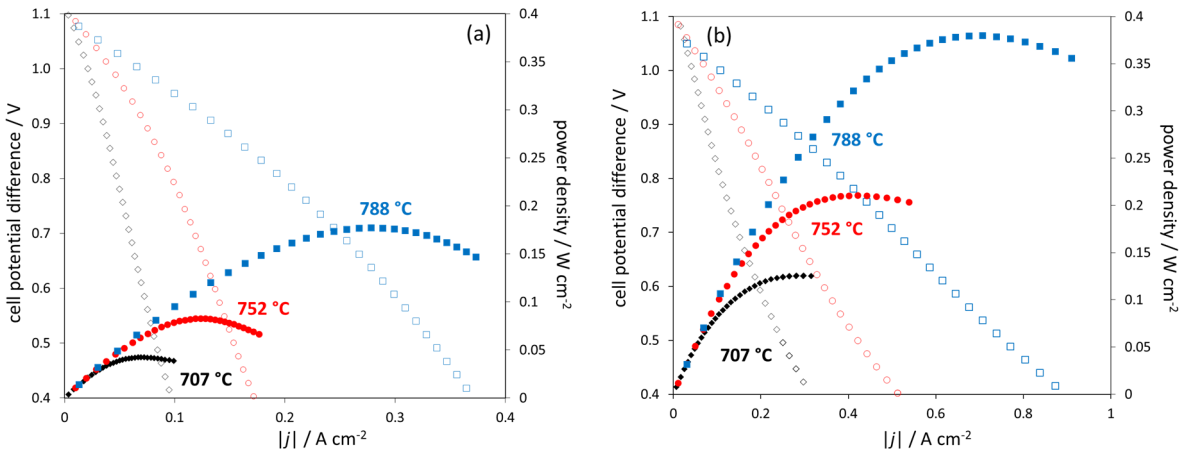


Figure 91. Effect of current density on cell potential difference (hollow markers) and power densities (filled markers) for cells operating with H_2 at 707, 752, and 788 °C with the YSZ-LSM electrodes sintered at (a) 1000 °C; and (b) 1100 °C. Cell potential difference scan rate = 20 mV s^{-1}.

Nyquist plots for the same SOERs at OCPD, are given in **Figure 92**. For all operating conditions, the total polarisation for the LSM sintered at 1000 °C was greater than at 1100 °C, suggesting that the TPB density was lower.

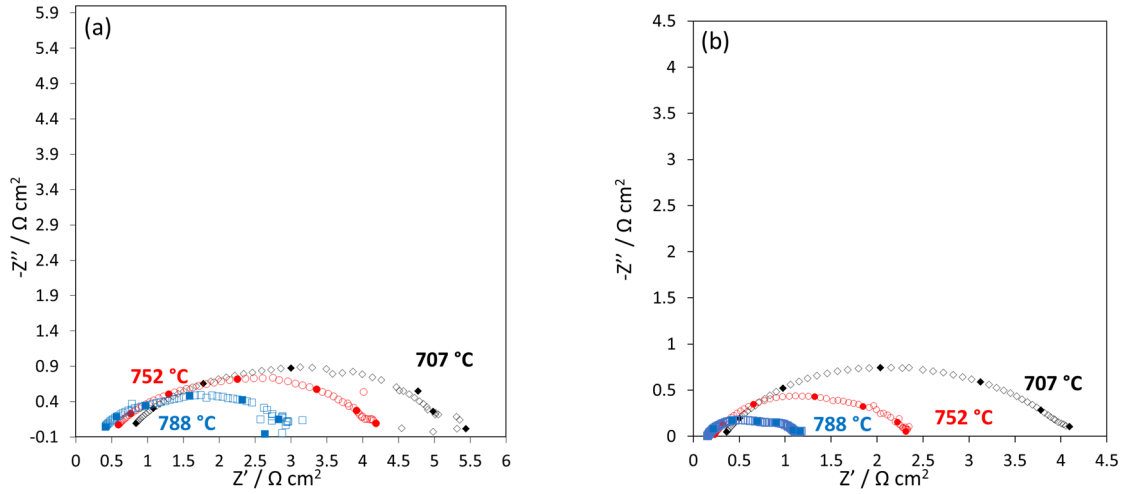


Figure 92. Nyquist plots for reactors at open circuit potential and operating with H_2 at 707, 752, and 788 °C. LSM electrode sintered at (a) 1000 °C; and (b) 1100 °C. Filled markers indicate order of magnitude intervals in frequency over 0.1 – 10^5 Hz.

Unlike the impedance measurements recorded for YSZ-LSM composite electrodes in Chapter 7, under all conditions except at 788 °C, for the LSM sintered at 1100 °C, only a single arc was evident. The summit frequencies for each arc present are shown in **Table 20**.

Table 20. Summit frequencies for the Nyquist plots given in **Figure 92** and **Figure 94**.

Sintering *T* / °C:	1000 °C / Hz		1100 °C / Hz	
Operating *T* (°C) / Gas mixture	H_2 / air	CO-CO_2 / air	H_2 / air	CO-CO_2 / air
707	80	20	50	50
752	50	30	200	200
788	60	50	500, 20*	500

* Both a high and low-frequency summit was observed, so both values are given.

The electrochemical characterisations for additional pillared oxygen-electrode SOFCs fabricated in an identical way are shown in Appendix 12: Electrochemical Characterisations of Pillar-array Oxygen-electrodes.

10.3.4. Electrolysis with CO/CO_2

The OCPDs at 707, 752, and 788 °C for the LSM sintered at 1000 and 1100 °C, were 1.007, 0.988, and 0.968 V, and 1.03, 0.988, and 0.967 V, respectively. These differed from the theoretical OCPDs of 0.989, 0.967, and 0.950 V at the same operating temperatures (27), but were highly reproducible between different SOERs. The reason for the slightly higher values

than expected could result from residual H_2 in the bulk gas stream, as all electrolysis measurements were conducted immediately after fuel cell mode with H_2, or more probably that the gas flow meters were not properly calibrated, so the CO/CO_2 ratio was higher than expected; the measured OCPDs suggested a CO/CO_2 ratio of *ca*. 1.4 – 1.6. **Figure 93** shows the measured current densities of the SOERs sintered at 1000 and 1100 °C with varying cell potential difference, for all operating temperatures. As with fuel cell mode, the performance of the LSM sintered at 1100 °C was greater than for LSM sintered at 1000 °C, by *ca*. a factor of 2. Some fuel cell mode measurements were taken, as shown, to investigate the reversibility of the SOERs.

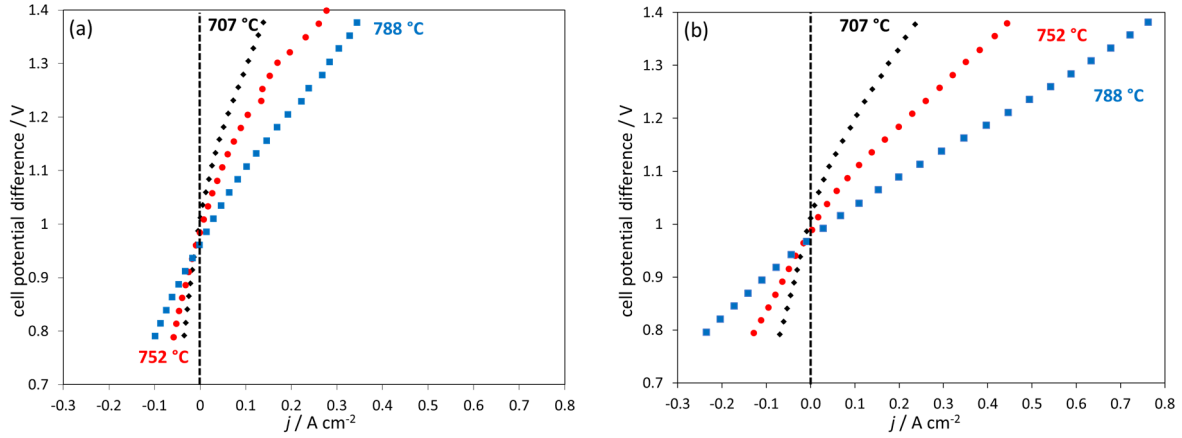


Figure 93. Effect of current density on cell potential differences for SOERs with LSM sintered at (a) 1000 °C; and (b) 1100 °C, operating with CO/CO_2.

Nyquist plots for the same SOERs and operating conditions are presented in **Figure 94**. For all arcs, only a single summit was observed, and the summit frequencies for each are given in **Table 20**. As with H_2 measurements, the total impedance for the LSM electrode sintered at 1000 °C was greater than at 1100 °C. For LSM sintered at 1000 °C, the high-frequency arc was apparent, but did not have a unique summit.

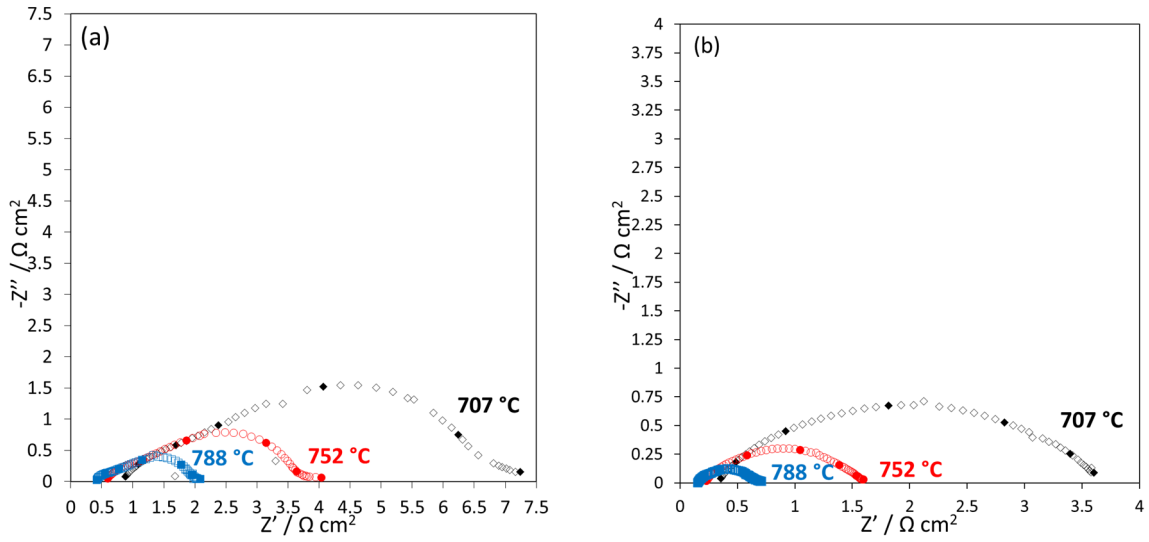


Figure 94. Nyquist plots for cells at OCPD and operating with CO/CO_2 at 707, 752, and 788 °C; LSM electrode sintered at (a) 1000 °C; and (b) 1100 °C. Filled markers indicate order of magnitude intervals in frequency over 0.1 – 10^5 Hz.

The electrochemical characterisations for an additional pillared oxygen-electrode SOE fabricated in an identical way is shown in Appendix 12: Electrochemical Characterisations of Pillar-array Oxygen-electrodes.

10.4. Discussion

Sintering 400 layers of LSM at 1100 °C resulted in a significant detachment of the LSM from the electrolyte and pillar base, shown in **Figure 90**. The simulation results shown in **Figure 83** show that the detached region was expected to have the greatest electrochemical activity, so this effect would have significantly decreased the electrochemical performance of the electrode. Despite the detachment, the maximum power density in fuel cell mode, and electrolytic current densities at 1.4 V, at 707, 752, and 788 °C, were 0.13, 0.21, and 0.38 W cm^{-2}, and 0.24, 0.44, and 0.76 A cm^{-2}, respectively. Comparing these to the electrochemical measurements of the composite YSZ-LSM electrode sintered at 1100 °C reported in Chapter 7, they were only *ca*. 45 – 55 % lower.

Evidence that the LSM shrinkage mechanism resulting in detachment from the electrolyte occurred during sintering was that the detached region of LSM was highly dense, compared to the LSM sintered to pillars (**Figure 90b**). The mechanism of detachment was analogous to the printed NiO electrolyte detachment, described in Section 5.4.2.4. Therefore, for the same LSM and pillar array, the most straightforward strategy to obviate LSM detachment from the electrolyte was to decrease the LSM layer thickness, and reduce total shrinkage by reducing the

sintering temperature to 1000 °C. As **Figure 89** shows clearly, this worked; however, the electrochemical performance was significantly reduced, with measured maximum fuel cell mode power densities and electrolytic current densities (1.4 V) at 707, 752, and 788 °C of 0.04, 0.08, and 0.18 W cm^{-2}, and 0.13, 0.28, and 0.35 A cm^{-2}, respectively (**Figure 91** and **Figure 93**). There were two explanations for the reduced electrochemical performance:

i) The thinner LSM layer increased ohmic potential losses for supply / removal of electrons to / from TPBs (reducing overpotential);

ii) The sintering temperature was insufficiently high for extensive YSZ|LSM sintering, resulting in a lower surface TPB density.

In the first instance, due to spatial current density distributions, the LSM ohmic potential loss could only be estimated by adjusting the model in Chapter 9 for the real LSM printed geometry, with the dimensions reported in Section 10.3.1. The predicted ohmic loss could then be found by simulating the geometry for a range of potential differences, identifying the solution that matched the measured total current density, and extracting the ohmic drop within the LSM phase for this solution. The following potential losses within the LSM phase (100 layers, sintered at 1000 °C) were found, under anodic and cathodic polarisations, at 707, 752, and 788 °C: 0, 0.02, 0.03 mV, and 0.01, 0.02, 0.03 mV, respectively. **Figure 95** shows the ohmic potential drop in LSM at 788 °C, 0.4 A cm^{-2}, anodic polarisation (the largest ohmic loss within LSM). As expected, it was highest at the pillar base, and decreased with pillar height due to lower currents and increasing distance, as in equation (34). These losses in potential were negligible, and did not explain the significant drop in performance.

Consequently, the latter reason was responsible for the loss in performance, *i.e.* reduced sintering temperature resulted in a significantly lower TPB density at the YSZ | LSM interface. 100 LSM layers provided adequate electrical contact between the LSM and Ag current collector, so future experiments should establish the relationship between the sintering temperature ($1000 < T\,(°C) < 1300$) and number of printed layers (≤ 100) that optimises TPB density.

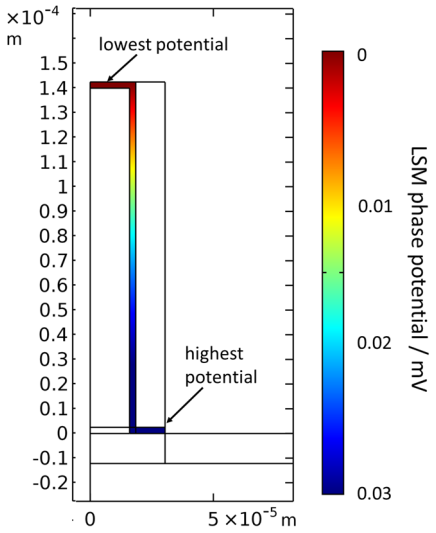


Figure 95. Simulated LSM phase potential for anodic polarisation at 788 °C, net current density 0.4 A cm^{-2}.

10.5. Conclusions

In this Chapter, the results of the electrochemical simulations reported in Chapter 9 were used to design tailored architectures for the oxygen-electrode of SOERs. Inkjet printing was used to fabricate the YSZ electrolyte and hexagonal pillar arrays on a NiO-YSZ substrate, which were co-sintered. The post-sintering pillar diameter, height and spacing were 32, 140, and 60 μm, respectively. LSM was inkjet printed onto the pillars to complete the oxygen-electrode, with varying thickness (2.5 – 7 μm) and sintering temperature (1000 – 1100 °C), to form the SOER: Ni-YSZ|YSZ|YSZ (pillars)|LSM.

The resulting SOERs were characterised electrochemically at 707 – 788 °C, as fuel cells operating with dry H_2, and electrolysers with CO/CO_2 (1/1 ratio). Power and current densities for 7 μm thick LSM sintered at 1100 °C were *ca*. 50 % lower than those achieved for the composite YSZ-LSM structures reported in Chapter 7. However, considerable detachment of the LSM layer from the pre-sintered YSZ was observed, which occurred during LSM sintering. This indicated that the electrochemical performance of the pillared electrodes could be increased significantly if detachment could be prevented. Decreasing LSM thickness and sintering temperature to 2.5 μm and 1000 °C, respectively, mitigated the LSM detachment; however, the resulting TPB density was significantly lower. Consequently, the SOER power and current densities, under the same operating conditions, were decreased by *ca*. 50 %.

The results reported here demonstrated that pillared oxygen-electrodes can be fabricated by inkjet printing, whereby each phase is localised to pre-determined locations within the

electrode. Complications occurred during the sintering of the LSM, but it seems probable that these can be avoided, which should result in electrodes with a competitive electrochemical performance to conventionally-fabricated composite YSZ-LSM electrodes; this will be the subject of future experiments.

11. Inkjet Printed NiO Electrode

Chapter Summary

This Chapter reports results of inkjet printing the LSM and NiO inks developed and reported in Sections 5.3 and 5.4, respectively, to fabricate the electrodes for the electrolyte-supported solid oxide fuel cell: Ni|YSZ|LSM. Electrochemical characterisations with varying temperature under hydrogen were performed. Chrono-potentiometric results with varying current densities over *ca*. 100 hours were taken to provide insights into the electrochemical behaviour of the inkjet printed electrodes.

11.1. Introduction

Printable and colloidally-stable inks to fabricate the functional layers of solid oxide electrochemical reactors (SOERs) were reported in previous chapters in this Thesis, and inkjet printed electrolytes and oxygen-electrodes were characterised electrochemically. In this Chapter, the optimised NiO ink and printing procedure developed and reported in Section 5.4 were deployed to fabricate the fuel-electrode of SOERs, replacing the conventionally-fabricated composite NiO-YSZ substrate used in previous experiments. The NiO-YSZ substrate mechanically-supported the SOER, and was *ca*. 400 μm thick (shown in **Figure 90c**); therefore, to ensure this SOER had sufficient mechanical strength for handling and testing, an electrolyte-supported geometry was adopted, with the structure Ni|YSZ (mechanical support)|LSM.

11.2. Materials and Methods

11.2.1. Substrate

Commercially-available, pre-sintered cylindrical YSZ substrates 250 μm thick, 25 mm diameter (Fuel Cell Materials, USA) were used as electrolyte supporting layers, either side of which the electrodes were inkjet printed.

11.2.2. Fuel-electrode Fabrication

NiO required a greater sintering temperature than LSM, therefore the fuel-electrode was fabricated before the oxygen-electrode. The aqueous NiO ink with composition reported in Section 5.4.2.2 was deposited using Dimatix DMC 10 pL droplet volume printheads (Fujifilm, USA), with an identical droplet ejection profile to that reported in Section 5.4.2.3. The splat diameter and droplet overlap on the substrate were 45 and 15 μm, respectively. 20 layers were inkjet printed onto the substrate to produce a cylindrical film of 7 mm diameter, which was sintered at 1300 °C with the temperature profile reported in Section 5.4.1.5.

11.2.3. Oxygen-electrode Fabrication

After sintering the NiO electrode, 14 layers of the butanol-based LSM ink developed and reported in Section 5.3 were inkjet printed onto the opposite side of the YSZ, using another Dimatix DMC 10 pL droplet volume printhead (Fujifilm, USA), to produce a cylindrical film of 10 mm diameter, co-axial with the NiO electrode. The droplet ejection profile was reported in Section 5.3.2.3; resulting structures were sintered at 1100 °C with the temperature profile reported in Section 10.2.4.

11.2.4. Electrochemical Characterisation

The SOERs were mounted in the experimental apparatus as previously (**Table 13**), where the silver wool and mesh were replaced by gold equivalents (0.05 mm diameter gold wire, 99.995 % purity, and 52 mesh woven from 0.102 mm diameter wire 99.99 % purity, respectively; Alfa Aesar, USA), to mitigate degradation resulting from Ag mobilisation (see Section 7.3.5).

NiO was reduced to Ni for *ca*. 1 h in a binary He and H_2 mixture at 707 °C (1 °C min^{-1} temperature gradient), at flow rates 30 and 5 cm^3 min^{-1}, respectively. Afterwards, the He supply was switched off, and the H_2 flow rate was increased to 20 cm^3 min^{-1} for an additional 30 minutes.

The oxygen-electrode was exposed to static air throughout. SOERs were electrochemically characterised in fuel cell mode using dry H_2 with 20 cm^3 min^{-1} flow rate, at operating temperatures of 707, 752, and 788 °C. Electrochemical impedance spectroscopy (10 mV p-p amplitude) at OCPD between 10^5 – 10^{-1} Hz, and experiments varying cell potential at 10 mV s^{-1} were performed for the electrochemical characterisation. Afterwards, chrono-potentiometric measurements were undertaken at various applied currents over *ca*. 100 hours.

11.3. Results and Discussion

11.3.1. Reactor Fabrication

A photograph of the NiO electrode is shown in **Figure 66a**. **Figure 96** shows SEM photomicrographs of the LSM electrode, after electrochemical characterisations. It appeared to be well adherent to the YSZ electrolyte, and was *ca*. 1.4 μm thick, equivalent to 100 nm $layer^{-1}$. Large pores were observed in the electrolyte, but were not believed to be percolated. The LSM surface was highly porous (**Figure 96b**), which should facilitate gas transport the TPBs located at the YSZ|LSM interface.

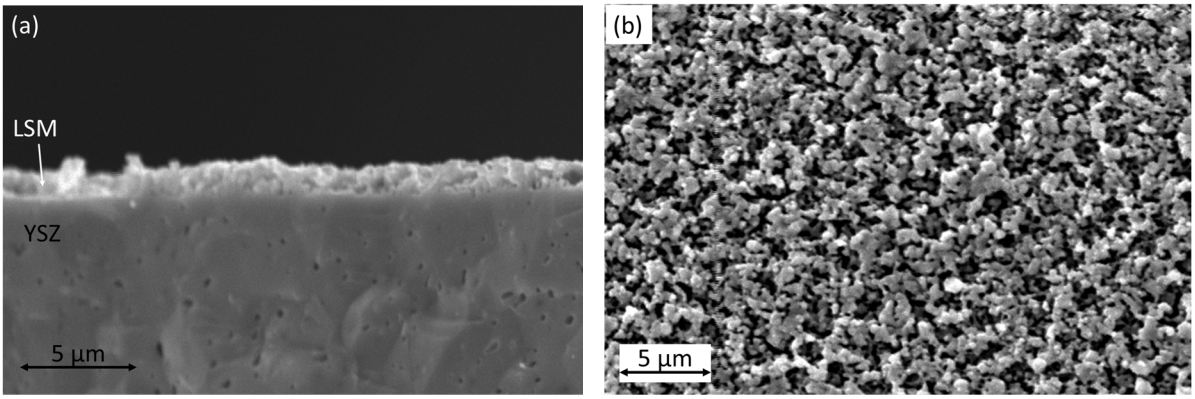


Figure 96. SEM photomicrographs of the printed LSM electrode after sintering and electrochemical characterisation (a) side; and (b) surface views. Dr. Tao Li, Imperial College London, performed the SEM experiments in this instance, (JEOL JSM-5610LV, Japan, 20 kV beam).

11.3.2. Electrochemical Characterisation

Impedance measurements at OCPD were taken periodically during the NiO reduction period at 707 °C; the results are shown, with duration into the reduction period, as Nyquist plots in **Figure 97a**. Evidently, with increasing reduction time, the impedance of the SOER increased up to *ca*. 50 minutes, beyond which it remained constant. Therefore, it can be concluded that reduction rate was negligible at > 50 minutes, indicating most NiO had been reduced.

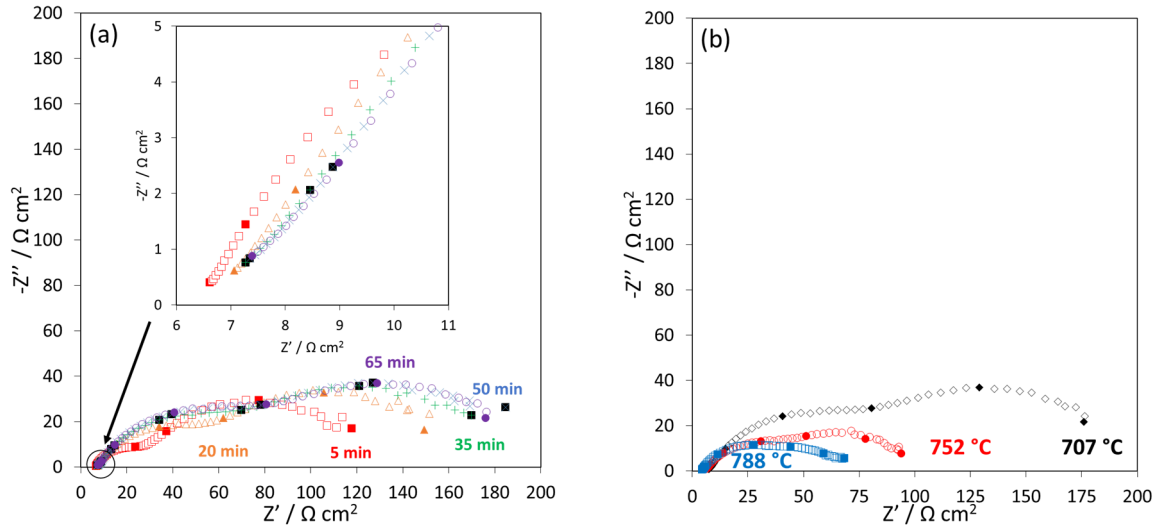


Figure 97. Nyquist plots showing impedance variation (a) with time during NiO reduction at 707 °C; and (b) with temperature. Filled markers denote decade intervals in frequency over 0.1 – 10^5 Hz.

During NiO reduction, two arcs for each impedance plot were evident, which corresponded to an intermediate-frequency process, occurring at *ca*. 50 Hz, and a low-frequency processes occurring at *ca*. 1 Hz. The summit frequencies listed in **Table 21** remained approximately equal, as expected because operating conditions remained constant; however, the SOER total impedance increased by *ca*. 50 % after 50 minutes of NiO reduction. Charge transfer processes are expected to have a characteristic frequency of *ca*. 1 – 10 kHz, so both arcs were believed to correspond to mass transport processes occurring in the fuel- and oxygen-electrodes. The summit frequency of the low-frequency arc remained approximately constant throughout, so this is believed to have correspond to mass transport within the porous LSM, which had a constant microstructure during reduction. Consequently, the summit frequency at *ca*. 50 Hz is believed to correspond to H_2 diffusion to TPBs within the porous Ni(O) electrode, which changed due to the varying Ni(O) microstructure. This assumption is consistent with the relative diffusion coefficients of H_2 and O_2 that can be approximated using equations (47) and (49), predicting that the diffusivity of H_2 was *ca*. 20 times greater than O_2 (in N_2) in equivalent microstructures.

Table 21. The summit frequencies for the Nyquist plots in **Figure 97**, where distinguishable, and OCPDs after NiO reduction.

Time / mins, or temperature	Intermediate summit frequency / Hz	Low summit frequency / Hz	OCPD / V
5	indistinct	1	-
20	50	0.6	-
35	indistinct	1	-
50	indistinct	1	-
65 (707 °C)	63	1	1.008
752 °C	63	2	0.980
788 °C	100	indistinct	0.975

The NiO reduction kinetics depend on microstructure, and are not equivalent to the shrinking-core mechanism because NiO reduction rate is independent of NiO surface area. As Ni forms, it agglomerates at an equivalent rate to NiO reduction (289), accompanied by an approximately 41 % reduction in volume (*c.f.* $\rho_{NiO} = 6.67$ g cm^{-3}; $\rho_{Ni} = 8.9$ g cm^{-3} (317, 318)). **Figure 98** shows schematically how this Ni coarsening mechanism could significantly reduce the TPB density, which is consistent with the increased SOER polarisation measured over time (319). The

sintered Ni|YSZ surface area is not expected to increase during NiO reduction because the surface energy of Ni (2.34 J m^{-2} (320)) > YSZ; therefore, the driving force for Ni coarsening is greater than Ni|YSZ surface area reduction. The inset Nyquist plot shown in **Figure 97a** shows that high-frequency processes (1 – 10 kHz) were essentially independent of TPB density, which agrees with the literature (319). At 0.1 Hz, a large capacitance was measured for all Nyquist plots suggesting that it was caused by a diffusion process.

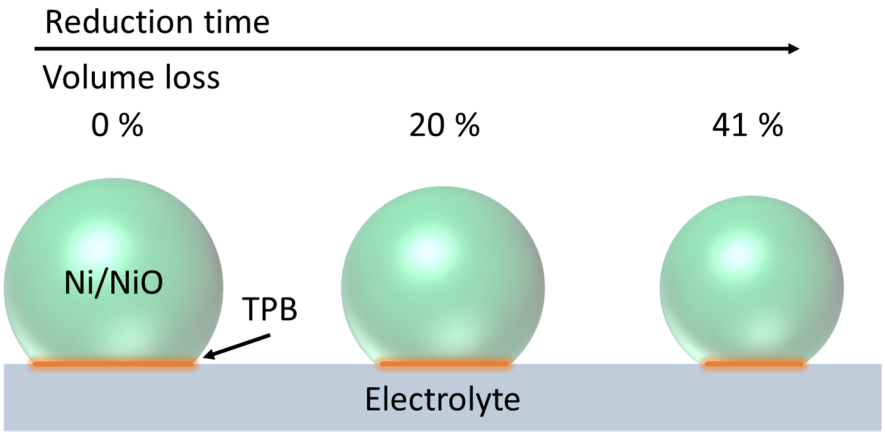


Figure 98. Schematic of TPB length decrease during NiO reduction.

Figure 97b shows SOER impedance variation at OCPD with increasing temperature; the reactor polarisation reduces due to enhanced electrochemical kinetics. Two arcs can be observed at all temperatures, with characteristic frequencies consistent with mass transport / conversion processes that dominated the SOER polarisation, given in **Table 21**. The measured OCPDs at each operating temperature are shown in **Table 21**; evidently, they were lower than the theoretically predicted values, probably due to gas leakage resulting from poor reactor sealing, as the electrolyte was very thick and expected to be gas-tight. The effect of current density on measured power densities at each operating temperature is shown in **Figure 99**. Maximum power densities of 2.2, 3.8, and 11 mW cm^{-2} were achieved at 707, 752, and 788 °C. These were significantly lower than peak power densities reported in previous chapters at the same temperatures due to the significantly lower TPB density at both electrodes and significantly thicker electrolyte (> 10 times as thick as previous experiments).

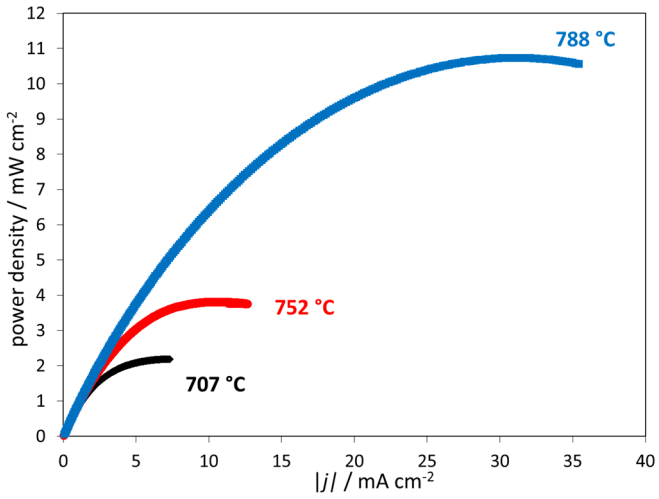


Figure 99. Effect of current density on power densities for cells operating with H_2 at 707, 752, and after 4 hours of chrono-potentiometry at 10.4 mA cm^{-2}, at 788 °C; scan rate was 10 mV s^{-1}.

The *j* - *U* measurements at 707 and 752 °C were taken within 5 minutes of reaching the indicated temperature. The measurement at 788 °C was taken after 4 hours of 10.4 mA cm^{-2} constant current (in fuel cell mode), shown by the red data points in **Figure 100**.

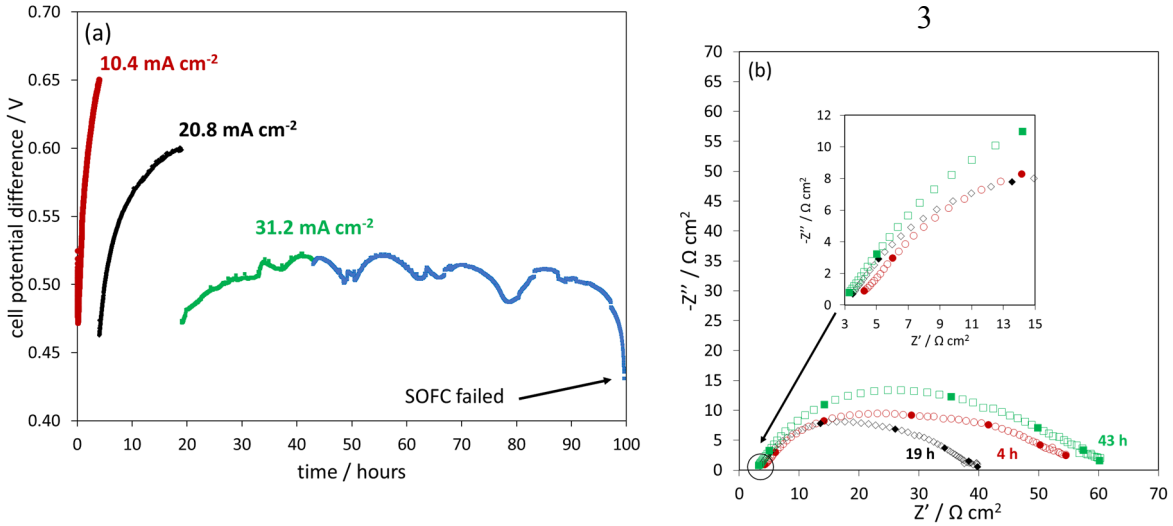


Figure 100. (a) Effect of applied current density on cell potential difference over time; and (b) Nyquist plots taken after each chrono-potentiometry measurement at OCPD (showing cumulative time) at 788 °C.

Evidently, during the chrono-potentiometry period, electrochemical performance increased significantly, and the cell overpotential reduced by *ca*. 175 mV. The current density was subsequently increased to 20.8 mA cm^{-2} for 15 hours, and electrochemical performance continued to increase so that a steady-state was not obtained after 19 hours of chrono-

potentiometry. Impedance measurements taken after 4 hours at 10.4 mA cm^{-2} (red) and 15 hours at 20.8 mA cm^{-2} (black) are shown in **Figure 100b**.

Between 4 – 19 hours of fuel cell operation, the high frequency (10^5 - 10^3 Hz) impedance measurements were unchanged; however, the total cell polarisation reduced by *ca*. 27 %, which was consistent with impedance measurements from a previous study on cathodically-polarised LSM (321). The most significantly different region of the Nyquist plots after 4 and 19 hours occurred at < 100 Hz, suggesting that changes in polarisation resulted from conversion / mass transport processes. This can be reasoned by considering the concentration of oxygen vacancies in LSM, which depends on polarisation history (107). After cathodic polarisation, LSM may be reduced, increasing the oxygen vacancy concentration within the lattice. This can activate a 'bulk' diffusion path through LSM, enhancing O^{2-} ion transport to TPBs (314), and changing the nature of the conversion between adsorbed O and O_2 (g). However, the impedance data recorded after 43 hours of fuel cell operation would appear to contradict this theory, indicating that total polarisation increased by *ca*. 50 %. This degradation mechanism could result from changes to the nickel electrode, *e.g*. due to additional Ni coarsening, which would reduce the TPB density and diminish performance, despite increased oxygen transport at the cathode. To prevent nickel coarsening from degrading electrochemical performance, it would be necessary to support the nickel catalyst on a thermally-stable substrate, which has been shown to significantly decrease coarsening of Ni catalysts (322). Supporting the Ni catalyst on alumina would mitigate coarsening, and allow structures to be produced with localised TPBs; however, a YSZ support would provide a significantly higher TPB density, and therefore would be preferable.

After *ca*. 95 hours of chrono-potentiometry, cell overpotential increased over 5 hours until it failed catastrophically; the OCPD was measured as -0.15 V indicating significant leakage of gas, probably through the electrolyte. After cooling the SOER, large cracks were observed that penetrated through the electrolyte, shown in **Figure 101**, which presumably caused the failure. It is not understood why this failure mechanism occurred; however, possible reasons include a change in sealant properties after reaction with the silver wires at high temperature, and a non-uniform temperature gradient over the SOER due to non-uniform heat generation within the furnace.

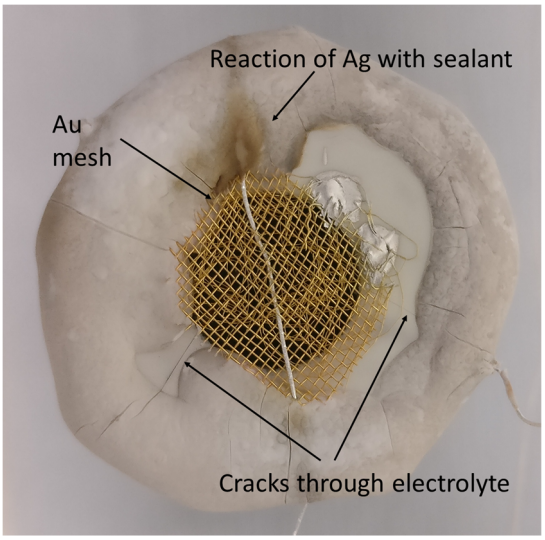


Figure 101. Photograph of the SOER mounted on an alumina tube for testing, with LSM electrode exposed.

11.4. Conclusions

In this Chapter, the butanol-based LSM and aqueous NiO inks developed and reported in Sections 5.3 and 5.4, respectively, were inkjet printed to fabricate the electrolyte-supported SOER: NiO (printed)|YSZ|LSM (printed). During the NiO reduction in diluted hydrogen, electrochemical impedance measurements were taken periodically which showed that the cell polarisation increased significantly over time. This was attributed to Ni coarsening, which reduced the TPB density. After completing NiO reduction, electrochemical impedance spectroscopy and varying cell potential difference measurements were taken at 707, 752, and 788 °C. Maximum power densities of 2.2, 3.8, and 11 mW cm^{-2} were achieved at the respective operating temperatures. Chrono-potentiometric experiments at various fuel cell mode current densities were completed at 788 °C, which significantly increased electrochemical performance due to LSM reduction, which increased oxygen vacancy concentration and activated a bulk O^{2-} ion transport pathway through LSM to the TPBs. However, after < 50 hours of fuel cell operation, electrochemical impedance measurements indicated that nickel coarsening had occurred and significantly reduced the TPB density. Therefore, for long-term operation, it would be necessary to support the nickel catalyst, *i.e.* on YSZ.

12. Conclusions and Future Work

Chapter Summary

This Chapter outlines the main results of this research project with respect to the objectives that were described in Chapter 3. Recommendations for future work are discussed.

12.1. Conclusions

The aim of this research project was to validate inkjet printing as an effective, scalable, environmentally benign fabrication method for solid oxide electrochemical reactors (SOERs) with enhanced electrochemical performances compared to those fabricated conventionally, using the most common materials:

- Yttria-stabilised Zirconia (YSZ)
- Gadolinium-doped Ceria (CGO)
- Lanthanum Strontium Manganite (LSM)
- Nickel Oxide (NiO)

After reviewing the literature covering ink formulation and inkjet printing the functional layers of SOERs, the research project objectives were devised. This Chapter explains how the results from this research project met the objectives, each as an individual sub-heading, and where relevant, recommended future work to accomplish the project aim is identified.

12.2. Aqueous Inks Formulation

Previously formulated inks for inkjet printing the functional layers of SOERs were primarily organic-based (*i.e.* ethanol, α-terpineol solutions). However, aqueous-based inks are more environmentally benign, hence suitable for manufacturing. After establishing that pH-induced colloidal stabilisation was unsuitable or ineffective for all conventional SOER materials, printable YSZ, CGO, LSM, and NiO inks were formulated, stabilised by organic electrostatic dispersants, and inkjet printed successfully. However, after heat treating the LSM films to combust organics and sinter the particles, they were destroyed by dispersant combustion. Unfortunately, an alternative dispersant could not be found; therefore, this should be the subject of future research. To complete the other objectives, a butanol-based LSM ink formulation was developed.

The high colloidal stabilities of the YSZ, CGO, and NiO inks were validated experimentally by the absence of sedimentation over months, and supported by DLVO theory predictions, confirming their essentially infinitely-long shelf-life, hence practicality for industrial processes.

12.3. Improving Lateral Resolution

The lateral resolution of inkjet printers depends critically on the ejected droplet spread diameter on the substrate, which is influenced primarily by the in-flight diameter and droplet placement

reproducibility. Both factors are determined by the printhead nozzle diameter and droplet ejection settings. To improve the resolution of inkjet printed deposits, printheads with smaller nozzle diameters (20 – 50 μm) were used. This required significantly smaller colloids than those reviewed in the literature, to prevent nozzle clogging. Using smaller particles promoted cracking in drying films, and delamination during sintering, which had not been reported previously. These problems were overcome to produce sintered functional layers of all materials attempted, suitable for SOERs.

The nominal volume of ejected droplets was limited to 10 – 30 pL; consequently, lateral resolution was limited to *ca*. 35 μm. The methodologies developed in this research project were designed to be applicable to the next generation of inkjet printer printheads that can eject droplets with < 1 pL volume.

12.4. Inkjet Printing 3D Microstructures

The literature review indicated that electrochemical performances of SOER electrodes fabricated by conventional, composite powder mixing methods were limited by unpredictable and irreproducible microstructures; three-dimensional, tailored, inkjet printed electrodes could overcome this problem.

To predict the optimal inkjet printed electrode microstructures, a finite element analysis model was constructed that simulated electrochemical and mass transport kinetics for different YSZ pillar array geometries over a range of operating temperatures and potential differences for the oxygen-electrode. The optimised YSZ microstructures were subsequently inkjet printed, and retained structural integrity, post-sintering, with a lateral resolution of *ca*. 35 μm and aspect ratio of *ca*. 4.4. LSM was inkjet printed onto the sintered YSZ microstructures, for application as an oxygen-electrode. After sintering, the LSM was well adhered to the pillar, but detached from the electrolyte; therefore, future experiments should optimise the LSM sintering profile and / or the pillar array geometry, to accommodate the sintering behaviour of LSM.

Furthermore, future experiments should introduce tailored microstructures into the fuel-electrode, *i.e.* Ni (printed)|YSZ pillars (printed)|YSZ|YSZ pillars (printed)|LSM (printed). This would require the pillar array geometry to be sufficiently close-packed to mechanically-support NiO, and prevent its coarsening during operation.

CGO has a greater conductivity than YSZ; however, it can become reduced during operation, and short circuit the SOER. Therefore, by inkjet printing CGO pillars onto a YSZ electrolyte, and overcoming differences in sintering behaviour, the performance of the pillared-electrodes

could be increased. Furthermore, the CGO could also act as a barrier layer covering the YSZ electrolyte, facilitating lanthanum strontium cobalt ferrite (LSCF) oxygen-electrodes.

12.5. Electrochemical Performance Validation

Initially, gas-tight YSZ electrolytes were inkjet printed and characterised electrochemically in electrolyser mode with CO/CO_2, demonstrating that inkjet printed electrolytes have equivalent electrochemical performances to conventionally-fabricated electrolytes for the Ni-YSZ supported SOER: Ni-YSZ|YSZ (printed)|LSM-YSZ|LSM.

Next, YSZ-LSM composite electrodes were inkjet printed to form the SOER: Ni-YSZ|YSZ (printed)|LSM-YSZ (printed)| LSM, and characterised in fuel cell and electrolyser modes with dry H_2 and CO/CO_2, respectively. Electrochemical results of inkjet printed YSZ-LSM electrodes reported in the literature were low due to the formation of a non-porous 'skin' at the outer electrode surface; this was avoided by optimising ink formulation, resulting in superior electrochemical performances.

The electrochemical performance of the inkjet printed, tailored oxygen-electrodes was measured for the SOER: Ni-YSZ|YSZ (printed)|YSZ pillar (printed)|LSM (printed) in fuel cell and electrolyser modes with dry H_2 and CO/CO_2, respectively. Electrochemical performances were *ca*. 50 % lower than for composite YSZ-LSM electrodes; however, this was promising as the LSM had detached from the electrolyte. Therefore, optimising the LSM layer structure and sintering profile, and characterising the electrodes electrochemically should be the subject of future research.

The SOER: Ni (printed)|YSZ|LSM (printed) was characterised electrochemically in fuel cell mode with dry H_2; however, degradation rates were high. This was caused by Ni coarsening over time; therefore, in future experiments Ni coarsening could be avoided by supporting the Ni on a YSZ scaffold, *i.e.* YSZ pillars, or mixing the NiO and YSZ inks to form a composite electrode.

CGO electrolytes and barrier layers suitable for SOERs were fabricated by inkjet printing; however, these were not comprehensively characterised electrochemically. Therefore, future research to develop colloidally-stable and printable (CGO-)LSCF inks could deploy the inkjet printed CGO electrolyte to produce the low-temperature SOER: Ni-CGO|CGO|CGO-LSCF (printed), or deploy CGO barrier layers to enable the SOER: Ni-YSZ|YSZ|CGO|CGO-LSCF.

13. Bibliography

1. G. W. Crabtree, M. S. Dresselhaus and M. V. Buchanan, *Physics Today* **2004**, 57, 39-44.
2. S. van de Graaff, *Energy Policy* **2016**, 97, 50-59.
3. National Grid, *Demand Data*, https://www.nationalgrid.com/uk/electricity/market-operations-and-data/data-explorer, (accessed 8th January 2018).
4. G. Hundleby and K. Freeman, *Unleashing Europe's Offshore Wind Potential: A New Resource Assessment*, BVG Associates, 2017.
5. M. Šúri, T. A. Huld, E. D. Dunlop and H. A. Ossenbrink, *Solar Energy* **2007**, 81, 1295-1305.
6. Department for Business, Energy & Industrial Strategy Press Office (UK Government) *Fuel Input for Electricity Generation*, https://view.officeapps.live.com/op/view.aspx?src=https://www.gov.uk/government/uploads/system/uploads/attachment_data/file/632667/DUKES_5.1.1.xls, 2017.
7. M. H. Albadi and E. F. El-Saadany, *Electric Power Systems Research* **2008**, 78, 1989-1996.
8. J. Torriti, M. G. Hassan and M. Leach, *Energy* **2010**, 35, 1575-1583.
9. P. Bradley, M. Leach and J. Torriti, *Energy Policy* **2013**, 52, 312-327.
10. X. Luo, J. Wang, M. Dooner and J. Clarke, *Applied Energy* **2015**, 137, 511-536.
11. S. J. Kazempour, M. P. Moghaddam, M. R. Haghifam and G. R. Yousefi, *Renewable Energy* **2009**, 34, 2630-2639.
12. M. Budt, D. Wolf, R. Span and J. Yan, *Applied Energy* **2016**, 170, 250-268.
13. H. Chen, T. N. Cong, W. Yang, C. Tan, Y. Li and Y. Ding, *Progress in Natural Science* **2009**, 19, 291-312.
14. J. Xu, R. Z. Wang and Y. Li, *Solar Energy* **2014**, 103, 610-638.
15. International Energy Agency, *Energy Storage*: https://www.iea.org/publications/freepublications/publication/TechnologyRoadmapEnergystorage.pdf, 2014.
16. E. Williams, *Dinorwig: the electric mountain*, National Grid PLC, 1991.
17. J. A. P. Lopes, N. Hatziargyriou, J. Mutale, P. Djapic and N. Jenkins, *Electric Power Systems Research* **2007**, 77, 1189-1203.
18. B. Snyder and M. J. Kaiser, *Renewable Energy* **2009**, 34, 1567-1578.
19. International Hydropower Association, https://www.hydropower.org/hydropower-

pumped-storage-tool, (accessed 9th January, 2018).
20. H. Cavendish, *Philosophical Transactions (1683-1775)* **1766**, 56, 141-184.
21. W. Nicholson, *Journal of Natural Philosophy, Chemistry and the Arts* **1802**, 5, 179.
22. J. Verne, *The Mysterious Island*, Pierre-Jules Hetzel, France, 1874.
23. R. Lan, J. T. S. Irvine and S. Tao, *International Journal of Hydrogen Energy* **2012**, 37, 1482-1494.
24. Centre for Disease Control and Prevention, *Carbon Monoxide*, https://www.cdc.gov/niosh/idlh/630080.html, (accessed 9th January, 2018).
25. World Nuclear Association, *Heat Values of Various Fuels*, http://www.world-nuclear.org/information-library/facts-and-figures/heat-values-of-various-fuels.aspx, (accessed 9th January, 2018).
26. M. W. J. Chase, *Journal of Physical and Chemical Reference Data Monographs* **1998**, 9, 1-1951.
27. K. Huang and J. B. Goodenough, *Solid Oxide Fuel Cell Technology*, Woodhead Publishing in Energy, Cambridge, 2009.
28. N. Muradov, *International Journal of Hydrogen Energy* **2001**, 26, 1165-1175.
29. M. Emons, K. Obata, T. Binhammer, A. Ovsianikov, B. N. Chichkov and U. Morgner, *Optical Materials Express* **2012**, 2, 942-947.
30. N. Z. Muradov, *International Journal of Hydrogen Energy* **1993**, 18, 211-215.
31. J.-P. Schirmann and P. Bourdauducq, in *Ullmann's Encyclopedia of Industrial Chemistry*, Wiley-VCH Verlag GmbH & Co. KGaA, 2000, pp. 79-96.
32. B. C. Ong, S. K. Kamarudin and S. Basri, *International Journal of Hydrogen Energy* **2017**, 42, 10142-10157.
33. G. Gahleitner, *International Journal of Hydrogen Energy* **2013**, 38, 2039-2061.
34. M. Little, M. Thomson and D. Infield, *International Journal of Hydrogen Energy* **2007**, 32, 1582-1588.
35. D. J. L. Brett, A. R. Kucernak, P. Aguiar, S. C. Atkins, N. P. Brandon, R. Clague, L. F. Cohen, G. Hinds, C. Kalyvas, G. J. Offer, B. Ladewig, R. Maher, A. Marquis, P. Shearing, N. Vasileiadis and V. Vesovic, *ChemPhysChem* **2010**, 11, 2714-2731.
36. AFC Energy PLC, *We are AFC Energy*, http://www.afcenergy.com/, (accessed 10th January, 2018).
37. ITM Power, *Products*, http://www.itm-power.com/products, (accessed 10th January, 2018).
38. Fuel Cell Energy, *Products*, https://www.fuelcellenergy.com/products/, (accessed 10th

January, 2018).

39. A. Hauch, S. D. Ebbesen, S. H. Jensen and M. Mogensen, *Journal of Materials Chemistry* **2008**, 18, 2331-2340.
40. M. N. Manage, D. Hodgson, N. Milligan, S. J. R. Simons and D. J. L. Brett, *International Journal of Hydrogen Energy* **2011**, 36, 5782-5796.
41. M. Gattrell, N. Gupta and A. Co, *Journal of Electroanalytical Chemistry* **2006**, 594, 1-19.
42. L. Kleiminger, T. Li, K. Li and G. H. Kelsall, *RSC Advances* **2014**, 4, 50003-50016.
43. M. Gao, B. Deng, Z. Chen, M. Tao and D. Wang, *Electrochemistry Communications* **2018**, 88, 79-82.
44. S. Wang and S. P. Jiang, *National Science Review* **2017**, 4, 163-166.
45. K. Xie, Y. Zhang, G. Meng and J. T. Irvine, *Journal of Materials Chemistry* **2011**, 21, 195-198.
46. P. A. Stuart, T. Unno, J. A. Kilner and S. J. Skinner, *Solid State Ionics* **2008**, 179, 1120-1124.
47. E. Fabbri, D. Pergolesi and E. Traversa, *Chemical Society Reviews* **2010**, 39, 4355-4369.
48. N. Zakowsky, S. Williamson and J. T. S. Irvine, *Solid State Ionics* **2005**, 176, 3019-3026.
49. E. Fabbri, A. D'Epifanio, E. Di Bartolomeo, S. Licoccia and E. Traversa, *Solid State Ionics* **2008**, 179, 558-564.
50. A. Hauch, K. Brodersen, M. Chen, C. Graves, S. H. Jensen, P. S. Jørgensen, P. V. Hendriksen, M. B. Mogensen, S. Ovtar and X. Sun, *ECS Transactions* **2017**, 75, 3-14.
51. S. C. Singhal, *Solid Oxide Fuel Cells VI*, The Electrochemical Society, Inc., Pennington, NJ, USA, 1999.
52. L. Kleiminger, *Solid Oxide Electrochemical Reactors and Processes for Carbon Dioxide and Water Splitting*, Ph.D. Thesis, Imperial College London, 2015.
53. A. Ursua, L. M. Gandia and P. Sanchis, *Proceedings of the IEEE* **2012**, 100, 410-426.
54. Y. Hori, H. Wakebe, T. Tsukamoto and O. Koga, *Electrochimica Acta* **1994**, 39, 1833-1839.
55. E. E. Benson, C. P. Kubiak, A. J. Sathrum and J. M. Smieja, *Chemical Society Reviews* **2009**, 38, 89-99.
56. M. Jitaru, *Journal of the University of Chemical Technology and Metallurgy* **2007**, 42, 333-344.

57. K. P. Kuhl, E. R. Cave, D. N. Abram and T. F. Jaramillo, *Energy & Environmental Science* **2012**, 5, 7050-7059.
58. R. Aydin and F. Köleli, *Journal of Electroanalytical Chemistry* **2002**, 535, 107-112.
59. S. Kaneco, Y. Ueno, H. Katsumata, T. Suzuki and K. Ohta, *Chemical Engineering Journal* **2006**, 119, 107-112.
60. M. Carmo, D. L. Fritz, J. Mergel and D. Stolten, *International Journal of Hydrogen Energy* **2013**, 38, 4901-4934.
61. R. L. Cook and A. F. Sammells, *Gas phase CO_2 reduction to hydrocarbons at solid polymer electrolyte cells*, US patent 4959131A, granted 25th September 1990.
62. C. Delacourt, P. L. Ridgway, J. B. Kerr and J. Newman, *Journal of The Electrochemical Society* **2008**, 155, B42-B49.
63. G. Centi, S. Perathoner, G. Winè and M. Gangeri, *Green Chemistry* **2007**, 9, 671-678.
64. V. Kaplan, E. Wachtel, K. Gartsman, Y. Feldman and I. Lubomirsky, *Journal of the Electrochemical Society* **2010**, 157, B552-B556.
65. Bloom Energy, Press Release: *Bloom Energy to Install First−Ever Highrise Project at Morgan Stanley Global Headquarters in New York City*, 2016.
66. C. Graves, S. D. Ebbesen, M. Mogensen and K. S. Lackner, *Renewable and Sustainable Energy Reviews* **2011**, 15, 1-23.
67. L. Bi, S. Boulfrad and E. Traversa, *Chemical Society Reviews* **2014**, 43, 8255-8270.
68. E. Ruiz-Trejo and J. Irvine, *Solid State Ionics* **2013**, 252, 157-164.
69. T. Norby, *ECS Transactions* **2017**, 80, 23-32.
70. Science Museum Group (UK), *Trough Battery 1801-1838*, https://collection.sciencemuseum.org.uk/objects/co6522, (accessed March 6th, 2018).
71. The Electrocheimcal Society, *Birth of Electrochemistry*, http://www.electrochem.org/birth-of-electrochemistry, (accessed 11th January, 2018).
72. M. Faraday, *Experimental Researches in Electricity 1839-1855, Volumes 1-3*, J. M. Dent & Sons, London, 1914.
73. C. F. Schoenbein, *Philosophical Magazine (III)* **1839**, 14, 43-45.
74. W. R. Grove, *Philosophical Magazine (III)* **1839**, 14, 127-130.
75. D. R. Gaskell, *Introduction to Thermodynamics of Materials*, Taylor & Francis, Oxford, UK, 3rd edn., 1995.
76. P. J. Lindstrom, *A Guide to the NIST Chemistry WebBook*, National Institute of Standards and Technology, https://webbook.nist.gov/chemistry/guide/ (accessed 11th

January, 2018).

77. J. O. M. Bockris and A. K. N. Reddy, *Moldern Electrochemistry*, Plenum Press, New York, 1977.
78. H. Cavendish, *Franklin Experiments and Observations on Electricity*, F. Newbery, London, 5 edn., 1774.
79. W. Beetz, *Annalen der Physik* **1854**, 168, 452-466.
80. H. Buff, *Justus Liebigs Annalen der Chemie* **1854**, 90, 257-283.
81. W. Nernst, *Material for electric-lamp glowers*, US patent 685730A, granted 29th October, 1901.
82. E. Baur and H. Preis, *Zeitschrift für Elektrochemie und angewandte physikalische Chemie* **1937**, 43, 727-732.
83. C. Wagner, *Naturwissenschaften* **1943**, 31, 265-268.
84. M. Martin, *Solid State Ionics* **2002**, 152-153, 15-17.
85. K. Kiukkola and C. Wagner, *Journal of the Electrochemical Society* **1957**, 104, 379-387.
86. H. S. Spacil, *Electrical Device including Nickel-containing Stabilized Zirconia Electrode*, US patent 3503809, granted 31st March 1964.
87. S. de Souza, S. J. Visco and L. C. De Jonghe, *Solid State Ionics* **1997**, 98, 57-61.
88. B. C. H. Steele and A. Heinzel, *Nature* **2001**, 414, 345-352.
89. A. Weber and E. Ivers-Tiffée, *Journal of Power Sources* **2004**, 127, 273-283.
90. Y. Tao, H. Nishino, S. Ashidate, H. Kokubo, M. Watanabe and H. Uchida, *Electrochimica Acta* **2009**, 54, 3309-3315.
91. S. H. Jensen, P. H. Larsen and M. Mogensen, *International Journal of Hydrogen Energy* **2007**, 32, 3253-3257.
92. C.-Y. Cheng, G. H. Kelsall and L. Kleiminger, *Journal of Applied Electrochemistry* **2013**, 43, 1131-1144.
93. F. Bidrawn, G. Kim, G. Corre, J. T. S. Irvine, J. M. Vohs and R. J. Gorte, *Solid State Letters* **2008**, 11, B167-B170.
94. S. R. Taylor, *Geochimica et Cosmochimica Acta* **1964**, 28, 1273-1285.
95. K. H. Wedepohl, *Geochimica et Cosmochimica Acta* **1995**, 59, 1217-1232.
96. H. Uchida, S.-i. Arisaka and M. Watanabe, *Electrochemical and Solid-State Letters* **1999**, 2, 428-430.
97. K. C. Wincewicz and J. S. Cooper, *Journal of Power Sources* **2005**, 140, 280-296.
98. O. Kubaschewski and C. B. Alcock, *Metallurgical Thermochemistry*, Pergamon,

Oxford, UK, 5 edn., 1979.

99. X. Sun, M. Chen, S. H. Jensen, S. D. Ebbesen, C. Graves and M. Mogensen, *International Journal of Hydrogen Energy* **2012**, 37, 17101-17110.
100. F. H. van Heuveln and H. J. M. Bouwmeester, *Journal of The Electrochemical Society* **1997**, 144, 134-140.
101. F. H. van Heuveln, H. J. M. Bouwmeester and F. P. F. van Berkel, *Journal of The Electrochemical Society* **1997**, 144, 126-133.
102. P. Kazempoor and R. J. Braun, *International Journal of Hydrogen Energy* **2015**, 40, 3599-3612.
103. K. Huang, M. Feng, J. B. Goodenough and C. Milliken, *Journal of The Electrochemical Society* **1997**, 144, 3620-3624.
104. H. Zhu and R. J. Kee, *Journal of The Electrochemical Society* **2008**, 155, B715-B729.
105. Y. Xie and X. Xue, *Solid State Ionics* **2012**, 224, 64-73.
106. B. Kenney and K. Karan, *Solid State Ionics* **2007**, 178, 297-306.
107. S. B. Adler, *Chemical Reviews* **2004**, 104, 4791-4844.
108. M. García-Camprubí, S. Izquierdo and N. Fueyo, *Renewable and Sustainable Energy Reviews* **2014**, 33, 701-718.
109. M. Ni, M. K. H. Leung and D. Y. C. Leung, *International Journal of Hydrogen Energy* **2007**, 32, 2305-2313.
110. J. Laurencin, D. Kane, G. Delette, J. Deseure and F. Lefebvre-Joud, *Journal of Power Sources* **2011**, 196, 2080-2093.
111. X. Jin and X. Xue, *Journal of Power Sources* **2010**, 195, 6652-6658.
112. K. Miyoshi, T. Miyamae, H. Iwai, M. Saito, M. Kishimoto and H. Yoshida, *Journal of Power Sources* **2016**, 315, 63-69.
113. D. G. Goodwin, H. Zhu, A. M. Colclasure and R. J. Kee, *Journal of The Electrochemical Society* **2009**, 156, B1004-B1021.
114. H. Zhu, R. J. Kee, V. M. Janardhanan, O. Deutschmann and D. G. Goodwin, *Journal of The Electrochemical Society* **2005**, 152, A2427-A2440.
115. S. P. Jiang and P. S. Badwal, *Journal of The Electrochemical Society* **1997**, 144, 3777-3784.
116. A. M. Sukeshini, B. Habibzadeh, B. P. Becker, C. A. Stoltz, B. W. Eichhorn and G. S. Jackson, *Journal of The Electrochemical Society* **2006**, 153, A705-A715.
117. J. Mizusaki, H. Tagawa, T. Saito, T. Yamamura, K. Kamitani, K. Hirano, S. Ehara, T. Takagi, T. Hikita, M. Ippommatsu, S. Nakagawa and K. Hashimoto, *Solid State Ionics*

1994, 70-71, 52-58.

118. W. He, W. Lv and J. H. Dickerson, *Gas Transport in Solid Oxide Fuel Cells*, Springer, London, 2014.
119. W. G. Bessler and S. Gewies, *Journal of The Electrochemical Society* **2007**, 154, B548-B559.
120. B. Tjaden, S. J. Cooper, D. J. L. Brett, D. Kramer and P. R. Shearing, *Current Opinion in Chemical Engineering* **2016**, 12, 44-51.
121. D. A. G. Bruggeman, *Annalen der Physik* **1935**, 416, 636-664.
122. B. Todd and J. B. Young, *Journal of Power Sources* **2002**, 110, 186-200.
123. C. J. G. Raw and C. P. Ellis, *The Journal of Chemical Physics* **1958**, 28, 1198-1200.
124. C. P. Ellis and C. J. G. Raw, *The Journal of Chemical Physics* **1959**, 30, 574-576.
125. S. P. S. Badwal, *Solid State Ionics* **1992**, 52, 23-32.
126. J. H. Nam and D. H. Jeon, *Electrochimica Acta* **2006**, 51, 3446-3460.
127. J. Will, A. Mitterdorfer, C. Kleinlogel, D. Perednis and L. J. Gauckler, *Solid State Ionics* **2000**, 131, 79-96.
128. N. H. Menzler, J. Malzbender, P. Schoderböck, R. Kauert and H. P. Buchkremer, *Fuel Cells* **2014**, 14, 96-106.
129. V. Karakoussis, N. P. Brandon, M. Leach and R. van der Vorst, *Journal of Power Sources* **2001**, 101, 10-26.
130. N. Brandon and D. Brett, *Philosophical Transactions of the Royal Society of London A: Mathematical, Physical and Engineering Sciences* **2006**, 364, 147-159.
131. P. S. Jørgensen, S. L. Ebbehøj and A. Hauch, *Journal of Power Sources* **2015**, 279, 686-693.
132. P. R. Shearing, D. J. L. Brett and N. P. Brandon, *International Materials Reviews* **2010**, 55, 347-363.
133. S. P. Jiang and J. Li, in *Solid Oxide Fuel Cells, Materials Porperties and Performance*, ed. J. W. Fergus, CRC Press, Boca Raton, FL, 2009, pp. 131-178.
134. J. R. Wilson, W. Kobsiriphat, R. Mendoza, H.-Y. Chen, J. M. Hiller, D. J. Miller, K. Thornton, P. W. Voorhees, S. B. Adler and S. A. Barnett, *Nauret Materials* **2006**, 5, 541-544.
135. J. S. Cronin, Y.-c. K. Chen-Wiegart, J. Wang and S. A. Barnett, *Journal of Power Sources* **2013**, 233, 174-179.
136. J. R. Wilson, A. T. Duong, M. Gameiro, H.-Y. Chen, K. Thornton, D. R. Mumm and S. A. Barnett, *Electrochemistry Communications* **2009**, 11, 1052-1056.

137. P. R. Shearing, J. Golbert, R. J. Chater and N. P. Brandon, *Chemical Engineering Science* **2009**, 64, 3928-3933.
138. A. Atkinson, S. Barnett, R. J. Gorte, J. T. S. Irvine, A. J. McEvoy, M. Mogensen, S. C. Singhal and J. Vohs, *Nature Materials* **2004**, 3, 17-27.
139. J. M. Vohs and R. J. Gorte, *Advanced Materials* **2009**, 21, 943-956.
140. E. D. Wachsman and K. T. Lee, *Science* **2011**, 334, 935-939.
141. S. P. Jiang, *International Journal of Hydrogen Energy* **2012**, 37, 449-470.
142. M. Kishimoto, M. Lomberg, E. Ruiz-Trejo and N. P. Brandon, *Journal of Power Sources* **2014**, 266, 291-295.
143. K. Nagato, S. Shinagawa, N. Shikazono, S. Iwasaki and M. Nakao, *ECS Transactions* **2015**, 68, 1309-1314.
144. Y. T. Chou, Y. T. Ko and M. F. Yan, *Journal of the American Ceramic Society* **1987**, 70, C280-C282.
145. N. M. Farandos, L. Kleiminger, T. Li, A. Hankin and G. H. Kelsall, *Electrochimica Acta* **2016**, 213, 324-331.
146. J. P. Kruth, *CIRP Annals - Manufacturing Technology* **1991**, 40, 603-614.
147. S. H. Huang, P. Liu, A. Mokasdar and L. Hou, *The International Journal of Advanced Manufacturing Technology* **2013**, 67, 1191-1203.
148. B. Derby, *Journal of the European Ceramic Society* **2011**, 31, 2543-2550.
149. J. Bharathan and Y. Yang, *Applied Physics Letters* **1998**, 72, 2660-2662.
150. J. Hoerber, J. Glasschroeder, M. Pfeffer, J. Schilp, M. Zaeh and J. Franke, *Procedia CIRP* **2014**, 17, 806-811.
151. M. Singh, H. M. Haverinen, P. Dhagat and G. E. Jabbour, *Advanced Materials* **2010**, 22, 673-685.
152. Q. Fu, E. Saiz and A. P. Tomsia, *Acta biomaterialia* **2011**, 7, 3547-3554.
153. J. Franco, P. Hunger, M. E. Launey, A. P. Tomsia and E. Saiz, *Acta biomaterialia* **2010**, 6, 218-228.
154. Markforged, *Products*, https://markforged.com/products/, (accessed 6th April, 2018).
155. M. Vaezi, H. Seitz and S. Yang, *The International Journal of Advanced Manufacturing Technology* **2013**, 67, 1721-1754.
156. FujiFilm Dimatix Inc. (USA), Report: *Jettable Fluid Formulation Guidelines*, May 16th 2013.
157. M. Lomberg, P. Boldrin, F. Tariq, G. Offer, B. Wu and N. P. Brandon, *ECS Transactions* **2015**, 68, 2119-2127.

158. P. Bertrand, F. Bayle, C. Combe, P. Goeuriot and I. Smurov, *Applied Surface Science* **2007**, 254, 989-992.
159. M. Schwentenwein and J. Homa, *International Journal of Applied Ceramic Technology* **2015**, 12, 1-7.
160. L. Andrés Díaz, R. Adrián de Blas, S. Martin, J. Christopher and H. Johannes, *Smart Materials and Structures* **2016**, 25, 054015-054025.
161. L. R. Meza, S. Das and J. R. Greer, *Science* **2014**, 345, 1322-1326.
162. J. Bauer, S. Hengsbach, I. Tesari, R. Schwaiger and O. Kraft, *Proceedings of the National Academy of Sciences* **2014**, 111, 2453-2458.
163. A. E. Jakus, S. L. Taylor, N. R. Geisendorfer, D. C. Dunand and R. N. Shah, *Advanced Functional Materials* **2015**, 25, 6985-6995.
164. E. Feilden, E. G.-T. Blanca, F. Giuliani, E. Saiz and L. Vandeperre, *Journal of the European Ceramic Society* **2016**, 36, 2525-2533.
165. E. Özkol, J. Ebert, K. Uibel, A. M. Wätjen and R. Telle, *Journal of the European Ceramic Society* **2009**, 29, 403-409.
166. J. Ebert, E. Özkol, A. Zeichner, K. Uibel, Ö. Weiss, U. Koops, R. Telle and H. Fischer, *Journal of Dental Research* **2009**, 88, 673-676.
167. M. Mott, J.-H. Song and J. R. G. Evans, *Journal of the American Ceramic Society* **1999**, 82, 1653-1658.
168. V. Esposito, C. Gadea, J. Hjelm, D. Marani, Q. Hu, K. Agersted, S. Ramousse and S. H. Jensen, *Journal of Power Sources* **2015**, 273, 89-95.
169. X. Zhao, J. R. G. Evans, M. J. Edirisinghe and J.-H. Song, *Journal of the American Ceramic Society* **2002**, 85, 2113-2115.
170. C. Li, H. Shi, R. Ran, C. Su and Z. Shao, *International Journal of Hydrogen Energy* **2013**, 38, 9310-9319.
171. J. Deckers, J. Vleugels and J.-P. Kruth, *Journal of Ceramic Science and Technology* **2014**, 5, 245-260.
172. J. Zhang, E. J. Liang and X. H. Zhang, *Journal of Power Sources* **2010**, 195, 6758-6763.
173. J. W. Halloran, *Annual Review of Materials Research* **2016**, 46, 19-40.
174. X. Zhang, X. N. Jiang and C. Sun, *Sensors and Actuators A: Physical* **1999**, 77, 149-156.
175. L. Li and J. T. Fourkas, *Materials Today* **2007**, 10, 30-37.
176. M. Deubel, G. von Freymann, M. Wegener, S. Pereira, K. Busch and C. M. Soukoulis, *Nature Materials* **2004**, 3, 444-447.

177. H.-B. Sun and S. Kawata, in *NMR • 3D Analysis • Photopolymerization*, eds. N. Fatkullin, T. Ikehara, H. Jinnai, S. Kawata, R. Kimmich, T. Nishi, Y. Nishikawa and H. B. Sun, Springer, Berlin, 2004, pp. 169-273.
178. T. A. Pham, D. P. Kim, T. W. Lim, S. H. Park, D. Y. Yang and K. S. Lee, *Advanced Functional Materials* **2006**, 16, 1235-1241.
179. L. C. Montemayor, L. R. Meza and J. R. Greer, *Advanced Engineering Materials* **2014**, 16, 184-189.
180. J. K. Gansel, M. Thiel, M. S. Rill, M. Decker, K. Bade, V. Saile, G. von Freymann, S. Linden and M. Wegener, *Science* **2009**, 325, 1513-1515.
181. J. A. Lewis, *Advanced Functional Materials* **2006**, 16, 2193-2204.
182. F. Burgher, Northwestern University, *Printing Clean Energy*, http://www.northwestern.edu/newscenter/stories/2016/03/geisendorfer-clean-energy.html, (accessed 1st August, 2016).
183. A. Clarke, S. Rieubland, *Continuous Inkjet Printing*, US patent 8186784 B2, granted 29th May 2012.
184. F. S. F. Brossard, V. Pecunia, A. J. Ramsay, J. P. Griffiths, M. Hugues and H. Sirringhaus, *Advanced Materials* **2017**, 29, 1704425-1704434.
185. N. Reis, C. Ainsley and B. Derby, *Journal of Applied Physics* **2005**, 97, 094903-094909.
186. J. Stringer and B. Derby, *Journal of the European Ceramic Society* **2009**, 29, 913-918.
187. H. Wijshoff, *Physics Reports* **2010**, 491, 77-177.
188. D. W. Loyer and S. L. Boden, *Universal Inkjet Printer Device and Methods*, US patent 7377605 B2, granted 27th May 2008.
189. E. Özkol, J. Ebert and R. Telle, *Journal of the European Ceramic Society* **2010**, 30, 1669-1678.
190. C. Li, H. Chen, H. Shi, M. O. Tade and Z. Shao, *Journal of Power Sources* **2015**, 273, 465-471.
191. X. Zhao, J. R. G. Evans, M. J. Edirisinghe and J. H. Song, *Journal of Materials Synthesis and Processing* **2001**, 9, 319-327.
192. K. Li, in *Ceramic Membranes for Separation and Reaction*, John Wiley & Sons, Ltd, 2007, pp. 21-57.
193. R. M. German, *Sintering: From Empirical Observations to Scientific Principles*, Elsevier, Waltham, MA, USA, 2014.
194. J. Fromm, *IMB Journal of Research and Development* **1984**, 28, 322-333.
195. N. Reis and B. Derby, *MRS Conference Proceedings, Materials develpment for direct*

write technologies, Materials Research Society **2000**, 625, 65-70.

196. D. Jang, D. Kim and J. Moon, *Langmuir* **2009**, 25, 2629-2635.
197. P. C. Duineveld, M. M. de Kok, M. Buechel, A. H. Sempel, K. A. H. Mutsaers, P. van der Weijer, I. G. J. Camps, T. J. M. van den Biggelaar, J.-E. J. M. Rubingh, and E. I. Haskal, *Proceedings of Organic Light-Emitting Materials and Devices V, SPIE*, 2002, 59-67.
198. C. D. Stow and M. G. Hadfeld, *Proceedings of the Royal Society of London A: Mathematical, Physical and Engineering Sciences* **1981**, 373, 419-441.
199. J. Q. Feng, *Journal of Imaging Science and Technology* **2002**, 46, 398-408.
200. Q. Xu and O. A. Basaran, *Physics of Fluids* **2007**, 19, 102111-102123.
201. I. M. Hutchings, G. D. Martin and S. D. Hoath, in *Fundamentals of Inkjet Printing: The Science of Inkjet and Droplets*, ed. S. D. Hoath, Wiley-VCH, Weinheim, Germany, 2016, pp. 8-12.
202. H. Dong, W. W. Carr and J. F. Morris, *Physics of Fluids* **2006**, 18, 072102-072118.
203. R. Noguera, M. Lejeune and T. Chartier, *Journal of the European Ceramic Society* **2005**, 25, 2055-2059.
204. A. Einstein, *Annalen der Physik* **1906**, 19, 289-306.
205. I. M. Krieger and T. J. Dougherty, *Journal of Rheology* **1959**, 3, 137.
206. M. Mooney, *Journal of Colloid and Interface Science* **1951**, 6, 162-170.
207. H. Eilers, *Kolloid-Zeitschrift* **1941**, 97, 313-321.
208. D. Quemada, *Rheologica Acta* **1977**, 16, 82-94.
209. J. V. Robinson, *Journal of Physical Chemistry* **1948**, 53, 1042-1056.
210. A. J. Hughes, *Nature* **1954**, 173, 1089-1090.
211. B. V. Derjaguin and L. D. Landau, *Acta Physicochimica URSS* **1941**, 14, 633-662.
212. E. J. W. Verwey and J. T. G. Overbeek, *Theory of the Stability of Lyophobic Colloids*, Elsevier, New York, 1948.
213. H. N. Lekkerkerker and R. Tuinier, *Colloids and the Depletion Interaction*, Springer Science, London, 2011.
214. D. C. Prieve and W. B. Russel, *Journal of Colloid and Interface Science* **1988**, 125, 1-13.
215. E. M. Lifshitz, *Soviet Physics* **1956**, 2, 73-83.
216. S. Bhattacharjee, M. Elimelech and M. Borkovec, *Croatica Chimica Acta* **1998**, 71, 883-903.
217. R. J. Hunter, in *Zeta Potential in Colloid Science*, eds. R. H. Ottewill and R. L. Rowell,

Academic Press, Oxford, Great Britain, 1981, pp. 59-124.
218. M. von Smoluchowski, *Zeitschrift für Physik* **1916**, 17, 557-585.
219. D. C. Henry, *Proceedings of the Royal Society of London. Series A* **1931**, 133, 106.
220. R. Tantra, P. Schulze and P. Quincey, *Particuology* **2010**, 8, 279-285.
221. H. Aljama, *Surface Modification of Silica nanoparticles using Surface Coupling Agents*, Ph.D Thesis, The Pennsylvania State University, 2010.
222. A. L. Loeb, P. H. Wiersma and J. T. G. Overbeek, *The Electric Double Layer around a Spherical Colloid Particle*, The MIT Press, Cambridge MA, 1961.
223. H. Ohshima, *Journal of Colloid and Interface Science* **2002**, 247, 18-23.
224. N. Fuchs, *Zeitschrift fur Physik* **1934**, 89, 736-743.
225. J. Eastman, in *Colloid Science*, ed. T. Cosgrove, Blackwell Publishing Ltd., 2009, pp. 36-49.
226. Y. H. Wang, X. Q. Liu and G. Y. Meng, *Ceramics International* **2007**, 33, 1025-1031.
227. S. Zürcher and T. Graule, *Journal of the European Ceramic Society* **2005**, 25, 863-873.
228. B. Derby and N. Reis, *Materials Research Society Bulletin* **2003**, 28, 815-818.
229. T. Mao, D. C. S. Kuhn and H. Tran, *AIChE Journal* **1997**, 43, 2169-2179.
230. M. Pasandideh-Fard, Y. Qiao, M., J. Chandra and J. Mostaghimi, *Physics of Fluids* **1996**, 8, 650-659.
231. B. L. Scheller and D. W. Bousfield, *Fluid Mechanics and Transport Phenomena* **1995**, 41, 1357-1367.
232. A. Asai, M. Shioya, S. Hirasawa and T. Okazaki, *The Journal of Imaging Science and Technology* **1993**, 37, 205-207.
233. H. Yoo and C. Kim, *Colloids and Surfaces A: Physicochemical and Engineering Aspects* **2015**, 468, 234-245.
234. A. L. Yarin, *Annual Review of Fluid Mechanics* **2006**, 38, 159-192.
235. J. Madejski, *International Journal of Heat and Mass Transfer* **1976**, 19, 1009-1013.
236. K. A. M. Seerden, N. Reis, J. R. G. Evans, P. S. Grant, J. W. Halloran and B. Derby, *Journal of the American Ceramic Society* **2001**, 84, 2514-2520.
237. A. P. Sommer and N. Rozlosnik, *Crystal Growth & Design* **2005**, 5, 551-557.
238. R. D. Deegan, O. Bakajin, T. F. Dupont, G. Huber, S. R. Nagel and T. A. Witten, *Nature* **1997**, 389, 827-829.
239. R. D. Deegan, O. Bakajin, T. F. Dupont, G. Huber, S. R. Nagel and T. A. Witten, *Physical Review E* **2000**, 62, 756-765.
240. Y. Zhang, L. Chen and J. R. G. Evans, *Langmuir* **2008**, 24, 3752-3758.

241. B.-J. de Gans and U. S. Schubert, *Langmuir* **2004**, 20, 7789-7793.
242. T. Cuk, S. M. Troian, C. M. Hong and S. Wagner, *Applied Physics Letters* **2000**, 77, 2063-2065.
243. R. I. Tomov, M. Krauz, J. Jewulski, S. C. Hopkins, J. R. Kluczowski, D. M. Glowacka and B. A. Glowacki, *Journal of Power Sources* **2010**, 195, 7160-7167.
244. C. Wang, R. I. Tomov, R. Vasant Kumar and B. A. Glowacki, *Journal of Materials Science* **2011**, 46, 6889-6896.
245. C. Wang, S. C. Hopkins, R. I. Tomov, R. V. Kumar and B. A. Glowacki, *Journal of the European Ceramic Society* **2012**, 32, 2317-2324.
246. A. M. El-Toni, T. Yamaguchi, S. Shimizu, Y. Fujishiro and M. Awano, *Journal of the American Ceramic Society* **2007**, 91, 346-349.
247. D. Young, A. M. Sukeshini, R. Cummins, H. Xiao, M. Rottmayer and T. Reitz, *Journal of Power Sources* **2008**, 184, 191-196.
248. R. I. Tomov, R. Duncan, M. Krauz, R. V. Kumar and B. A. Glowacki, *E3S Web of Conferences* **2016**, 10, 00098-00106.
249. G. D. Han, K. C. Neoh, K. Bae, H. J. Choi, S. W. Park, J.-W. Son and J. H. Shim, *Journal of Power Sources* **2016**, 306, 503-509.
250. T. Y. Hill, T. L. Reitz and H. Huang, *Materials Research Bulletin* **2016**, 84, 1-27.
251. N. Yashiro, T. Usui and K. Kikuta, *Journal of the European Ceramic Society* **2010**, 30, 2093-2098.
252. M. A. Sukeshini, R. Cummins, T. L. Reitz and R. M. Miller, *Journal of the American Ceramic Society* **2009**, 92, 2913-2919.
253. N. P. Sullivan, *Inkjet Printing of Dense and Porous Ceramic Layers onto Porous Substrates for Manufacturing Ceramic Electrochemical Devices*, US patent 2014/0072702, application 13th March 2014.
254. N. Faino, W. Rosehsteel, B. Gorman and N. P. Sullivan, *ECS Transactions* **2011**, 35, 593-600.
255. J. L. Wheeler, N. P. Sullivan and J. M. Porter, *Sensors and Actuators B: Chemical* **2013**, 183, 194-200.
256. J. F. B. Rasmussen, P. V. Hendriksen and A. Hagen, *Fuel Cells* **2008**, 8, 385-393.
257. C. Kubota, Y. Ito and K. Kikuta, *Journal of the Ceramic Society of Japan* **2008**, 116, 792-796.
258. T. Y. Hill, T. L. Reitz, M. A. Rottmayer and H. Huang, *ECS Journal of Solid State Science and Technology* **2015**, 4, P3015-P3019.

259. FujiFilm Dimatix USA Inc., Data Sheet: *Sapphire QS-256/30 AAA Inkjet Printhead*, 2014.
260. J. C. Ruiz-Morales, J. Canales-Vazquez, J. Pena-Martinez, D. Marrero-Lopez, J. T. S. Irvine and P. Nunez, *Journal of Materials Chemistry* **2006**, 16, 540-542.
261. A. R. Hanifi, M. Zazulak, T. H. Etsell and P. Sarkar, *Powder Technology* **2012**, 231, 35-43.
262. M. Kosmulski, *Colloids and Surfaces A: Physicochemical and Engineering Aspects* **2003**, 222, 113-118.
263. J. C. Farinas, R. Moreno, J. Requena and J. S. Moya, *Materials Science and Engineering* **1989**, 109, 97-99.
264. Z. Xie, J. Ma, Q. Xu, Y. Huang and Y.-B. Cheng, *Ceramics International* **2004**, 30, 219-224.
265. D. D. Wagman, W. H. Evans, V. B. Parker, R. H. Schumm, I. Halow, S. M. Bailey, K. L. Chumey and R. L. Nutall, *Journal of Physical and Chemical Reference Data* **1982** 11 (Supplement 2), 110.
266. A. F. Routh, *Reports on Progress in Physics* **2013**, 76, 046603-046633.
267. W. B. Russel, N. Wu and W. Man, *Langmuir* **2008**, 24, 1721-1730.
268. H. M. Jaeger and S. R. Nagel, *Science* **1992**, 255, 1523-1531.
269. A. Selçuk and A. Atkinson, *Journal of the European Ceramic Society* **1997**, 17, 1523-1532.
270. T. Ye, Z. Suo and A. G. Evans, *International Journal of Solids Structures* **1992**, 29, 2639-2648.
271. J. W. Fergus, *Solid State Ionics* **2006**, 177, 1529-1541.
272. B. C. H. Steele, *Solid State Ionics* **2000**, 129, 95-110.
273. S. Uhlenbruck, T. Moskalewicz, N. Jordan, H. J. Penkalla and H. P. Buchkremer, *Solid State Ionics* **2009**, 180, 418-423.
274. W. G. Wang and M. Mogensen, *Solid State Ionics* **2005**, 176, 457-462.
275. M. J. López-Robledo, J. Silva-Treviño, T. Molina and R. Moreno, *Journal of the European Ceramic Society* **2013**, 33, 297-303.
276. I. Jesswein, T. Hirth and T. Schiestel, *Journal of Membrane Science* **2017**, 541, 281-290.
277. D. Quéré, *Annual Review of Fluid Mechanics* **1999**, 31, 347-384.
278. A. J. Bard, R. Parsons, J. Jordan, *Standard potentials in aqueous solution*, M. Dekker, New York, 1985.

279. T. P. Bigioni, X.-M. Lin, T. T. Nguyen, E. I. Corwin, T. A. Witten and H. M. Jaeger, *Nature Materials* **2006**, 5, 265-270.
280. N. M. Farandos, T. Li and G. H. Kelsall, *Electrochimica Acta* **2018**, 270, 264-273.
281. L. Gomez, M. T. Colomer, J. Escobar and R. Moreno, *Journal of the European Ceramic Society* **2013**, 33, 1137-1143.
282. K. S. Howe, E. R. Clark, J. Bowen and K. Kendall, *International Journal of Hydrogen Energy* **2013**, 38, 1731-1736.
283. Eastman Chemical Company, Report: *Butvar Polyvinyl Resins*, 2017.
284. Y. B. Tewari, M. M. Miller and S. P. Wasik, *Journal of Research of the National Bureau of Standards* **1982**, 87, 155-158.
285. Y. Chen, L. Yang, F. Ren and K. An, *Scientific Reports* **2014**, 4, 5179-5188.
286. A. F. Routh and W. B. Zimmerman, *Chemical Engineering Science* **2004**, 59, 2961-2968.
287. H. R. Kemme and S. I. Kreps, *Journal of Chemical & Engineering Data* **1969**, 14, 98-102.
288. O. A. Pickett and J. M. Peterson, *Industrial & Engineering Chemistry* **1929**, 21, 325-326.
289. J. T. Richardson, R. Scates and M. V. Twigg, *Applied Catalysis A: General* **2003**, 246, 137-150.
290. Y. Kamikoriyama and S. Ogata, *Aqueous Nickel Slurry, Method for Preparing the Same and Conductive Paste*, US patent 6746628 B2, granted 8th June 2004.
291. N. Hernández, R. Moreno, A. J. Sánchez-Herencia and J. L. G. Fierro, *The Journal of Physical Chemistry B* **2005**, 109, 4470-4474.
292. L. Zhang, S. P. Jiang, W. Wang and Y. Zhang, *Journal of Power Sources* **2007**, 170, 55-60.
293. P. M. Oliver, G. W. Watson and S. C. Parker, *Physical Review B* **1995**, 52, 5323-5329.
294. A. Tsoga and P. Nikolopoulos, *Journal of Materials Science* **1996**, 31, 5409-5413.
295. H.-Y. Chen, H.-C. Yu, J. Scott Cronin, J. R. Wilson, S. A. Barnett and K. Thornton, *Journal of Power Sources* **2011**, 196, 1333-1337.
296. L. Kleiminger, T. Li, K. Li and G. H. Kelsall, *Electrochimica Acta* **2015**, 179, 565-577.
297. C. Graves, S. D. Ebbesen, S. H. Jensen, S. B. Simonsen and M. B. Mogensen, *Nature Materials* **2015**, 14, 239-244.
298. S. P. Jiang and S. H. Chan, *Materials Science and Technology* **2004**, 20, 1109-1118.
299. M. J. Jørgensen, S. Primdahl, C. Bagger and M. Mogensen, *Solid State Ionics* **2001**,

139, 1-11.

300. K. Wiik, C. R. Schmidt, S. Faaland, S. Shamsili, M.-A. Einarsrud and T. Grande, *Journal of the American Ceramic Society* **1999**, 82, 721-728.
301. M. J. Jørgensen and M. Mogensen, *Journal of The Electrochemical Society* **2001**, 148, A433-A422.
302. S. Y. Gómez and D. Hotza, *Renewable and Sustainable Energy Reviews* **2016**, 61, 155-174.
303. T. Li, M. F. Rabuni, L. Kleiminger, B. Wang, G. H. Kelsall, U. W. Hartley and K. Li, *Energy & Environmental Science* **2016**, 9, 3682-3686.
304. S. D. Ebbesen and M. Mogensen, *Journal of Power Sources* **2009**, 193, 349-358.
305. C. Graves, S. D. Ebbesen and M. Mogensen, *Solid State Ionics* **2011**, 192, 398-403.
306. K. Huang and J. B. Goodenough, in *Solid Oxide Fuel Cell Technology*, Woodhead Publishing Limited, Cambridge, 2009, ch. 1.
307. G. A. Hughes, K. Yakal-Kremski, A. V. Call and S. A. Barnett, *Journal of The Electrochemical Society* **2012**, 159, F858-F863.
308. R. Williams, in *The Geometrical Foundation of Natural Structure?: A Source Book of Design*, New York: Dover, 1979, ch. 2.3, pp. 49.
309. R. M. Ormerod, *Chemical Society Reviews* **2003**, 32, 17-28.
310. S. C. Paulson and V. I. Birss, *Journal of The Electrochemical Society* **2004**, 151, A1961-A1968.
311. S. P. Jiang and X. Chen, *International Journal of Hydrogen Energy* **2014**, 39, 505-531.
312. A. Hauch, S. D. Ebbesen, S. H. Jensen and M. Mogensen, *Journal of The Electrochemical Society* **2008**, 155, B1184-B1193.
313. L. Holzer, B. Iwanschitz, T. Hocker, B. Münch, M. Prestat, D. Wiedenmann, U. Vogt, P. Holtappels, J. Sfeir, A. Mai and T. Graule, *Journal of Power Sources* **2011**, 196, 1279-1294.
314. V. Brichzin, J. Fleig, H. U. Habermeier, G. Cristiani and J. Maier, *Solid State Ionics* **2002**, 152–153, 499-507.
315. A. Ghosh, A. K. Sahu, A. K. Gulnar and A. K. Suri, *Scripta Materialia* **2005**, 52, 1305-1309.
316. D. W. Ni, K. B. Andersen and V. Esposito, *Journal of the European Ceramic Society* **2014**, 34, 3769-3778.
317. Sigma Aldrich Corporation, *Nickel(II) oxide*, https://www.sigmaaldrich.com/catalog/product/aldrich/637130?lang=en&region=GB,

(accessed 21st March, 2018).

318. Sigma Aldrich Corporation, *Nickel*, https://www.sigmaaldrich.com/catalog/product/aldrich/577995?lang=en&region=GB, (accessed 21st March, 2018).
319. A. Bieberle and L. J. Gauckler, *Solid State Ionics* **2000**, 135, 337-345.
320. E. A. Clark, R. Yeske and H. K. Birnbaum, *Metallurgical Transactions A* **1980**, 11, 1903-1908.
321. S. P. Jiang and J. G. Love, *Solid State Ionics* **2001**, 138, 183-190.
322. J. T. Richardson, R. M. Scates and M. V. Twigg, *Applied Catalysis A: General* **2004**, 267, 35-46.
323. P. Briois, F. Lapostolle, V. Demange, E. Djurado and A. Billard, *Surface and Coatings Technology* **2007**, 201, 6012-6018.
324. I. Thormählen, J. Straub and U. Grigull, *Journal of Physical and Chemical Reference Data* **1985**, 14, 933-945.
325. N. H. Perry, S. Kim and T. O. Mason, *Journal of Materials Science* **2008**, 43, 4684-4692.
326. B. B. Owen, R. C. Miller, C. E. Milner and H. L. Cogan, *The Journal of Physical Chemistry* **1961**, 65, 2065-2070.
327. D. W. van Krevelen, in *Propeties of Polymers*, Elsevier, Amsterdam, 3rd edn., 1990, ch. 11, pp. 319-352.
328. S. Asakura and F. Oosawa, *Journal of Polymer Science* **1958**, 33, 183-192.
329. A. Hartridge, M. G. Krishna and A. K. Bhattacharya, *Journal of Physics and Chemistry of Solids* **1998**, 59, 859-866.
330. M. Mogensen, N. M. Sammes and G. A. Tompsett, *Solid State Ionics* **2000**, 129, 63-94.
331. A. A. Al-Ghamdi, W. E. Mahmoud, S. J. Yaghmour and F. M. Al-Marzouki, *Journal of Alloys and Compounds* **2009**, 486, 9-13.
332. K. V. Rao and A. Smakula, *Journal of Applied Physics* **1965**, 36, 2031-2038.
333. M. P. Fewell, Australian Government Department of Defense, *Area of Common Overlap of Three Circles* 2006.
334. Croda Europe Ltd, Homecare Report: *Natsurf 265*, 2013.
335. E. Perry Murray, M. J. Sever and S. A. Barnett, *Solid State Ionics* **2002**, 148, 27-34.
336. V. Dusastre and J. A. Kilner, *Solid State Ionics* **1999**, 126, 163-174.
337. R. Fernández-González, T. Molina, S. Savvin, R. Moreno, A. Makradi and P. Núñez, *Journal of the European Ceramic Society* **2014**, 34, 953-959.

338. L. W. Tai, M. M. Nasrallah, H. U. Anderson, D. M. Sparlin and S. R. Sehlin, *Solid State Ionics* **1995**, 76, 273-283.
339. S. Badwal, D. Fini, F. Ciacchi, C. Munnings, J. Kimpton and J. Drennan, *Journal of Materials Chemistry A* **2013**, 1, 10768-10782.
340. S. B. Adler, *Solid State Ionics* **1998**, 111, 125-134.
341. H. J. M. Bouwmeester, H. Kruidhof and A. J. Burggraaf, *Solid State Ionics* **1994**, 72, 185-194.
342. J. Nielsen, T. Jacobsen and M. Wandel, *Electrochimica Acta* **2011**, 56, 7963-7974.
343. Y. Xu, N. Farandos, M. Rosa, P. Zielke, V. Esposito, P. Vang Hendriksen, S. H. Jensen, T. Li, G. Kelsall and R. Kiebach, *International Journal of Applied Ceramic Technology* **2018**, 15, 315-327.

14. Appendices

14.1. Appendix 1: DLVO Theory for Aqueous Dispersions

Between adjacent YSZ particles dispersed in water, *i.e.* i = 1 = 2 = YSZ, i = 3 = H_2O, the Hamaker constant can be calculated by modifying equation (62), as shown in equation (88).

$$A_H = \frac{3}{4} k_B T \left(\frac{\chi_{\mathrm{YSZ}} - \chi_{\mathrm{INK}}}{\chi_{\mathrm{YSZ}} + \chi_{\mathrm{INK}}}\right)^2 + \frac{3 h_p \psi_n}{8\sqrt{2}} \left(\frac{(\lambda_{\mathrm{YSZ}}{}^2 - \lambda_{\mathrm{INK}}{}^2)^2}{\sqrt{(\lambda_{\mathrm{YSZ}}{}^2 + \lambda_{\mathrm{INK}}{}^2)^2 (2\lambda_{\mathrm{YSZ}}{}^2) + \sqrt{(\lambda_{\mathrm{YSZ}}{}^2 + \lambda_{\mathrm{INK}}{}^2)}}} \right) \quad (88)$$

The refractive indices of YSZ and the ink continuous medium (approximated as water) for a photon at the limit of the visible light range (380 nm wavelength) are 2.15 and 1.34, respectively (323, 324). The dielectric constant of YSZ is *ca*. 25 (325). To approximate the dielectric constant of the solvent medium, an arithmetic average of H_2O (χ = 78.4) and PEG 35000 ($\chi \simeq$ 2.5) was taken, to give χ_{INK} = 40 (326, 327). Therefore, $A_H = 1.5\times10^{-20}$ J.

For the SA YSZ particles, r_p = 97 μm, μ = 4.7 mPa s, and for the YSZ solids loading of 24 wt% (Ink 1), the YSZ loading was 5 vol%. The measured zeta potential of YSZ particles in 10 mM aqueous KCl was *ca*. -45 mV. Approximating the size of a dissolved PEG 35000 molecule as 0.25 nm, with a molecular weight of 35000 kg $kmol^{-1}$, the depletion potential can be calculated according to equation (63) (328). Combining all interaction potentials, the total interaction energy between a pair of YSZ particles dispersed in the ink is shown in **Figure 102**.

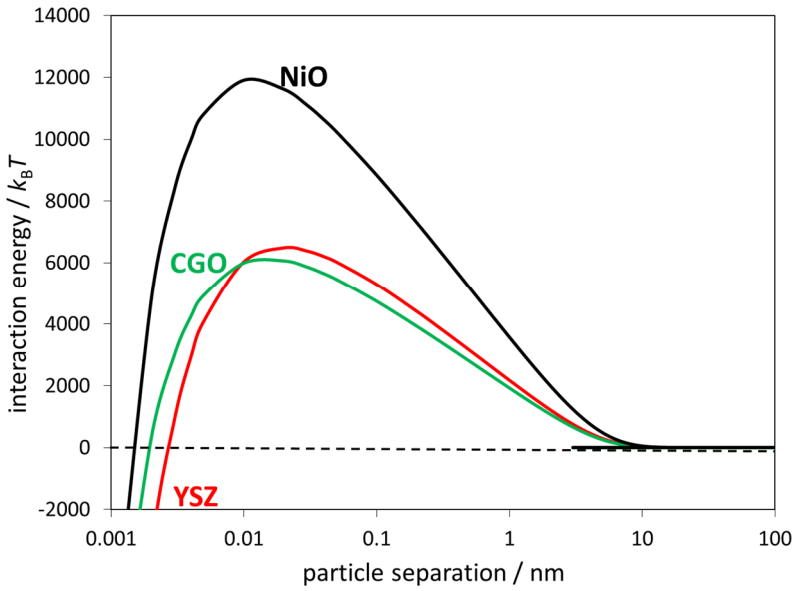


Figure 102. Variation of interaction energy with inter-particle separation between pairs of YSZ, CGO, and NiO particles in their respective ink formulations.

The refractive index (800 nm wavelength) and dielectric constant for CGO are 1.74 and 11, respectively (329, 330). The refractive index (800 nm wavelength) and dielectric constant (at 298 K) for NiO are *ca*. 1.7, and 11.9, respectively (331, 332). Therefore, with measured zeta potentials, the interaction energy between NiO and CGO particle pairs was also estimated using the DLVO Theory model, as shown in **Figure 102**.

The maximum energy barriers against aggregation for the YSZ, CGO, and NiO inks were 6380, 6070, and 11900 k_BT, respectively; the corresponding dispersion half-lives, calculated by numerically integrating the interaction potentials, as shown in equation (70), were all essentially infinite.

14.2. Appendix 2: Modelling Centrifugation

Separation of aggregates with $r_p > 400$ nm was achieved via centrifugation. Larger aggregates sediment due to centrifugation with a greater velocity than small aggregates, as predicted by the Stokes equation. Modifying the Stokes equation to include the relative centrifugal force (RCF), as shown in equation (89), and specifying that the lager particles must be separated out from the ink in ≤ 120 s, it was possible to calculate the required RCF. Assuming the height of ink in the centrifugation tube was 12 cm and the height of the sediment is negligible in comparison, in order for the aggregates of $r_p > 400$ nm at the top of the ink to sediment in 120 s in an aqueous medium with $\mu = 1.1$ mPa s adjusted for particle content, $u_s = 0.001$ m s^{-1}. This required an RCF of 700 as shown in equation (90). **Figure 103** shows a comparison for the RCF required, as a function of centrifugation duration, for particles of different maximum permissible sizes.

$$u_s = \frac{4{r_p}^2 \Delta\rho g}{18\mu} \rightarrow \frac{4{r_p}^2 \Delta\rho g(\mathrm{RCF})}{18\mu} \quad (89)$$

$$\mathrm{RCF} = \frac{18\mu u_s}{4{r_p}^2 \Delta\rho g} \approx \frac{18 \times 1.1 \times 10^{-3} \times 0.001}{4 \times (400 \times 10^{-9})^2 \times 4500 \times 9.81} = 700 \quad (90)$$

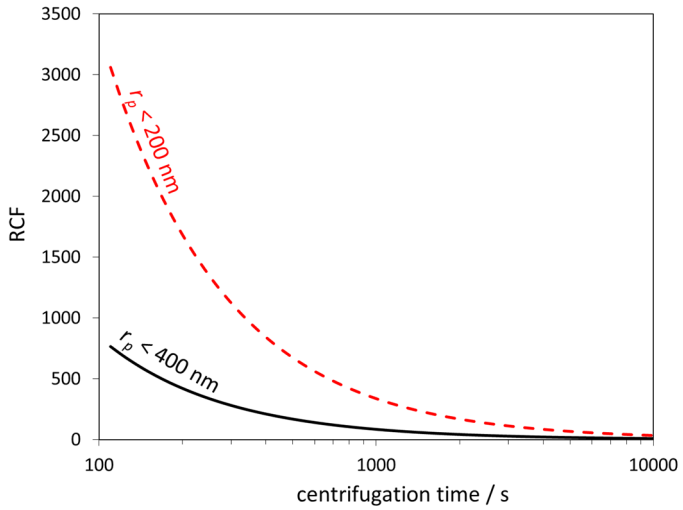


Figure 103. The RCF required to separate aggregates from a dispersion for two maximum particle sizes, $r_p < 400$ nm, and $r_p < 200$ nm. As expected, larger particles require a lower RCF for a given centrifugation duration than smaller particles.

14.3. Appendix 3: Particle Surface Coverage

The CAD software allowed both square and hexagonal droplet deposition lattices within inkjet printed shapes, where the surface droplet coverage could be increased by introducing an overlap between adjacent droplets on the substrate. Assuming droplet properties were equivalent to the bulk ink, the properties of a single droplet were known (*i.e.* volume fraction and particle size), and D_i and D_m could be measured. Therefore, to predict droplet coverage on the substrate surface, properties should be normalised to a single droplet.

Normalising the droplet radius, after settling on the substrate (assuming no splashing occurred) *i.e.* D_m, to unity, the area overlap between coordinated droplets was calculated (essentially the area of two identically-sized segments, calculated with the standard segment area formula) and is shown in **Table 22**. To calculate the total area of overlap for a single splat, *i.e.* number of droplets per droplet area within a single layer, the overlap between coordinated droplets need be multiplied only by the lattice coordination number, equal to 4 and 6 for square and hexagonal lattices, respectively.

Table 22. The overlapped area for varying droplet diameter overlap, for both square and hexagonal droplet deposition lattices (between pairs and 3 droplets), as a fraction of a single droplet (projected) area.

Droplet diameter overlap / %	Square area overlap (pairs) / %	Hexagonal area overlap (pairs) / %	Hexagonal area overlap (triplets) / %*
10	4	4	0
20	10	9	5
30	19	8**	31

* The three-droplet overlap was calculated using the circular triangle equation reported in reference (333); ** the overlap between pairs decreased because a higher fraction of the overlap area was between triplets.

The surface coverage (*SC*), defined as the ratio of the particles total projected area within a single droplet to the area of a single droplet splat (*i.e.* the number of particle monolayers of coverage), could be calculated, assuming the particles are hexagonally close packed on the substrate, *i.e.* a particle in-plane fraction of 0.91, as shown by equation (91). The lattice coordination number and overlap between pairs (i = 2) and triplets (i = 3) are represented by β and A_i, respectively.

$$SC = \frac{N_p\left(\pi {r_p}^2\right)}{\pi {D_m}^2 / 4} \frac{1}{0.91}\left(1 + \beta \sum_{2}^{3} A_i\right) = \frac{N_p {r_p}^2}{{D_m}^2} \frac{4}{0.91}\left(1 + \beta \sum_{2}^{3} A_i\right) \quad (91)$$

Where N_p is the number of particles deposited per splat, *i.e.* the number of particles per droplet, which could be calculated using equation (92), assuming particles were spherical with a uniform radius.

$$N_p = \frac{\varphi_0 \frac{4}{3}\pi\left(\frac{D_i}{2}\right)^3}{\frac{4}{3}\pi {r_p}^3} = \frac{\varphi_0 {D_i}^3}{8{r_p}^3} \quad (92)$$

Combining equations (91) and (92), an expression relating *SC* with droplet, particle, and ink properties, is derived (93).

$$SC = \frac{\varphi_0 {D_i}^3}{r_p {D_m}^2}\frac{1}{1.82}\left(1 + \beta \sum_2^3 A_i\right) \quad (93)$$

Values for A_i are given in **Table 22**.

14.4. Appendix 4: Natsurf 265 Surface Tension Effects

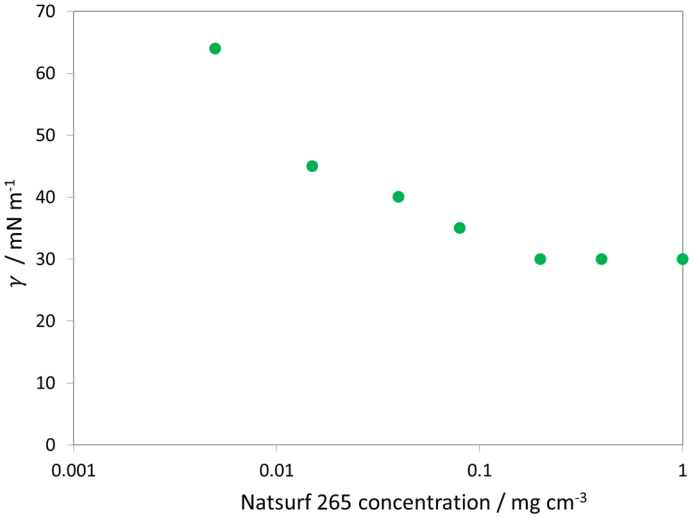


Figure 104. Relationship between surface tension and aqueous Natsurf 265 (Croda, UK) concentration. Data from (334).

14.5. Appendix 5: Critical Cracking Thickness Calculations

Equation (76) was used to calculate the critical cracking thicknesses for the ink formulations, using relationships from the literature to predict the effective shear modulus (G_S) and Poisson's ratio (ζ_p), as shown by equations (94) and (95), respectively (269).

$$G_S = \frac{G_0\left(1-\varepsilon_p\right)^2}{1+\varepsilon_p\left(\frac{11-19\zeta_0}{4+4\zeta_0}\right)} \quad (94)$$

$$\zeta_p = 0.25\frac{4\zeta_0+3\varepsilon_p-7\varepsilon_p\zeta_0}{1+2\varepsilon_p-3\varepsilon_p\zeta_0} \quad (95)$$

ε_p represents the particle porosity, determined from BET measurements. G_0 and ζ_0 for YSZ are equal to 83.3 GPa and 0.316, respectively.

14.6. Appendix 6: Evaluating Infinite Shear Rate Viscosity

As ink is ejected through printhead nozzles, it experiences extremely high shear rates that are unobtainable with the concentric cylinder viscometer that was used for all viscosity measurements in this research project. Therefore, for highly shear-thinning inks, the viscosity at the printhead nozzle conditions had to be estimated for predictions of ink printability. This was done graphically, where data points were converted into a linear form, as shown (for the CGO ink reported in Section 5.2) in **Figure 105**. Using MS Excel software (Microsoft, USA) to fit a linear trend line to the points, as shown, the *y*-axis intercept could be found, and used to estimate infinitely-high shear rate viscosity.

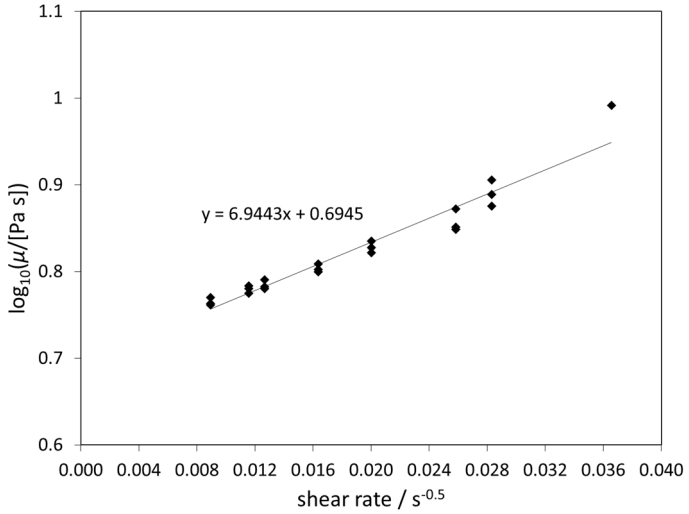


Figure 105. Linear viscosity – shear rate relationship.

14.7. Appendix 7: Formulation of Aqueous LSCF Ink

14.7.1. Introduction

$La_{0.6}Sr_{0.4}Co_{0.2}Fe_{0.8}O_{3-x}$ (LSCF) is a mixed ionic – electronic conductor with high activity to oxygen reduction / oxidation kinetics at low temperatures; therefore, it is an attractive oxygen-electrode material for low temperature SOERs. Like other cobalt-containing compounds, they react chemically with YSZ at high temperature to form insulating phases (335), and consequently a chemically-inert CGO barrier layer is often deployed. To facilitate sintering and reduce electrode polarisation, composite CGO-LSCF electrodes are usually deployed (336), and consequently, for LSCF dispersed in water, it must be negatively charged to avoid hetero-coagulating with CGO (**Figure 42**). The isoelectric point of LSCF was identified as *ca*. pH 6 (**Figure 106a**), and addition of the ammonium salt of the polyacrylic acid Duramax 3005 (Rohm and Haas, USA) facilitated colloidal stability at alkaline conditions (**Figure 106b**), at which solubility of the constituent elements in water was low (**Figure 106c**).

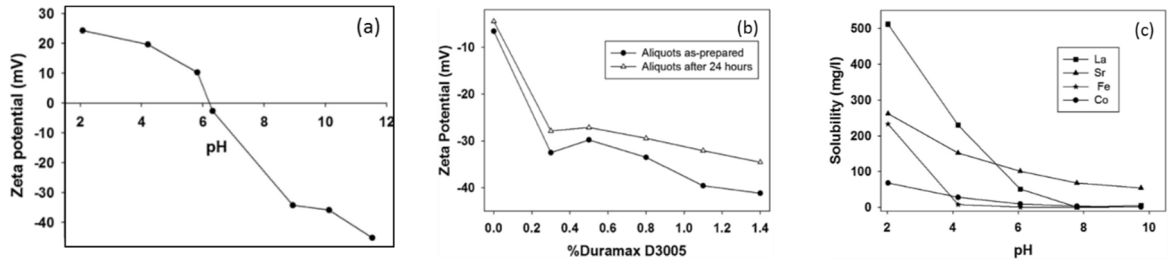


Figure 106. Zeta potential variation with (a) pH; (b) Duramax 3005 concentration at pH 6.8 – 8; and (c) solubility of the constituent elements with varying pH (10^{-2} mol dm^{-3} KCl). Reproduced with permission from (337).

The PSD of the LSCF particles was too large for inkjet printing, and the physical properties were adjusted for use in tape casting, which is very different to inkjet printing. In addition, the LSCF was sintered to itself, however, in a practical device it would have to sinter to (pre-sintered, highly dense) CGO barrier layers. Therefore, the remainder of this Section concerns the development and inkjet printing of an aqueous LSCF ink used to fabricate the oxygen-electrode of SOERs, and preliminary printing and heat treatment results.

14.7.2. Materials and Methods

LSCF (Fuel Cell Materials, USA) was dispersed in de-ionised water using an ultrasonication probe. Dispersion pH was adjusted using aqueous ammonia. PSD was measured by DLS after centrifugation at 1300 RCF for 1 minute, and syringe filtering (450 nm, Cole Parmer, UK).

Surface area was measured by BET. Four electrostatic dispersants were trialled for LSCF, and are described in **Table 23**. Final mass fractions were determined by TGA.

Table 23. Summary of dispersants trialled for aqueous LSCF dispersions.

Dispersant	Description	Manufacturer
Dispex A40	Polyacrylic acid salt	BASF, Germany
Disperbyk 2012	Amine	BYK Additives Ltd, UK
Dispex Ultra FA 4416	Alcohol	BASF, Germany
Duramax D3005	Polycarboxylate	Rohm and Haas (Dow Chemicals), USA

After mixing appropriate volumes of the optimised LSCF ink developed in this Section with the CGO ink developed in Section 5.2 for a final CGO:LSCF ratio of 1:1, 50 layers of the colloidally-stable, printable CGO-LSCF ink were inkjet printed using a Dimatix DMC 10 pL printhead (Fujifilm, USA) onto a sintered NiO-YSZ|YSZ|CGO substrate (see Appendix 8: Preliminary Electrochemical Characterisation of Inkjet Printed CGO Functional Layers) with a square droplet deposition lattice, D_m = 80 μm and droplet overlap of 50 %. The resultant structure was heated to 600 °C for 2 h to combust organics, then to 1150 °C for 3 hours, and finally cooled to room temperature; all temperature ramp rates were 4 °C min^{-1}.

14.7.3. Results and Discussion

The mass-specific surface area of the LSCF particles was 9.4 m^2 g^{-1}. Dispex A40 and Disperbyk-2012 appeared to reduce the stability of the LSCF particles (at concentrations up to 100 mg m^{-2}) and sedimentation was observed within minutes, presumably due to non-adsorbance to the particle surface and resulting (attractive) depletion potentials. The zeta potentials measured for the other dispersants across a pH range from 9.5 to 11.8 are shown in **Figure 107a**. Evidently, Duramax 3005 resulted in the greatest colloidal stability at pH 9.5. However, this is predicted to decrease over time, as shown by **Figure 106b**, which could become problematic if inks require a long shelf-life.

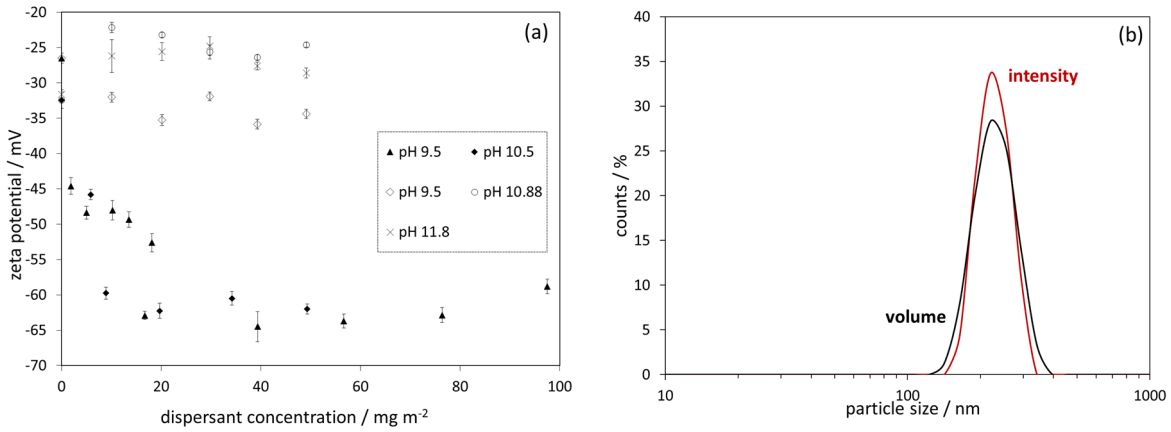


Figure 107. (a) Zeta potential variation of LSCF particles with varying dispersant concentration and pH in water: Dispex Ultra FA 4416 (no-fill markers) and Duramax D3005 (filled black markers); and (b) PSD of the LSCF particles.

To adjust physical properties for printability for the pure LSCF dispersion, 10 mg cm^{-3} PEG 35000 and 0.2 mg cm^{-3} Natsurf 265 were added, to increase viscosity and decrease surface tension, respectively. Using 20 mg m^{-2} Duramax D3005, the resulting solid loading, ρ, η, and γ were 13 wt%, 1.15 g cm^{-3}, 8.0 mPa s (taken as the infinite shear rate viscosity as it was shear thinning as shown in **Figure 108**), and 28 mN m^{-1}, respectively. After mixing with the aqueous CGO ink and homogenising with the ultrasonication probe, the viscosity was too low, therefore the PEG 35000 concentration was adjusted to 20 mg cm^{-3}, resulting in a more-Newtonian viscosity, as shown in **Figure 108**. The resulting Oh^{-1} number was 4.4, indicating printability. The optimal ejection profile was 10 to -10 V over 5 µs, lowering the voltage further to -30 V over 5 µs, raising the voltage to 50 V over 5 µs, dwelling for 5 µs, before decreasing the voltage to 10 V over 5 µs; droplet ejection frequency was 500 Hz.

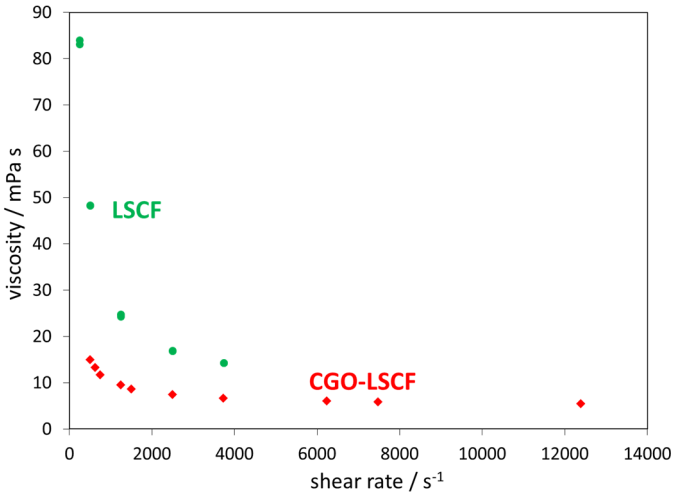


Figure 108. Viscosity – shear rate relationship for LSCF and composite CGO-LSCF inks.

After inkjet printing and sintering, a photograph of the CGO-LSCF surface was taken, shown in **Figure 109a** at high magnification. The CGO-LSCF appeared to form clusters which were cracked extensively, leaving much of the CGO substrate below uncovered. There did not appear to be a radial relationship with the cracking in the CGO-LSCF deposit (**Figure 109b**), which occurred with inkjet printed NiO films in Section 5.4. Therefore, cracking was not believed to be a result of shrinkage during sintering (the volume fraction of LSCF within the printed deposit was 50 vol% (*c.f.* ρ_{LSCF} = 7.14 g cm^{-3}, ρ_{CGO} = 7.2 g cm^{-3} (338, 339)), but occurred during (traumatic) dispersant combustion which destroyed the CGO-LSCF film.

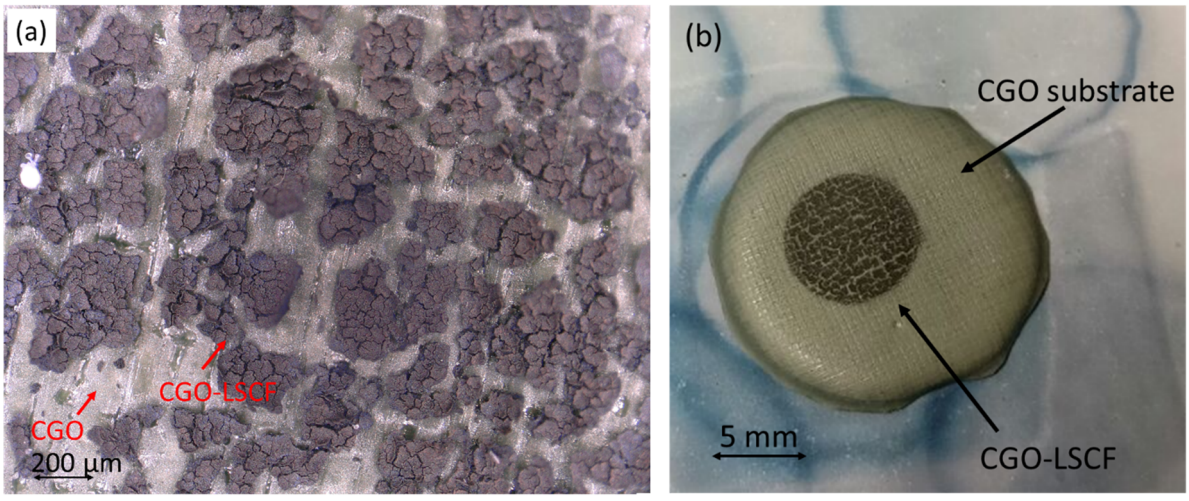


Figure 109. Surface-view photographs of the sintered CGO-LSCF layer.

14.8. Appendix 8: Preliminary Electrochemical Characterisation of Inkjet Printed CGO Functional Layers

The aqueous CGO ink developed in Section 5.2 was used to inkjet print the barrier layer of the SOER: Ni-YSZ|YSZ|CGO|CGO-LSCF to determine its utility for reversible SOERs.

14.8.1. Materials and Methods

Eight layers of the YSZ 'Ink 1' developed in Section 5.1 were inkjet printed onto a NiO-YSZ substrate, fabricated as described in Section 5.1.1.3, to produce a NiO-YSZ|YSZ substrate using an identical printing procedure as described in Section 6.2.1 (without application of the YSZ-LSM electrode). Eight layers of the aqueous CGO ink developed in Section 5.2 were inkjet printed subsequently onto the NiO-YSZ|YSZ structure using the Dimatix Q-Class Sapphire printhead (Fujifilm, USA). The splat diameter, droplet overlap, and deposition lattice, were 80 μm, 40 %, and square, respectively. The droplet ejection profile was identical to that described in Section 5.2. After drying, the resulting structure was co-sintered, with an identical temperature profile as reported in Section 5.2.2.4.

$La_{0.6}Sr_{0.4}Co_{0.2}Fe_{0.8}O_{3-x}$ (LSCF, Fuel Cell Materials, USA) and CGO particles were dispersed separately in butanol at mass concentrations of 30 wt%, each. Polyvinyl butyral (Butvar B-98, Sigma Aldrich, USA) was added at a concentration of 10 mg cm^{-3} as a binder and thickener to each dispersion. After centrifugation at 1200 RCF for 4 minutes, and subsequent filtering with a 450 nm syringe filter (Cole Parmer, UK), mass concentrations were determined using TGA as 6 and 16 wt%, for LSCF and CGO, respectively. The PSD for LSCF after centrifugation and filtering is shown in **Figure 107b**; the average size was 220 nm, and therefore not expected to block the printhead nozzles. The PSD for the CGO particles was shown in **Figure 43**.

A composite ink was then made with CGO:LSCF in a 1:1 mass ratio to aid sintering and reduce electrode polarisation (336). Stability was confirmed by the absence of visible sedimentation over a period of 3 months. The total solids loading, ρ, η, γ, and Oh^{-1} were 9 wt%, 1.11 g cm^{-3}, 5.0 mPa s (Newtonian), 30 mN m^{-1}, and 5.2, respectively.

A Dimatix DMC 10 pL droplet volume printhead (Fujifilm, USA) was used to deposit 140 layers (50 % diameter overlap) of the CGO-LSCF onto the sintered NiO-YSZ | YSZ | CGO structure to fabricate the oxygen-electrode. The voltage ejection profile was: 15 to 0 V over 2 μs, a rise to 40 V over 2 μs, remaining at 40 V for 2 μs, and finally back to 15 V over 2 μs. The structure was heated to 600 °C for 2 hours at 2 °C min^{-1}, then to 1050 °C for 2 hours at 2.5 °C min^{-1}, and finally cooled to room temperature at 5 °C min^{-1}.

The SOER was mounted into the experimental equipment with the procedures outlined in **Table 13**, modified to include a steam generator (Bronkhorst, Netherlands, setting 80 °C) with electric line heaters from the source to the reactor, set at 120 °C. Prior to electrochemical characterisation, the NiO in the fuel-electrode was reduced with an identical procedure to that described in Section 6.2.2. The SOER was electrochemically characterised using two-probes in a H_2-H_2O-He mixture with flow rates 22.5, 40, and 21.7 cm^3 min^{-1}, respectively, by electrochemical impedance spectroscopy and current density measurements with varying cell potential difference at 10 mV s^{-1}, over a range of operating temperatures.

14.8.2. Results and Discussion

The thicknesses of the post sintered YSZ, CGO, and CGO-LSCF layers were 16, 6, and 9 μm, respectively, which were determined from the SEM photomicrograph shown in **Figure 110**. Each layer appeared to be well adherent to adjacent layers; large pores were present within the CGO barrier layer as in Section 8.3.4. The normalised thickness of each printed LSCF layer was 65 nm; the thicknesses of the inkjet printed YSZ and CGO layers were approximately equal to those reported in Sections 5.1 and 5.2, respectively.

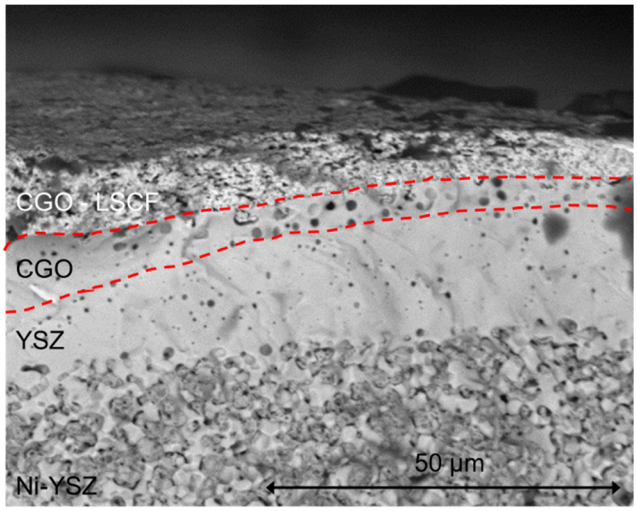


Figure 110. Cross-sectional SEM photomicrograph of the NiO-YSZ|YSZ|CGO|CGO-LSCF SOER.

The open circuit potential differences were measured as 0.911 - 0.897 V at 660 - 788 °C, which were close to the theoretical values (**Figure 13**), indicating the electrolyte and sealant were gas-tight. Electrochemical characterisation results are shown in **Figure 111**. Compared to the electrochemical performance of inkjet printed YSZ-LSM electrodes (Chapter 7), the performance of the CGO-LSCF electrodes was significantly lower, *ca*. 90 % lower current densities. Although the electrolyte was approximately twice as thick, at the low current densities

achieved here the overpotential loss through the electrolyte and barrier layers would be insignificant, and as the NiO-YSZ substrate was identical to previous experiments, the CGO-LSCF functional layer was responsible for the loss in performance. The discontinuities in the *j* – *U* plot at 660 °C were attributed to poor current collector contact with the electrode(s), which was mitigated at higher temperatures due to sintering of Ag to the electrode(s), and its thermal expansion, increasing the interfacial area for electron conduction.

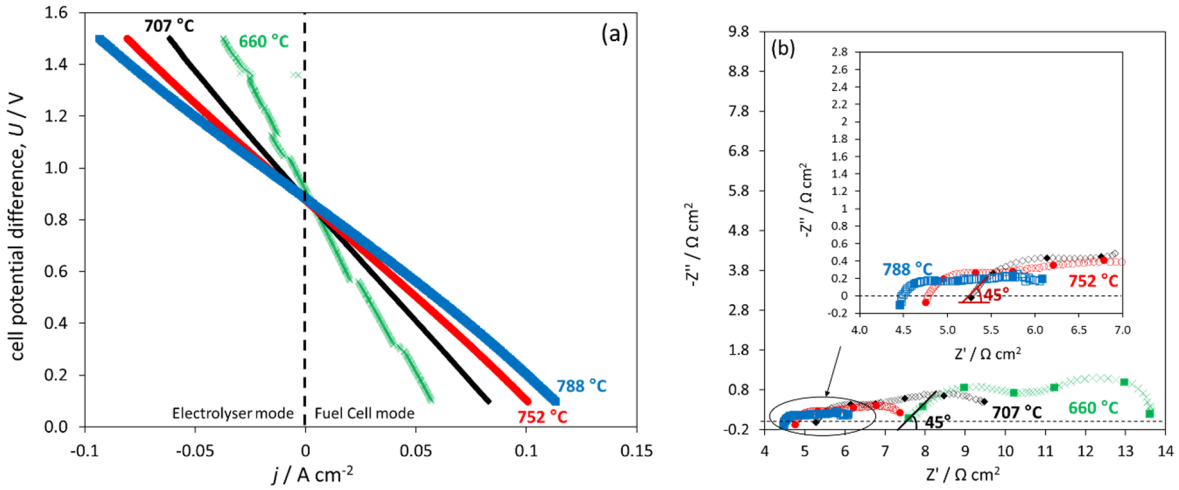


Figure 111. (a) Cell potential difference variation with current density and temperature; and (b) Nyquist plots at OCPD at each operating temperature, filled markers indicate decade intervals in frequency.

The inkjet printed CGO-LSCF electrode was only 9 μm thick, however the electro-active thickness of LSCF-based, and similar mixed ionic – electronic conductors (*i.e.* $La_{0.6}Ca_{0.4}Co_{0.8}Fe_{0.2}O_{3-\delta}$, $La_{0.6}Sr_{0.4}Co_xNi_{1-x}O_{3-\delta}$) electrodes is known to be (significantly) greater (depending on microstructure) (340, 341); therefore, for future experiments the number of printed layers should be increased.

Two arcs were evident for each Nyquist plot, at characteristically different summit frequencies reported in **Table 24**. Summit frequencies for the high and low-frequency arcs indicate that they corresponded to an O^{2-} ion exchange and a diffusion process, respectively, with approximately equal contributions to the total SOER polarisation at each temperature.

Table 24. Summit frequencies for the arcs in the Nyquist plots in **Figure 111b**.

T / °C	High-frequency arc / Hz	Low-frequency arc / Hz
660	630	2
707	1000	0.63
752	1260	1
788	2000	1

At 660 and 707 °C, Warburg behaviour can be seen at high frequencies, evidenced by the 45° slope in the Nyquist plots. This suggests that the impedance follows Gerischer-like behaviour, where at high frequencies the performance is controlled by an oxygen reaction on the LSCF surface (342). This result is consistent with appropriately-thick electrodes. However, Warburg behaviour in the 752 and 788 °C Nyquist plots is not observed, and only a small fraction of the polarisation resistance was present at < 1 Hz. Therefore, as mass transport is not performance limiting, any oxygen partial pressure gradient within the CGO-LSCF electrode may be neglected, and it may be concluded that performance was limited by an insufficiently-thick CGO-LSCF electrode.

14.9. Appendix 9: Electrochemical Characterisation of YSZ-LSM SOERs

The additional electrochemical characterisations for the SOFCs operating on dry H_2, reported in Chapter 7, are given in **Figure 112**.

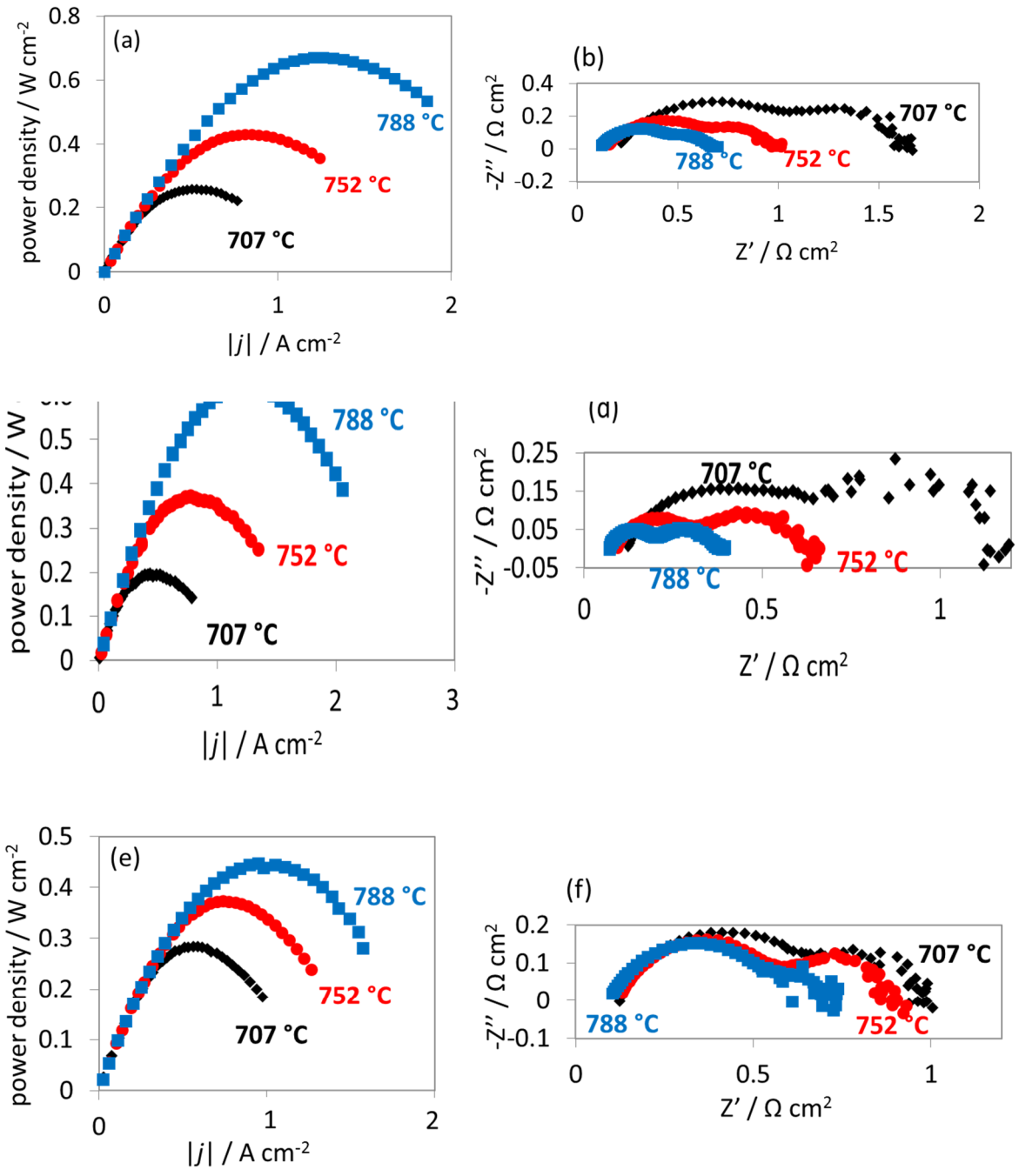


Figure 112. Electrochemical characterisations of SOFCs with inkjet printed YSZ-LSM electrode sintered at 1100 °C (a,b), and 1200 °C (c-f). Each set of results was obtained from a different SOFC.

To facilitate analysis of the Nyquist plots in the main report, complementary Bode plots are presented in **Figure 113a** and **Figure 113b**, for the cathodes sintered at 1100 and 1200 °C, respectively.

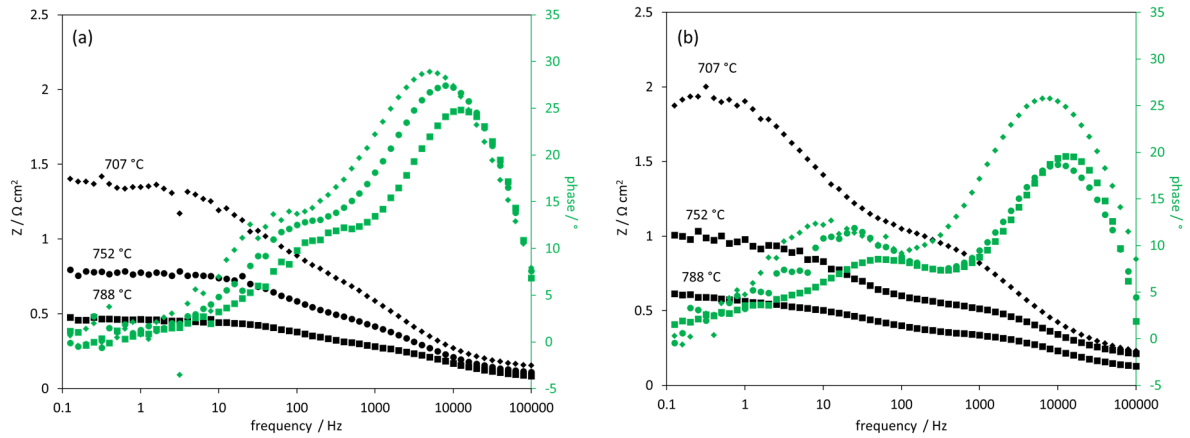


Figure 113. Bode plots for cathodes sintered at (a) 1100; and (b) 1200 °C at OCPD and varying operating temperature.

14.10. Appendix 10: Effect of Scan Rate on CO_2 Reduction Measurements

For CO_2 electrolyser mode, the SOER potential difference scan rate was increased to 60 mV s^{-1}, compared to 20 mV s^{-1} for H_2 fuel cell mode. This did not significantly effect the current density measurements, as shown in **Figure 114**, for CO_2 electrolysis conditions at 707 °C.

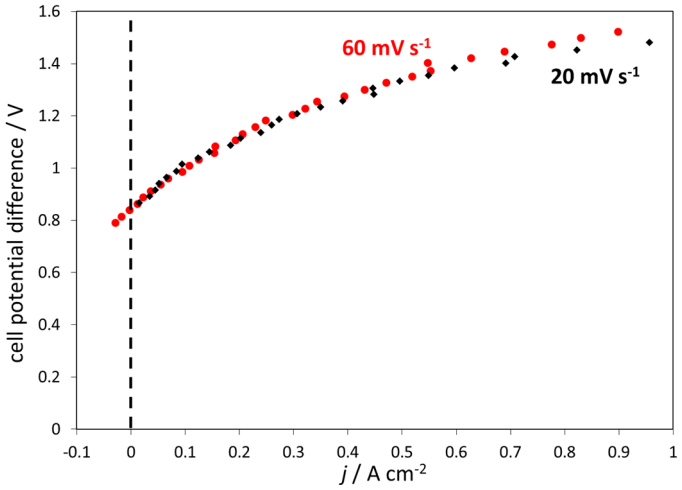


Figure 114. Effect of current density on SOER potential difference, for 20 and 60 mV s^{-1} cell potential difference scan rate.

14.11. Appendix 11: Reduction of Oxygen-electrode Overpotential with pO_2

The equation for the O_2 / O^{2-} reduction / oxidation reaction is given in equation (42); therefore, the latter part of this equation shows how overpotential changes with oxygen partial pressure. Considering the pressure build-up in a non-percolating pore during electrolysis, the decrease in overpotential (at 750 °C operating temperature) has been plotted in **Figure 115**, assuming an oxygen mole fraction within the non-percolating pore of unity. Even at a pore pressure of 100 bar, the decrease in overpotential is < 0.14 V, and consequently, O_2 is likely to continue to be evolved into the pore.

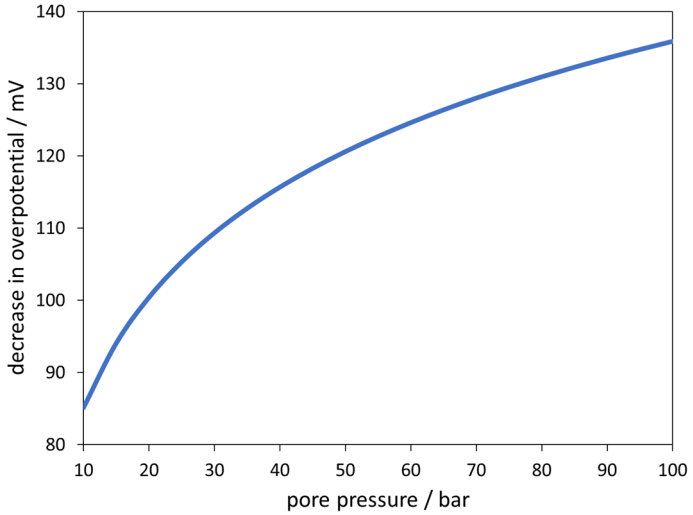
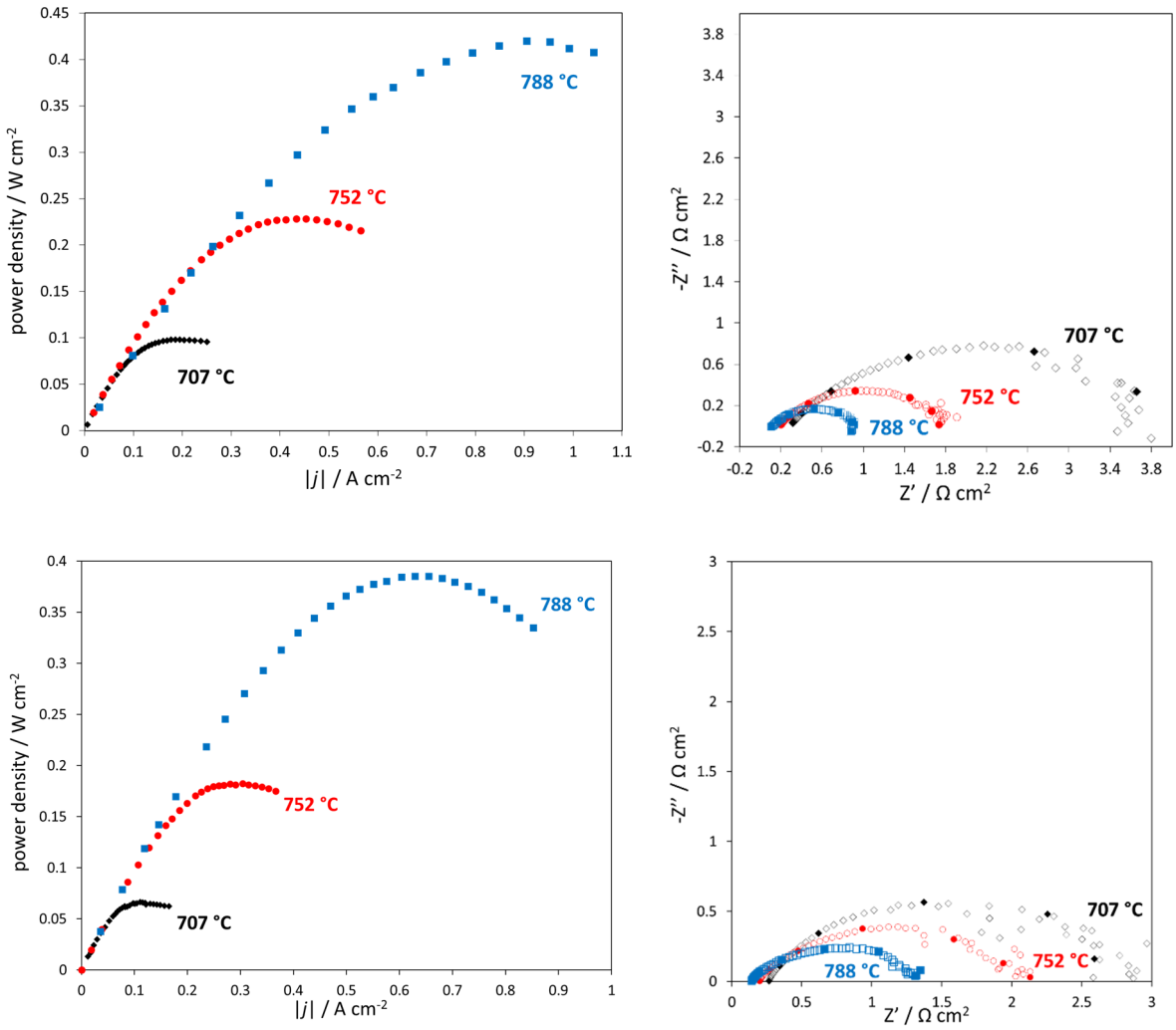


Figure 115. Predicted decrease in O^{2-} ion oxidation reaction overpotential with local O_2 pressure.

14.12. Appendix 12: Electrochemical Characterisations of Pillar-array Oxygen-electrodes

Additional SOERs with pillar array electrodes, with LSM sintered at 1100 °C were characterised electrochemically, under identical conditions as those reported in Chapter 10. The results for fuel cell and electrolysis operation are shown in **Figure 116**, where each row corresponds to an individual SOER.

H_2 -air



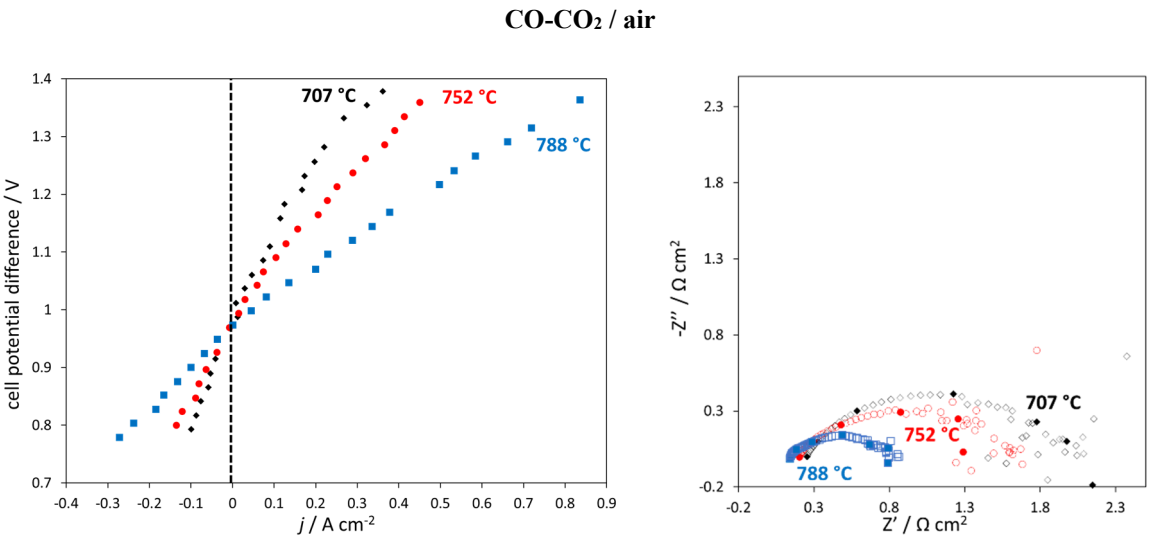


Figure 116. Fuel cell / electrolysis mode power / current densities for different SOERs with LSM sintered at 1100 °C, together with corresponding Nyquist plots at OCPD, where decade intervals are denoted by filled markers between 0.1 – 10^5 Hz.

14.13. Appendix 13: Collaboration with the Department of Energy Conversion and Storage, Technical University of Denmark (DTU)

14.13.1. Introduction

Several researchers at the Department of Energy Conversion, DTU, were interested in fabricating solid oxide electrochemical reactors using inkjet printing, primarily to fabricate thin electrolytes and barrier layers. After I visited DTU during April 2017, I supplied them with printable, aqueous-based YSZ and CGO inks, with the formulations described in Sections 5.1 and 5.2, respectively, which they used to develop their own inkjet printing process.

In addition, the group at DTU supplied me with an aqueous CGO nanoparticle dispersion, which had been produced via a continuous hydrothermal flow synthesis process. My contribution to inkjet printing these particles is outlined in the remainder of this Appendix sub-section. The results of this collaboration ultimately resulted in a publication (343).

14.13.2. Materials and Methods

The as-supplied CGO nanoparticle dispersion was concentrated via evaporation, resulting in a CGO mass fraction of 7 wt%. For printability, 10 mg cm^{-3} PEG 35000 was added, to raise the viscosity, which was essentially Newtonian, and equal to 2.1 mPa s. Surface tension was decreased immediately prior to printing using Natsurf 265 (0.2 mg cm^{-3}), and was measured as 27.2 mN m^{-1}, and the ink density was 1.08 g cm^{-3}. Using the Dimatix DMC (10 pL nominal droplet volume) printhead (Fujifilm, USA), the resulting Oh^{-1} number was 12. Although this was outside of the conventionally-accepted limit of printability, droplet ejection was satisfactory for printing thin CGO films. The optimised printer settings were 0 – 50 V over 5 µs, hold for 5 µs, decrease to 10 V over 5 µs, hold for 5 µs, and decrease to 0 V over 5 µs. Droplet ejection frequency was 3.48 kHz (100 mm s^{-1} printhead speed). Droplet splat diameter and overlap were 80 and 50 µm, respectively, for a square droplet deposition lattice.

The substrate was equivalent to the NiO-CGO prepared by Dr. Tao Li, described in Section 5.2.1.3.

Three sets of films, of 1, 5, 10, and 20 layers were inkjet printed onto the substrate to produce squares of 7 mm side length. 4 minute drying intervals were left between successive layers, without which extensive cracking occurred in all printed films. After printing and drying, the films and substrate were co-sintered with the following temperature profile: 0-650 °C at 4 °C min^{-1}; dwell for 4 hours, 650-1300 °C at 15 °C min^{-1}; dwell for 8 hours. For some samples,

the temperature was raised to 1500 °C at 15 °C min^{-1}; dwell for a further 8 hours, before cooling to room temperature at 4 °C min^{-1}.

14.13.3. Results and Discussion

Figure 117 shows surface-view photographs of the printed CGO films, before sintering. Evidently, cracking was extensive at > 5 printed layers. This cracking occurred during the drying process, and was a consequence of the very small CGO particle size (*ca*. 11 nm), which significantly reduced the critical cracking thickness, as explained in Section 5.1.2.

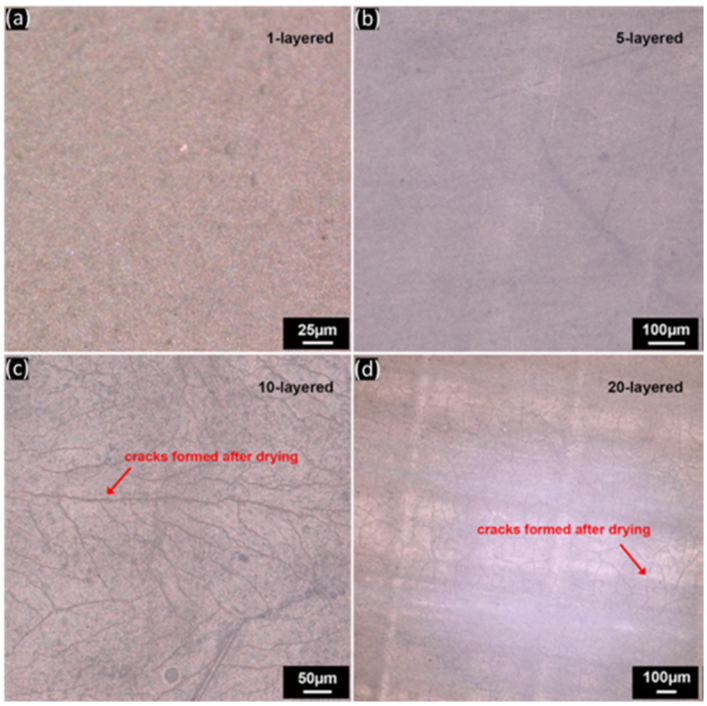


Figure 117. Surface view photographs of the pre-sintered CGO film (a) 1; (b) 5; (c) 10; and (d) 20 layers thick. Reproduced with permission from (343).

After sintering the films, microstructures were imaged using SEM (LEO Gemini 1525 field emission gun SEM, Zeiss, Germany), by Dr. Tao Li, Imperial College London. The results are shown in **Figure 118**. At 1300 °C, CGO film density was very low, despite the primary CGO particles being smaller than comparative sintering studies, so the sintered film would be unsuitable for a gas-tight electrolyte. Increasing the sintering temperature to 1500 °C, film density was high, although some pin holes were observed on the surface. It is unknown whether the pin holes penetrated through the CGO film depth. Consequently, the 5 layer CGO film sintered at 1500 °C could find utility as a barrier layer between YSZ and LSCF.

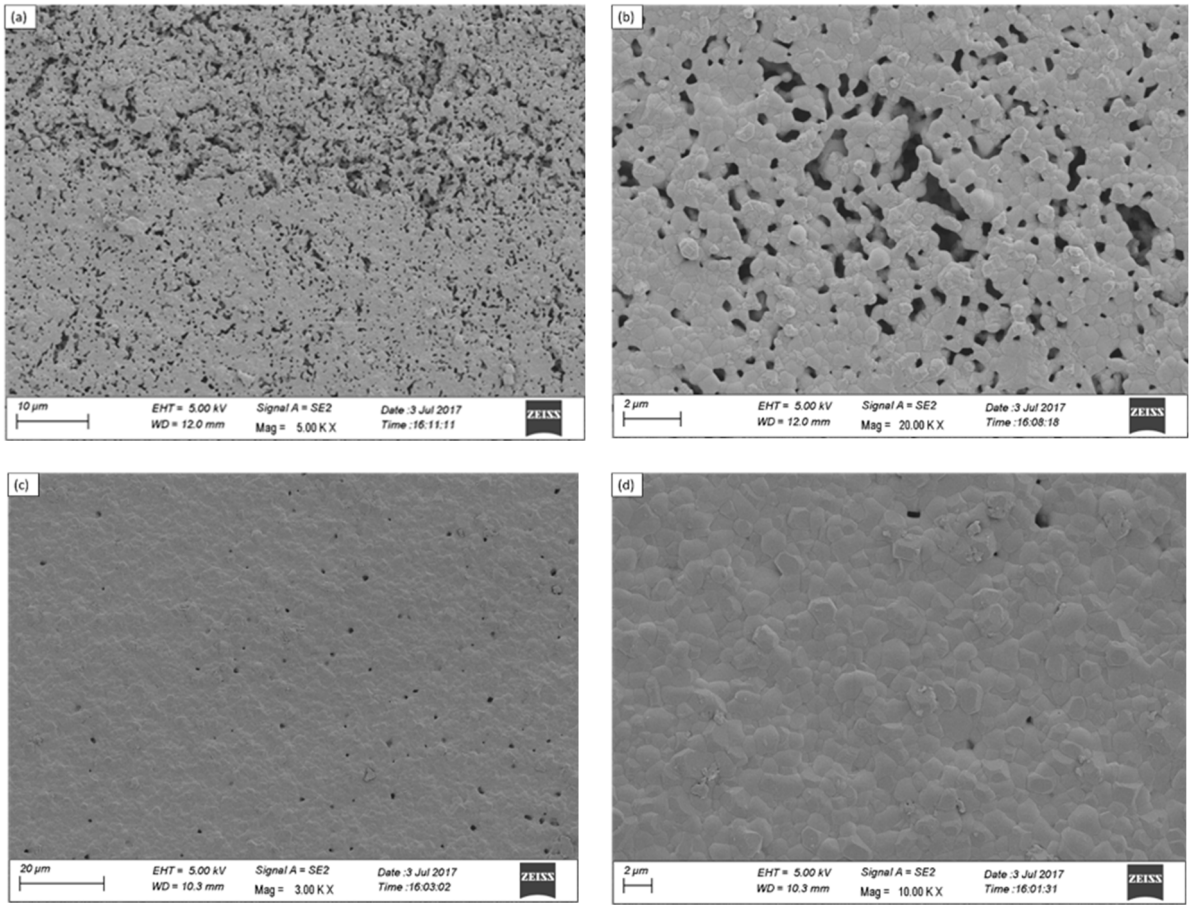


Figure 118. SEM micrographs of the sintered 5-layer CGO film at (a, b) 1300; and (c, d) 1500 °C.

For additional details on particle preparation, results and discussion, the reader is referred to the published article (343).

15. Re-use of Content from the Literature

Where figures or tables within the main Thesis were reproduced from the literature, permission was sought from the copyright holders to reproduce the content in this Thesis. These are given, with reference order numbers from the publishers when provided, in **Table 25**.

Table 25. Granted copyright permissions for re-use of content from the literature.

Caption label and number	Page number	Reference	Permission granted	Comments
Figure 3b	28	(15)	Yes	Permission granted via email exchange
Figure 4	29	(19)	Yes	Permission granted via email exchange
Figure 6	33	(33)	Yes	Elsevier license number: 4302491134948
Figure 7	37	(70)	Yes	Reproduced under the Creative Commons License (https://creativecommons.org/licenses/by/4.0/)
Figure 10	42	(52)	Yes	Reproduced under the Creative Commons License (https://creativecommons.org/licenses/by/4.0/)
Figure 15	56	(112)	Yes	Elsevier license number: 4302500465984
Figure 17	61	(137)	Yes	Elsevier license number: 4302501051905
Figure 22	71	(203)	Yes	Elsevier license number: 4302501438553
Figure 24	77	(185)	Yes	Elsevier license number: 4302510579289
Figure 25	84	(170)	Yes	Elsevier license number: 4302590339120
Figure 26	86	(251)	Yes	Elsevier license number: 4302590737382
Figure 27	88	(249)	Yes	Elsevier license number: 4302591099541
Figure 28	89	(250)	Yes	Elsevier license number: 4302971463125
Figure 29	90	(247)	Yes	Elsevier license number: 4302980329053
Figure 30	93	(246)	Yes	John Wiley and Sons license number: 4302980802323
Figure 32	95	(252)	Yes	John Wiley and Sons license number: 4302981222983
Figure 33	107	(261)	Yes	Elsevier license number: 4302990456986
Figure 35	111	(145)	Yes	

Figure 36	112		Yes	Reproduced under the Creative Commons License (https://creativecommons.org/licenses/by/4.0/)
Figure 37	114		Yes	
Figure 40	119	(275)	Yes	Elsevier license number: 4303000789732
Figure 47	128	(281)	Yes	Elsevier license number: 4303001177154
Figure 49	133	(280)	Yes	Reproduced under the Creative Commons License (https://creativecommons.org/licenses/by/4.0/)
Figure 56	138			
Figure 58	143	(291, 292)	Yes	Reproduced with permission from the American Chemical Society
			Yes	Elsevier license number: 4303010281693
Figure 67	154		Yes	
Figure 68	155	(145)	Yes	
Figure 69	155		Yes	
Figure 70	156		Yes	
Figure 71	161		Yes	
Figure 72	162		Yes	Reproduced under the Creative Commons License (https://creativecommons.org/licenses/by/4.0/)
Figure 73	164	(280)	Yes	
Figure 74	164		Yes	
Figure 75	166		Yes	
Figure 76	167		Yes	
Figure 77	172	(145)	Yes	
Figure 78	173		Yes	
Figure 106	241	(337)	Yes	Elsevier license number: 4321361337376
Figure 117	256	(343)	Yes	John Wiley and Sons license number: 4341880525497